

UNIVERSITY OF RIJEKA
FACULTY OF CIVIL ENGINEERING

Ivana Ban

**A Model for Skid Resistance Prediction
Based on Non-Standard Pavement Surface
Texture Parameters**

DOCTORAL THESIS

Rijeka, 2023.

UNIVERSITY OF RIJEKA
FACULTY OF CIVIL ENGINEERING

Ivana Ban

**A Model for Skid Resistance Prediction
Based on Non-Standard Pavement Surface
Texture Parameters**

DOCTORAL THESIS

Supervisor: prof. dr. sc. Aleksandra Deluka-Tibljaš

Co-supervisor: izv. prof. dr. sc. Igor Ružić

Rijeka, 2023.

SVEUČILIŠTE U RIJECI
GRAĐEVINSKI FAKULTET

Ivana Ban

**Model predikcije hvatljivosti temeljen na
nestandardnim parametrima teksture
kolnika**

DOKTORSKI RAD

Rijeka, 2023.

SVEUČILIŠTE U RIJECI
GRAĐEVINSKI FAKULTET

Ivana Ban

**Model predikcije hvatljivosti temeljen na
nestandardnim parametrima teksture
kolnika**

DOKTORSKI RAD

Mentorica: prof. dr. sc. Aleksandra Deluka-Tibljaš

Komentor: izv. prof. dr. sc. Igor Ružić

Rijeka, 2023.

Mentorica rada: prof.dr.sc. Aleksandra-Deluka Tibljaš

Komentor rada: izv.prof.dr.sc. Igor Ružić

Doktorski rad obranjen je dana _____ na Građevinskom fakultetu u Rijeci,
pred Povjerenstvom u sastavu:

1. doc. dr. sc. Sanja Šurdonja

Sveučilište u Rijeci Građevinski fakultet, predsjednica

2. izv. prof. dr. sc. Ivana Barišić

Sveučilište J. J. Strossmayera u Osijeku, Građevinski i arhitektonski fakultet, članica

3. prof. dr. sc. Ivica Kožar

Sveučilište u Rijeci Građevinski fakultet, član

Acknowledgments

Zahvale

Abstract

The research presented in this thesis focused on the development of a prediction model for friction performance of asphalt pavements quantified as skid resistance, accounting for the non-standard texture parameters. Pavement friction results from a complex interplay of many influencing parameters that can be grouped in four distinct groups: surface roughness properties, driving properties, vehicle tire properties and environmental influences. Surface roughness properties were selected as the key influencing factor in this research. There are two specific texture roughness scales relevant for pavement's friction performance: micro-texture and macro-texture. Current standardized practice enables the determination of macro-texture indicators, commonly related to friction performance measured on the roads. Despite the effort to establish a relationship between the standard texture indicators and friction performance, there still exists no unique model which would provide a reliable and unambiguous prediction of friction from the traditionally determined texture roughness properties.

To investigate the relationship between pavement friction performance and surface roughness on both relevant texture scales, an alternative method based on remote sensing technology was developed in this thesis. The method utilized a digital camera for the acquisition of multiple pavement surface images from a close range, further used for the creation of a 3D digital surface model. The method was called Close-Range Orthogonal Photogrammetry - CROP method. Created 3D digital surface models enabled the analysis of multiple roughness parameters on micro- and macro-texture levels. The CROP method was optimized for the data acquisition procedure, photographic equipment used and procedure for digital surface model processing and analysis. The accuracy of CROP method was verified by performance comparison to a benchmark technology for 3D digital model creation – a high precision 3D laser scanner. Selected non-standard texture parameters were used as predictors in the development of a friction prediction model, performed in regression analysis framework. Friction performance was quantified by skid resistance measurements of the analysed surfaces, performed by a stationary low-speed measurement device. Four different regression-based models were established and compared for the model performance assessment, accounting for the model predictive strength evaluated by coefficient of determination values and selected error metric. The optimal model was defined by partial least squares regression, with two non-standard texture parameters selected as the most influential for the prediction of pavement surface friction performance. In comparison to the performance of simple linear regression model

accounting for a single traditional texture indicator Mean Profile Depth, the model developed in the thesis obtained better performance for the prediction of skid resistance.

Keywords: *pavement friction, skid resistance, pavement texture, experimental analysis, close-range photogrammetry, digital surface models, non-standard texture parameters, regression analysis framework, partial least squares, prediction model*

Sažetak

Istraživanje predstavljeno u ovom doktorskom radu usmjereno je na razvoj modela predikcije hvatljivosti, uzimajući u obzir nestandardne parametre teksture kolnika. Hvatljivost na kolniku složen je fenomen koji proizlazi iz međusobnog djelovanja mnogih utjecajnih parametara koji se mogu grupirati u četiri različite skupine: svojstva hrapavosti površine, svojstva vožnje, svojstva pneumatika vozila i utjecaji okoliša. Svojstva hrapavosti površine odabrana su kao ključni utjecajni faktor u ovom istraživanju. Dvije su specifične razine hrapavosti teksture relevantne za hvatljivost: mikrotekstura i makrotekstura. Standardizirana praksa omogućuje određivanje pokazatelja makroteksture, koji se uobičajeno povezuju sa izmjerenim svojstvom hvatljivosti na kolniku. Unatoč naporima da se uspostavi odnos između standardnih pokazatelja teksture i hvatljivosti, još uvijek ne postoji jedinstveni model koji bi pružio pouzdano i nedvosmisleno predviđanje hvatljivosti iz tradicionalno određenih svojstava hrapavosti teksture.

Kako bi se istražio odnos između hvatljivosti kolnika i hrapavosti površine na obje relevantne razine teksture, u ovom je doktorskom radu razvijena alternativna metoda temeljena na tehnologiji daljinskih istraživanja. U metodi je korištena digitalna kamera za prikupljanje većeg broja fotografija površine kolnika iz neposredne blizine, koje se dalje koriste za izradu trodimenzionalnog digitalnog modela površine. Metoda je nazvana Close-Range Orthogonal Photogrammetry (Ortogonalna fotogrametrija bliskog dometa) - CROP metoda. Izrađeni trodimenzionalni digitalni modeli površina omogućili su analizu nekoliko parametara hrapavosti na razini mikro i makro teksture. CROP metoda optimizirana je za postupak prikupljanja podataka, korištenu fotografsku opremu te postupak obrade i analize digitalnog modela površine. Točnost CROP metode potvrđena je usporedbom sa referentnom tehnologijom za kreiranje 3D digitalnog modela – 3D laserskim skenerom visoke preciznosti. Odabrani nestandardni parametri teksture korišteni su kao ulazni parametri u razvoju modela predikcije hvatljivosti, izvedenog u okviru regresijske analize. Hvatljivost je kvantificirana mjerenjem otpora klizanja analiziranih površina standardnim stacionarnim mjernim uređajem pri malim brzinama. Četiri različita regresijska modela uspostavljena su i uspoređena za procjenu izvedbe modela, uzimajući u obzir snagu predviđanja modela procijenjenu iz koeficijenta determinacije i odabrane metrike pogreške. Optimalni model definiran je djelomičnom regresijom najmanjih kvadrata, s dva nestandardna parametra teksture odabranima kao najutjecajnijima za predviđanje hvatljivosti. U usporedbi sa jednostavnim modelom linearne regresije, koji uzima u obzir samo srednju dubinu profila kao tradicionalni

indikator teksture, model predikcije hvatljivosti razvijen u ovom doktorskom radu postigao je bolju izvedbu.

Ključne riječi: *trenje na kolniku, otpor klizanju, tekstura kolnika, eksperimentalna analiza, fotogrametrija bliskog dometa, digitalni modeli površine, nestandardni parametri teksture, regresijska analiza, djelomični najmanji kvadrati, model predviđanja*

Content

Acknowledgments.....	I
Zahvale	I
Abstract	II
Sažetak.....	IV
1. Introduction.....	2
1.1. Research background.....	3
1.2. Friction terminology explication	5
1.3. Problem statement and research aims.....	6
1.4. Research scope and limitations.....	7
1.5. Thesis outline.....	8
2. Pavement friction	11
2.1. Friction force and coefficient of friction	12
2.2. Contact mechanics on rough surfaces	13
2.2.1. Rough contact theories.....	14
2.2.2. Rubber friction theories	16
2.2.3. Numerical methods for rough contact mechanics.....	19
2.3. Friction mechanisms on pavement surfaces	20
2.4. Factors affecting pavement friction.....	23
2.4.1. Pavement surface properties	24
2.4.2. Environmental impacts	24
2.4.3. Driving parameters.....	25
2.4.4. Tire properties	27
2.5. Measurement and characterization of pavement friction	28
2.5.1. Pavement friction measurement methods	28
2.5.2. Pavement friction indicators	34

2.5.3. Pavement friction performance evaluation in Croatia	39
2.6. Existing models for pavement friction prediction	40
2.6.1. Analytical models	42
2.6.2. Numerical models	42
2.6.3. Empirical models	45
2.6.3.1. Simple empirical prediction models.....	45
2.6.3.2. Complex empirical prediction models	47
2.6.3.3. Empirical models with texture as the main influencing parameter.....	48
2.7. Pavement friction – summary.....	50
3. Pavement texture properties related to friction.....	52
3.1. Pavement texture definition and classification	53
3.2. Pavement micro-texture properties.....	56
3.3. Pavement macro-texture properties	59
3.4. Macro-texture evaluation by standard measurement methods	62
3.4.1. Standard macro-texture measurement devices.....	63
3.4.2. Macro-texture performance evaluation.....	65
3.4.3. Pavement macro-texture prediction models.....	68
3.5. Alternative methods for pavement surface texture characterization	71
3.5.1. Profile-related and surface-related parameters from European standards EN ISO 21920-2 and EN ISO 25178-2	72
3.5.2. Mathematical representations of texture roughness features	77
3.6. Advanced methods for pavement texture data assessment.....	79
3.6.1. Photometric methods	79
3.6.2. Laser scanning methods.....	86
3.7. Pavement texture properties related to friction performance - summary	91
4. Preliminary investigation of pavement texture – friction relationship .	94
4.1. Friction and texture data collection	95

4.2. Data analysis.....	97
4.3. Discussion.....	100
5. Methodology development for pavement texture data analysis	101
5.1. Photogrammetry method applicability for pavement texture characterization	102
5.1.1. Asphalt specimen properties and friction performance evaluation.....	102
5.1.2. Selection of data acquisition procedure	104
5.1.3. Surface roughness characterization for created digital surface model (DSM)	108
5.2. CROP method performance testing	112
5.2.1. Image acquisition and DSM creation.....	113
5.2.2. Resulting DSM properties.....	115
5.2.3. Surface roughness features analysis.....	117
5.2.3.1. DPC properties and profile extraction settings optimization	117
5.2.3.2. Profile geometry and roughness analysis	120
5.2.3.3. Comparison of texture parameters values	122
5.3. Verification of the proposed CROP method.....	126
5.3.1. 3D laser scanning procedure and the resulting DSM properties.....	129
5.3.2. Photogrammetry procedure and resulting DSM properties	131
5.4. Discussion.....	140
6. Development of a friction performance prediction model.....	144
6.1. Application of CROP method - field investigation	146
6.1.1. Friction data collection	147
6.1.2. Texture data collection and determination of surface texture parameters	149
6.2. Exploratory data analysis (EDA).....	153
6.2.1. Friction data analysis	153
6.2.2. Profile-related texture data analysis.....	154
6.2.3. Surface – related texture parameters.....	159
6.2.4. Correlation analysis.....	168

6.3. Multiple linear regression (MLR) models	171
6.3.1. Basic multiple linear regression (MLR) model	172
6.3.2. Feature engineering (FE) procedures	175
6.3.2.1. Ridge regression	179
6.3.2.2. PCA regression.....	180
6.3.2.3. PLS regression.....	182
6.3.3. Multiple polynomial regression (MPR)	184
6.4. Discussion.....	186
6.5. Machine learning methods for friction prediction model development	188
6.5.1. Application of Support Vector Regression (SVR) algorithm	192
6.5.2. Application of Random Forest (RF) regression algorithm	195
6.5.3. Discussion	198
7. Conclusions and further research perspectives	199
7.1. Discussion of the overall research results.....	200
7.2. Research limitations	205
7.3. Final conclusions	206
7.4. Future research perspectives.....	207
List of Figures	208
List of Tables.....	212
References	216
Curriculum Vitae	237

1. Introduction

This Chapter provides a brief description of the research problem investigated in this thesis. The relevance of the pavement friction performance for traffic safety is addressed as the main motivation for the research. The defined research aims and hypotheses are given, together with the scope of this research. A brief description of research methodology is given. A textual description and graphical summary of the thesis structure is presented at the end of the introductory chapter.

1.1. Research background

Traffic safety of road users is, together with the road capacity, the most important functional feature when the motorized road traffic is considered. Three main influencing factors are responsible for adequate traffic safety: drivers' behaviour, vehicle properties and road properties (*Bilten o sigurnosti cestovnog prometa*, 2021). More than half of traffic accidents in Croatia are caused by drivers' behaviour (57%), and in combination with road properties drivers are responsible for 35% of severe traffic accidents (*Nacionalni plan sigurnosti cestovnog prometa RH*, 2021). Most traffic accidents with serious health or fatal outcomes occur when the driving speed is not adjusted to given traffic conditions, either speed limit, weather conditions or road surface conditions (39%). To address the drivers' behaviour as the main influencing factor for road safety improvements, national regulations are directed towards the increase of driving culture by strictly penalizing the most severe traffic violations (*Bilten o sigurnosti cestovnog prometa*, 2021). As the negative behavioral effect could never be fully excluded, European policies for road safety adopted the so-called „Safe System Approach“ (SSA), accounting for policies and measures which will be „forgiving“ for road users and reduce the negative effect of drivers' risky behaviour (*Transport Research Centre*, 2008).

The SSA has four key factors: safe infrastructure, safe road usage, safe vehicles and fast and efficient emergency services. Safe infrastructure is the key factor relevant for civil engineering practices dealing with safe road geometry and pavement design. It includes measures and activities pointed towards the reduction of severe traffic accidents. Safety inspection and analysis of existing and new roads by regular monitoring campaigns where road functional properties related to traffic safety are analysed is one of the activities defined in the Croatian national plan for road safety (*Nacionalni plan sigurnosti cestovnog prometa RH*, 2021).

There are multiple elements of road infrastructure that have to be considered in the process of planning, design, construction and maintenance of safe road infrastructure. Pavement surface friction is one of the most important functional features as it directly impacts the safety of road users (Wambold et al., 1995). It is a physical phenomenon occurring on the contact between the vehicle tire and pavement surface, which controls the stability of the vehicle in motion and contributes to vehicle stopping when a braking maneuver is applied. Insufficient friction between the vehicle tire and pavement surface results in an uncontrolled vehicle motion and disables the driver to stop the vehicle, which could lead to road accidents with negative

financial, health or fatal outcomes. Therefore, the adequate friction performance is an important aspect of road safety management under jurisdiction of road agencies.

Friction performance on roads is mostly quantified by a non-dimensional friction coefficient, resulting from the friction force that occurs on the contact surface between the vehicle and pavement (Hall et al., 2009). The magnitude of friction coefficient depends on many influential parameters, which can be categorized into four main groups: pavement surface properties, driving properties, vehicle tire properties and environmental conditions. The parameters that can be defined and controlled by pavement engineering practice are related to the pavement surface properties. The most relevant surface features related to friction are roughness characteristics, defined by pavement texture. Pavement texture is categorized by different texture levels, where each level governs a certain driving effect (Wambold et al., 1995). Two texture levels related to friction performance are micro- and macro-texture, defined by certain wavelength and amplitude range and resulting from the properties of pavement constituent materials and construction methods (Kogbara et al., 2016).

Pavement friction performance is regularly monitored on roads by standardized measurement procedures and evaluated by defined threshold values of friction coefficient, specific for each country and defined by national regulations. Inadequate friction performance reduces the safety level and contributes to an increased risk of traffic accidents occurrence. Besides friction, texture level is also monitored as a part of pavement performance evaluation. Texture measurements produce a single texture indicator, mostly on macro-texture level. They are not affected by any influencing factor but provide a geometrical description of roughness feature, which makes them an objective descriptor of friction related pavement performance (Kogbara et al., 2016; Wang et al., 2011).

The intention to relate friction performance with pavement texture has been a focal point of numerous research dealing with pavement friction phenomenon (Fwa, 2021). To do so, prediction models were developed in numerical and empirical framework. These models account for a single texture property evaluated by traditional measurement methods or include the effect of other influencing factors, such as vehicle speed, traffic load effect or environmental conditions. The quality of developed models varies significantly, from no predictive strength to almost perfect prediction based on included influencing parameters. There exists no uniquely applicable prediction model, especially in case where influencing parameters other than texture were included in the model development. When the model is established only from the

traditionally evaluated texture properties, the predictive strength of the model is usually weak. The reason is the generalization of surface roughness features to a single indicator, which cannot describe the true effect that texture has on the friction performance.

In recent two decades, the effect of texture roughness to friction performance has been investigated by remote sensing technologies (Matlack et al., 2023; Yu et al., 2020). These technologies provide a more detailed insight to pavement surface morphology and enable the extraction of roughness parameters on texture micro- and macro-scale, used for friction prediction models establishment. Two most common technologies used for pavement texture analysis are photogrammetry and laser scanning which enable the creation of 3D digital surface models, further analysed in terms of roughness properties related to friction. In comparison to the friction prediction models developed from the traditional texture characterization methods, the models where alternative roughness parameters are the predictors obtained better performance (Q. J. Li et al., 2020&2017).

1.2. Friction terminology explication

Two different terms can be found in the literature regarding the pavement surface frictional performance: pavement friction and skid resistance (*ROSANNE Project Deliverable D4.1*, 2014). Pavement friction is a term related to the physical phenomenon, describing the grip developed on the contact between a particular road surface and vehicle tire, influenced by a number of parameters. Skid resistance refers to the road surface's contribution to the frictional performance determined by a standardized measurement procedure, performed under dry or wet surface conditions. The measurement result is expressed as „skid number“. In general, the term “friction” represents the phenomenon itself and the term “skid resistance” represents the pavement surface's functional property related to the measured frictional performance.

This research is focused on the investigation of pavement surface friction performance affected by surface roughness properties. Friction performance was evaluated by a standard measurement procedure in dry surface conditions, resulting in friction indicator called Skid Resistance Tester number. The term „skid resistance“ was used in the thesis title as the prediction models for friction performance developed in this research were established on dry surface skid resistance measurements. However, the term „pavement friction“ will be used further in the thesis as a synonym to „skid resistance“, for the sake of simplicity and broader analysis of pavement frictional properties presented in Chapters 2 and 3.

1.3. Problem statement and research aims

The main objective of this research is the prediction of pavement friction performance based on texture properties. The initial idea was motivated by the availability of measurement equipment for texture characterization in the Transportation laboratory of Faculty of Civil Engineering Rijeka. The intention was to utilize the traditional measurement methods to relate measured pavement texture with friction performance. Several measurement campaigns were performed in cooperation with Croatian road agencies, resulting in a large database of friction and texture values collected on different types of roads and under different climatic conditions. The goal was to develop a friction prediction model based on texture indicators derived from traditional measurement methods. Texture measurements were simpler than friction measurements, as they did not require any additional resources such as water supply or traffic regulation during the measurement procedure and provided indicators which are objective representation of texture roughness features. Conducted analyses however did not result in a significant or reliable friction prediction model (Pranjić et al., 2020).

To address the problem of defining a friction prediction model from texture roughness features, the analysis of an advanced method for a detailed texture characterization was done. The method is based on photogrammetry, an image-based measurement methodology which enables the interpretation of the relevant properties extracted from the digital reconstruction of an object captured by images (Luhmann et al., 2006). A special case of photogrammetry, called close-range photogrammetry was utilized in this research for pavement surface texture data collection on sub-millimeter scale.

The results of the preliminary research of texture-friction relationship establishment by traditional measurement methods and the potential of photogrammetry method for a detailed pavement texture roughness description formed the main research aim of this thesis - to establish a reliable prediction model for friction performance based on non-standard texture parameters, derived from the digital pavement surface representation produced by close-range photogrammetry method.

To reach this aim, following research goals were defined:

- 1.) Establish a photogrammetry-based data collection procedure which will produce digital surface representations with sufficient precision and accuracy for the analysis of pavement texture morphology on relevant texture scales. By defining a suitable data collection procedure, pavement texture features could be extracted from the reconstructed digital surface models.

2.) Determine the texture roughness parameters with a significant influence on pavement friction performance.

3.) Define a friction prediction model in regression analysis framework by using selected texture roughness parameters as model predictors. Several models were proposed and evaluated by selected performance measures to determine the optimal model.

The defined research aim and corresponding research goals were pointed towards the confirmation or rejection of the following thesis hypotheses:

H1: *Close-range photogrammetry based method is suitable for the determination of non-standard pavement texture parameters.*

H2: *Non-standard pavement texture parameters enable a more detailed description of surface roughness properties related to the pavement friction performance in comparison to traditional texture descriptors.*

H3: *Non-standard pavement texture parameters can be used for the definition of a friction prediction model which is more reliable in comparison to the prediction models defined from traditional texture indicators.*

1.4. Research scope and limitations

Pavement friction is addressed as a highly complex phenomenon influenced by many parameters and a complete understanding of the friction mechanism on tire-pavement interface would be reachable if all the influential factors were considered. The research scope in this thesis was limited to investigation of pavement texture properties related to friction performance. The roughness characteristics were investigated at two texture levels relevant for friction: macro-texture and to a certain extent micro-texture, following the technical limitations of utilized equipment for data collection.

To reach the defined research aim and the corresponding research goals, a thorough investigation of advanced photogrammetry-based method for data acquisition was conducted, including the analysis of the method's performance in different data acquisition setups. The relative camera position to the pavement's surface, number of acquired images and differences in photographic equipment used were evaluated. The properties of pavement surface's digital models created by different data acquisition setups were analyzed to evaluate the performance

of method's variants. The optimal method was verified by a selected benchmark remote sensing technology for small-scale measurements.

The development of a friction prediction model based on non-standard texture parameters obtained by advanced texture measurement method was done in regression analysis framework, which was found to be suitable for the determination of cause-effect relationships and predictions from two or more variables determined empirically, in this case the texture parameters and friction performance (Uyanık & Güler, 2013).

1.5.Thesis outline

The research activities and results obtained in this thesis are structured in seven chapters: Introduction, Pavement friction, Pavement texture properties related to friction, Preliminary research of texture-friction relationship, Development of CROP method, Development of friction prediction model and Research conclusions and further plans (Figure 1.1).

The *Introduction* chapter (1) summarizes the relevance of the problem, defined research aim and hypothesis, research scope and limitations and provides a schematic overview of thesis content. The chapter *Pavement friction* (2) is a state-of-the-art overview of the friction phenomenon in general and in the context of pavement functional performance. It provides a thorough analysis of the influencing factors, measurement methods and friction performance characterization incorporated in national regulations in Croatia, European Union and worldwide. In this chapter, existing friction performance prediction models are analysed and uniquely classified to simple and complex prediction models, with respect to the number of influencing parameters they account for and to the framework they were developed in. The chapter *Pavement texture properties related to friction* (3) is devoted to an overview of pavement texture properties, as the texture was selected as the key influencing parameter of this research. Pavement texture classification according to World Road Association PIARC is given, with the emphasis on two friction-related texture levels: micro-texture and macro-texture. Traditional methods for texture measurement and characterization are reviewed, pointing out the deficiencies of such methods in friction performance assessment via texture properties. Advanced methods for texture characterization and evaluation are described as an introduction to the development of a novel methodology for texture analysis, based on remote sensing photogrammetry technology. The chapter *Preliminary investigation of pavement texture-friction relationship* (4) presents the results obtained from the initial attempt to relate

pavement texture and friction performance determined by traditional measurement methods. The results presented in this chapter are published in Pranjić et al., 2020. The following chapter (5) *Methodology development for pavement texture data analysis* describes the research activities performed with the aim to establish a photogrammetry-based methodology for texture data acquisition and analysis. A part of the research presented in this Chapter was published in Pranjić & Deluka-Tibljaš, 2022. The CROP method was utilized for the acquisition of texture dataset, used for the development of a friction prediction model based on non-standard texture roughness parameters, described in chapter (6) *Development of a friction performance prediction model*. The final chapter (7) *Research conclusions and further research perspectives* provides a summary of performed research and discusses the importance and relevance of research findings with respect to the existing research results in the field. The limitations, disadvantages and weak points of the performed research are pointed out, together with the opened research questions and further research plans.

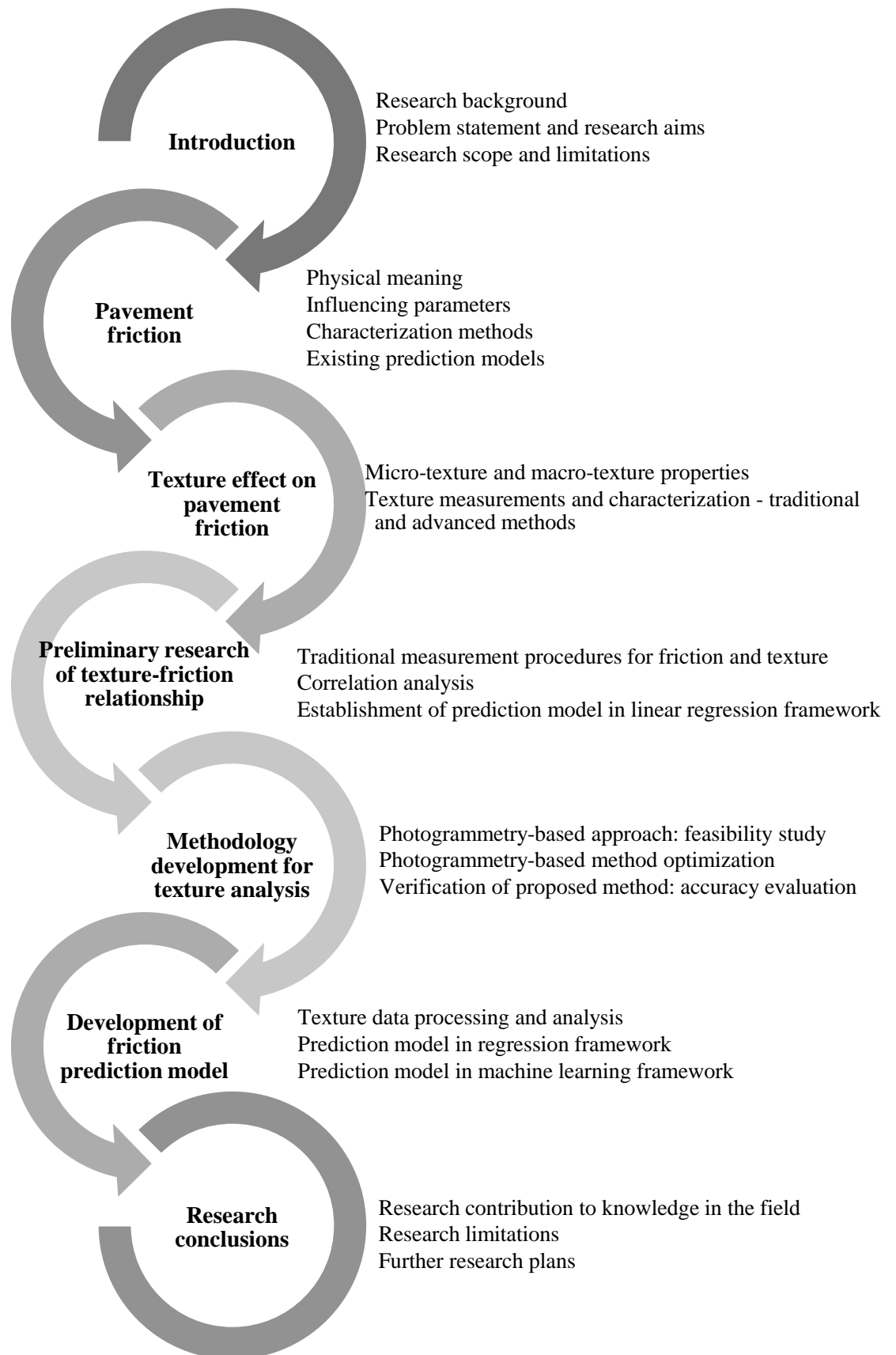


Figure 1.1 A schematic overview of research activities performed in this thesis

2. Pavement friction

In this Chapter an insight to the theory of friction and rough contact mechanics is given. The physical meaning of friction and its application to the analysis of a rough contact problem in the pavement surface – vehicle tire system is described. An overview of key influencing factors for pavement friction realization is provided. Standard methods for pavement friction measurements and established pavement friction indicators are presented and discussed. The models developed for the prediction of pavement frictional performance based on different influencing factors are analysed. A summary of the most important findings for the pavement friction analysis is given in the final section of this Chapter.

2.1. Friction force and coefficient of friction

Friction is a resistive force that occurs when one body moves over another body. It is generated at the contact surface between two bodies and directed opposite to the direction of motion, acting to try to stop the relative motion of the moving body. The forces present in this system are the normal load F , acting perpendicular to the contact surface, and the tangential (friction) force T , acting parallel to the contact surface. The proportionality between the tangential force and normal load is defined by the coefficient of friction, which occurs on the contact surface between the bodies (Figure 2.1).

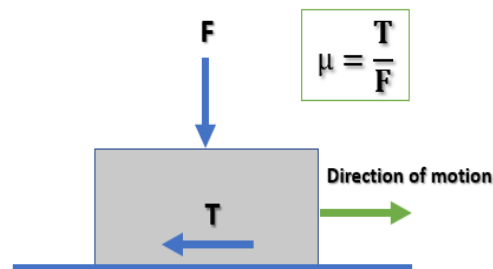


Figure 2.1. Definition of friction coefficient μ as a ratio between tangential friction force (T) and Normal force (F)

Friction coefficient can be either static or kinetic, depending on the relative motion of the system. If the ratio between friction force and normal force is below the critical value no motion occurs, and the ratio is defined as static coefficient of friction (Vakis et al., 2018). If the critical value of the friction force is overcome, motion occurs and the proportionality between the normal and tangential force is now defined as the kinetic coefficient of friction. If the motion is sliding, kinetic friction is defined as sliding friction. If the moving body is in rolling motion, the coefficient of friction is defined as rolling friction (Figure 2.2).

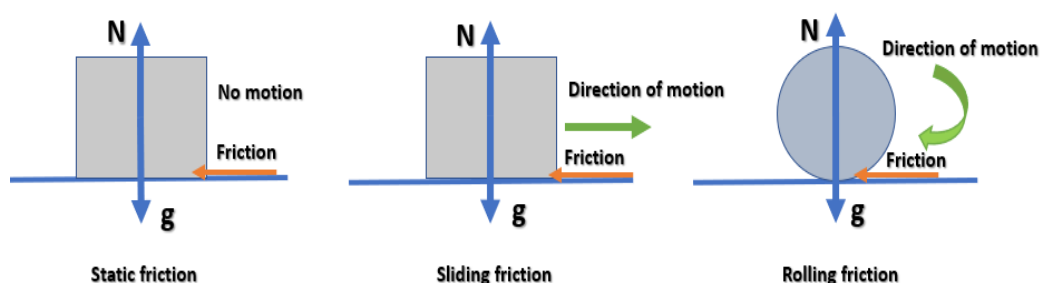


Figure 2.2. Difference between static, sliding and rolling friction

The fundamental friction laws described above are defined by Amontons and Coulomb (Vakis et al., 2018). They state that the friction force is proportional to normal load and

independent of the apparent contact area (1st and 2nd Amontons law) and that kinetic friction is independent of sliding speed (Coulomb law). According to the Amontons and Coulomb laws of friction, both the static and kinetic coefficients of friction are defined as constants that are independent of the contact area and sliding velocity (Barber, 2018; Popov, 2010). However, this constant proportionality depends on several influencing factors, for example the surface roughness, properties of the interacting materials and thermal conditions but also contact time and sliding velocity. Therefore, the basic friction laws are extended to more complex frictional laws to account for all the influencing variables for applications that cannot be described by the basic friction law (Vakis et al., 2018).

Static friction coefficient is greater than kinetic friction coefficient, as stated by Euler. The linearity of the normal and frictional force defined by the Amontons and Coulomb law is applicable just for a limited range of forces and must be interpreted carefully for materials such as polymers or elastomers where the actual contact area differs significantly from the apparent contact area (Popov, 2010). However, for contact problems with friction observed at the macro level, the fundamental friction laws can be used not just for the definition of frictional behavior, but also for the comparison to experimental results (Paggi & Hills, 2020).

2.2. Contact mechanics on rough surfaces

Surface roughness is an important parameter in the friction phenomenon as it determines the size of the actual contact area between two bodies in contact (Vakis et al., 2018). If at least one of the contacting bodies surfaces is rough, the actual contact area is much smaller than the nominal contact area equivalent to the true contact area in case of a smooth contact (Figure 2.3). The contact pressure is a function of the real contact area and the applied normal load. Therefore, the coefficient of friction derived from the ratio between tangential and normal force directly depends on the real contact area. An adequate representation of the surface roughness is crucial for determining the frictional behavior of bodies in contact. Contact mechanics represents a fundamental discipline focused on the study of the

deformation that occurs when two bodies come into contact and the resulting effects, including friction (Popov, 2010).

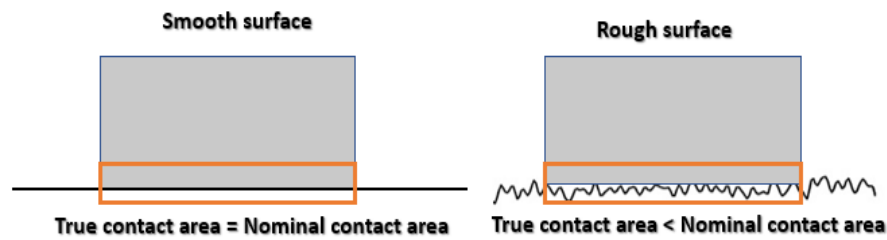


Figure 2.3. Difference between contact area for smooth contact (left) and rough contact (right)

2.2.1. Rough contact theories

The study of the contact mechanics problem began with the Hertzian theory in 1882, as a contact between two single non-deformable asperities of a parabolic shape in the contact zone (Persson, 2006). The contact was assumed to be frictionless and the proportion of the squeezing force F and resulting contact area A was non-linear, defined as $A \sim F^{(2/3)}$. Hertz extended his single contact model to a rough surface contact model, where the surface roughness was defined as a regular array of parabolic asperities and the contact theory was applied to each asperity of the surface (Vakis et al., 2018). This was the simplest asperity contact model, representing a basis for later smooth contact theories, e.g. JKR theory (1971.) and DMT theory (1975.), but also for several non-smooth contact theories, e.g., Archard (1957.) and Greenwood and Williamson (1966.) contact theories, which account for the effect of surface roughness on the mechanical response of the system.

The effect of surface roughness to the frictional response was first addressed by Bowden and Tabor (1950.), who introduced the importance of roughness in frictional contact by distinguishing between the actual contact area and the apparent contact area caused by the roughness of the contacting bodies (Vakis et al., 2018). Because of the importance of surface roughness to the problem of contact mechanics, this theory became a basis for the development of rough contact mechanics theories. In general, the rough contact problem is described by two main theories: Greenwood and Williamson (GW) theory and Persson's theory of rubber friction. Greenwood and Williamson (1966) introduced the multi-asperity-based contact model, while Persson's theory is based on the pressure probability distribution function and includes real surface roughness (Persson, 2001).

Greenwood and Williamson (GW) theory is a pioneering approach to rough contact mechanics, predicting the load-displacement behaviour of contacting surfaces by

considering the height distribution of the asperities (Ciavarella et al., 2008). This theory assumes that the surface roughness can be described by a set of asperities whose peak heights follow a normal distribution, they have an equal radius of curvature and the contact between them is assumed to be independent since they are separated by distances at which their mutual influence can be neglected. Another assumption is the approximate proportionality of the contact area and the applied load and the contact between two surfaces is described by the Hertzian contact theory (Vakis et al., 2018.). By neglecting the interaction between the asperities, GW theory is physically incorrect and affects the resulting forces in the contact theory. Nonetheless, the GW theory was a basis for the development of some advanced multi-asperity contact theories such as Nayak's theory or BGT theory (Vakis et al., 2018). Two main drawbacks of the multi-asperity theories are the assumption that there is no interaction between asperities and the lack of inclusion of real surface roughness, which has multi-scale characteristics and is crucial for defining a contact problem with roughness and friction. Contact models with multiple asperities are generally correct only for very low pressures and small contact areas due to the simple representation of surface roughness and in cases when long-range elastic coupling is neglected.

A fundamentally different approach to rough contact mechanics was given by Persson (2001), whose theory considers a very large contact area and high squeezing forces that cause a nearly complete contact at the interface (Persson, 2006). The stress distribution at the contacting interface is calculated by a diffusion-like equation, considering the stress as the spatial variable and magnification level as the time variable. The magnification level ζ is determined as the ratio between contact length L and shortest surface wavelength λ that can be detected at a given magnification level ζ . For low magnification levels, the contacting interface appears to be smooth, and the true contact area is equal to the nominal contact area. By increasing the magnification of the contacting interface ($\zeta=10$ or $\zeta=100$) in a way that more roughness components are observed, non-contact regions occur, and the stress distribution function propagates as a Gaussian distribution (Figure 2.4.).

Persson's theory predicts that the contact area evolves as an error function from zero to full contact, and it is approximately valid for all squeezing forces. The linearity of Persson's theory holds for realistic area/pressure intervals and provides accurate predictions for full contact conditions and approximate results for partial contact cases. Persson's theory was originally developed to implement the theory of rubber friction on rough road surfaces,

incorporating rubber-like materials such as vehicle tyres that exhibit viscoelastic behaviour when in contact with the road surface (Vakis et al., 2018).

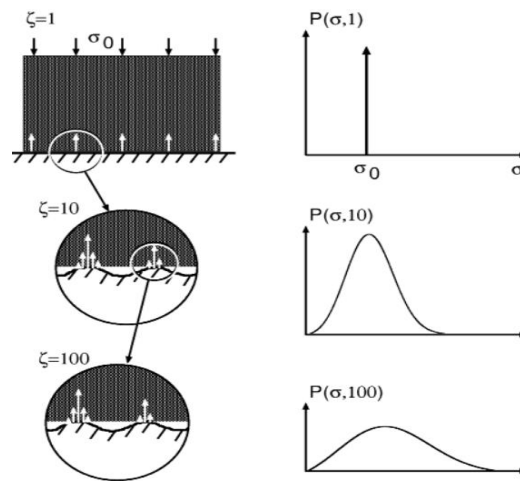


Figure 2.4. The effect of magnification level on the contacting interface and the distribution of the stress function defined in Persson's contact theory (Persson, 2001)

2.2.2. Rubber friction theories

The theory of rubber friction assumes that friction results from energy dissipation during the deformation process of the elastomer when in contact with rough surface irregularities. Rubber friction differs significantly from the frictional behaviour of other solids due to the specific properties of rubber: very low modulus of elasticity and high internal friction over a wide range of frequencies (Persson, 2001). The pioneering experimental studies by Grosch (1962) showed that rubber friction is mainly related to the internal friction of the rubber, leading to a coefficient of friction that depends on sliding speed and temperature (Lorenz et al., 2011). These findings led to the conclusion that the frictional force depends on the internal friction of the rubber, mainly related to the bulk property of the rubber (Persson, 2001). The effect of sliding velocity and the temperature dependence of the rubber define its viscoelastic character, which in general has a phase difference between stress and strain originating from internal energy dissipation (Lorenz et al., 2015).

In rubber friction theory, the assumption is that the surface roughness of a rigid body causes the deformation of the viscoelastic rubber body during the rolling or sliding motion. This results in energy dissipation in the bulk of the rubber. Direct bonding between the rubber molecules and the rough substrate followed by viscoelastic deformation and bond breaking contributes to the energy dissipation and sliding friction. In rubber friction theory, three main components of frictional force are distinguished: adhesion, hysteresis and wear. Each of these components contributes to rubber friction in a different way and on different length

scales as a result of complex interactions between the materials in contact. The adhesion and hysteresis contribution to the pavement friction are described more in detail in section 2.3. In a discussion about rubber friction theories by (Genovese et al., 2019), two theories were selected as significant with respect to their possible application to quantitative frictional models - Persson's rubber friction theory and Heinrich and Klüppel's rubber friction theory.

Persson's theory of rubber friction states that the main contribution to the frictional response comes from the viscoelastic energy dissipation on the rubber surface in contact with rough surface. This phenomenon is a result of the forces acting on the contacting interface, observed within the hysteretic contribution to the friction force and without the consideration of the adhesion effect, excluded due to the small true contact area. The kinetic rubber friction coefficient μ_{kin} derived by Persson (2001) is dependent on the rubber viscoelastic complex modulus and rough surface representation as power spectral density function at a specific velocity (Persson et al., 2005). Surface roughness is considered within a limited range of wave vectors related to real physical lengths of the observed problem, specifically the texture wavelengths corresponding to the friction relevant texture scales. Persson's theory emphasizes the importance of inclusion of all relevant length scales in the determination of frictional response for rubber friction, which is proven to be a sound approach verified by conducted numerical and experimental investigations (Lorenz, 2012; Ueckermann et al., 2015).

Heinrich and Klüppel's (HK) rubber friction theory accounts for the different contributions of energy dissipation during the sliding of a rubber on a self-affine rough surface (Heinrich & Klüppel, 2008). This theory includes fractal analysis of texture, characterized as a self-affine surface with three characteristic roughness descriptors: the Hurst exponent related to the fractal dimension and two correlation lengths parallel and perpendicular to the surface and related to the height-difference correlation. Texture roughness is described by the fractal dimension of the surface D , such that $2 \leq D \leq 3$, used for the calculation of Hurst exponent. The original HK rubber friction theory used the elastic contact model defined by GW theory, which was found to be applicable only for a limited roughness spectrum (Genovese et al., 2019). A later generalization of HK theory included the viscoelastic contact, which showed to be effective for the description of the rubber friction theory (Heinrich & Klüppel, 2008). The kinetic friction coefficient in HK theory is defined as a sum of frictional coefficients resulting from the dissipation mechanisms adhesion and

hysteresis. The adhesion-related friction coefficient is determined as a ratio of adhesion force, calculated from the shear stress in the actual contact area and the load-dependent size of actual contact area, and normal load. The hysteresis-related friction coefficient is defined as velocity-dependent and it is calculated as a ratio of hysteresis friction force, determined from the material parameters of the rubber (loss modulus and thickness of the rubber layer) and surface roughness power spectral density function, and normal load.

Rubber friction theories are developed as analytical approach to the friction phenomenon on rough contact interface, where the surface roughness characteristics are included as analytical functions, for example power spectral density functions or fractal functions. Limit ranges of roughness values are often discussed in terms of their relevance to the prediction of friction coefficient, so there is no unique rule or range of values defined for usage in friction prediction models (Genovese et al., 2019). The fractal description of the surface roughness used in analytical models cannot accurately describe the real topology of engineering and natural surfaces (Paggi & Hills, 2020).

Contact problems are in general considered as non-linear due to the material behaviour or geometrical non-linearities of the observed problem (Renaud et al., 2005; Vakis et al., 2018). Rough profiles of the contacting bodies can be conforming as for a fracture induced interface, or non-conforming as for an interface between two different bodies. For rough contact problems with non-conforming surfaces, the contact area is a priori unknown due to the changes in the position over the time or the applied load, which yields non-linearity of the problem (Paggi & Hills, 2020).

To overcome the limitations of analytical methods regarding the non-linearity of the problem, numerical methods are utilized for explicit solutions. The numerical approach doesn't require the approximations of surface topology or contact conditions that are necessary in analytical solutions. In terms of numerical analysis of rough contact problems including friction, the most common methods employed are the finite element method (FEM) and the boundary element method (BEM) (Vakis et al., 2018; Paggi & Hills, 2020). Both methods can solve rough contact problems and the selection of a specific method depends on the nature of the problem. Numerical methods can be computationally complex due to the non-linear nature of the problem, especially for multi-scale problems, which could result in absence of solution convergence. Recently, standard numerical methods are supplemented with multi-scale and hybrid methods which are less computational

demanding but still accurate enough to predict the frictional response of a pavement in a realistic way ((Putignano & Carbone, 2014; Paggi & Hills, 2020).

2.2.3. Numerical methods for rough contact mechanics

Boundary element method (BEM) is a numerical method utilized for solving multiscale rough contact problems mostly in the linear elastic regime and for small deformations assumption, where only the surface of the bodies in contact must be discretized without the need for surface interpolation techniques to discretize the interface (Bugnicourt et al., 2017; Putignano & Carbone, 2014). In order to be able to use BEM it is necessary to know the surface topography of the bodies in contact defined in a matrix form as a set of coordinates. As the contacting surfaces are non-conformal, the contacting area is unknown, and this results in a non-linear and complex problem. BEM is a good numerical method for solving contact problems of rough bodies in linear elasticity regime with the possibility of its extension to some more complex problems including material non-linearity or contact problems involving friction by introducing some simplifications of the problem (Nguyen & Hwu, 2019). The advantage of the BEM is the fact that it does not require the discretization of the entire bulk but only the rough interface for the problem solution, which significantly reduces the computational time in comparison to the FEM. The main drawback of this method is that it is not generally applicable for more complex problems that involve both constitutive and geometric non-linearities in large deformations framework, as is the rubber friction problem on rough surfaces. For such problems, the FEM is preferable even if it is more computationally demanding than BEM.

Finite element method (FEM) is a numerical method that can deal with the non-linear complexity of the contact problem in different aspects - the non-linear material model, the multiscale roughness character, the time and velocity dependence, the temperature effect etc. (Vakis et al., 2018). With FEM employed in contact modelling, it is necessary to discretize the entire volume of the bodies in contact and define proper contact interaction scheme on the contacting interface. FEM is capable of an explicit definition of stress-strain relationship by including a constitutive material model of any kind, for both infinitesimal and finite strain formulations (Srirangam et al., 2017). The possibilities of numerical modelling of contact engineering problems with FEM results in higher computational complexity in comparison to BEM, but the method is inevitable for problems that cannot be solved by BEM - for example problems with large deformations, large sliding contacts, problems with non-linear material behaviour, etc. (Vakis et.al, 2018). In general, the FEM

solution of rough contact problems includes the phase where the contact area is defined by applying contact search algorithms (Hyun et al., 2004) and afterwards the enforcement of contact conditions, once when the true contact area is defined. The methods for defining contact conditions differ for the compenetrating condition, for example the penalty method allows a certain compenetrating level while methods based on Lagrange multipliers explicitly impose there is no compenetrating at the contacting interface. Resulting system of non-linear equations is usually solved by an appropriate algorithm, in most cases Newton-Raphson iterative scheme (Wriggers & Reinelt, 2009).

Multiscale and hybrid modelling approach considers interaction between several different numerical models defined for different problem scales. When this approach is exploited for rough contact problems, the multitude of the scales is caused by multiple scales of rough geometrical features, defined as a spatially multiscale problem (Vakis et al., 2018). For a multiscale problem it is important to define the governing physical processes in each of the observed scales and the hierarchy and independence between the defined problem scales (Hou et al., 2018; Luan et al., 2006). An example is a multiscale rough contact model where the upper scale model is treated with FEM and it determines the state for the lower - microscale model, which is treated with BEM and provides the contact interface properties relevant for the macroscale model (Wriggers & Reinelt, 2009). A FEM-BEM approach that involves an interface FE for modelling interface interaction on macroscale and BEM for modelling the solution of the contact problem on microscale is another example of multiscale modelling (Bonari et al., 2020; Bonari & Paggi, 2020). In this approach, scale coupling is enforced by passing the calculated value of the normal gap at each integration point of the interface FE observed at macroscale to the BEM procedure for the normal contact problem solution at the microscale, without the need for the roughness topology simplification. An extension of this approach is a hybrid FEM, where the exact height field of the rough profile is stored nodal-wise inside the novel MPJR finite element. This framework is recently extended to frictional simulations as shown in (Bonari et al., 2021, 2022).

2.3. Friction mechanisms on pavement surfaces

Pavement surface frictional performance is characterized by a non-dimensional friction coefficient, calculated as a ratio between the traction friction force and wheel load (Figure 2.5) (Fwa, 2017). The friction force is the tangential force that occurs between the tire tread

of a vehicle in motion and the pavement surface, in the direction opposite to the direction of motion. The vehicle load is normal force perpendicular to the pavement surface (Hall et al., 2009).

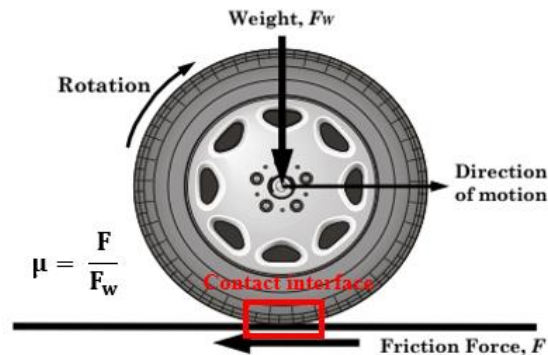


Figure 2.5. Pavement friction phenomenon and forces in the system (from Hall et al., 2009)

The interaction mechanism between the pavement surface and vehicle tire is crucial for understanding the pavement friction phenomenon. Pavement surface is considered to be rigid as its deformations in the system are negligible in comparison to the deformations of vehicle rubber (Al-Assi & Kassem, 2017; Alhasan et al., 2018a; Wriggers & Reinelt, 2009). Rubber is the main component of vehicle tires. It is characterized as an elastomer which undergoes finite deformations during the vehicle motion over the pavement surface due to the material characteristics of the rubber bulk. The friction mechanism on tire-pavement interface is described by the theory of rubber friction. Two friction force components recognized in the rubber friction theory are relevant for pavement friction phenomenon: adhesion and hysteresis. Each of these components contributes to the friction realization differently on a different roughness scale.

Adhesion (Figure 2.6 a, c) is a result of intermolecular contact between two materials, caused by attractive Van der Waals dipole forces (Wriggers & Reinelt, 2009). When the micro-asperities of two surfaces are in contact, dipole Van der Waals forces attract and hold the two asperities together and prevent their separation. Van der Waals forces that occur on a molecular level between two different materials in contact are not particularly strong and they need a very close contact for their activation. Adhesion is very dependent on the size of the true contact area, so in the perspective of rough pavement surfaces in contact with the rubber tire, the adhesion force plays a minor role in the friction phenomenon. This is even more emphasized if the contact is lubricated, i.e. if a water layer exists between the pavement surface and vehicle tire. However, adhesion is the most representative component

of the friction force for low sliding velocities and dry surface conditions. Here, the pavement surface properties related to the micro-roughness scale geometry and material features contribute significantly to the friction performance. Studies show that there is a noticeable correlation between the adhesive bond energy and the friction coefficient on the rubber - pavement contact, which implies that the increase in the adhesion force results in an increase of the friction coefficient (Al-Assi & Kassem, 2017).

Hysteresis (Figure 2.6 b, d) is the result of the rubber material bulk deformation when it contacts the surface irregularities and undergoes permanent plastic deformation while passing over the rough surface (Al-Assi & Kassem, 2017, Srirangam et al., 2017). Bulk deformation causes energy loss during the sliding movement. The rubber undergoes compression-expansion cycles while moving over the rough surface asperities. When a deformable rubber material is pressed against a rigid and rough surface asperity, the stress distribution causes the rubber to deform, resulting in energy loss. The resulting deformation is the potential energy stored in the rubber bulk. After passing over the asperity, the rubber returns to its initial state and the material is relaxed. Part of the stored potential energy is recovered and the other part is lost in the form of heat. The irreversible energy loss is known as hysteresis. The hysteresis effect to the friction phenomenon lies in the fact that asperities induce energy dissipation on the contact between the tire and the pavement. Rougher surfaces will produce greater energy loss and consequently larger friction coefficient. Hysteresis is considered to be a governing friction force component for high-speed and larger texture scales, especially for wet pavement surfaces. Furthermore, as tire rubber is a viscoelastic material, a significant contribution to the phenomenon is given by the sliding speed and the temperature (Hall et al., 2009).

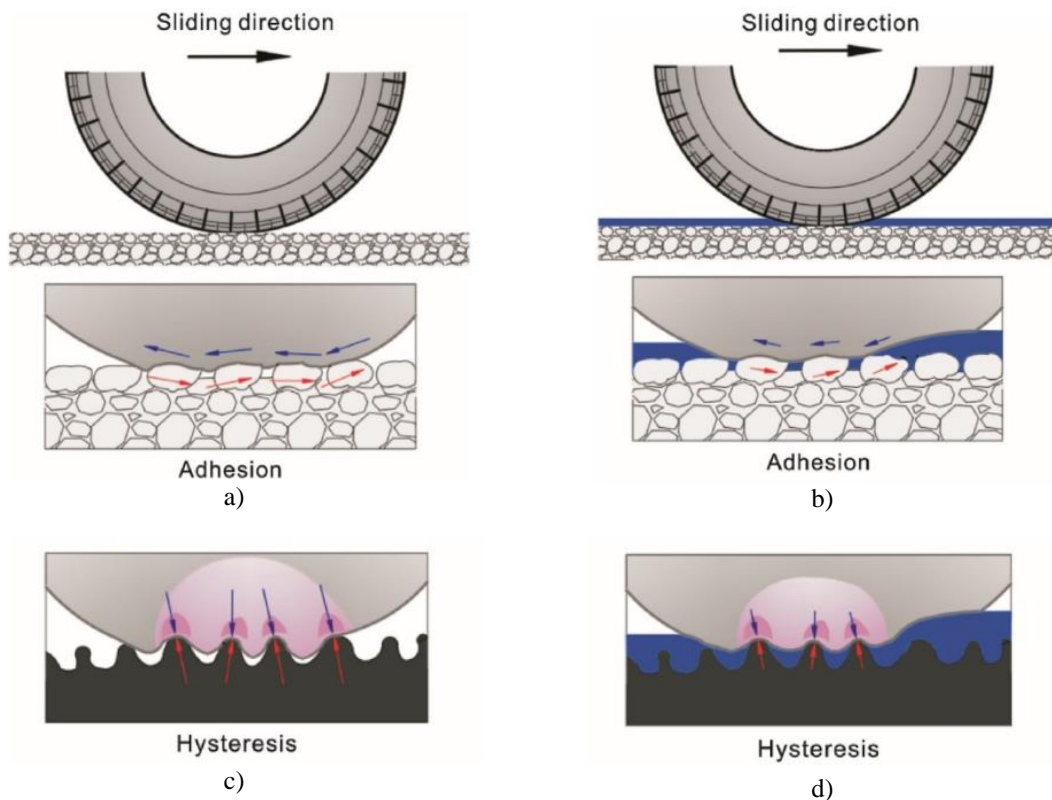


Figure 2.6. Adhesion and hysteresis mechanisms of pavement friction on dry (a,c) and wet (b,d) pavement surfaces (from Fwa, 2021)

2.4. Factors affecting pavement friction

The frictional response of a pavement results from the interplay of several factors that can be grouped into four main categories (Hall et al., 2009, Kogbara et al., 2016, Yu et al., 2020, Kumar & Gupta, 2021):

- pavement surface properties,
- environmental impacts,
- driving parameters
- vehicle tire properties

Each group of properties contributes to the frictional performance specifically and for a comprehensive understanding of the friction phenomenon the best approach would be to consider the effect of all the influencing parameters in these groups. As such approach would result in a highly complex framework, researches usually focus on several interacting parameters to gain insight into pavement frictional properties (Kogbara et al., 2016). The following sections provide an overview of the most important influencing parameters in each group of properties.

2.4.1. Pavement surface properties

Surface properties related to the pavement friction performance are mostly considered as the texture-related properties, stemming from the characteristics of the pavement material and construction method. The material characteristics are resulting from the asphalt mixture type, whose properties define the surface texture characteristics on friction-related texture scales, micro-texture and macro-texture (Wambold et al., 1995). Each of the relevant texture levels has a different influence on the pavement friction performance. By referring to the friction mechanisms adhesion and hysteresis described in section 2.2., micro-texture scale is responsible for the most of the adhesion contribution and macro-texture governs the hysteresis effect.

Micro-texture mostly results from the aggregate particles properties so it is usually referred to as “the texture of the aggregates”. Macro-texture results from the asphalt mixture properties and surface layer construction method, therefore it is referred to as “the texture of the pavement”. Surface-related texture properties are thoroughly observed in Chapter 3 as the texture was selected to be the key parameter for friction performance assessment in this research.

2.4.2. Environmental impacts

Three major environmental impacts related to the pavement frictional performance are temperature, presence of water on the surface and various contaminations of the surface (Kogbara et al., 2016). These effects are not controllable as they mostly depend on the seasonal climatic variations or unexpected events.

The influence of temperature on frictional performance is investigated mostly within the effect of the seasonal variations in winter and summer period. In general, pavement frictional performance decreases with an increase of temperature (Khasawneh et al., 2012). This is due to the viscoelastic nature of the problem and the changes of rubber and pavement stiffness with the temperature changes. An increase of the rubber resilience on higher temperatures causes the decrease of the hysteretic losses and consequently reduced frictional performance. This is why pavement frictional performance monitoring is mostly performed during the summer, as the critical values occur on higher temperatures. On the other hand, higher frictional performance on lower temperatures results from an increase in aggregate roughness due to the winter maintenance procedures and aggregate natural weathering processes (Kogbara et al., 2016). Also, as winter season tends to have higher

amounts of precipitation, road surfaces are less contaminated and therefore aggregate's textures are more exposed and consequently providing higher friction values.

The presence of water on the pavement surface in general has a negative effect on the frictional performance (Kumar & Gupta, 2021). When the pavement surface is wet, a thin water film occurs between the vehicle tire and pavement, lubricating the contact area and reducing the friction. For pavement surfaces with lower macro-texture values, the presence of water is critical for the hydroplaning effect appearance. Water fills the texture cavities and additionally reduces the surface roughness, making it very slippery especially under high driving speeds. The positive effect of the water presence is obtained if the surface's macro-texture level is satisfactory so the water does not retain on the pavement or if the pavement type is open-graded (porous) asphalt mixture so the water is drained from the surface to the pavement base layers. In such cases, the intensive rainfall washes out the pavement and removes the contaminants which might contribute to the polishing of the surface texture under the traffic load (Kogbara et al., 2016).

The contaminants negatively affect the pavement frictional performance by smoothing the surface for two main reasons (Kumar & Gupta, 2021). If they are largely accumulated on the surface, they tend to fill up the texture cavities and thus smooth the surface. This often happens during the dry season, when no intensive rainfall could wash out the pavement surface. The second reason is the polishing effect of the contaminants under the traffic load. This is specific for fine-grained contaminants such as dust and sand particles, chipped fine aggregates and similar. Viscous-type contaminants such as motor oils or ice and snow reduce the frictional performance similar to the presence of water, making the contact area more slippery. Several models and research results about the effect of contaminants on the friction were listed in (Alauddin Ahammed & Tighe, 2010), concluding that there is no consensus over their influence and pointed out the importance of both seasonal temperature variations and pavement type used for the prediction of frictional response of the surface.

2.4.3. Driving parameters

Pavement surface friction is highly related to the vehicle speed and driving manoeuvres (Hall et al, 2009). During the vehicle motion, two speeds are present in the system: vehicle speed usually defined as or the operating speed, and rolling tire speed which depends on the tire radius and angular velocity. The difference between these two speeds is called the slip speed. When a vehicle tire is in free rolling mode, meaning there is no braking manoeuvre, the vehicle speed and tire speed are equal. The slip speed changes when a breaking

manoeuvre is applied. During the braking, the vehicle tire is blocked and can no longer have the same speed as the vehicle. In this case the slip speed increases and the ratio between slip speed and vehicle speed is called the slip ratio. The pavement frictional performance changes with respect to the change in the slip ratio (C. Huang & Huang, 2014). After obtaining a peak friction value at the critical slip value equal to 10-20% of the slip ratio, the frictional performance decreases to the value of sliding friction at 100% slip, when vehicle tire is fully blocked and its speed is equal to zero (Figure 2.7).

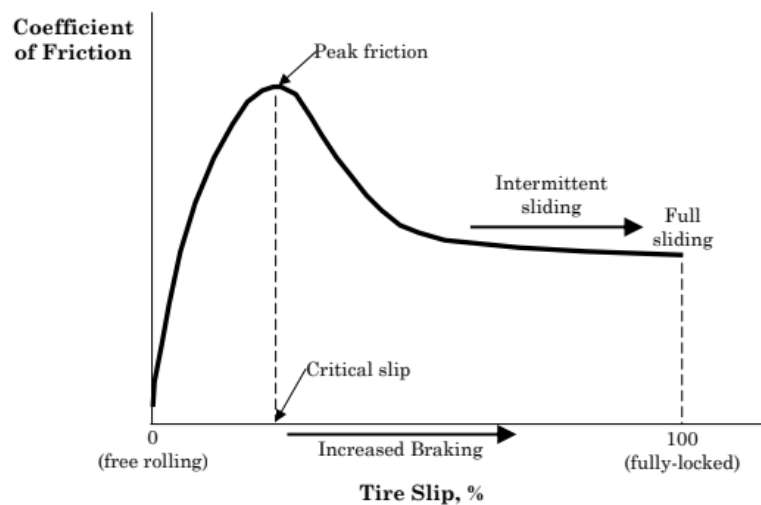


Figure 2.7. Slip ratio versus pavement friction performance (Hall et al., 2009)

When considering the influence of speed on the friction realization, it is well known that low speed frictional performance depends on the micro-texture properties of the pavement surface and macro-texture is a predominant factor for friction realization at high speeds (Yu et al., 2020). Another important speed-related observation is that the micro-texture governs the peak value of the friction coefficient obtained at a critical slip speed value and macro-texture is responsible for the slope of the friction curve after the peak friction is obtained (Figure 2.8).

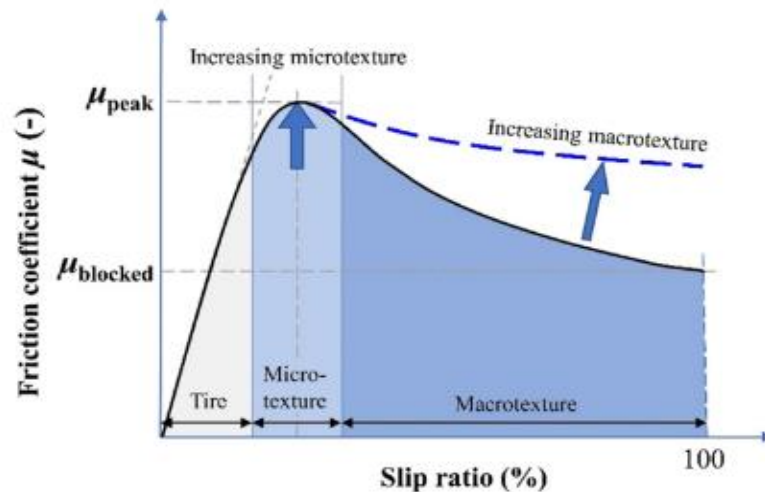


Figure 2.8. The effect of different texture levels on the slip ratio (Yu et al., 2020)

2.4.4. Tire properties

Tire properties have an important effect on the pavement friction phenomenon being a body in contact to the pavement surface. The rubber as a constituent material dictates the material behavior law and consequently the friction coefficient realization on the contacting interface. Besides the material properties, the condition of vehicle tires plays a significant role in the friction realization (Hall et al., 2009). Vehicle tires have a tread so they can provide a better grip and efficient surface water evacuation when the road surface is wet. Another important tire property is the inflation pressure, which affects the contact area and resulting contact pressure. In cases when the tires are under-inflated, contact area increases causing the decrease in contact pressure and consequently the decrease in frictional performance. If the tire is overinflated, the true contact area reduces and the contact pressure increases. Therefore, no significant pavement friction loss occurs (Hall et al., 2009).

In the pursuit for the prediction of tire-pavement friction performance, a notable amount of research was oriented on the tire behavior modeling resulting in both analytical and numerical solutions for the problem (Yu et al., 2020). Tire performance-oriented research is mostly driven by the automotive industry, emphasizing the importance of further research and development of the tire properties related to the friction performance. From the pavement engineering perspective, the effect of tire properties is less important for the observed phenomenon than the effect of the pavement properties and therefore won't be further analyzed in this thesis.

Table 2.1 summarizes the main influencing parameters described in previous sections, emphasizing the positive or negative effect that each parameter has on the pavement friction properties.

Table 2.1. A summary of the positive and negative effects of the key influencing parameters for pavement friction performance

Influencing parameter	Pavement surface properties	Environmental impacts	Driving parameters	Tire properties
Positive effect	<ul style="list-style-type: none"> → high micro-texture and macro-texture levels → “positive” texture with asperities pointed upwards 	<ul style="list-style-type: none"> → lower temperatures → dry weather 	<ul style="list-style-type: none"> → moderate vehicle speed → straight road sections → quasi steady-state driving conditions 	<ul style="list-style-type: none"> → new, well-treaded tires
Negative effect	<ul style="list-style-type: none"> → low micro- and macro-texture values, “negative” texture with significant amount of texture valleys and cavities 	<ul style="list-style-type: none"> → temperature increase → rainfall → surface contaminants (debris, dust etc.) 	<ul style="list-style-type: none"> → Increase in vehicle speed → curved road sections with high super-elevations → braking manoeuvres 	<ul style="list-style-type: none"> → under-inflated, worn out tires

2.5. Measurement and characterization of pavement friction

To characterize the frictional performance of a pavement, road authorities perform friction measurements and categorize the measured values according to available national regulations or technical standards. The measurements are usually performed as a part of a periodical monitoring program or in cases of reduced road safety level when traffic accidents occur frequently on a specific location. In such cases, measured frictional performance is compared to the defined threshold values defined in the regulations and standards. In this Section, an overview of methods for pavement friction measurement is given, including the description of standard measurement methods and resulting friction performance indicators. A comparison of limit values for friction indices according to the Croatian national regulations and some internationally recommended indicators is provided.

2.5.1. Pavement friction measurement methods

The quantification of pavement frictional performance is obtained by different measuring principles and corresponding devices. In general, all measuring devices operate on a principle of detecting a resistive force that occurs when a rubber object slides over a

pavement surface. The differences between the measuring devices are in the measuring speed, slip ratio and friction force direction (Rajaei et al., 2016). The choice of an appropriate measuring device depends on the measuring conditions, target speed for the friction estimation and limiting factors such as device availability.

Traditionally, friction measurement methods are grouped into stationary and dynamic methods. The difference is in the relative position of the measuring device with respect to the measured surface. Stationary methods imply a fixed position of the measuring device, while dynamic measuring methods entail movement of the measuring device. Stationary devices are more common for laboratory testing of friction performance or for single-spot measurements in situ, while dynamic devices are usually exploited for road network monitoring and measurements of longer road sections where frictional performance has to be assessed. A schematic representation of the most common stationary and dynamic friction measurement devices is given in Figure 2.9.

The widely used single-spot methods for pavement friction estimation are pendulum-based measurements and rotating plate-based measurements (Figure 2.9, i-vi). Both methods estimate the friction performance from the kinetic energy loss due to the contact between the rubber pads characteristic for the devices and the pavement surface (Hall et al., 2009). The measuring speed for such devices are different. Pendulum-based devices always operate under the same measuring speed, while rotating-plate devices can have variable measuring speeds. The value of slip ratio is unknown for such devices (Yu et al., 2020).

The friction value from pendulum-based devices (Figure 2.9, i) is a result of the resistance that a specific pavement surface provides against the swinging pendulum movement. The kinetic energy of a pendulum reduces as the rubber is sliding over the surface and it is converted to potential energy for a maximum height, which in the end represents the measuring result. The measurement speed is a fixed value and it is approximately 10 km/h. Therefore, pendulum-based devices are categorized as low-speed friction measurements but also as an indirect estimation of pavement surface micro-texture performance (Kogbara et al., 2016). They enable relatively easy and low cost measurements. The operating principle is simple so no specific training is needed for its usage and the device is easily transferable. However, such devices cannot yield results that are comparable to the real interface contact conditions due to its operating principle. Also, the results can be very sensitive to the

subjectivity of the measurement due to the purely mechanical principle of device adjustment prior to the measurements and influence of the operator's measuring skills.

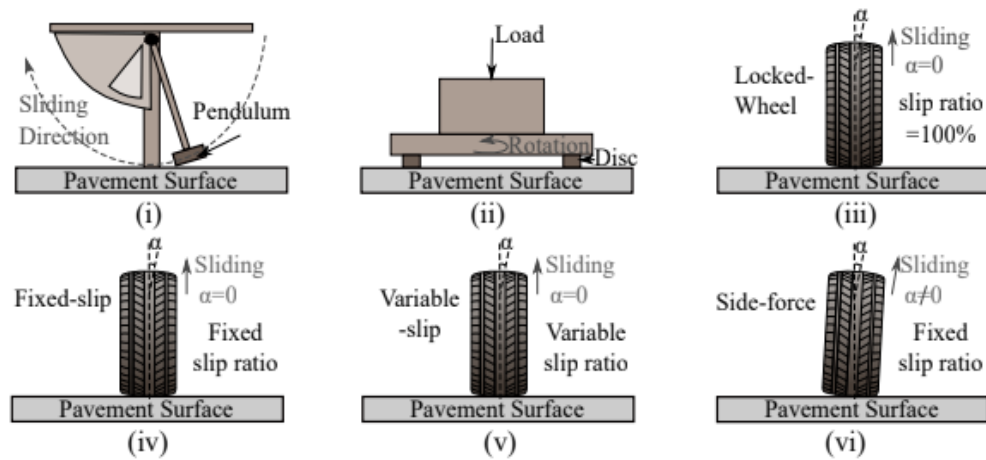


Figure 2.9. Friction measurement devices with different operating principles: (i) pendulum-based devices, (ii) single-spot dynamic friction testers, (iii) locked wheel dynamic testers, (iv) fixed slip dynamic testers, (v) variable slip dynamic testers, (vi) sideway force testers (Rajaei et al., 2016)

Single-spot dynamic friction testers (Figure 2.9, ii) operate on a principle of rotating disc with rubber pads attached to its bottom, which come into contact with pavement surfaces at different speeds. The device measures the momentum at which the rubber pads are rotating for a given measuring speed. As the speed can be varied, this type of equipment can be used to determine the dependency of the friction performance with respect to different speeds. Similar to the pendulum-based devices, they can be also made as field testing equipment, therefore portable and easy to operate with. Another advantage is lack of subjectivity due to the operator's experience as the device operates automatically. Even though it is a single-spot measuring device, it can represent the friction performance at high speeds, up to 90 km/h (Wallman & Åström, 2001).

Dynamic methods for friction performance estimation are related to the in-situ testing as they imply high speed testing devices. They are categorized according to the operating principle into four modes: locked wheel, fixed slip, variable slip and sideway force (Hall et al., 2009). The sliding process is controlled by the wheel blocking process specific for different measurement devices.

Locked wheel friction devices (Figure 2.9, iii) have a slip ratio of 100%, meaning that the measuring wheel is fully blocked and sliding occurs. The friction performance is measured in the direction of vehicle movement for a given operating vehicle speed. This type of device produces a longitudinal friction coefficient as a friction estimation. The devices that operate

under fixed slip (Figure 2.9, iv) and variable slip mode (Figure 2.9, v) have one or two measuring wheels which can have a fixed slip ratio usually up to 20%, or variable slip ratios which are predetermined. Sideway force devices (Figure 2.9, vi) are different from the aforementioned for the position of the measuring wheel. In such devices, the measuring wheel is dilated from the vehicle movement axis for a constant angle and usually has a constant slip ratio (also up to 20%). The angle between the direction of motion and turned wheel is called slip angle, which generates the sideway friction coefficient. In this way, the friction performance related to the vehicle stability and manoeuvring performance in the curves can be assessed.

The main advantage of the dynamic friction measuring devices is that they represent the actual contact conditions and frictional response of a pavement much more realistic than the single-spot low speed measurements (Yu et al., 2020). As these measurements are performed at driving speeds, no traffic interruption is necessary. The devices are capable of continuous data acquisition. Therefore, they represent the friction performance of the entire road section and not only a single location. The main drawback of the dynamic friction measurement systems is that they are more resource – consuming in comparison to the single-spot measurements. Dynamic devices provide longitudinal friction coefficient and they have the advantage of higher measuring speeds, better mobility performances as they are generally smaller and mostly trailer-based, but require an addition of accompanying vehicle carrying a water tank which can be a limiting factor in the measurement length range (Andriejauskas et al., 2014). The sideway operating devices are larger and consequently more expensive for the operation, obtain lower measuring speeds but have an integrated water tank so the measurements can be continuous and long distance. For a heavily uneven road surface, sideway force devices can suffer from measuring wheel damage (Yu et al., 2020). A summary of selected traditional measuring methods and corresponding devices mostly related to European practice is given in Table 2.2 (Andriejauskas et al., 2014).

Both stationary and dynamic measurement methods estimate the pavement frictional performance based on the contact between the rubber of the measuring device and the pavement surface. In such measurements, factors such as surface and rubber temperature, rubber material properties, measurement speed, operator's skills, measuring device characteristics and similar affect the measurement result. For different types of measuring devices, pavement frictional performance is expressed through different friction values. The diversity of operating principles and the measuring procedures make it impossible to define

a unique friction indicator. The PIARC association performed a series of harmonization campaigns in order to derive such an indicator, by carrying out extensive measurement programmes with various texture and friction measuring devices. The result was a common harmonization index called International Friction Index (IFI), formulated in such way that for a given texture measurement expressed in millimetres and friction value adjusted to 60 km/h from the actual performed measurements at different slip speeds, a friction number at 60 km/h can be estimated. This procedure however, accounts for the calibration coefficients that are device specific, therefore any other device that was not a part of the harmonization campaign couldn't be used for the estimation of a standardized friction index expressed as IFI. Following, a number of researches attempted to exploit the IFI concept for the harmonization of friction measurements was prompted, but the results didn't seem to be satisfying enough (Ahammed & Tighe, 2012).

Table 2.2. An overview of friction measurement devices used in Europe (Andriejauskas et al., 2014)

Device	Type	Operating principle	Measurement parameters	Resulting friction indicator
Skid Resistance Tester (SRT)	Stationary (lab/field)	Pendulum: friction is estimated from the kinetic energy loss in the sliding process of a rubber attached to the pendulum arm	Operating speed: approx. 10 km/h Measured surface area: approx 9 000 mm ²	Skid Resistance Number
Dynamic Friction Tester (DFT)	Stationary (lab/field)	Rotating plate: friction is estimated from the decrease of the target speed to zero	Operating speed: 0 – 80 km/h Measured surface area: approx. 65 000 mm ²	Friction coefficient
Wehner/Schulze Machine (W/S)	Stationary (lab)	Rotating plate: friction is estimated from the contact between the rotation beads accelerated to a target speed and wetted test surface	Operating speed: 60 km/h Measured surface area: approx. 40 000 mm ²	Friction coefficient
GripTester	Moving	Fixed slip: friction is estimated from the wheel dragging force and wheel load, as the rotation of the measuring wheel is partially confined with a fixed slip ratio. The devices are usually operating under wet conditions with controlled water film thickness.	Operating speed: 5-100 km/h Slip ratio: 15% Measurement interval: various	Longitudinal Friction Coefficient (LFC)
RoadSTAR			Operating speed: 30/60 km/h Slip ratio: 18% Measurement interval: 50 m	
BV-11			Operating speed: 70 km/h Slip ratio: 17% Measurement interval: 20 m	
ROAR			Operating speed: > 50 km/h Slip ratio: 20% Measurement interval: > 5 m	
IMAG (variable slip mode)		Variable slip: the test wheel rotates freely, therefore friction can be estimated for different slip ratios	Operating speed: 65 km/h Slip ratio: up to 100%	
SRM			Operating speed: 40/60/80 km/h Slip ratio: 15% or 100% Measurement interval: 20 m	
Skiddometer BV-8			Operating speed: 40/60/80 km/h Slip ratio: 14% or 100% Measurement interval: 30-50 m	
ADHERA			Locked wheel: friction is estimated from the resisting force generated in	

		full sliding conditions, as the measuring wheel is fully locked	Slip ratio: 100% Measurement interval: 20 m	
SRT-3			Operating speed: 60 km/h Slip ratio: 100%	
IMAG (locked wheel mode)			Operating speed: 65 km/h Slip ratio: 100%	
SCRIM		Sideway force: friction is estimated from the ratio of generated side force, which stems from the slip angle between the measuring wheel and moving direction	Operating speed: 50 km/h Slip angle: 20° Measurement interval: >10 m	Sideway Friction Coefficient (SFC)
MuMeter			Operating speed: 60 km/h Slip angle: 7,5°	MuMeter Number (MuN)

2.5.2. Pavement friction indicators

Traditional friction measuring devices provide a friction performance estimation in the form of a specific pavement friction performance indicator, which depends on the operating principles of the devices and specific measurement conditions (Table 2.2). The selection of measuring devices and resulting friction performance indicators depends on the national regulations and accepted standards and practices for practical use in road management. The most commonly used friction measurement devices in Europe are SRT Pendulum device, Grip Tester and SCRIM (Andriejauskas et al. 2014). The SRT is mostly used for quality control assessment or for location-based friction performance measurements. In general, European countries are more leaning towards fixed-slip and sideway force slip devices for network monitoring purposes, while US countries mostly use the devices based on locked slip principle (Yu et al., 2020).

European normative documents consider the friction measurement procedures within several standards and technical specifications. In European standard EN 13036-4: *Road and airfield surface characteristics – Test methods – Part 4: Method for measurement of slip/skid resistance of a surface: The pendulum test*, a procedure for friction performance determination by means of a stationary pendulum device is defined. Technical specification CEN/TS 13036-2: *Road and airfield surface characteristics – Test methods – Part 2: Assessment of the skid resistance of a road pavement surface by the use of dynamic measuring systems* describes the necessary procedures for friction measurements conducted by the dynamic friction measuring devices, whose specifications are given in CEN/TS 15901-1 to -10 series of technical specifications. The devices listed in CEN 13036-2

technical specification are characterized as „permitted for friction measurements, with a described measuring principle and procedure“. The measuring results are used for the estimation of Skid Resistance Index (SRI), together with the texture measurements, device-specific calibration parameters and adjusted slip speed.

The determination of friction performance threshold values depends on the national policies of road agencies and in general, it is very different among countries. Authors Astrom and Wallman (2001) analysed the measurement methods, resulting friction indicators and their relation to the traffic safety to define the friction coefficient threshold value in several European countries (Table 2.3). An American technical document AASHTO's Guide for Pavement Friction (Hall et al., 2009) provided an overview of threshold values for friction performance in UK, New Zealand, Maryland, USA and Australia related to the road categories or specific road network sites (Table 2.4). This document also encourages the establishment of investigatory and intervention friction threshold levels as a part of pavement friction management program. Methods for defining investigatory and intervention levels of pavement friction are proposed, based on historical friction data collected on a particular road and traffic accident data. The investigatory and intervention levels are set to be corresponding to a notable decrease of friction values or an increase in traffic accidents number.

Table 2.3. Required friction levels in some EU countries (Wallman and Astrom, 2001; Litzka et al., 2008)

Country	Required friction level (friction coefficient)	Measurement device principle
Austria	0.38	Fixed slip
Belgium	0.4	Sideway force
Denmark	0.5 (60 km/h)	Sideway force
Germany	0.3 (80 km/h), 0.39 (60 km/h), 0.48 (40 km/h)	Sideway force
Sweden	0.5	Sideway force
Finland	0.4 (80 km/h), 0.5 (100 km/h), 0.6 (120 km/h)	Locked wheel or sideway force
Netherlands	0.51 (50 km/h)	Fixed slip
Poland	0.35 (60 km/h)	Locked wheel
Slovenia	0.45 (50 km/h), 0.39 (70 km/h), 0.33 (90 km/h)	Sideway force

Table 2.4. Threshold friction levels in non-EU countries (Hall et al., 2009)

Country	Required friction level at 50 km/h	Comments about threshold values and site specifics
UK	0.30 – 0.55 for Friction Number (FN)	Threshold values are different for specific road categories, intersections and road design elements (curvature radius, vertical gradient)
New Zealand	0.35 – 0.55 for Sideway Friction Coefficient (SFC)	Threshold values defined for different types of approaches and intersections, pedestrian crossings, bridges and road categories
Maryland, USA	35 – 55 for Friction Number (FN)	Threshold values defined for various intersection types, pedestrian crossings, highway categories and road design elements (curvature radius, vertical gradient)
Australia	0.35 – 0.60 for primary and secondary roads with > 2500 veh/lane/day 0.30 – 0.55 for secondary roads with < 2500 veh/lane/day	Threshold values defined for various intersection types, pedestrian crossings, road design elements (curvature radius, vertical gradient) and road categories

In 2004, COST Action 354 Project was launched in several EU countries with the objective to define a set of uniform pavement performance indicators and indexes (Litzka et al., 2008). The project deliverables were presented in COST Action 354 Final Report (2008), where a set of performance indicators (PI) related to a specific technical parameter (TP) obtained from different measuring procedures was given. COST Action 354 proposed a unique performance indicator for friction performance assessment for two types of measuring devices – sideways friction coefficient devices and longitudinal friction coefficient devices, with respect to the measurement speed of each device. To evaluate the performance indicator (PI_F) of frictional properties expressed as Skid Resistance, the transformation functions were derived to calculate the PI from the measured values. The Action's Final Report (2008) presented a range of values for the proposed technical parameters (TP) for pavement friction estimation and the transformation equations for the calculation of the Performance Index from the obtained technical parameter values (Table 2.5).

Table 2.5. Proposed transfer functions for the friction Technical Parameters analyzed in COST 354 Action (Litzka et al., 2008)

Technical Parameter	Measurement speed	Transfer functions for Performance Indicator calculation
Sideway Friction Coefficient - SFC	60 km/h	$PI_F = \text{Max} (0; \text{Min} (5; (-17.600 \text{ SFC} + 11.205)))$
Longitudinal Friction Coefficient – LFC	50 km/h	$PI_F = \text{Max} (0; \text{Min} (5; (-13.875 \text{ LFC} + 9.338)))$

The conclusions derived in the COST 354 Final Report emphasize that the obtained PI's serve only as a recommendation for road agencies, without the proposal of target or limit values for any of the derived indicators. This conclusion is corroborated with a statement that threshold values strongly depend on the road type and characteristics, but also on the desired serviceability level for a specific road. Therefore, the values given as results of this Action serve only as a recommendation or a guideline in pavement management assessment. The Report gives some recommendations regarding the range of calculated Performance Indicator values within the defined grades (0-5), specifying that lower grade value represents better performance (Table 2.6).

Table 2.6. Performance Index grades for friction determined by two different measurement devices and resulting Technical Parameters SFC and LFC, (Litzka et al., 2008)

	Very Good > Very Poor				
Skid Resistance Performance Index (PI_F)	0 - 1	1 - 2	2 - 3	3 - 4	4 - 5
SFC (60 km/h)	0.64 - 0.58	0.58 - 0.52	0.52 - 0.47	0.47 - 0.41	0.41 - 0.35
LFC (50 km/h)	0.67 - 0.60	0.60 - 0.53	0.53 - 0.46	0.46 - 0.38	0.38 - 0.31

A collaborative European project ROSANNE was launched in 2013, with the aim of development and harmonization of pavement performance measurement methods in terms of friction, noise and rolling resistance (Birkner et al., 2016). The objectives of the ROSANNE project in the context of pavement frictional performance was to harmonize the friction measurements by defining the conversion factors for the devices with similar operating principles. The texture influence was evaluated by exploring the usage of texture parameters derived by non-contact measurement methods for a better description of its effect to the pavement frictional performance. The ROSANNE Project reviewed the national policies and established thresholds for the frictional performance in participating European countries, different for the monitoring of the existing pavements or the acceptance of newly built ones. A summary of friction measurement devices with specified friction coefficient type (depending on the measurement principle of the used device) and defined threshold values for new pavements and pavements in use for different road categories can be found in the Project deliverable D 4.1 *Definition of boundaries and requirements for the common scale for harmonization of skid resistance measurements* (Goubert et al., 2014). The analysis of existing practice for frictional performance assessment in the participating

countries showed that almost all of them have a defined threshold for friction, but only nine out of 20 demand a threshold value for texture acceptance and eight for texture monitoring (Table 2.7).

The ROSANNE project was a continuation of the TYROSAFE project (2008-2010), a collaborative European action with the aim of coordination and preparation for the harmonization of frictional performance assessment Europe (Haider & Conter, 2010). TYROSAFE delivered a report about skid resistance policies and standards in Europe for 17 participating countries, showing the threshold levels for frictional performance are very different among them. They were different for the performance indices and influencing parameters taken into consideration, but also for the investigatory timetables and levels of road network where the monitoring is performed.

Table 2.7. National policies of friction and texture monitoring for ROSANNE project participating countries (Goubert et al., 2014)

Country	Acceptance		Road monitoring	
	Friction	Texture	Friction	Texture
France	-	X	X	X
UK	X	X	X	X
Germany	X	X	X	-
Denmark	X	-	X	-
Spain	X	X	X	X
Slovenia	X	-	X	X
Portugal	X	X	X	X
Italy	-	-	-	-
Czech Republic	X	X	X	X
Sweden	X	X	-	X
Norway	-	-	-	-
Finland	-	-	-	-
Belgium	X	X	X	-
Netherlands	X	-	X	-
Austria	X	-	X	X
Switzerland	X	X	X	-
Hungary	X	-	X	-
Slovakia	X	-	X	-
Romania	X	-	-	-
Poland	X	-	X	-

A thorough investigation of skid resistance policies was performed with results presented in the TYROSAFE Project Deliverable D06 (Nitsche & Spielhofer, 2009). The measurement procedures and used devices, the purpose of measurements and the frequency of road network monitoring are very different among the participating countries. The

existence of threshold values for frictional performance assessment determined in the TYROSAFE project is shown in Figure 2.10.

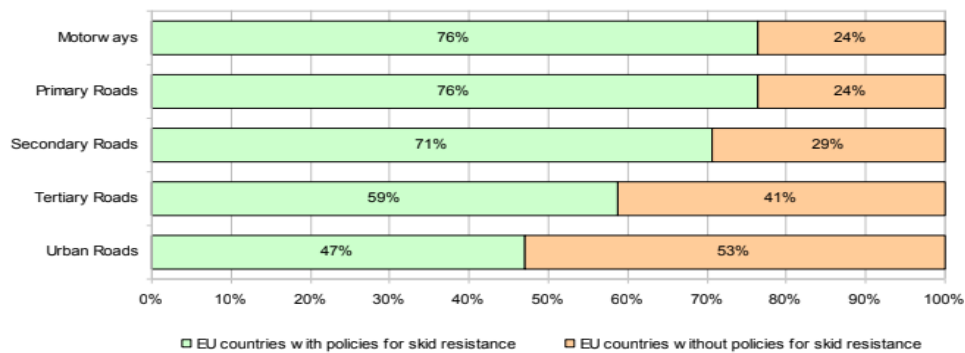


Figure 2.10. TYROSAFE project analysis of friction national policies (Nitsche & Spielhofer, 2009)

2.5.3. Pavement friction performance evaluation in Croatia

European Normative documents are incorporated in the Croatian national regulations and technical specifications for the pavement frictional characteristics assessment. The friction performance estimation is mostly related to the road safety topic, mentioned in two national laws: The road law (*Zakon o cestama*, NN 04/23) and The road safety law (*Zakon o sigurnosti prometa na cestama*, NN 114/22). In these documents, pavement friction is considered as a part of safety and maintenance activities that road authorities should perform, but no specific actions or requirements are mentioned. There are several rulebooks that are considering the issue of pavement friction with respect to the road safety requirements, but again no particular demand is expressed. The rulebook on activities and procedures for improving the safety of road infrastructure and road safety auditing (*Pravilnik o aktivnostima i postupcima za poboljšanje sigurnosti cestovne infrastrukture i reviziji cestovne sigurnosti*, NN 55/2022-739) defines that one of the activities for the road safety estimation is pavement skid resistance. The rulebook for road safety improvement activities (*Pravilnik o aktivnostima poboljšanja sigurnosti TEM cesta*, NN 74/2013-1485) provides guidelines for the revision of the road safety, including the pavement condition as one of necessary input parameters. It also states that if some road sections have a reduced safety level measured in number of accidents with fatal outcome, the increase of pavement skid resistance performance has to be performed. The rulebook for road safety maintenance (*Pravilnik o održavanju cesta*, NN 90/2014-1826) provides a list of activities that have to be performed in a specific timeframe, including the pavement inspections which include the estimation of pavement friction performance.

The only Croatian regulation document that gives a specification for minimal requirements for pavement friction performance is Technical specification for asphalt pavements (*Tehnički propis za asfaltne kolnike*, NN 48/2021-977). This document defines the properties that have to be inspected on installed road surface layers, including the skid resistance and texture as a part of friction performance estimation. The EN standards for inspecting the relevant friction-related surface properties are specified, with respect to the road category and testing frequency on newly built roads or roads in use. Technical specification defines the threshold values for friction performance as skid resistance values, SRT and texture properties as Mean Texture Depth (MTD) values. The values are given for different types of asphalt pavements and different road categories (Table 2.8). The document also specifies the minimal requirements for friction performance of pavement surface at the end of road warranty period, with respect to the aggregate type used in the asphalt mixture (Table 2.9).

Table 2.8 Friction performance requirements for newly built roads - acceptance criterion (*Tehnički propis za asfaltne kolnike*, 2021)

Asphalt pavement surface property	Skid resistance	
National standard for determination	(HRN) EN 13036-4	
Technical parameter	SRT	
Minimal required SRT value for different road categories		Comments
Highways	58	For all asphalt mixture types used for surface layers in Croatia except for overlays, where the SRT value has to be > 60 for primary and secondary roads and > 55 for noncategorized roads
Primary and secondary roads	55	

Table 2.9. Friction performance requirements at the end of warranty period for different aggregate types in asphalt mixture (*Tehnički propis za asfaltne kolnike*, 2021)

Aggregate type	AG1	AG2 and AG3	AG4
SRT limit value: 2-year warranty period	58	55	45
SRT limit value: 5-year warranty period	53	50	40

2.6. Existing models for pavement friction prediction

Direct estimation of pavement friction by employing the measuring techniques described in previous section provides unambiguous friction value, which facilitates the characterization of pavement friction performance for both researchers and practitioners. However, some limitations emerge from the direct friction estimation. The repeatability and accuracy of the performed measurements are affected by the testing and environmental conditions (Yu et

al., 2020). Another issue is the simplified assumption of the contact behavior on the tire-pavement interface in some measurement procedures, which makes it difficult to understand the actual friction mechanism. Friction measurement campaigns can be heavily resource and time - consuming , especially in cases of friction performance estimation by dynamic measurements with real-scale measuring devices.

To overcome the difficulties of direct pavement friction performance estimation by traditional measurement methods, the development of a prediction model based on one or more factors affecting pavement frictional performance has been one of the main topics in the research field. The framework for the development of a prediction model can be analytical, numerical or empirical (Yu et al., 2020). When a prediction model is being defined in any of the frameworks, the complexity of a model increases for a larger number of influencing parameters included. Simple prediction models account for a small number of influencing parameters. Complex prediction models account for several influencing parameters in the same group or from different parameters' groups. The complexity of a model stems from the computational environment in which the model was developed. An example of a simple friction prediction model would be an analytical model observing only influence of speed to the friction performance, or an empirical model predicting friction performance on a single texture indicator. Some examples of complex models are numerical models developed in the finite element framework or empirical models defined with several influencing parameters: texture properties, climate effects or vehicle speed.

In this Section, existing friction prediction models were reviewed and addressed as simple or complex with respect to the number of influencing factors they account for and the approach adopted for the prediction model establishment. The systematization of prediction models is shown in Figure 2.11. A special attention was given to the empirical prediction models accounting for texture features as the main influencing parameter.

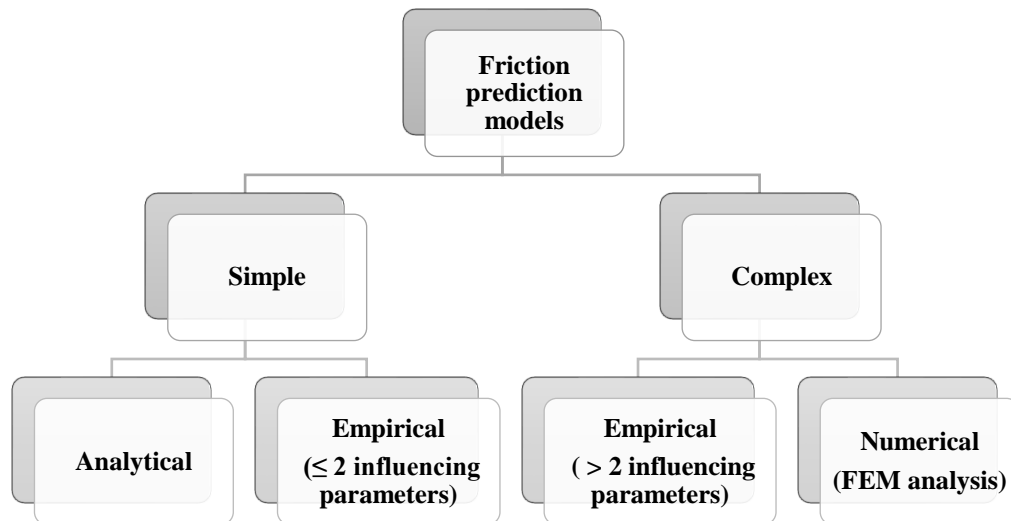


Figure 2.11. Friction prediction models – a schematic overview

2.6.1. Analytical models

Analytical models represent the pioneering approach of rough contact mechanics modelling and the prediction of surface's frictional performance based on rubber friction theory. Such models are developed by Greenwood and Williams, Grosch, Persson, Heinrich and Kluppel and others, as described in sections 2.2.1 and 2.2.2. In analytical models, friction prediction is evaluated by accounting for the influence of surface roughness, tire rubber material properties and/or speed. The explanation of friction phenomenon is limited due to the approximations and assumptions specific for the applied theory and usually fail to accurately predict the non-linear behaviour of the observed problem. They are applicable only for small deformation ranges, which is not the case in the tire-pavement interaction. Also, they cannot account for the transient contact conditions, due to the braking or acceleration or existence of a water film on the pavement surface (Yu et al., 2020). Analytical models are therefore characterized as simple models as the number of influencing factors is generally small and the friction performance prediction is limited due to the models' simplifications.

2.6.2. Numerical models

Numerical methods for pavement friction modelling are an extension of analytical methods, where the problem non-linearities resulting from the rough contact interface and viscoelastic material behaviour could be addressed without the problem generalization and solved in the large deformation framework, as described in section 2.2.3. The most common numerical method for pavement friction modelling is the finite element method (FEM), in

which modelling of vehicle tires, pavement structure and the contact between these two bodies is needed for the simulation of the physical problem (Peng et al., 2019; Z. Yang et al., 2019). This framework requires the discretization of both vehicle tires and the pavement structure, which results in high computational complexity of the FE numerical model. Tire modelling requires not only the definition of the material model, which is commonly selected as hyper elastic or viscoelastic, but also the specification of the loading scenario and the influence of tire anisotropy caused by the different stiffnesses of the vehicle wheels (Yu et al., 2020). Even though it is possible to simulate the tire-pavement interaction in a 2D framework, the best simulation results comparable to the actual physical problems are obtained by 3D interaction models. Pavement structure modelling is even more demanding because it requires the discretization of the surface texture irregularities, but it is inevitable if the goal of the simulation is to evaluate the frictional response in the tire-pavement interaction. An overview of research of pavement frictional performance done in the numerical FEM framework is given in Table 2.10.

The main advantage of numerical models is their ability of friction performance prediction by including the actual effects of the selected model parameters, without the need to simplify or approximate any influence as is the case for the analytical models. The numerical models are considered as complex models for friction prediction as they account for more than one influencing parameter and they are computationally demanding, which means they require a deep understanding of rough contact mechanics and friction theories, but also FEM expertise with accompanying computational structure (adequate hardware and software for FE analysis). This is a major drawback for numerical models in terms of practical applications.

Table 2.10. Examples of FEM application for numerical modelling of pavement friction phenomenon

Authors	Model parameters	Model dimension	Contact simulation	Model output
Fwa, 2017	Water film thickness, sliding speed	2D	Coulomb friction law (+Navier-Stokes equations and standard κ - ϵ model for the fluid behaviour description)	The contact model solves the coupled tire-fluid-pavement interaction problem
Srirangam et al., 2017	Surface morphology, pavement material, loading pressure, sliding speed	3D	surface-to-surface contact algorithm (suitable for the large deformation framework)	Frictional response is evaluated through the calculation of sliding friction coefficient as the ratio between the resultant tangential force and applied normal force
Yu et al., 2017	elastic properties (recoverable resilient deformation) of various pavement structures and system variables: tread deformation at the contacting interface, actual contact area and the braking force	3D	dynamic friction contact analysis (3D tire-pavement interaction model)	Pavement elasticity influences the real contact area
Wagner et al., 2017	rubber friction components - adhesion and hysteresis, multi-scale surface roughness	2D	viscoelastic material model and robust surface-to-surface contact algorithm for hysteresis modelling, different surface contact conditions on macroscopic level for adhesion modelling	Low-speed sliding friction on rough and rigid pavement surfaces
Tang et al., 2018	asphalt mixture components: aggregates, bitumen and air voids (modelled by microstructure FE meshes where aggregates were modelled as elastic material and binder was modelled as viscoelastic material), the effect of high temperatures	3D	surface-to-surface contact algorithm	Frictional response is derived from the theory of hysteresis-induced energy dissipation
Peng et al., 2019	3D pavement surface model reconstructed from high resolution pavement texture data, assumption of pavement rigidity and rubber hyper-elastic characterization, water effect	3D	Exponential decay friction model	Friction coefficient from the resultant tangential force vs. applied normal load (with and without the effect of water)
Liu et al., 2019	Pavement texture, effect of water, effect of different vehicle movements (braking, turning)	2D	Persson's friction theory for the calculation of kinetic friction coefficient	integrated tire-vehicle model for the prediction of frictional performance of wet pavements

2.6.3. Empirical models

Empirical prediction models are developed from the experimentally obtained data for different groups of influencing parameters. They investigate the relationship between one or more influencing parameters and the frictional performance, usually by inferential statistics methods (Rezaei & Masad, 2013a). By following the classification of friction prediction models in Figure 11, an empirical model is considered to be simple if it accounts for a maximum of two influencing parameters, and complex if it observes multiple influencing parameters. Simple empirical models usually investigate the influence of a single pavement surface roughness indicator, the influence of speed or the combined effect of these two parameters.

2.6.3.1. Simple empirical prediction models

Simple empirical models aim to predict the friction performance by observing a single influencing parameter, most commonly the measured pavement texture indicator. Additionally, the friction measurement device speed is accounted in the prediction model and the final model outcome is adjusted according to the measurement speed. All the other influencing parameters are usually neglected in the prediction model. Such models have a straightforward interpretation and provide a direct causality of friction performance based on the evaluated texture property.

Two widely known simple two-parameter empirical prediction models are The Penn State model and the PIARC model (Fwa, 2021). Both models predict the frictional performance of a wet pavement (i.e. skid resistance) by pavement surface texture characteristic and vehicle speed. The Penn State model (1978) accounts for friction with respect to the various vehicle speeds and texture dependable constants. This model is developed from skid resistance measurements performed by a small scale standard static measuring method – pendulum device and at various test speeds by a dynamic full-scale measuring method. The model also contains parameters related to the micro-texture and macro-texture of the pavement surface. By employing this model, it is possible to determine the threshold values of pavement frictional performance for a given vehicle speed, with respect to the surface properties (Fwa, 2017).

The Penn State model was a basis for the development of the PIARC model, resulting from the International PIARC experiment for pavement friction harmonization launched in 1991. This extensive experimental program gathered sixteen world countries in the pursuit for a worldwide acceptable friction performance indicator, derived from on-site measurements of friction and texture. The participants had to provide at least one representative friction and texture measurement device as a collaborator in extensive measurement campaign. The obtained

friction and texture data was used for the establishment of friction and texture relationship between different measurement principles and devices. The harmonization procedure outcome was a unique friction performance indicator, the International Friction Index - IFI. The IFI was defined as a function of two parameters: Friction Number (F60) and Speed Number (Sp). The former is a friction performance indicator, adjusted from the measurement outputs of different devices to the friction value at common slip speed of 60 km/h. The latter is a texture performance indicator, estimated from the texture measurements. According to the PIARC prediction model, the friction value F at any given slip speed S can be estimated as

$$F(S) = F_{60} e^{\left[\frac{(60-S)}{S_p}\right]}$$

with F60 calculated as

$$F_{60} = A + BFR_{60} + CT_x$$

where A, B and C are the calibration constants, specific for a particular friction and texture measurement device and FR60 is determined as

$$FR_{60} = FRS e^{\left[\frac{(S-60)}{S_p}\right]}$$

from the actual friction value measured by the system (FRS) and the slip speed of the measuring system (S) adjusted by the speed number Sp. The speed number Sp is a parameter estimated from the texture measurements as

$$S_p = a + b T_x$$

with a and b being constants depending on the applied measurement device and Tx texture measurement output.

The PIARC experiment results provided a unique harmonization procedure for friction performance assessment by a single friction indicator, including both friction and texture measurements. The obtained results were limited to the participating measurement devices, since the derived calibration constants used in the calculation expressions were device-specific. PIARC model considered only macro-texture indicators in the friction prediction model, neglecting the influence of micro-texture to the pavement frictional performance.

The Penn State and PIARC friction prediction models are applicable for the steady-state driving conditions, where no changes in the driving speed or direction of motion occur. As the frictional

phenomenon on the tire-road interface is mostly a dynamic process, steady-state models are not suitable for the actual behaviour simulations (Canudas-De-Wit et al., 2002). Dynamic friction models were developed to capture the dynamic tire-road contact behaviour, where the influence of speed gradient is highlighted as an influential parameter, therefore they can also be considered as simple one-parameter friction prediction models. The frictional behaviour in dynamic models is described by ordinary differential equations for lumped models, assuming point contact between pavement and tire. Some examples are the Dahl friction model which accounts for friction as a function of displacement and speed effect is observed only through the relative speed direction sign (positive or negative), the Brush model where the frictional response is assumed from the tire deformation and stiffness with respect to the kinematics of the system including the speed gradient, or the Lu-Gre kinematic model where the effect of speed is accounted for by employing the Stribeck effect characteristic for lubricated contact. The distributed kinetic friction models follow the tribology approach, where the frictional response is assumed on a larger area than just a single point. This area is called the contact area and it represents a zone where vehicle tires and pavement surface are in partial or full contact. The frictional response is mostly realized in the zone of full contact and it depends on the ratio between the size of the full contact zone and contact area in total.

2.6.3.2. Complex empirical prediction models

The complex empirical models observe more influencing parameters from the same group or from several different parameters' groups. An example of a complex empirical prediction model including more influencing parameters from the same group would be a model accounting for the effect of different asphalt mixture properties: aggregate type and gradation, binder type and amount, different construction methods and different asphalt mixture types (Hall et al., 2009). These models are usually pointed towards the influence analysis of a specific property (or properties) to the texture performance related to the friction realization. Complex empirical models with several influencing parameters from different groups account for their combined effect on the friction realization. Some examples are the friction prediction model developed from asphalt mixture surface properties evaluated during different polishing stages at different test temperatures (Khasawneh et al., 2012), friction prediction model based on the effect of environmental seasonal variations and traffic load (Pomoni et al., 2020) or the prediction model accounting for the traffic load, pavement age and asphalt mixture properties (Pérez-Acebo et al., 2019).

2.6.3.3. Empirical models with texture as the main influencing parameter

Prediction models based on texture features are mostly derived from extensive measurements of relevant pavement surface properties, performed by traditional measurement devices. They can be simple if only a single texture parameter is related to the friction performance, or complex if other influencing parameters, such as traffic load, pavement type or environmental effects are included in the prediction model. An overview of some existing friction prediction models with texture as the main influencing parameter is given in Table 2.11.

Table 2.11. Overview of empirical friction prediction models with texture emphasized as the main predictor for friction performance

Authors	Research aim	Influencing parameters	Results	Model complexity
Ergun et al., 2005	To predict the friction performance on different pavements from micro- and macro-texture features and examine the speed effect	Texture (micro-texture characterized by specific wavelengths and macro-texture characterized with traditional texture indicator), Pavement type, Speed	$R^2 = 0.89$ for friction prediction from the combined micro- and macro-texture effects, with respect to the slip speed	Complex
Dell'Acqua et al., 2011	To predict the friction performance from micro- and macro-texture features on a specific pavement type (porpous asphalt)	Texture (micro-texture estimated indirectly by pendulum device measurements and macro-texture characterized with traditional texture indicator)	$R^2 = 0.74$ for friction prediction from the combined micro- and macro-texture effects	Simple
Ahammed & Tighe, 2012	To investigate the correlation between different texture characterization methods and friction performance determined from high-speed measurement device	Texture (micro-texture estimated indirectly by pendulum device measurements and macro-texture characterized with traditional texture indicator), Friction measurement equipment tire properties	$R = 0.53$ for measured friction and macro-texture indicator, $R = 0.85$ for measured friction and micro-texture indicator, Negative texture-friction correlation obtained for ribbed tire and positive correlation obtained for smooth test tire	Complex
Kotek & Kováč, 2015	To investigate the correlation between different texture characterization methods and friction performance from measurement device	Texture (micro-texture estimated indirectly by pendulum device measurements and macro-texture characterized with traditional texture indicator), Friction measurement	$R^2 = 0.80$ for prediction model accounting for micro- and macro-texture effect and smooth tire, $R^2 = 0.88$ for for prediction model accounting for micro- and macro-texture and ribbed tire	Complex

		equipment tire properties		
Kargah-Ostadi & Howard, 2015	To investigate the relation between friction performance and macro-texture indicator	Traditional macro-texture indicator, Friction measurement speed	$R^2 = 0.11$ regardless of the measurement speed, $R^2 = 0.73$ for high-speed measurements (70 km/h)	Simple
Meegoda & Gao, 2015	To investigate the effect of macro-texture level and effect of water on the friction performance	Traditional macro-texture indicator and defined limit values	No correlation observed for all observed texture parameter values, $R^2 = -0.85$ for texture values with profile depths > 0.9 mm, The effect of water film is included as an explanation of correlation absence for lower texture indicator values	Complex
Miao et al., 2016	To investigate the cumulative traffic effect on polishing resistance of different pavement types (indirect friction performance)	Traditional macro-texture indicator, cumulated traffic load (2-year period), 4 pavement types	Texture-friction relationship is clear for two pavement types, but no exact measurement of correlation strength was provided	Complex
Chou et al., 2017	To investigate the correlation between traditional texture indicators and high-speed friction measurements	Two traditional macro-texture indicators	no significant correlation	Simple
Basu & Chowdhury, 2017	To investigate the correlation between traditional texture indicators and low-speed friction measurements	Traditional macro-texture indicator	no significant correlation	Simple
G. Yang et al., 2018	To investigate the correlation between traditional texture indicators and high-speed friction measurements	Traditional macro-texture indicator	no significant correlation	Simple
Kouchaki et al., 2018	To investigate the effect of texture measurement equipment on measured friction performance	Traditional texture indicator obtained by two different devices, Friction measurement speed	$R^2 = 0.57$ for low-speed friction measurements, $R^2 = 0.79$ for high-speed friction measurements	Simple
Islam et al., 2019	To investigate the correlation between traditional texture indicator and high-speed friction measurements on different road network levels	Traditional macro-texture indicator, Network level (whole road network, project level network with specified pavement types)	No significant correlation on whole road network level investigation, $R^2 = 0.84$ and $R^2 = 0.97$ for project level network investigation on two different pavement types	Simple
Li et al., 2020	To investigate the correlation between traditional texture	Traditional macro-texture indicator	$R^2 = 0.58$	Simple

	indicators and high-speed friction measurements			
Pomoni et al., 2020	To investigate the texture, long-term seasonal variation and traffic load effect on friction performance	Traditional macro-texture indicator, cumulative traffic load effect, Climate characteristics in Mediterranean zone (wet/dry seasons)	A strong but negative correlation with $R^2 = -0.8$ for texture and friction indicators (explained by the effect of micro-texture which was not evaluated in this research)	Complex

2.7. Pavement friction – summary

Previous sections provided the most important findings related to the pavement friction phenomenon selected from the performed extensive literature review. The theory of rough contact mechanics and physical effects to the pavement friction were analysed. The contribution of the most relevant influencing parameters to the pavement friction phenomenon was overviewed. The methods for pavement friction measurements and classification of pavement friction performance according to the relevant European standards, available technical specifications, collaborative projects' deliverables and most common practices in European countries, including Croatia were given. The existing models for the prediction of friction performance were analysed and grouped according to the number of influencing parameters included in the model definition and with respect to the analytical, numerical or empirical nature of the model. To summarize, here are some important findings about the pavement friction:

- friction coefficient results from the magnitude of friction force, which depends on the size of true contact area between pavement surface and vehicle tire
- true contact area is a function of surface roughness characteristics, therefore pavement friction phenomenon should be observed in rough contact mechanics framework
- the complexity of the phenomenon is multi-dimensional: it accounts for a multitude of roughness scales, non-linear behaviour of the tire rubber, the effect of velocity and temperature in a non-linear behaviour regime and the influence of external non-controllable environmental parameters
- pavement friction performance assessment is not unique, as there exists multiple standardized measurement devices and corresponding resulting parameters for friction performance characterization

- development of different pavement friction prediction models represents an attempt to exclude the actual friction measurements and estimate the friction performance from the selected influencing parameters in a simple or more complex manner

The existing empirical models for friction prediction based on texture indicators as the governing influence parameter were overviewed. The obtained results are not unique as some indicate a strong and positive relationship between texture indicators and friction performance and satisfactory coefficient of determination for the proposed prediction models, while others failed to establish a reliable prediction model showing that no significant correlation could be obtained between texture features and friction performance.

The research performed in this thesis focused on development of a friction performance prediction model based on the influence of pavement surface roughness characteristics, resulting from the texture features. Other influencing parameters were neglected. Therefore, the next Chapter is devoted to an overview of pavement texture properties and characterization methods.

3. Pavement texture properties related to friction

Pavement surface texture is a controllable friction influencing parameter that can be defined, monitored and maintained by pavement engineering practices. To address the importance of the texture in the analysis of pavement friction problem, a detailed overview of important texture properties and characterization procedures relevant for the friction performance is given in this Chapter, including:

- *texture definition and classification with respect to its effect on friction performance*
- *texture-related properties relevant for pavement friction performance*
- *standard methods for pavement texture measurement and characterization*
- *alternative texture features characterization by roughness parameters defined in European standards EN ISO 21920-2 and EN ISO 25178-2*
- *advanced methods for pavement texture characterization*

3.1. Pavement texture definition and classification

Pavement texture represents pavement surface deviations from a true planar surface within a specific wavelength range (EN ISO 13473-1: *Characterization of pavement texture by use of surface profiles – Part 1: Determination of Mean Profile Depth*). The deviations from true planar surface are resulting from peaks and valleys formed by aggregate particles in the asphalt mixture. Texture wavelength represents a horizontal distance between two consecutive texture peaks when observed along a single texture profile. Texture profile is defined as a 2D surface representation, extracted from an observed surface as a cross section perpendicular to the surface plane in a specific length (Figure 3.1.). From the extracted texture profile, texture wavelengths can be determined and texture can be classified accordingly. Another texture descriptor that can be evaluated from the surface profile is the amplitude, which is the peak-to-valley height difference between two consecutive extreme profile points. Characteristic texture dimensions in horizontal and vertical direction are given in Figure 3.2.

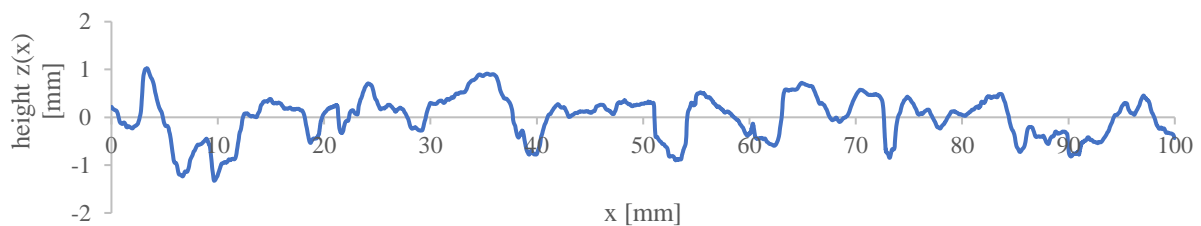


Figure 3.1. An example of full-length profile

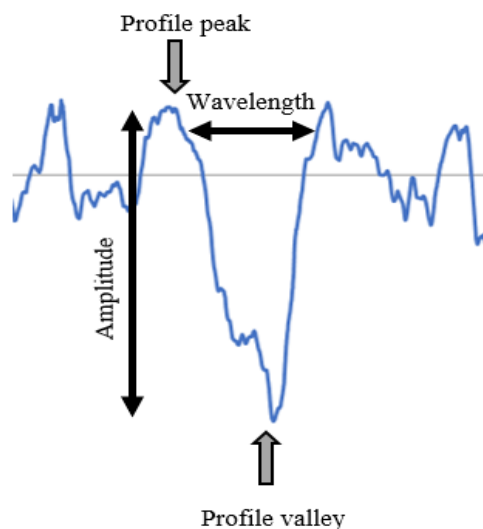


Figure 3.2 Characteristic profile-related texture dimensions

Texture wavelengths and amplitudes are used for the characterization of different texture levels. The first classification of pavement texture according to the profile's geometrical features was presented by Permanent International Association of Road Congresses - PIARC in 1983. Texture was divided in three categories: micro-texture, macro-texture and mega-texture, with respect to the limit values of wavelength and amplitude ranges specific for each texture level. In 1987, PIARC redefined the texture categories with respect to the influence that each texture level has on a specific phenomenon influencing the riding quality (Figure 3.3 and 3.4). Additional texture level was introduced – unevenness or roughness. Texture levels were defined by limit values of wavelengths and amplitudes and such categorization was adopted by national standards and specifications such as American Society of Testing Materials (ASTM), European International Organization for Standardization (ISO) or German Institute for Standardization (DIN). Texture categorization established by PIARC in 1987, was further applied in all research considering the influence of texture features on pavement frictional performance.

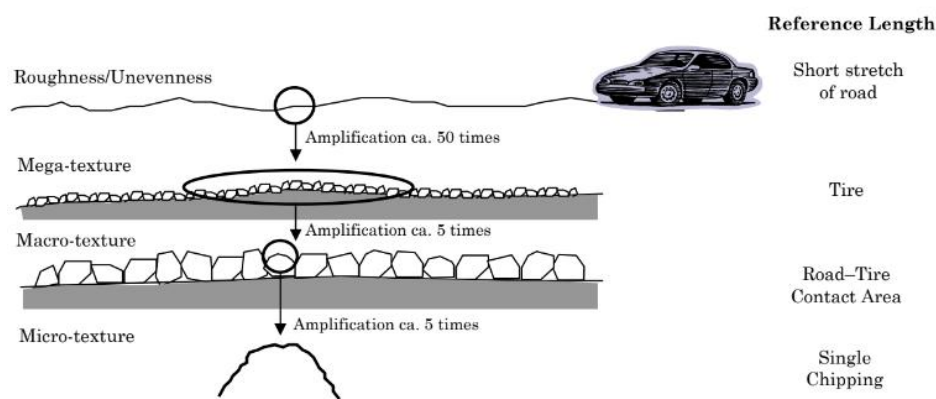


Figure 3.3. Texture classification by PIARC with four texture levels and different reference lengths of a pavement at which they are relevant (Hall et al., 2009)

Following the PIARC texture categorization, European Standard EN ISO 13473 series recognizes four texture levels with different influences on the pavement surface performance. Texture ranges are listed and described in Table 3.1. Micro-texture is the smallest texture level mostly related to the texture of the aggregate particles in the asphalt mixture. Macro-texture is the rough surface texture resulting from the asphalt mixture properties. Mega-texture represents the surface irregularities that can be categorized as roughness of the road surface itself, mostly coming from the mechanical and structural properties of pavement construction and installation procedure. Unevenness represents pavement surface texture which comprises surface defects much larger in comparison to other texture levels, resulting from structural damage of the

pavement construction. When the observed pavement property is the friction performance, micro-texture and macro-texture levels are considered as relevant. Even though they both have an important influence on the friction phenomenon and shouldn't be neglected, usually one of them is investigated thoroughly within a single research, depending on the scope of the investigation and the expected results (Kogbara et al., 2016; L. Li et al., 2016).

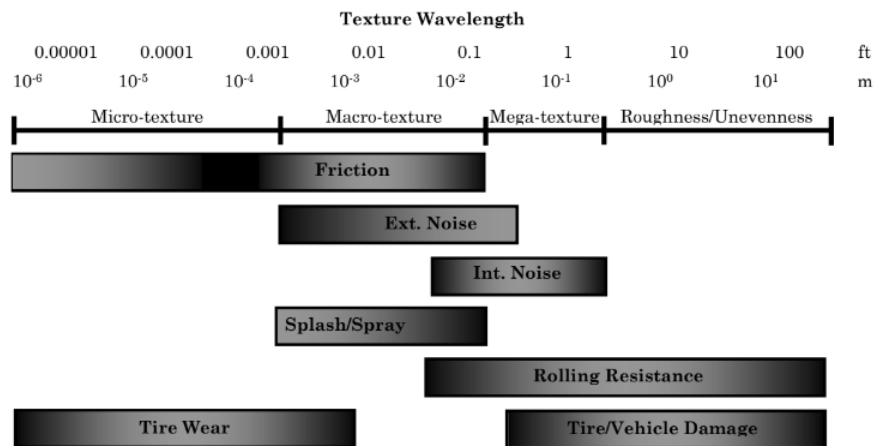


Figure 3.4. Texture levels according to the PIARC categorization and the specific effect on the pavement surface-vehicle interaction (Hall et al., 2009)

Table 3.1 Pavement texture levels and classification with respect to the wavelengths and amplitudes and the effect on the pavement-vehicle interaction phenomenon

Texture level	Wavelength range	Amplitude range	Reference length	Influence on phenomena
Micro-texture	< 0.5 mm	0.001 – 0.5 mm	Aggregate particle	Tire wear, low speed friction
Macro-texture	0.5 – 50 mm	0.1 – 20 mm	Tire-pavement contact area (tire tread elements)	High speed friction, aquaplaning, splash/spray effect, noise
Mega-texture	50 – 500 mm	0.1 – 50 mm	Tire-pavement interface	Noise, rolling resistance
Unevenness	0.5 – 50 m	>0.5 m	Road segment	Riding quality, smoothness, serviceability

In wet road conditions, the contribution of both texture levels is important for the friction realization on wet pavement-tire contact. Micro-texture enables the quick dispersion of water film covering the pavement surface while macro-texture helps with water drainage and reduces the hydroplaning effect (Mataei et al., 2018). The combined effect of both texture levels reflects on the friction performance of pavement surfaces for different vehicle speeds. There are four categories of pavement surface different for the variety in micro- and macro-texture properties

affecting the sliding friction differently with increase of vehicle speed (Hall et al., 2009). Surfaces with high micro-texture and low macro-texture are considered to be smooth and harsh (plot A') and those with high micro- and macro- texture are categorized as rough and harsh (plot B'). For low micro-texture values, surfaces are described as smooth and polished if they also have low macro-texture values (plot C') and rough and polished if the macro-texture values are satisfying (plot D'). Micro-texture magnitude dominantly influences the value of sliding friction coefficient and macro-texture governs the decrease rate of friction coefficient with an increase in vehicle speed (Figure 3.5).

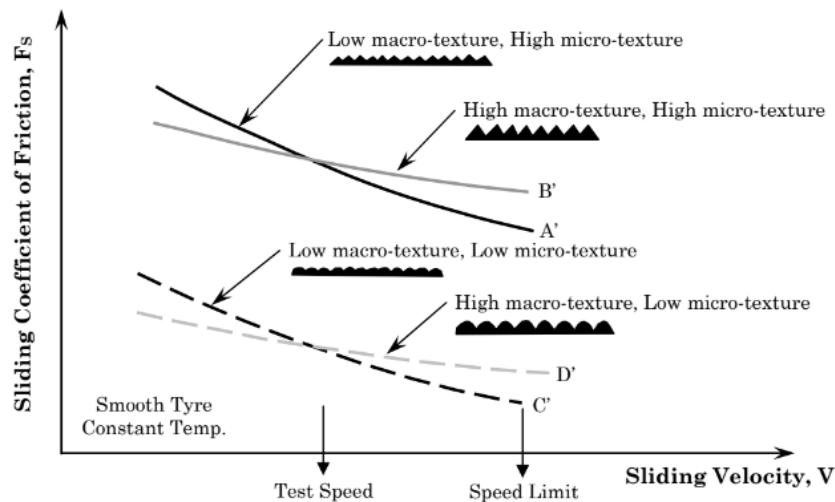


Figure 3.5. The combined effects of micro-texture and macro-texture on friction performance for an increase in vehicle speed (Hall et al., 2009)

3.2. Pavement micro-texture properties

Pavement micro-texture represents surface texture level with wavelengths and amplitudes below 0.5 mm (EN ISO 13473-1). This texture level is hardly visible or not visible at all to the naked eye in its full range (Figure 3.6). It can be described as the pavement surface roughness at the microscopic level interacting with the tire rubber on a molecular scale and thus contributing to the adhesion part of total friction force (Kogbara et al, 2016). When inspecting pavement texture characteristics on low-speed roads, the values of micro-texture are usually more emphasized and related to the available skid resistance level. Research by Kogbara et al., 2016 pointed out the importance of micro-texture for both wet and dry pavements and relevance for the frictional properties regardless of the driving speed.

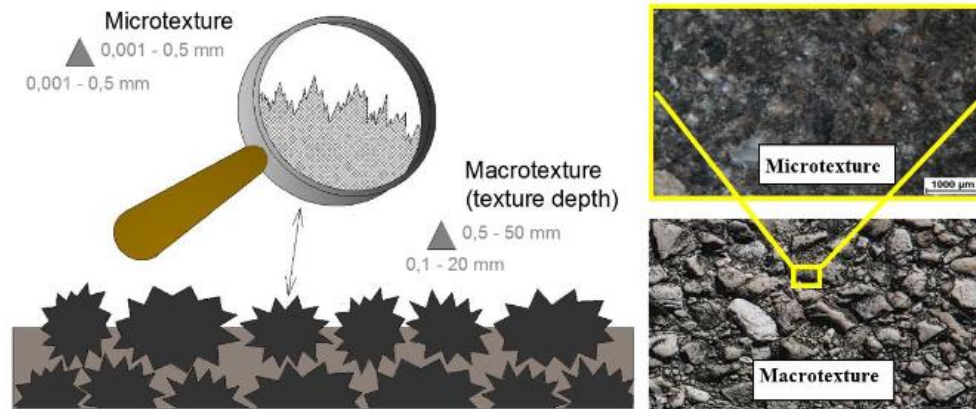


Figure 3.6. Micro-texture level of pavement surface roughness (Kotek&Kovac, 2015)

Pavement micro-texture results mostly from the mineral properties of aggregates in the asphalt mixture, therefore it is commonly referred to as the texture of the aggregate particles (Yu et al., 2020). The most important aggregate properties in relation to the micro-texture are geometric characteristics such as shape and size, and petrological and physical properties, mostly resistance to polishing (Florková & Komačka, 2015). Aggregate origin significantly affects the micro-texture performance. Aggregates such as eruptive, basalt or granite produce higher levels of micro-texture while aggregates of limestone origin result in lower micro-texture levels. Fine aggregate particles (< 2 mm) of the basalt origin tend to increase the micro-texture if their amount in the asphalt mixture increases (Kumar & Gupta, 2021).

Conclusions derived from the research by Ergun et al. (2005) state that micro-texture is an indicator of the pavement surface's polishing resistance directly affecting pavement surface frictional properties. In order to quantify the polishing resistance of different aggregate types, a polished stone value (PSV) test is performed, resulting in PSV values categorized according to the achieved test result (EN 1097-8: *Tests for mechanical and physical properties of aggregates -- Part 8: Determination of the polished stone value*). National regulations give recommendations or requirements for minimal PSV values for different road categories and traffic loads, limiting the choice of an adequate aggregate in the asphalt mixture production. Some European countries give a detailed tables of minimal PSV requirements for different road categories, road network sites or traffic load (Descantes & Hamard, 2015; Senga et al., 2013). In Croatia, Technical specifications for asphalt pavements (*Tehnički propis za asfaltne kolnike*, 2021) defines that a minimal PSV value for pavement surface layers with aggregate mixtures containing mostly eruptive stone (AG1-AG2 and AG3) is PSV 50, while mixtures containing both eruptive and limestone material have a minimal requirement of PSV 30.

Traffic load polishes the pavement surface and decreases the roughness of the aggregate particles exposed to this effect. The polishing effect of traffic influences micro-texture the most, as it is the most exposed part of pavement surface in contact with the tire rubber (Nataadmadja et al., 2015). When aggregates are exposed to the polishing, two effects arise: smoothing and abrasion (J. Liu et al., 2020). The size of these effects depends on the aggregates mineralogy properties. Smoothing is considered as polishing in general as this process results in smooth aggregate surfaces without any micro-texture. The abrasion effect results in new surface micro-texture due to the loss of mineral grains in the aggregate which is composed of minerals with different hardness. If the aggregate material consists of several minerals with different hardness, both effects occur during the polishing process. Aggregates with better polishing resistance provide a better long-term friction performance of pavement surface (Kumar & Gupta, 2021).

Although micro-texture is recognized as an important parameter for pavement friction performance characterization, there is still no standardized method for its direct determination (Zuniga-Garcia & Prozzi, 2019). It is difficult to measure the micro-texture directly on site since it involves small-scale roughness that cannot be captured by traditional texture measuring techniques applied for macro-texture characterization (Sansoni et al., 2009). The most common micro-texture characterization is by low-speed friction measurements with pendulum devices. The measurement result expressed as friction value is a representation of pavement surface micro-texture and not the accurate value. The obtained friction coefficient from the pendulum measurements includes the effects of both texture levels, but also other factors in the measurement procedure, such as surface temperature, rubber slider hardness and some non-controllable factors related to the subjectivity of the measurement method (Kogbara et al 2016). Some researchers investigated the possibility of direct micro-texture characterization by determining shape related roughness parameters of aggregates in order to connect it to the pavement friction, achieving satisfactory results (Do et al., 2009; Dunford et al., 2012; Nataadmadja et al., 2015). Texture is characterized by high-resolution devices such as microscopes, which enable a detailed analysis of surface morphology at micro-roughness levels. This measurement procedure is called aggregate image measuring system – AIMS, utilized to investigate the effect of polishing on the aggregates texture (Araujo et al., 2015; Rezaei et al., 2011). AIMS texture analysis was applied in laboratory conditions and required sophisticated equipment and educated operators. The investigation of micro-roughness effects on the frictional performance is done on aggregate stone samples and not on asphalt mixture

samples. Therefore, real on-road conditions of tire rubber-pavement surface contact related to micro-texture performance cannot be described completely by such analyses.

Recently, advanced non-contact optical-based methods are used for in-situ characterization of texture's micro-roughness features (S. Chen et al., 2022). These methods rely on spatial texture measurements and resulting digital texture models from which various roughness parameters can be extracted, regardless of the texture level. Besides the roughness parameters, digital texture models can be used for the calculation of specific functions describing the surface texture, for example power spectral density function or height difference correlation function related to the fractal nature of pavement texture. The important feature of such methods is that they do not constraint any of the texture levels responsible for the friction realization.

3.3. Pavement macro-texture properties

Macro-texture is defined as a range of surface texture with wavelengths between 0.5 mm and 50 mm and amplitudes between 0.5 mm and 20 mm (PIARC, 1995). It is the road surface texture visible to the naked eye, resulting from asphalt mixture properties and surface layer construction method (Figure 3.7). Macro-texture contributes to pavement friction performance through the hysteresis component of friction force caused by energy loss in the tire rubber deformation process when in contact with pavement surface. Surfaces with coarser texture will induce larger tire deformations when vehicle is passing over, causing increase in energy dissipation and resulting in greater frictional response on the contact area.

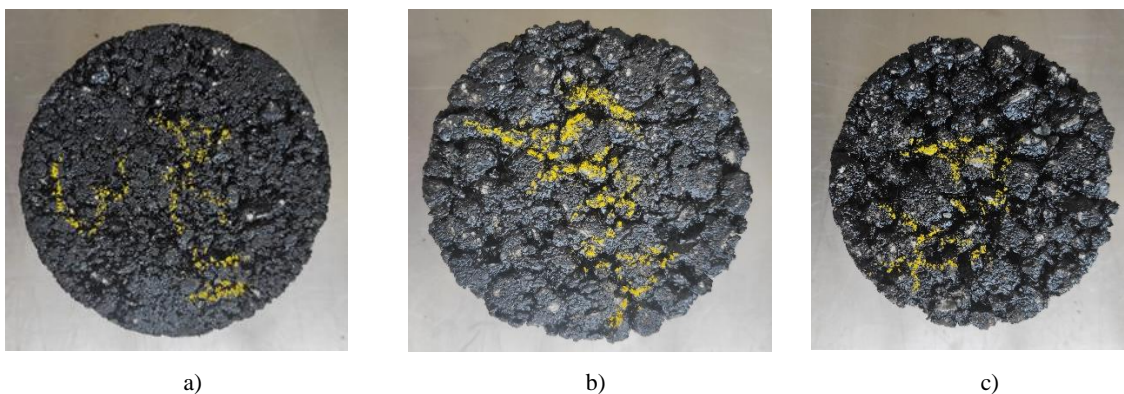


Figure 3.7. Macro-texture of different asphalt mixtures on laboratory samples: a) dense-graded mixture HMA, b) gap-graded mixture SMA, c) porous mixture PA (author's images, 2023)

Macro-texture is responsible for friction performance at high-speed driving conditions and under wet surface conditions (S. Chen et al., 2022). For higher macro-texture values, the excess water covering the surface will be successfully drained away without forming a slippery water film that can fill up the texture cavities and reduce both adhesion and hysteresis components of

friction force (Kogbara et al. 2016). In this way, the dangerous hydroplaning effect is reduced and its influence on the friction realization is disabled. Therefore, sufficient level of macro-texture, together with adequate micro-texture level, provides safe driving conditions.

The most significant parameters responsible for macro-texture are related to the asphalt mixture properties. Those are mainly aggregate mineralogy, distribution and gradation in the mixture, binder type and binder content, air voids content and filler to binder ratio (Araujo et al., 2015; Yu et al., 2020). Despite the fact that the listed properties are well recognized in the research community as governing for macro-texture, there is still no standardized procedure for evaluation of pavement macro-texture prior to the surface layer installation. Most of the asphalt mixture design standards focus on mechanical and volumetric properties of asphalt mixtures, neglecting the effect that mixture properties could have on the friction performance ((D. Chen et al., 2015). Therefore, it is still not possible to predict the friction performance of an asphalt mixture based on the mixture properties. Texture and friction performance are evaluated only on installed roads by traditional measurement procedures and categorized by measured texture and friction indicator values.

The most important asphalt mixture properties that influence the roughness of the pavement surface are the aggregate grains properties: aggregate type, aggregate gradation and nominal maximum aggregate size in the mixture (Hall et al., 2009). Aggregate type used in the mixture governs the asphalt mixture resistance to polishing after the initial binder film covering the aggregate particles is worn out by traffic polishing effect. Aggregates such as basalt, granite, sandstone and crushed gravel are considered as favorable in the asphalt mixture for better friction performance while dolomite or limestone aggregates are more prone to polishing and therefore, the usage of such aggregate types is discouraged for high pavement friction demands (Kogbara et al., 2016). Aggregate's resistance to polishing is evaluated by PSV value, elaborated in section 4.2. Aggregate's geometrical properties such as shape, angularity and soundness govern the initial arrangement of the aggregate in the mixture and contribute to the resulting macro-texture of the surface (Araujo et al., 2015).

The coarse/fine aggregate particles ratio will also affect the macro-texture values. Coarse aggregate content governs the aggregate arrangement and interaction with the binder in the mixture, which are mixture properties closely related to the pavement friction performance. Mixtures with higher amounts of fine aggregates will result in lower macro-texture values (Hall et al., 2009; Iuele, 2016; Rezaei & Masad, 2013). Asphalt mixtures designed as gap-graded or

discontinuous, such as stone mastic asphalt (SMA) or porous asphalt (PA) mixtures have a higher content of coarse aggregate particles and therefore provide better friction performance with higher macro-texture values in comparison to dense-graded mixtures (Araujo et al., 2015; Dell'Acqua et al., 2011; Rezaei & Masad, 2013a; Xie et al., 2019). If the mixture is designed to be as close to the maximum density line, this will reduce the macro-texture of the pavement surface as the amount of fine aggregates is similar to the amount of coarse aggregates (Praticò et al., 2015; Praticò & Vaiana, 2013; Vaiana et al., 2012). Any deviation from the maximum density line will increase the amount of air voids volume in the mixture and increase the surface texture (Sullivan, 2005). However, increase in air voids volume might affect the mixture stability and degrade the properties such as aging, permeability or fatigue. Therefore, the bitumen content in the mixture should be adjusted if the mixture is designed to have a higher amount of air voids. The influence of Nominal Maximum Aggregate Size on the realized macro-texture of the mixture is very straightforward – larger NMAAS causes higher macro-texture values (D. Chen, 2020; Vaiana et al., 2012).

Another influencing mixture related parameter is the bitumen amount and type. In standard hot asphalt mixtures bitumen is used as a main binding agent (Kogbara et al., 2016). Asphalt mixtures containing higher bitumen amounts tend to have lower macro-texture values (Asi, 2007; Sullivan, 2005). This is because bitumen envelops aggregate grains in the mixture creating a film on the pavement surface and reducing both micro- and macro- texture in the pavement early life. If the bitumen amount is high, it will also fill up the cavities in the gap-graded mixtures with higher amounts of coarse aggregates and reduce the texture performance. Influence of bitumen type is observed by evaluating the frictional performance of asphalt mixtures with standard and modified bitumen. A research performed by (J.-S. Chen et al., 2013) investigated the effect of various bitumen types on the frictional performance of asphalt mixtures, showing no significant difference in the obtained results. The SKIDGRIP project launched at the University of Ulster, 2003 investigated the effect of various aggregate and bitumen combinations on the early-life friction performance, concluding that aggregate type and its properties related to moisture sensitivity significantly influence the speed of bitumen coat stripping on the pavement surface. Polymer modified bitumens tend to retain longer on the pavement surface and therefore extend the initial stage of lower friction performance as they cover the aggregate particles on the surface (Woodward & Jellie, 2003).

Besides the dominant effect of asphalt mixture properties on macro-texture realization, surface layer construction techniques can also influence texture performance. Compaction efforts,

compaction type and surface layer thickness are recognized as the most relevant (Pratico et al., 2010). Compaction energy and type of compaction affect the air voids content in the mixture, which is a macro-texture related property. Higher compaction energy and vibrating compaction reduces the air voids amount and decreases the macro-texture performance. An increase of asphalt surface layer thickness influences texture performance negatively (Cantisani et al., 2016). A summary of overviewed asphalt mixture properties and their positive and negative influence on pavement macro-texture is given in Table 3.2.

Table 3.2. Positive and negative effects of asphalt mixture properties on the pavement macro-texture

Asphalt mixture property	Positive influence	Negative influence
Aggregate type	→ Basalt, Granite, Sandstone, Crushed gravel, Gabbro, Greywacke	→ Limestone, Dolomite, Dolerite, River gravel, Quartzite
Aggregate material properties	→ Higher PSV test values → Higher LA abrasion and Micro-Deval wear test values → Lower water sensitivity → Lower aggregate soundness values (degradation resulting from environmental effects)	→ Lower PSV test values → Lower LA abrasion and Micro-Deval wear test values → Higher water sensitivity → Higher aggregate soundness values (degradation resulting from environmental effects)
Aggregate shape properties	→ Sharp and angular-shaped particles	→ Flat and elongated, rounded aggregate particles
Aggregate size properties	→ Coarse aggregates (> 2mm) → Larger NMAAS	→ Fine aggregates (< 2mm)
Asphalt mixture type	→ Gap-graded or open-graded mixtures (SMA or PA)	→ Dense-graded mixtures with smaller NMAAS (AC8)
Asphalt mixture gradation	→ Higher amount of coarse aggregate particles → Deviations from maximum density line → Increase in air voids volume (VMA)	→ Higher amount of fine aggregate particles → Mixture designed to follow maximum density line
Asphalt bitumen properties	→ Lower bitumen content in the mixture → Standard bitumen type usage for early-life friction performance	→ Bitumen content higher than optimal → Polymer modified bitumen for early-life friction performance
Construction method	→ Static compaction → Lower compaction energy → Lower surface layer thickness	→ Vibrating compaction → Higher compaction energy → Higher surface layer thickness

3.4. Macro-texture evaluation by standard measurement methods

Macro-texture is regularly monitored on road network as it is recognized as an important performance indicator for pavement functional performance assessment. It is usually evaluated

by volumetric or geometrical characteristics measured on constructed pavements by standardized test methods and described by a corresponding pavement macro-texture indicator. Based on the measured values of macro-texture indicators, pavement texture is characterized as either having a positive effect on friction performance or as a critical for pavement friction performance, if the determined macro-texture indicators are below the threshold values. The common methods for pavement macro-texture characterization can be used either on-site or in laboratory conditions. They are generally divided into contact and non-contact measurement methods (W. Wang et al., 2011b).

3.4.1. Standard macro-texture measurement devices

The most common contact measurement methods are the volumetric methods: Sand Patch test and the Outflow Meter test (Table 3.3). The measurement procedure for the Sand Patch volumetric method is defined in European standard EN 13036-1: *Road and airfield surface characteristics – Test methods – Part 1: Measurement of pavement surface macrotexture depth using a volumetric patch technique*. The Outflow Meter test is defined in American standard ASTM E2380/E2380M-15: *Standard Test Method for Measuring Pavement Texture Drainage Using an Outflow Meter*. Measurement results of Sand Patch test are expressed as a volumetric indicator of macro-texture describing its depth Mean Texture Depth – MTD in millimeters. For the Outflow Meter test, texture is indirectly estimated from the time needed for a fixed volume of water to evacuate from a measured cylinder with a rubber bottom (W. Wang et al., 2011b). Volumetric contact methods are mostly exploited for a single spot measurement on constructed roads, or for the evaluation of achieved pavement texture on the laboratory produced samples. They are widely used, relatively simple and inexpensive. The contact methods are static and relatively slow, demanding the traffic regulation if they are performed on-site (Kumar & Gupta, 2021). Test results are related to a very small area of surface texture; therefore, they cannot present an overall texture characteristic of a larger road section. They are also very sensitive to operator performance.

The non-contact measurements are conducted with laser or other sensor devices detecting the heights of the texture profile along the measuring path (Wang et al., 2011). The most common non-contact stationary device is Circular Texture Meter – CTM, operating as a rotational device and generating surface texture profiles along the circular path. Non-contact sensor technologies are widespread for dynamic measurement systems. Such devices are usually mounted on vehicles and operate at normal vehicle speeds characteristic of the particular road on which the texture measurements take place.

Table 3.3. Volumetric contact methods for macro-texture characterization

Macro-texture measurement method	Measurement procedure	Macro-texture performance indicator
Sand Patch Method	a known volume of sand or glass beads is spread over the pavement surface and macro-texture indicator is calculated from the ratio of the volume and the circular area where the measuring sand was spreaded	Mean Texture Depth – MTD [mm]
Outflow Meter Test	the flow time of water released from a specific cylindrical device is an indirect macro-texture measure. The water drainage rate evaluated through this test is a representation of surface hydroplaning potential	Outflow Time – OFT [s]

High-speed automated measurement systems enable fast and relatively simple acquisition of large datasets, without the need for traffic regulation. There is a vast number of such devices used worldwide for road network monitoring and they are usually combined with other pavement performance measurements, for example roughness on mega-texture level, rutting, pavement friction etc. European standard EN ISO 13473-3: *Characterization of pavement texture by use of surface profiles – Part 3: Specification and classification of profilometers* gives a general classification of non-contact texture measurement devices with respect to the mobility of devices and operating principle. Furthermore, the EN standard specifies the texture wavelength range classes in horizontal and vertical direction and provides an information about applicability of a specific profilometric device for measurements of a certain texture class (Table 3.4).

Table 3.4. Properties of profilometric devices for pavement texture characterization (EN ISO 13473-3)

Profilometric device type	Measurement procedure requirements	Operating speed	Wavelength range covered by measurements [mm]
Stationary – slow	Single-spot measurements, requires traffic closure on the measurement site	Required measurement time for a single-spot measurement is ≥ 60 s	0.05 – 0.16 0.20 – 0.50 0.63 – 2.0 > 2.5
Stationary - fast	Single-spot measurements, does not require traffic closure on the measurement site	Required measurement time for a single-spot measurement is < 60 s	0.20 – 0.50 0.63 – 2.0 > 2.5
Mobile – low speed	Vehicle-mounted devices, continuous measurement of texture features, suitable for roads of lower category (urban roads)	< 60 km/h	0.20 – 0.50 0.63 – 2.0 > 2.5
Mobile – high speed	Vehicle-mounted devices, continuous measurement of texture features, suitable for roads of higher category (highways, primary roads)	≥ 60 km/h	0.63 – 2.0 > 2.5

3.4.2. Macro-texture performance evaluation

The standard volumetric indicator for macro-texture performance evaluation mean texture depth - MTD is calculated following the standard EN 13036-1 as

$$MTD = \frac{4V}{\pi D^2} [mm]$$

where V is the known volume of a cylinder filled with the measuring material (sand or glass spheres) and D is the average measured diameter of pavement surface covered by the measuring material.

The standard profile-related texture indicator Mean Profile Depth – MPD is determined by following the European Standard EN ISO 13473-1: *Characterization of pavement texture by use of surface profiles — Part 1: Determination of mean profile depth* which defines the terms, expressions and parameters relevant for the calculation of MPD as an average value of profile depth. It is evaluated over a 100 mm long baseline, calculated from the peak profile height determined on the first and the second half of profile baseline (Figure 3.8) as

$$MPD = \frac{M1 + M2}{2} - PP [mm]$$

where M1 is the peak profile height on the first baseline half, M2 is the peak profile height on the second baseline half and PP is the mean profile level.

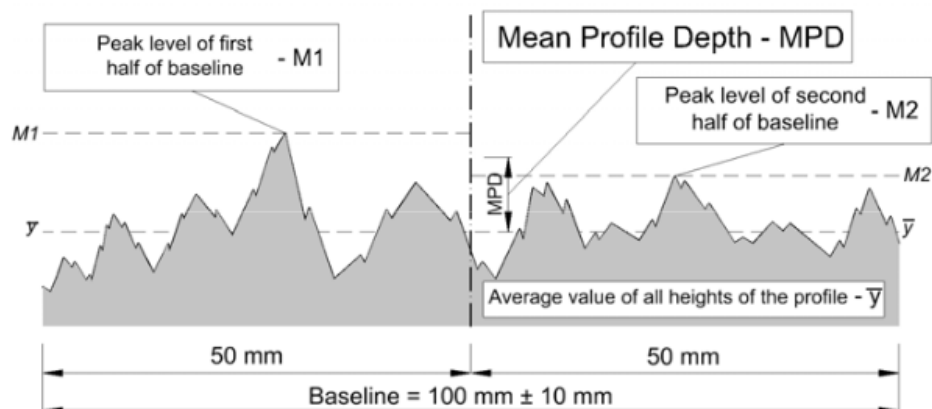


Figure 3.8. The physical meaning of MPD profile-related texture parameter (Kovač et al., 2015)

MPD is used to calculate another common macro-texture indicator, estimated texture depth (ETD). This indicator is an approximation of texture depth, evaluated from the profilometric measurements and established as a comparison of non-contact texture profile measurements

and contact volumetric texture measurement. ETD is calculated by an expression defined in EN ISO 13473-1 as

$$ETD = 0.8 MPD + 0.2$$

MTD and MPD are the most common macro-texture indicators for performance evaluation on road network in Europe. The ROSANNE project Final Output Summary (Birkner et al., 2016) showed that the texture evaluation in terms of frictional performance assessment is not included in skid resistance policies in all participating countries. Not even half of the countries involved in the project had defined texture threshold values, even though texture is acknowledged as one of the crucial pavement properties for friction realization. Aavik et al., 2013. analyzed the existence of threshold texture values in several European countries (Table 3.5) and showed that only four countries had the fully developed limit values for measured texture parameters MPD and SMTD (Sensor-measured Texture Depth).

Table 3.5. Summary of macro-texture evaluation in European countries for road authorities decision making policies and data analysis (Aavik et al., 2013)

Country	Macro-texture measurements	Macro-texture parameters	Limit values for macro-texture parameters
Belgium	yes	MPD	Under development
Lithuania	yes	MPD	no
Slovenia	yes	SMTD	yes
Norway	yes	-	Under development
France	yes	MPD	yes
UK	yes	SMTD	yes
Italy	yes	MPD (and others)	Under development
Latvia	yes	MPD	no
Finland	yes	RMS	Under development
Denmark	yes	MPD	yes
Sweden	yes	MPD	Under development
Estonia	yes	MPD, RMS	Under development

The COST Action Project 354 described in Chapter 2 resulted in a set of pavement performance indicators (PI's) amongst which is the macro-texture indicator expressed as measured technical parameter MPD. Similar to the friction performance indicator (PI_F) expressed through technical parameters LFC or SFC, macro-texture performance indicator (PI_T) was defined as a range of MPD values categorized from very good to very poor performance with grades from 0 to 5 (Table 3.6).

Table 3.6. Macro-texture performance indicator values expressed in MPD, (Litzka et al., 2008)

Macro-texture Performance Index (PI_T)	Very Good > Very Poor				
	0 - 1	1 - 2	2 - 3	3 - 4	4 - 5
MPD [mm] for highways and primary roads	1.25 - 1.06	1.06 - 0.87	0.87 - 0.68	0.68 - 0.49	0.49 - 0.30
MPD [mm] for secondary and local roads	1.01 - 0.87	0.87 - 0.72	0.72 - 0.58	0.58 - 0.43	0.43 - 0.29

In Croatia, macro-texture measurement is a standardized procedure described by two European normative documents, where the procedures and measurement equipment for the determination of volumetric and profilometric macro-texture indicators are defined (Table 3.7). The threshold values of measured macro-texture indicators are defined in Technical specifications for asphalt pavements (*Tehnički propis za asfaltne konike*, 2021), but only for the macro-texture indicator determined from the volumetric measurements. The threshold values are defined for different asphalt mixture types and road categories. By comparing the values given for different road categories it can be seen that they have the same threshold value, regardless of the road category.

Table 3.7. Threshold values for macro-texture performance assesment in Croatia (Technical specification for asphalt pavements, 2021)

European Normative document	Measurement procedure	Measuring equipment	Macro-texture indicator	Limit value (following Croatian Technical specifications for asphalt pavements)
EN 13036-1	Volumetric	Sand Patch Test apparatus	MTD [mm]	Defined for different asphalt mixture type (and road category): AC8, AC11 ≥ 0.35 SMA8 ≥ 0.5 ; SMA11 ≥ 0.6 PA8 ≥ 0.7 ; PA11 ≥ 0.9 BBTM 8 ≥ 0.6 ; BBTM11 ≥ 0.8
EN ISO 13473-1	Profilometric	Profilometer system with mechanical, electro-optical, acoustical sensor type or video camera capable of moving along/across the inspected surface	MPD [mm] ETD [mm]	Not specified

The frequency of macro-texture testing is defined as a single spot measurement for every 0,01 km² of highways and higher category roads (1st and 2nd category roads), either newly built or

in service (*Tehnički propis za asfaltne konike*, 2021). This survey is part of a quality control program conducted prior to road opening or in time periods specific for the road category. For example, highways have a predetermined five-year period between two road monitoring campaigns, while for other road categories Croatian regulations do not specify this interval. Profilometric measurements and resulting macro-texture indicators are not recognized in Croatian Technical specification.

MTD and MPD describe a general macro-texture performance, which is often related to the pavement friction performance in pavement performance assessment programs. However, the characterization of pavement texture by traditional indicators can oversimplify the true texture properties. They generalize texture's volumetric and geometric properties into one single indicator (Li et al., 2017.). For example, two asphalt mixtures can have equal MPD values even though the measured frictional performance is completely different (El Gendy et al., 2011). Therefore, pavement texture characterization by standard macro-texture indicators might not be sufficient for a complete description of the pavement texture-friction relationship (El Gendy et al., 2011; Elunai et al., 2011; Hu et al., 2016; Kogbara et al., 2018).

3.4.3. Pavement macro-texture prediction models

Macro-texture prediction models were developed to overcome the absence of recommendations for the design properties of asphalt mixtures which would result in a specific macro-texture level of a constructed pavement. The aim of these models was to predict the macro-texture level of a given asphalt mixture by considering the most important mixture properties listed in Table 3.2. The proposed macro-texture prediction models were mostly empirical and developed by inferential statistics methods, where selected asphalt mixture properties were used as predictors for the mixture's macro-texture evaluation expressed by one of the standard macro-texture indicators.

Table 3.8 provides an overview of proposed prediction models and resulting statistics based on selected asphalt mixture properties. Model outputs are mostly standard macro-texture indicators MTD, MPD or ETD. Some authors chose an alternative texture indicator level of texture L_{TX} related to the frequency of selected texture wavelength range to evaluate the influence of mixture properties to the texture. A recent model (W. Huang et al., 2022) predicted the macro-texture performance by including other influential factors, such as traffic load and environmental effects of temperature, rainfall and humidity.

Table 3.8. Macro-texture prediction models based on asphalt mixture properties

Authors	Model formulation	Model parameters	Model statistics
Stroup-Gardiner & Brown, 2000	$ETD = 0.0198 \text{ NMAS} - 0.004984 \text{ P}_{4.75} + 0.138 \text{ Cc} + 0.004861 \text{ Cu}$	ETD – Estimated Texture Depth [mm] NMAS – Nominal Maximum Aggregate Size [mm] P _{4,75} – percent passing 4,75 mm sieve [%] Cc – coefficient of curvature (aggregate shape) Cu – coefficient of uniformity (aggregate gradation)	R ² = 0.65
Davis et al., 2001	$MPD = -3.596 + 0.1796 \text{ NMS} + 0.0913 \text{ PP}_{200} - 0.0294 \text{ VTM}_{\text{Lab}} + 0.1503 \text{ VMA}_{\text{Lab}}$	MPD - Mean Profile Depth [mm] NMS - Nominal Maximum Aggregate Size [mm] PP ₂₀₀ - percentage passing the #200 sieve size [%] VTM _{Lab} - total voids in the mix [%] VMA _{Lab} - voids in the mineral aggregate [%]	R ² =0.97
Flintsch et al., 2003	$MPD = -2.896 + 0.2993 \text{ NMS} + 0.0698 \text{ VMA}$	MPD - Mean Profile Depth [mm] NMS - Nominal Maximum Aggregate Size [mm] VMA - voids in the mineral aggregate [%]	R ² =0.965
Hanson & Prowell, 2003	$MTD = 0.6421 \text{ FM}^2 - 5.235 \text{ FM} + 11.224$ $MPD = 0.4973 \text{ FM}^2 - 3.926 \text{ FM} + 8.287$ $MPD = 0.2421 \text{ FM}^2 - 1.576 \text{ FM} + 2.727$	MTD – Mean Texture Depth [mm] MPD – Mean Profile Depth [mm] FM - fineness modulus (aggregate gradation)	R ² = 0.62 R ² = 0.84 R ² = 0.93
Sullivan, 2005	$MPD = 0.025 \Omega^2 + 0.037 \Omega - 0.0265 \text{ P}_b + 0.052$	MPD – Mean Profile Depth [mm] Ω – weighted distance from the maximum density line (function of NMAS and aggregate gradation) P _b - binder content in the mixture [% by weight]	R ² = 0.96
Goodman et al., 2006	$MTD = 0.24 + 0.981 \left(\frac{\text{FM} \cdot \text{VMA}}{\text{P}_{4.75} \cdot \text{BRD}} \right)$	MTD – Mean Texture Depth [mm] FM - fineness modulus (aggregate gradation) VMA - voids in the mineral aggregate [%] P _{4,75} – percent passing 4,75 mm sieve [%] BRD - bulk relative density of the compacted field	R ² = 0.95
D'Apuzzo et al., 2012	$ETD = 1.287 \cdot \frac{\text{VMA}^{1.4} \cdot \text{C}_c^{0.105}}{\text{P}_b^{0.786} \cdot \text{P}_{4.75}^{0.899}}$	ETD – Estimated Texture Depth [mm] VMA - voids in the mineral aggregate [%] Cc – coefficient of curvature (aggregate shape) P _b - binder content in the mixture [% by weight] P _{4,75} – percent passing 4,75 mm sieve [%]	R ² = 0.54

<p>Praticò et al., 2015</p>	$VB = \frac{Q_B}{\gamma_B} \cdot r^2 \cdot 4\alpha$ $AAR = \frac{V_A \cdot \gamma_A}{A_{SH}}$ $SH = \frac{V_{SH}}{A_{SH}}$	<p>VB – bitumen volume [cm³] Q_B – bitumen application rate [g/cm²] γ_B – bitumen density [g/cm³] r – modelled aggregate particle radius [cm] α – particle shape coefficient AAR – aggregate application rate [g/cm²] V_A – volume of single aggregate particle [cm³] γ_A – average specific gravity of single aggregate particle [g/cm³] A_{SH} – surface elementary area [cm²] SH – sand height [cm] V_{SH} – sand volume [cm³]</p>	<p>Not specified</p>
<p>D. Chen et al., 2015</p>	$L_{TX}(\lambda) = a_1 + a_2 \cdot \log\left(\frac{\lambda}{\lambda_0}\right) + \left(a_3 + a_4 \cdot \log\left(\frac{\lambda}{\lambda_0}\right)\right) \cdot \frac{VV}{VFA} + \left(a_5 + a_6 \cdot \log\left(\frac{\lambda}{\lambda_0}\right)\right) \cdot \frac{D_{90}}{D_f \cdot \sin\theta \cdot \Phi} + \left(a_7 + a_8 \cdot \log\left(\frac{\lambda}{\lambda_0}\right)\right) \cdot \frac{1}{PZL}$	<p>L_{TX} - level of mixture surface texture [db(A)] λ - central texture wavelength in octave band [mm] λ₀ - central texture wavelength of 31,5 mm in octave band (covering texture levels from 25-50 mm) VV - volume of air voids [%] VFA - voids filled with asphalt [%] D₉₀ - aggregate particle size in 90% passing ratio [mm] D_f - fractal dimension of aggregate gradation sin θ - aggregate direction angle sine Φ - regulation degree of aggregate PZL - contact length amongst aggregate particles [mm] a_i – model coefficients determined by Levenberg-Marquardt algorithm (RMS error minimization)</p>	<p>R² = 0.87</p>
<p>Praticò&Briante, 2020</p>	<p>a) $L_{TX}(\lambda_j) = \sum_{i=1}^n a_{ij} \cdot (P_i - P_j)$ b) $L_{TX}(\lambda_j) = \sum_{i=1}^n a_{ij} \cdot P_{ij} + c_j$ c) $L_{TX}(\lambda_j) = a_j N_{MAS70} + b_j Q_{R,0.9/70} + c_j Q_{F,0.9/70}$ d) $L_{TX}(\lambda_j) = a_j N_{MAS70} + b_j Q_{R,0.9/70} + c_j Q_{F,0.9/70} + d_j$ e) $L_{TX}(\lambda_j) = L_{TX}(\lambda^*) + m_j \cdot \text{abs}\left[\log_{10}\left(\frac{\lambda_j}{\lambda^*}\right)\right]$ f) $L_{TX}(\lambda_j) = L_{TX}(\lambda^*) + m_j \cdot \text{abs}\left[\log_{10}\left(\frac{\lambda_j}{\lambda^*}\right)\right] + c_j$ g) $L_{TX}(\lambda_j) = L_{TX}(\lambda^*) + m_j \cdot \text{abs}\left\{\log_{10}\left[\left(\frac{\lambda_j}{a \cdot N_{MAS70}}\right)\right]\right\} + b_j \cdot N_{MAS70}$</p>	<p>L_{TX} - texture level λ_j j-th wavelength P_i - percentage passing at the i-th sieve; P_j - percentage passing at the j-th sieve [%] N_{MAS70}- largest sieve that retains some of the aggregate particles but not more than 30 percent by weight [mm] Q_{R,0.9/70}- fraction of aggregate passing the N_{MAS90} sieve and retained at a sieve that corresponds to 90% of N_{MAS70} Q_{F,0.9/70}- fraction of aggregate passing the 90% of N_{MAS90} sieve and retained at a sieve that corresponds to 0.063 mm λ* - maximum wavelength [mm] a_j, b_j, c_j, d_j, m_j – model constants</p>	<p>a) R² = 0.87 b) R² = 0.86 c) R² = 0.49 d) R² = 0.67 e) R² = 0.81 f) R² = 0.95 g) R² = 0.80 h) R² = 0.78</p>

	$h) L_{TX}(\lambda_j) = L_{TX}(\lambda^*) + m_j \cdot \text{abs} \left\{ \log_{10} \left[\left(\frac{\lambda_j}{a \cdot NMA S_{70}} \right) \right] \right\} + b_j \cdot NMA S_{70} + c_j$		
Huang et al., 2022	$SMTD_{it} = 3.8721 - 0.0588 \log(CSAL_{it}) + 0.0008 MAT_{it} - 0.0021 MAH_{it} - 0.0007 MAR_{it} - 4.6375 CA_{it} + 1.0111 FAC_{it} - 2.6346 FAF_{it} + u_i$	CSAL - cumulative number of axles loads MAT - monthly average temperature MAH - monthly average relative humidity MAR - monthly rainfall CA - coarse aggregate ratio (shape of the coarse aggregate portion of the gradation) FAC - fine aggregate coarse ratio (interlocking and filling effects of the coarser portion in fine aggregate) FAF - fine aggregate fine ratio (filling compactness of the finer portion in fine aggregate)	$R^2 = 0.47 - 0.73$ (R^2 strongly depends on the asphalt mixture and time scale with respect to short-term or long-term predictions)

3.5. Alternative methods for pavement surface texture characterization

To extend the standard description of pavement texture properties by traditional texture indicators, alternative methods for texture characterization emerged in the research community with the aim of a more detailed texture description and more reliable estimation of pavement frictional properties based on texture features. Pavement surface is rough and irregular, with more or less visible texture features, depending on the scale of observation. Texture roughness features can be observed in two-dimensional and three-dimensional framework, with traditional texture performance indicators MPD and MTD as the representatives of these two categories, respectively. Besides the traditional texture indicators strictly related to the pavement texture, there exists several groups of general roughness parameters which could be used for pavement texture features characterization. Similar to the traditional parameters, they are distinguished for the dimensionality of the analysis framework: 2D or profile-related and 3D or surface-related parameters (Kogbara et al., 2018). Profile-related parameters are used to characterize the texture properties along the inspected profile and surface-related parameters describe the texture properties on the inspected surface. Another alternative method of pavement texture

characterization is by mathematical functions which can capture the roughness features of an observed surface.

Following sections provide an overview of alternative texture roughness characterization methods by two European standards: EN ISO 21920-2: *Geometrical product specifications (GPS) — Surface texture: Profile — Part 2: Terms, definitions and surface texture parameters* and EN ISO 25178-2: *Geometrical product specifications (GPS) — Surface texture: Areal — Part 2: Terms, definitions and surface texture parameters*. The former relates to profile-based parameters and latter defines the surface-based texture parameters. The standards are not related to any specific surface type but provide the definitions of geometrical properties for texture profiles and surfaces in general on different roughness scales. The most common mathematical representations of surface roughness used for the pavement texture characterization in analytical and numerical models for friction prediction are also presented.

3.5.1. Profile-related and surface-related parameters from European standards EN ISO 21920-2 and EN ISO 25178-2

Profile-related parameters are calculated from 2D surface roughness representations – profiles, and categorized in two main groups according to EN ISO 21920-2: field parameters, related to the texture features of a full length continuous scale-limited profile and feature parameters, related to the texture features of smaller sections of a full-length continuous profile. The full length of a continuous profile is addressed as profile evaluation length l_e and profile subsections are addressed as profile section lengths l_s (Figure 3.9). Field parameters are further divided into four smaller groups, distinct for the profile property they are describing: height, spatial, hybrid and material parameters. Height parameters are calculated from the profile ordinate values $z(x)$, spatial parameters are describing the spatial relationship between the geometrical irregularities of a profile, hybrid parameters are calculated from the local gradient of height $dz(x)/dx$ and material parameters reflect the profile properties related to the material ratio functions: material length, material ratio, material ratio curve, inverse material ratio, height density, material probability curve, material volume and void volume. Feature parameters mostly describe the properties of profile amplitudes Z_{sc} and wavelengths X_{sc} determined for smaller profile sections defined by section lengths. An overview of all texture parameters specified in the EN ISO 21920-2 standard is provided in Figure 3.10. The calculation expressions for all profile-related texture parameters in corresponding groups can be found in the referenced standard.

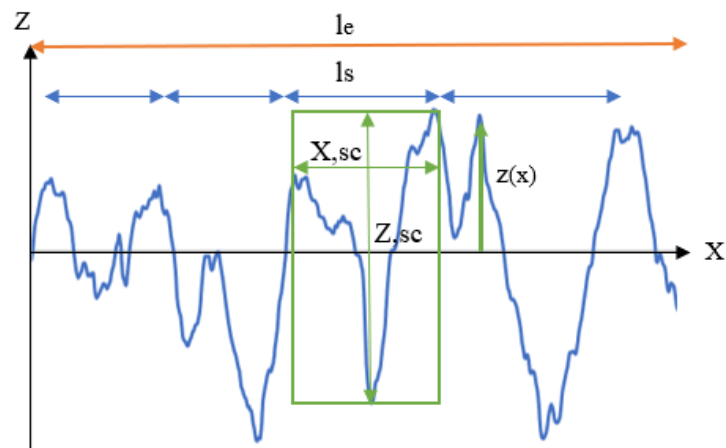


Figure 3.9. Characteristic horizontal and vertical dimensions for profile roughness analysis according to EN ISO 21920-2

Surface-related texture parameters defined in EN ISO 25178-2 are determined from obtained surface representations. The parameters are evaluated from the scale-limited primary surfaces, which are basically originally captured surfaces filtered by a high-pass F-filter which removes the surface form and low-pass S-filter which removes the small scale lateral roughness components. Surface-related parameters are distinguished as field parameters, further divided into four groups similar to the profile-related roughness description, and parameters resulting from the feature characterization procedure. An overview of field parameters is given in Figure 3.10. Feature characterization doesn't involve any specific parameters definition, as for the profile-related characterization. Instead, a five-stage process is defined for the feature characterization including the selection of texture feature type, segmentation, significant features determination, features attribute selection and quantification of statistics attributed to the selected features. Each stage of the process is elaborated in the standard, providing the definition for each performed activity or selected feature in a specific stage, the corresponding designation and threshold values, if available. The final step of feature characterization procedure involves the nomination of obtained feature parameters. The standard defines ten feature parameters names, listed in Figure 3.11.

By comparing the 2D and 3D parameters from Figures 3.10 and 3.11, there are some notable similarities. A limited amount of research was found to corroborate this observation. Bitelli et al., 2012. stated that most profile parameters defined in ISO 4287 (a former version of ISO 21920-2 standard) can be extended to surface parameters by applying adequate mathematical expressions. However, no such procedures were explicitly defined. Harcarik & Jankovych, 2016 investigated the relationship between profile and surface texture parameters, obtaining

high coefficients of determination for surface parameters calculated from their profile equivalents. In their conclusion the importance of further analysis on larger dataset to ensure the validity of the promising results was emphasized. Pavement texture characterization by profile-related and surface-related parameters is feasible. The most common EN ISO 21920-2 texture parameters applied to the investigation of pavement texture features are selected from the height and feature parameters groups (Bitelli et al., 2012; Callai et al., 2022; Zuniga-Garcia & Prozzi, 2019). Pavement surfaces can be characterized as scale-limited surfaces with respect to the defined texture level ranges, while the irrelevant texture geometry features can be filtered out. Research in the field of pavement texture characterization by alternative texture indicators already exists and the analyses showed that alternative texture roughness features could improve the understanding of pavement friction phenomenon (Kogbara et al., 2018). Surface-related parameters give much detailed insight of roughness properties than profile-related parameters extracted from the same surface (Hu et al., 2016; Pawlus et al., 2021). However, the alternative texture parameters cannot be obtained by standard pavement texture evaluation methods. To gain a better insight into pavement texture-friction relationship by including alternative texture indicators, research community turned to alternative methods for texture data acquisition. These methods produce high precision and realistic digital surface representations which can further be analysed in the domain of 2D and 3D texture parameters.

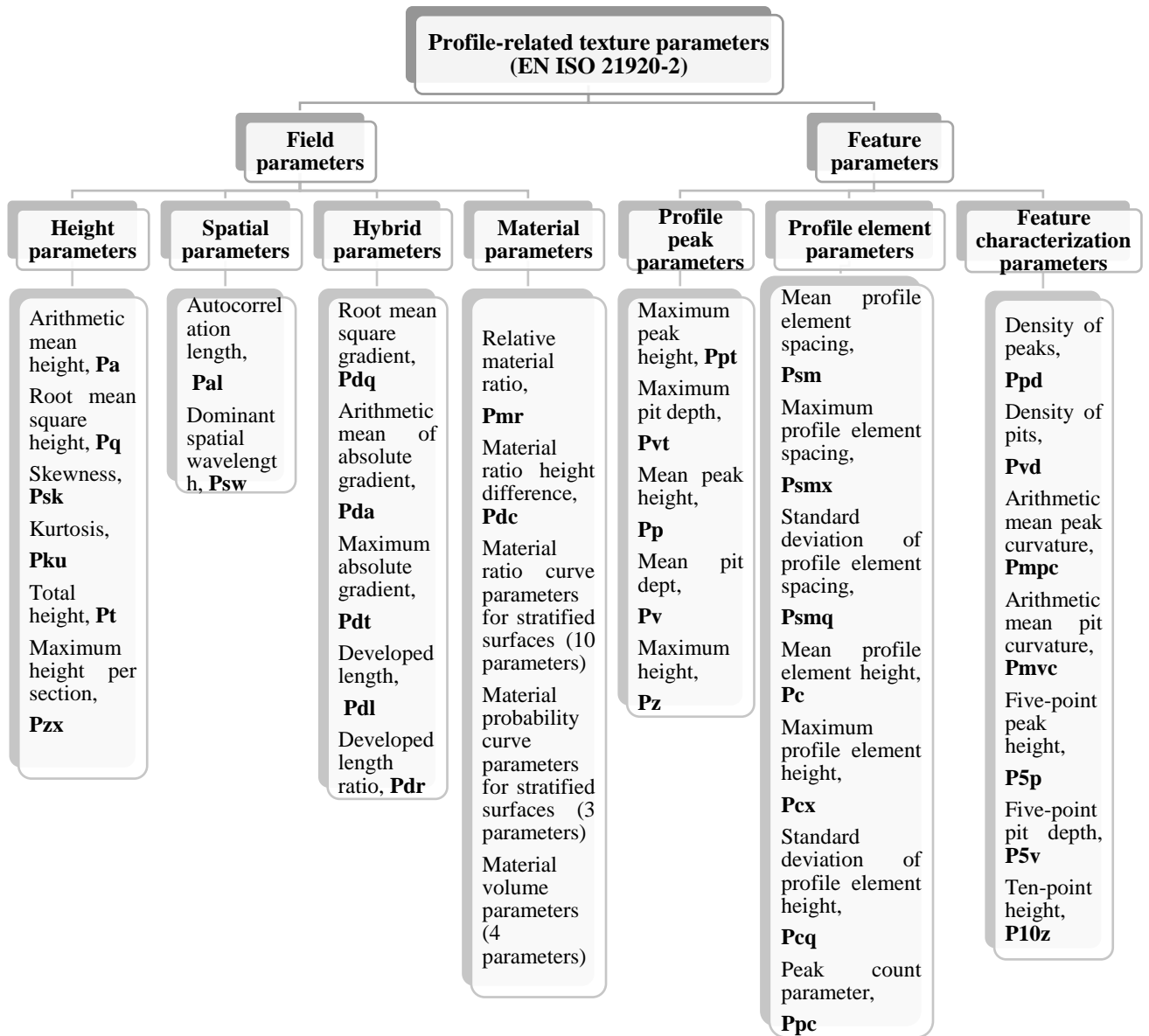


Figure 3.10. Profile-related texture roughness parameters from EN ISO 21920-2

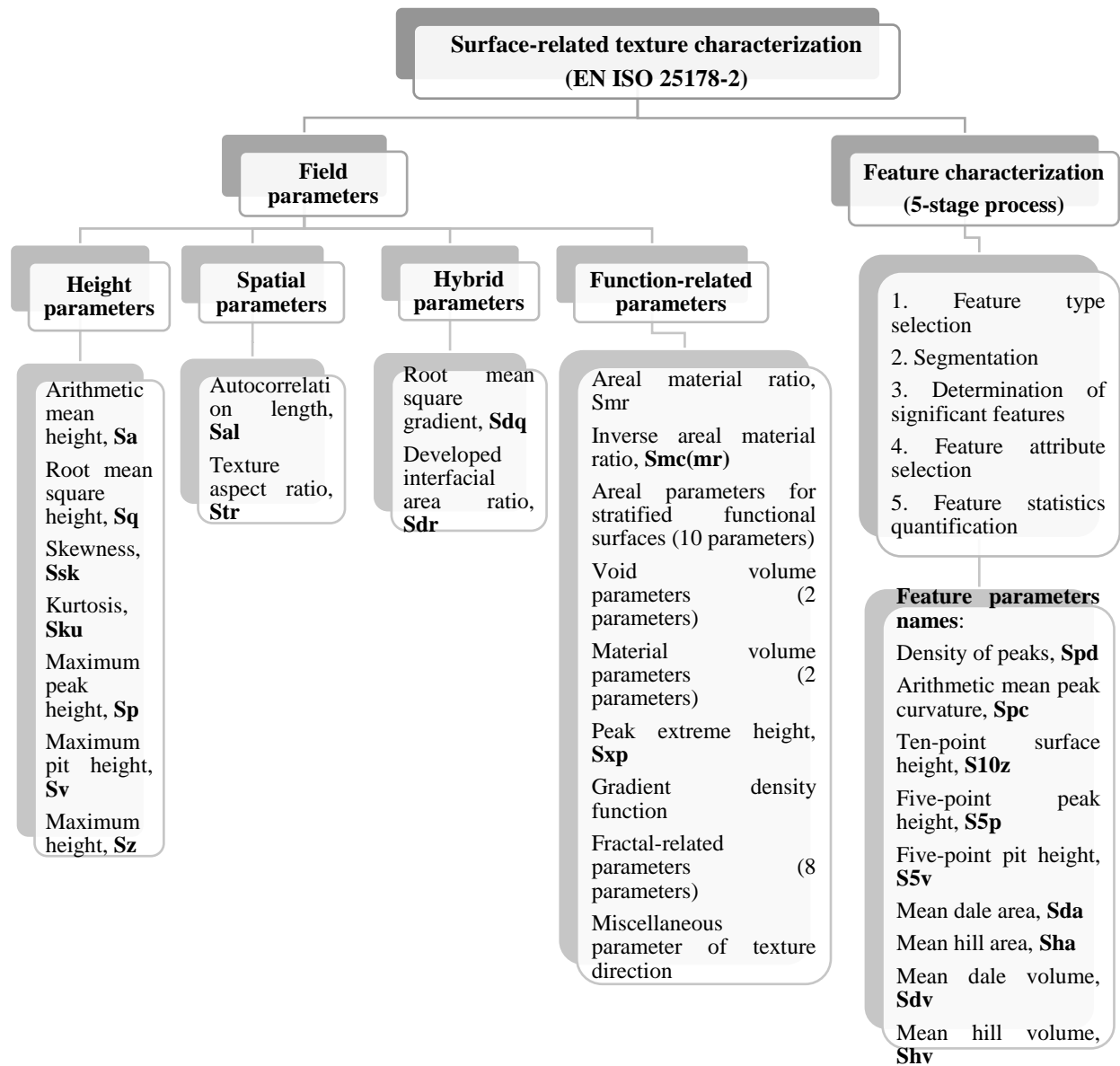


Figure 3.11. Surface-related texture roughness characterization from EN ISO 25178-2

3.5.2. Mathematical representations of texture roughness features

Pavement surfaces are considered to be self-affine and randomly rough. This means they have a repeated texture fashion regardless of the observation scale. Such surfaces are called fractals (Figure 3.12), defined by fractal dimension D_f which describes the complexity of an object's geometry (Kokkalis & Panagouli, 1998). Fractal character of an object can be described by Hurst exponent, H related to the fractal dimension as $D_f = 3 - H$. The mathematical description of fractal geometry of pavement surfaces is given by a fractal interpolation function (FIF). This function is used for the calculation of profile's fractal dimension with a known set of descriptive points. The FIF can be related to frictional performance of investigated surfaces (Roh & Rhee, 2006) or for the estimation of fractal dimension from standard texture indicators such as MPD (W. Wang et al., 2011b). FIFs contain specific roughness parameters which indicate surface properties related to its frictional performance (C. Huang, 2010). Fractal theory is a basis for height difference correlation functions exploited for roughness characterization of pavement surfaces (S. Chen et al., 2022; Torbruegge & Wies, 2015).

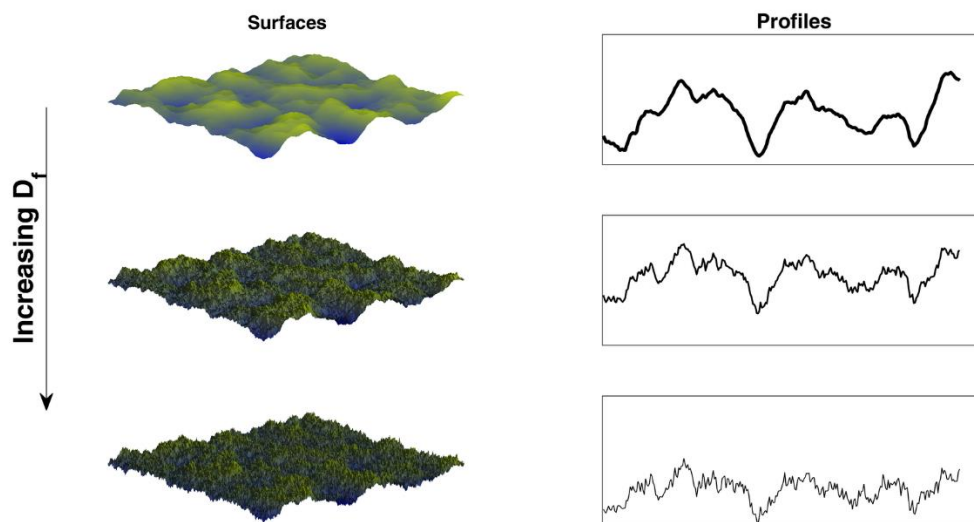


Figure 3.12. Fractal nature of rough surfaces with an increase of fractal dimension D_f , (https://www.wikiwand.com/en/Fractal_dimension, accessed 19.5.2023)

One of the most common mathematical descriptors of self-affine fractal surface roughness exploited in contact mechanics models is the power spectral density function - PSD. This function enables the identification of different spatial frequencies or wave vectors obtained by surface decomposition (Jacobs et al., 2017). Being defined by wavelengths and amplitudes, texture can be analysed within the frequency domain. The statistical information on the surface topology, without the resolution effect, is contained in the PSD function. Different asphalt mixtures produce different PSD functions due to the varieties in the texture features, resulting

from the mixture properties (Figure 3.12). Characterization of pavement texture properties by PSD functions is exploited in contact mechanics theories and applications developed for the estimation of target surface properties, for example the evaluation of true contact area or calculation of friction coefficient. One of the examples is Persson's friction theory, where the entire PSD of a rough surface is taken as input for calculation of friction coefficient (Lorenz et al., 2011; Persson et al., 2005). The estimation of pavement friction performance by PSD surface roughness characterization can be found in research by Alhasan et al., 2018; Deng et al., 2021; Hartikainen et al., 2014; Kienle et al., 2020; Mahboob Kanafi & Tuononen, 2017; Serigos et al., 2014; Yan et al., 2020; Yun et al., 2020 and others.

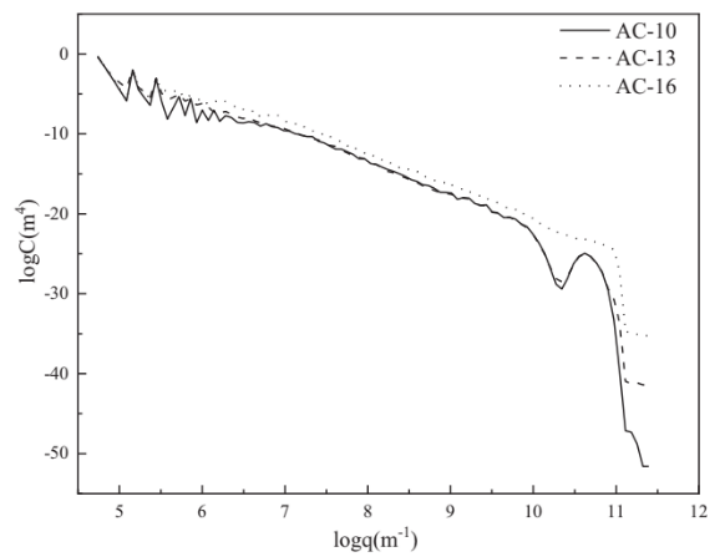


Figure 3.13. PSD function of different asphalt pavement types (Deng et al., 2021)

A European Normative document ISO/TS 13473-4: *Characterization of pavement texture by use of surface profiles — Part 4: Spectral analysis of surface profiles* provides three different methods for spectral analysis of pavement surface profiles, applicable for all random signal types including the pavement surface profiles. Another method for texture features analysis in the spectral domain is by using wavelet transformations, enabling the analysis in frequency domain with the preservation of spatial reference in 1D or 2D domain (S. Chen et al., 2022). The limiting properties of 1D analysis are profile analysis only in one direction and poor correlation of derived indicators with micro-texture and 2D analysis enables the separation of two texture scales by wavelet decomposition (Q. J. Li et al., 2017; Zelelew et al., 2013).

3.6. Advanced methods for pavement texture data assessment

3.6.1. Photometric methods

Photogrammetry is an optical imaging technique which utilizes images captured by digital cameras for the reconstruction of a 3D model of the photographed object (Sansoni et al., 2009). Photogrammetry methods result in 3D object coordinates derived from image measurements from which geometric features and graphical information can be derived (Luhmann et al., 2006). It is mostly used for measurements of feature types on the reconstructed objects, generated by the triangulation bundle adjustment principle to produce the point coordinates from the acquired images (Han et al., 2012). The geometrical model and the orientation of the light rays' bundles are present in the photogrammetric relationship, developed by analytical expressions and implemented by least squares procedure. The photogrammetric procedure consists of five general steps that have to be followed to obtain a representative and meaningful result (Sansoni et al., 2009). The first step is equipment preparation and adjustment, which includes selection of a proper camera and its calibration. Afterwards, data acquisition is initiated by image acquisition following the defined procedures and properties, for example the number of images and ratio of image overlapping. The next step is generation of a 3D dense point cloud (DPC) object from the geometrical information obtained from the captured images. The DPC holds image information in a form of 3D point coordinates describing the object's features and presents a basis for the surface reconstruction and texture mapping. By following the aforementioned steps, the reconstructed object of interest can be used for further measurements.

Photogrammetry is used for the investigation of geometrical and other spatial features for all kinds of objects in very different observation scales. There are two general types of photogrammetry, terrestrial and aerial (Luhmann et al., 2006). The difference is in the camera position, which can either be on the ground or in the air. A special case of terrestrial photogrammetry is the close-range photogrammetry (CRP). This technique is applied for the inspection of objects that are up to 300 m far from the camera and from approximately 1 m to 200 m in size, with accuracies from under 0.1 mm to 1 cm depending on the specifics of the field of application. Photogrammetry has a wide variety of applications in many fields; architecture, engineering, forensics, medicine, archaeology, industrial manufacturing applications and monitoring of geological hazards are just a few to mention. From the engineering aspect, some of the most common research problems utilizing photometric technologies are related to the monitoring of various structures and analysis of their intrinsic properties and evolution due to relevant external or internal influences.

Photogrammetry application in civil engineering can be found in different topics and different problem scales. Photogrammetry techniques are exploited for the creation of digital terrain models with very high accuracy, which enables the analysis of morphological changes in natural structures, such as coastal erosion monitoring (Ružić et al., 2014, 2015), monitoring of nourished gravel beaches (Pikelj et al., 2018; Tadić et al., 2022). Authors James et al., 2019 published a guideline paper for the photogrammetry applications in geomorphological research, providing a systematic set of recommendations and benchmark standards for an adequate usage of photogrammetry, especially SfM technique for various applications in the field of geomorphology. Another purpose is the identification and risk assessment for the environmental hazards, such as flooding or landslides (Pajalić et al., 2021; Zazo et al., 2018). An important photogrammetry application is for the monitoring of civil engineering structures and materials and assessment of their physical and functional condition (Barazzetti & Scaioni, 2010; Han et al., 2012; Maas & Hampel, 2006; Y. Tang et al., 2019). A systematical review of the current application of 3D reconstruction methods in civil engineering was done by Ma & Liu, 2018. The advantages of using such methods are pointed out, together with the possible enhancements and possible applications to other civil engineering areas.

Photogrammetry is used in the analysis of pavement properties in 2D and 3D frameworks. Pavement surface images can be analysed by application of an adequate image analysis method, for example grayscale image analysis by PSD functions, wavelets or edge detection techniques. Image analysis results are used to explain the effect of asphalt mixture properties on surface roughness characteristics. Mixture design parameters such as aggregate gradation, air voids content or the bitumen amount in the mixture can be assessed from the surface images. They can be correlated to the surface frictional properties determined by standard measurement procedures. 2D images cannot provide information about pavement texture morphology as they do not contain the surface height information. When the acquired pavement surface images are utilized for the 3D reconstruction of the pavement surface morphology including surface heights, the obtained digital surface models (DSM) enable the analysis of profile and surface related roughness parameters described in Figures 3.10 and 3.11. Photogrammetry applications in 2D and 3D framework for pavement texture characterization are overviewed in Table 3.9.

Table 3.9. Research results exploiting photogrammetry method for pavement texture characterization and analysis

Research framework	Authors	Measurement methodology	Texture parameters	Results
2D image analysis	Ergun et al., 2005	NIAS (New Image Analysis System) for micro-texture analysis, with CCD microscopic camera, illumination system, scanner for image data digitalization and XY positioning system	Texture and spectral parameters were calculated and used for the development of a friction prediction model	Proposed friction prediction model based on texture indicators calculated from NIAS has a good correspondence with the measured friction coefficient on all investigated road sections ($R^2 = 0.89$)
	Elunai et al., 2010	Digital 7.2 MPix camera positioned 80 cm above the pavement surface	2D images were analyzed in the frequency domain by Fast Fourier Transform, autocorrelation function and wavelets	The obtained texture indicators resulting from frequency-domain analysis showed good correlation with the measured SMTD values ($R^2 > 0.8$ for all three methods)
	Elunai et al., 2011	Digital 7.2 MPix camera capturing pavement surface images at different angles (60° and 90°), analyzed by means of edge detection technique - an accurate determination of aggregate size from their boundaries	SMTD values determined by the laser profilometer	Results of correlation analysis between EDPC values (results of edge detection technique for aggregate size distribution assessment) obtained from the image analysis method and measured SMTD values on pavements in use showed that the proposed method is suitable for the evaluation of road surface macro-texture performance and can supplement the traditional measurement techniques ($R^2 = 0.94$)
	Rezaei et al., 2011	AIMS (Aggregate Image Measurement System) - digital camera with five different zoom levels and special lighting, mounted on a rotating tray	Macro-texture MPD and RMS texture indicators	AIMS-derived MPD values have a significant correlation ($R^2=0.93$) with MPD values obtained by CTM measurements on pavements in use for segments with 50 mm length. RMS parameter derived from the AIMS has a relatively strong relationship with the MPD measured in the field ($R^2=0.75$)
	Specht et al., 2013	A conventional digital camera (no further specifications)	Spectral domain analysis by FFT algorithm to obtain spatial data	Correlation analysis showed that an exponential function can define the texture parameter by using FFT, with $R^2 = 0.87$ for the comparison with the experimental data evaluated by a traditional sand patch test (MTD)

	D. Chen et al., 2015	ITAM (Image Texture Analysis Method) system (office scanner and custom made software for data analysis based on Matlab 2014a, Visual Studio 2013 and Install Shield 2010)	Spectral domain analysis by Fourier transform, texture distribution spectral indicators $L_{TX,m}$, PSD and standard profile indicator MPD	Calculated texture parameters obtained from the ITAM system were compared to the ones obtained by stationary laser profilometer SLP, with $R^2 = 0.92$ for MPD and $R^2 = 0.93$ for $L_{TX,m}$
3D digital surface model analysis	Gendy & Shalaby, 2007	Four-source photometric stereo technique including one 5.1 MPix digital camera and four light sources adaptable by its height and angle, enclosed in a box that isolates the ambient light	MPD	The correlation analysis for MPD obtained on real surfaces and on DSM showed a strong agreement with $R^2 = 0.82 - 0.92$ (depending on the zenith angle of the camera)
	El Gendy et al., 2011	Non-contact texture measurement device PhotoTexture (based on El Gendy and Shalaby, 2007)	MPD, RMS and PSD function	Surface texture indicators were correlated to friction performance measured on-site by a dynamic friction measuring device (GripTester), with $R^2 = 0.52$ for MPD, $R^2 = 0.55$ for RMS and $R^2 = 0.55$ for PSD.
	Woodward et al., 2014	CRP method with a single digital 10Mpix camera for image acquisition and Topcon ImageMaster software for surface model reconstruction	MTD	Obtained $R^2 = 0.92$ for MTD calculated from the DSM and sand patch measurements.
	McQuaid et al., 2014	CRP method (from Woodward et al., 2014)	Surface-related parameters V_{mp} , V_{mc} , V_{vc} , V_{vv}	Calculated parameters from the CRP method were compared to high-resolution laser scanning method (HRS) resulting parameters, showing good agreement between parameters determined by different methods for HMA mixtures, when adequate filtering procedures are applied to the DSMs
	Mahboob Kanafi et al., 2015	Optical portable non-contact 3D-profilometer featuring a digital camera for data acquisition and illumination system and image post-processing Matlab	R_q , R_{sk} , PSD Hurst exponent	Selected texture parameters were evaluated during six-month period on different asphalt mixtures, represented by height maps from the ODSCAD. The results showed that the texture parameters estimated from surface representations could represent the texture evolution

		based software ODSCAD, capturing 10 measurements of surface topography at each test site		trend due to the polishing effect of traffic, pavement age and seasonal variations. The relationship with texture and friction was explored through Rq and Hurst exponent evolution, showing no significant correlation
	Puzzo et al., 2017	Five different digital cameras for Structure from Motion (SfM) data acquisition: one reflex camera with 12 Mpix, two compact cameras with 10 and 14 Mpix resolution and two smartphone cameras with 8 Mpix and 5 Mpix resolution, minimal number of images was 11 for each camera. The digital surface models were created by Autodesk 123 Catch computer vision software	MTD, MPD	A strong correlation between DSM calculated MTD and MPD and measured MTD for all five cameras (all $R^2 > 0.90$)
	Alamdarlo & Hesami, 2018	Photometric system with a single 12.1 Mpix camera and four light sources assembled on a circular frame for asphalt specimen analysis, changing the zenith angle (relative position of the camera and the light source) for eleven different degrees. A total of 44 images was taken for each specimen, used for the 3D surface reconstruction by a Matlab-based algorithm	MTD	For a different zenith angle, the calculated value of MTD was different (an increase in zenith angle decreased the value of MTD), an optimal position was explored by comparing the calculated MTD to the measured MTD for different specimen types. The results of the study indicate that different texture depths require different zenith angles in order to obtain high accuracy results
	Kogbara et al., 2018	CRP method with a single camera capturing 12 images of a test section, used for 3D surface reconstruction in 3DF Zephyr software	Surface roughness parameters: Sa, Sq, Vmp, Vmc, Spd and Spc calculated for five scenarios of texture morphology adjustments: form removal (F-filter), robust Gaussian filter	Multiple linear regression analysis between surface roughness parameters for all five scenarios and measured friction performance by a dynamic high-speed tester (GripNumber) showed that a notable relationship between texture parameters and friction

			for micro-texture roughness and macro-texture waviness and top 1 mm and top 2 mm heights filtering to remove extreme surface elevation points (0.5% of the whole DPC)	performance is obtained for case 5 scenario, where top 2 mm surface was observed: $R^2 = 0.62$ for Spd and Spc as significant texture indicators for the prediction model
	Y. Wang et al., 2019	Photometric stereo system equipped with a camera and six light sources fixed in different directions under six angles, resulting in six images from which the 3D surface is reconstructed	MTD, RMS, MPD, wavelength-correlated indicators rms-wavelength λ , average spacing of single peak S and rough area ratio on the surface R, shape-correlated indicators Ssk, average tilt angle Θ and anisotropic degree K – all texture indicators were determined for micro- and macro-texture levels in 2D and 3D framework	MTD, land Ssk determined for 2D morphology (profile) and 3D morphology (surface) were different: MTD was higher for 3D framework and λ was higher for 2D framework, Ssk showed no trend. Macro-texture indicators MTD, RMS and MPD showed positive correlation with measured friction performance, higher for macro-texture indicators ($R^2 = 0.81$ for BPN and $R^2 = 0.6$ for DF60), λ showed moderate negative correlation to friction performance at both texture level ($R^2 = 0.51 - 0.75$), S showed negative and weak to moderate correlation ($R^2 = 0.38 - 0.71$), R showed positive weak to moderate relation ($R^2 = 0.37 - 0.61$), Θ showed moderate positive relation ($R^2 = 0.43 - 0.62$) and Ssk and K showed no correlation to the measured friction.
	Edmondson et al., 2019	Photogrammetry based method Structure from Motion (SfM) with a single-lens digital camera (50 mm) capturing images on three different heights (500, 600 and 750 mm), further processed in Agisoft Photoscan software for 3D surface reconstruction	Surface roughness parameters: Sq, Ssk, Sp, Sv, Spd and Spc determined for filtered and unfiltered surfaces (the filter was applied to extract only macro-texture related surface morphology)	SfM method performance was evaluated with respect to two laser scanning methods (terrestrial laser scanner-TLS and 3D smart laser sensor). The performed 2D cross-correlation analysis showed good agreement between texture parameters determined from SFM and 3D laser sensor (obtained corell. coefficient was 0.73 for filtered surfaces)
	J. Chen et al., 2019	Automatic close range photogrammetry (ACRP) system for real-time monitoring of the anti skid pavement performance: a custom-made platform with three curcularly arranged	MTD, RMS	The ACRP derived texture parameters were compared to sand patch method for the MTD evaluation and laser scanner device ZGScan for RMS evaluation – the obtained mean relative errors were 0.5% for MTD and 0.25 % for RMS. The obtained $R^2=0.9945$ for MTD obtained by sand patch method and ACRP.

		cameras for simultaneous image acquisition and shadowless lighting system + Matlab/Python-based 3D surface reconstruction software module		
	Al-Assi et al., 2020	CRP method with 20.1. Mpix camera capturing 9-12 images of asphalt specimen surface and used for the creation of DSM by 3DF Zephyr	Mean micro-texture and macro-texture depth (in accordance to US Standard ASTM E 1845-9)	Texture parameters calculated from DSM correlate well with measured texture indicators: $R^2 = 0.85$ for macro-texture indicator MTD and $R^2 = 0.91$ for indirect micro-texture indicator DFT20 (estimated by a low-speed friction measurement device). Derived texture indicators were used as inputs in friction prediction model based on Persson's theory as PSD function, which showed high coincidence with the measured friction values on both laboratory samples ($R^2 = 0.90$) and field test sections ($R^2 = 0.97$)
	D. Chen, 2020	Non-destructive 3D image analysis method based on asphalt mixture design parameters - 3D ITAM: a digital camera captures tricolour images (red, green and blue) of asphalt specimen. 2D tricolour images are used for 3D surface reconstruction by Frankot-Chellappa algorithm for global integration	MTD and spectral texture indicators $L_{TX,m}$ (mixture surface profile level in a specific wavelength range m in decibels): $m = 0.5-31.5$ for macro-texture and $0.13-0.5$ for micro-texture)	3D ITAM calculated MTD and $L_{TX,0.5-31.5}$ correlate well with sand patch test MTD measurements ($R^2 = 0.81$), $L_{TX,0.13-0.5}$ correlates well with friction coefficient measured by dynamic friction tester HFM ($R^2 = 0.88$)
	Huyan et al., 2020	A system equipped by two cameras and a structured light module with a control panel for asphalt specimen testing	Macro-texture analysis (micro-texture was filtered out by robust Gaussian filter) by profile-related roughness indicators: Pa, Pq, Psk, Pku, Sm, peak distance, rms-slope, rms-wavelength, surface roughness area ratio and MTD	Ra, MTD, and rms-wavelength are the most significant indicators that should be considered as priorities for analyzing the friction levels, having correlation coefficients higher than 0.7 with measured friction expressed in BPN
	Tian et al., 2020	Smartphone-integrated two 12 MPix cameras, taking 20-32	MPD	The proposed method was validated with laser texture scanner LTS measurement of MPD, showing a mean

		pavement surface images at each test site. Afterwards, a DPC object was generated to calculate texture indicator MPD by		difference of 4% and maximum difference of 9% between the photometric and laser scanner derived texture indicator
	Medeiros et al., 2021	CRP method with 24.1 Mpix DSLR camera capturing 8 images of a test site, used for 3D surface reconstruction in a photogrammetry specialized software 3DF Zephyr	MPD and surface-related parameters Sa, Sq, Sp, Sz, Vmp, Vmc	DSM derived texture indicators were compared to MTD from sand patch test and BPN from pendulum test, showing moderate to strong correlation to texture measurement ($R^2 = 0.47$ for Sz to 0.92 for MPD) and no correlation with the measured friction

3.6.2. Laser scanning methods

Laser scanning technology is a remote sensing technology based on the triangulation principle, where the distance and the angle between the laser source and sensor are known, therefore the distance between the laser source and any point on the scanned object surface can be evaluated (Mathavan et al., 2015). A similar workflow is typical for all laser scanning devices: the scanner emits light beams on the target area of the inspected surface, which reflects the signal back to the sensor and from the known geometrical relations between the scanner and the surface, point coordinates of the scanned surface can be evaluated (Bitelli et al., 2012; T. Wang et al., 2020). After the scanning procedure is finished, the spatial data is stored as a dense point cloud and ready for further processing. Laser scanning technology is an efficient way for collecting surface morphology data necessary for the calculation of roughness features (Tonietto et al., 2019). The main advantage of this technology is the ability to collect a significantly large amount of data in short time (Pawłowicz et al., 2018).

Laser scanning technology in civil engineering has a wide variety of applications, including structural documentation and digitalization of existing civil engineering structures, creation of a current-state benchmark object for the structural analysis under extreme loadings, creation of a construction site models, creation of natural morphological structures relevant for the civil engineering applications, quantitative surveys, quality control, structural redesign etc (Edl et al., 2018). This non-contact method provides very accurate digital representations of real structures by a significant amount of data, allowing the reconstruction of a complete scanned object, without the need for the object discretization by the reference points (Gonzalez-Jorge et al., 2012).

The application of laser scanning technology for pavement texture characterization is present in standard texture measurement methods such as stationary CTM device or mobile profilometers (Yu et al., 2020). It is applied as one-dimensional laser scanner recording the surface roughness features along the measurement path. The measurement procedure is fast and accurate and the measurement output is mostly the standard macro-texture indicator MPD (S. Chen et al., 2022).

In recent decade, advanced 3D laser scanning technology has been utilized to obtain pavement surface digital representations with high precision and accuracy. 3D laser scanning devices are capable of capturing high precision surface spatial characteristics and therefore, enable the texture characterization by 2D and 3D roughness indicators overviewed in section 3.6. (Kogbara et al., 2016; Matlack et al., 2023). Similar to the texture roughness parameters obtained by photogrammetry methods, 3D laser scanner derived parameters could provide more thorough insight into texture-friction relationship in comparison to standard methods for texture performance assessment. An overview of research utilizing 3D laser scanning technology for alternative pavement texture characterization is given in Table 3.10.

Table 3.10. Research results for pavement texture roughness features analysis by 3D laser scanning methods for data acquisition

Authors	Research aims	Texture data acquisition device and data analysis software	Analyzed alternative texture parameters	Research results and conclusions
Bitelli et al., 2012	To develop and implement new methodologies for texture data acquisition in laboratory and in situ monitoring of pavement texture	Next Engine® 3D laser scanner, data analysis software not specified	Profile-related parameters R_a , R_{sk} , R_{ku} , R_k , R_{pk} , R_{vk} transferred to corresponding 3D areal parameters by adequate mathematical expressions; additionally volume parameters V_{mp} , V_{mc} , V_{vc} and V_{vv}	Laser scanning devices enable the acquisition of texture data and calculation of new texture indicators, which represent a complete texture characterization and provide further possibilities of pavement surface performances evaluation.
Čelko et al., 2016	To test the advanced methods for pavement texture characterization in 3D framework and evaluate friction performance by the tested equipment	3D handheld self-orienting scanner ZScanner®800, Matlab-based algorithm	Profile-related parameters R_p , R_v , R_t , R_a , R_q , R_{sk} , R_{ku} , spectral density – PSD, hybrid parameters Texture ratio TR, Root mean square slope R_{dq} , spacing parameter R_{Sm}	A strong correlation was obtained between texture parameters determined by standard measurement methods and standard texture parameter MPD calculated from 3D scanning surface representations ($R^2 = 0.94$ for MTD and $R^2 = 0.85$ for MPD). Friction performance determined by standard methods showed moderate

				correlation to the standard texture parameter MPD obtained by 3D scanner ($R^2 = 0.5-0.69$ for different friction measurement devices). Obtained correlation between friction and alternative texture parameters was weak to moderate, the highest $R^2 = 0.59$ was obtained for R_p parameter)
L. Li et al., 2016	To develop a pavement friction prediction model based on alternative texture parameters for roughness characterization, including amplitude, spacing, and functional parameters	PaveVision3D Ultra system, data analysis software not specified	Surface-related parameters S_q , S_{sk} , S_{ku} , Texture aspect ratio (TAR), Surface developed interfacial area ratio (Sdr), Surface bearing index (SBI)	Pavement friction prediction model developed from six texture indicators obtained strong correlation with measured friction values with $R^2 = 0.95$
Hu et al., 2016	To analyze the influence of texture parameters determined from 3D surface representation on pavement frictional performance.	3D scanner (HandySCAN 300, Creaform Inc, Canada), Matlab	Surface-related parameters S_a , S_q , S_{sk} , S_{ku} , root-mean-Sdq, Sdr, Spd, Spc and surface fractal dimension (Sfd)	Spd and Spc parameters influence friction coefficient significantly and positively, therefore dynamic friction coefficient models were developed based on these two parameters, with $R^2 = 0.76 - 0.83$ for different test speeds. Multiple parameters prediction models are more reliable than the single parameter models. Ssk and Sfd have a significant relationship with Spd and Spc, but no obvious influence on friction coefficient based on linear regression analysis. Parameters S_a , S_{ku} , Sdq and Sdr have insignificant effect on dynamic friction coefficient.
Q.J. Li et al., 2017	To characterize pavement texture attributes and develop the relationship between pavement friction and texture by texture roughness surface-related parameters from EN ISO25178-2	LS-40 portable 3-D surface analyzer, MountainsMap software	23 surface-related parameters from amplitude, spatial, hybrid and material volume groups and feature parameters	Ssk (amplitude), Vmc (volume parameter) and Spd (feature parameter) can relate the pavement texture at the macro-level and the micro-level for friction in wet conditions at high and low speeds, respectively. The developed prediction models produce fairly accurate friction predictions with $R^2 = 0.54-0.58$ for different test speeds, but perform better in comparison to prediction models based on single texture indicator MPD. The selected 3-

				D texture parameters provide a better alternative to characterize texture attributes with respect to pavement friction performance and have the potential to replace the existing contact-based friction measurement methodologies.
Alhasan et al., 2018	To utilize 3D texture digital representation for the calculation of texture parameters for the friction prediction model based on Persson's friction theory.	Laser texture scanner (LTS) 9400HD, Ames Engineering and accompanying software tool	PSD function of texture, Hurst exponent, MPD	Fractal definition of surface texture by Hurst exponent and corresponding PSD function provide a physical explanation of surface texture effect on frictional performance when combined with the traditional texture characterization parameter MPD (also calculated from digital surface representation) in the friction prediction model (obtained $R^2 = 0.71$ for models including both roughness definitions)
Miao et al., 2019	To investigate the decay behavior of pavement surface characterized in 3D framework through the entropy theory	3D scanner (HandySCAN 300, Creafom Inc., Quebec, Canada), Geomagis Studio image analysis software	Surface images reconstructed from the scanned data are converted to grayscale so the entropy characterization can be applied from the probability of the grey level G at point x,y describing a pixel	Entropy theory can be applied for macro-texture characterization as it shows significant differences among the different pavement types, while for the micro-texture this is not very obvious. The similar conclusion is given for the decay characteristics of macrotexture described by entropy theory.
Q. J. Li et al., 2020	To investigate and identify various pavement texture and aggregate parameters and their correlation to the friction performance	LS-40 portable 3-D surface analyzer	Texture entropy (Tetp) and texture aspect ratio (Str), Aggregate feature parameters Spd, Spc, Sdv, Aggregate height parameter Ssk, Aggregate material ratio & volume parameter Smr.	All analyzed texture parameters influence friction performance significantly, especially Tetp (textural parameter) and Spc (feature parameter). The proposed prediction model obtained $R^2 = 0.78$ in comparison to measurement results. Friction prediction model is more reliable in case if alternative parameters are included, and not only the standard MPD parameter.
T. Wang et al., 2020	To investigate the effect of compactness on the texture and friction during the polishing process on asphalt specimens	3D scanner (HandySCAN 300, Creafom Inc., Quebec, Canada), Matlab	Surface-related parameters Sq and Sdr	Increase of compactness reduces the texture parameters and produces smoother surfaces, reducing the frictional performance of pavement surface

Yun et al., 2020	To investigate the effect of pavement texture roughness on multiple scales on the real contact area	3D scanner (HandySCAN 300, Creaform Inc., Quebec, Canada), data analysis software not specified	Surface-related parameter Sq	The contact area decreases sharply with the scale decrease until the observing scale of 0.6 mm, when it stabilizes and it is considered as the real contact area. Real contact area is significantly affected by surface roughness, decreasing with Sq increase following a power function.
Chen et al., 2021	To evaluate the spatial distribution of texture by proposed texture section method for direct measurement and evaluation of texture roughness features	A self-developed 3D laser scanner system, Special softwares for data acquisition and display, Matlab for data stitching into an image and further data analysis	Profile-related parameter Rq, texture distribution density for micro- and macro-texture levels (calculated as the ratio between texture 3D surface area and plane area of the texture section)	Texture distribution density index can be used for the characterization of pavement surface roughness, and it can be a reference for multi-scale texture characterization; Rq parameter has a great fluctuation on different profiles and it is difficult to characterize the roughness using only this profile parameter
Deng et al., 2021	To predict pavement surface friction performance on effective contact area as a function of PSD for optimal texture wavelengths for micro- and macro-texture levels	LS-40 3D laser scanner and accompanying software for data export in txd files	Texture surface PSD function	Macro-texture wavelength of 5.06 mm and micro-texture wavelength of 0.33 mm wavelength influence pavement friction the most. Calculated PSD functions of the optimal texture wavelengths are combined with the effective contact area for the establishment of friction prediction model, resulting in model performance with $R^2 = 0.6$ for predicted versus measured friction values.
Kováč et al., 2021	To investigate the possibility of friction performance prediction based on the 3D texture parameters calculated from surface representations obtained by laser scanner	Self developed Static road scanner (SRS), Matlab	Surface-related parameters Spc, Sdq, Spk, Smr, Svk, Sk, Vvp, Vmp	Parameter Smr (valley material portion) related to micro-texture and parameter Sp related to macro-texture showed the most significant individual influence on friction performance. From the testing of mutual combinations of different texture parameters at both texture levels for the prediction of the friction performance, the conclusion is that it is mostly influenced by the microtexture of the surface. The best correlation was achieved for the combination of micro-texture parameters Sdq, Sk, and Smr with macro-texture parameter Spc with $R^2 = 0.84$
Sha et al., 2021	To explore the optimal sampling interval and	3D scanner (HandySCAN 300, Creaform	Surface-related parameters Sq, Sdq, Spd, Spc, Vmp, Vmc	Pavement surface evaluation area has to be larger than $80 \times 80 \text{ mm}^2$ to ensure that the

	evaluation area for 3D analysis of selected texture parameters and provide a reliable reference for texture characterization in 3D framework and relate it to the road performance	Inc., Quebec, Canada), data analysis software not specified		difference between the average of five calculated 3D parameters and the true value is less than approx. 10%. Also, parameter sensitivity to the size of the sampling interval is different, so it is necessary to use the same sampling interval for highly sensitive parameters.
Zou et al., 2021	To analyze the evolution of surface texture due to the traffic polishing effects by monitoring texture parameters obtained by surface laser scanning	LS-40 3D laser scanner (HyMIT Measurement Technology, Austin, TX, USA), data analysis software not specified	Twenty surface related parameters calculated for micro- and macro-texture levels separately, including amplitude, spacing, hybrid, functional and feature parameters defined in EN ISO 25178-2	Changes in texture parameters under traffic polishing action are notable for all groups of monitored parameters except for spatial characteristics
Song, 2022	To investigate the relation between friction performance and texture morphology parameters determined on different asphalt specimens	3D laser scanner, Matlab	Profile-related parameters Ra, Rsk, Rku, Fractal dimension (D), Areal material ratio curve Smr(c)	Friction performance is higher for higher Ra and Rsk values, while higher Rku values are related to lower friction performance; larger fractal dimension indicates rougher surface with better friction performance; the parameters in areal material ratio curve don't have a unique effect on friction performance therefore the coupling effect of the factors should be taken into consideration.

3.7. Pavement texture properties related to friction performance - summary

Pavement texture is recognized as one of the most influential parameters for the friction performance. It mostly results from the asphalt mixture properties and pavement surface layer construction method, therefore it is controllable by pavement engineering practice. Texture ranges are well defined by unique texture levels from micro-texture to unevenness and the effect of each texture level to a driving-related phenomenon is distinguished. Two texture levels related to the pavement friction performance are micro-texture and macro-texture. The contributions of asphalt mixture constituents and mixture features to each friction-related texture level are recognized, however there exists no standardized asphalt mixture design procedure which would produce a specific level of macro-texture. The research oriented towards the texture performance estimation from the asphalt mixture design parameters seeks

for a prediction model where a standard texture indicator would be a function of specific mixture parameters, such as aggregate shape property, mixture gradation or bitumen amount.

Pavement texture is evaluated on constructed roads by established methods for macro-texture measurement, resulting in a single texture indicator generalizing a volumetric or geometric roughness property. The obtained values of texture indicators characterize texture performance according to the defined thresholds for the corresponding indicator, showing a positive or negative effect of texture on pavement surface frictional performance. To address the generalization of the texture performance by a single indicator, new methods for texture characterization and evaluation are utilized in research exploring texture-friction relationship. Such methods are based on contactless measurements of 3D pavement surface characteristics, from which roughness parameters can be extracted as profile-related or surface-related parameters or specific mathematical function, describing the roughness spectral properties.

The primary objective of advanced methods is to provide a detailed representation of the pavement surface morphology so the additional texture descriptors can be evaluated. Two main types of devices are used for the texture data assessment: digital cameras and laser scanners. Digital cameras are used dually: texture properties can be evaluated in 2D framework directly from the captured images or the images are used for the 3D surface reconstruction. 3D laser scanners are different from traditional line laser devices in profilometers as they capture the areal properties of inspected surfaces instead of just surface profiles. Both data acquisition methods require additional analysis of obtained surfaces, contrary to the standard texture evaluation methods producing a single texture indicator as the measurement output. However, the amount of texture data obtained by the advanced methods is incomparable to the single texture indicator derived from traditional texture measurement methods.

An overview of research utilizing contactless measurements for pavement texture assessment showed a promising potential of advanced roughness characterization methods. Both photogrammetry and laser scanning methods enable the surface roughness features analysis in profile-related and surface-related framework. Correlation analyses showed a very good coincidence between traditional texture indicators MTD or MPD calculated from the digital surface models and values obtained by traditional measurement techniques. Texture roughness parameters described in EN ISO 21920-2 and EN ISO 25178-2 can be evaluated from the digital surface models obtained by any of the methods. The advantage of photogrammetry methods is the availability of measurement equipment, i.e. digital cameras. Research results showed that

even the off-the-shelf technology available in smartphone-integrated cameras can produce DSMs with sufficient level of precision and accuracy for the pavement texture roughness analysis and evaluation. Laser scanners enable faster data acquisition and DSM creation in comparison to digital cameras, but they are less available and more expensive than digital cameras. Research results showed that advanced methods for texture assesment could provide a detailed insight to pavement texture-friction relationship with a proper selection of texture-related roughness parameters.

4. Preliminary investigation of pavement texture – friction relationship

The investigation of pavement texture-friction relationship establishment was first performed for a dataset of texture and friction measurements obtained by traditional measurement procedures: high-speed friction tester and high-speed laser profilometer. The analysed data was collected on several highway sections in Croatia within a routine road network monitoring program and after the pavement surface rehabilitation activities applied to the road sections having critical values of friction (Analiza vrijednosti makroteksture i hvatljivosti na definiranim dionicama autocesta A3 i A4 nakon hrapavljenja površine kolnika-Izvyještaj, 2019). The results of the preliminary research are published in a paper by Pranjic et al., 2020.

4.1. Friction and texture data collection

The database used in the preliminary study was collected on highway sections in Croatia selected as the road segments having critically low values of friction detected during a routine road network monitoring program. Friction and texture measurements were performed before and after pavement surface rehabilitation activities applied to the road sections having critical values of friction (*Analiza vrijednosti makroteksture i hvatljivosti na definiranim dionicama autocesta A3 i A4 nakon hrapavljenja površine kolnika-Izveštaj*, 2019). The measurements took place on selected driving and passing lane sections with the overall length of 10.5 kilometers (Figure 4.1). All measurements were performed in same environmental conditions: air temperature between 10°C and 15°C and no precipitation.

Measured values before and after the pavement rehabilitation actions were compared to the threshold values for pavement friction and texture performance indicators defined in the COST 354 Action Program Final report, described in Chapters 2 and 3. This was done as no official Croatian regulative document recognizes the outputs of dynamic friction and texture measurements as pavement performance indicators.

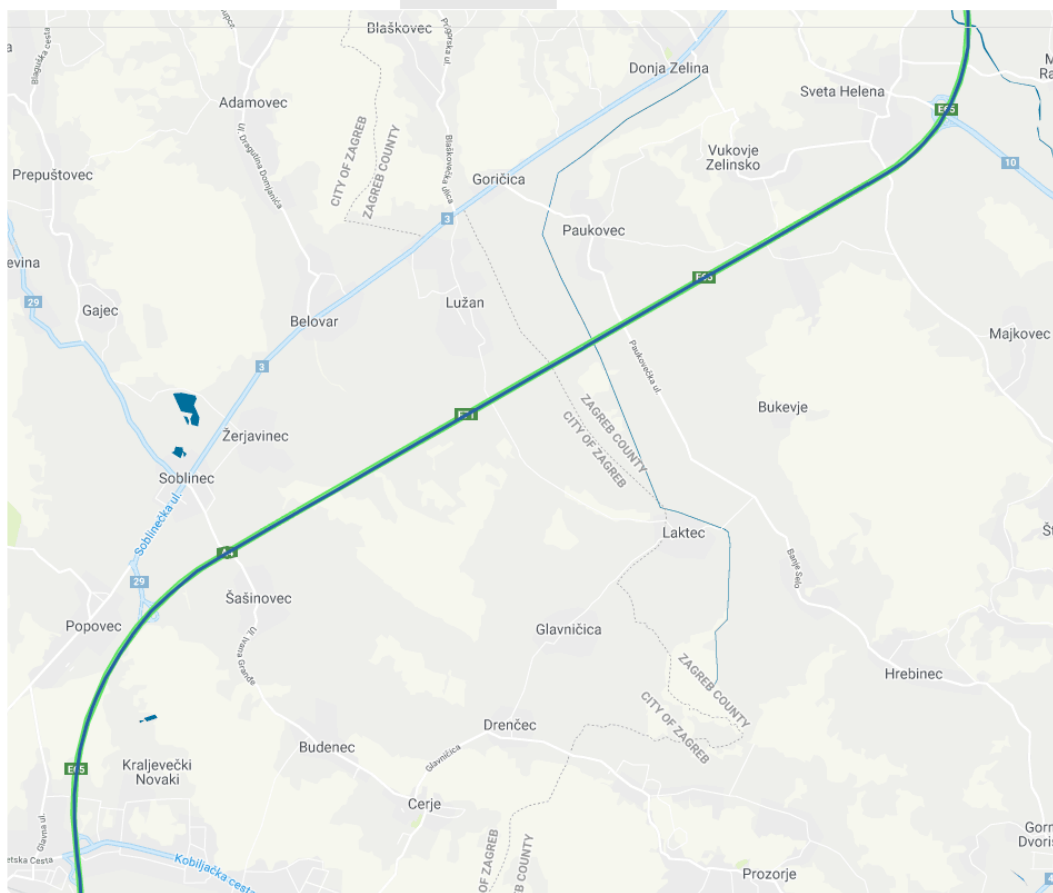


Figure 4.1 The measured highway section A4, junction Popovec – Sveta Helena (*Analiza vrijednosti makroteksture i hvatljivosti na definiranim dionicama autocesta..., - Izveštaj*, 2019)

Friction measurements were performed by a high-speed friction tester Surface friction trailer ASFT SFT0532 (Figure 4.2a). The friction tester was a trailer-type device, mounted on a towing vehicle. The measurements were performed following the CEN/TS 13036-2: *Road and airfield surface characteristics – Test methods – Part 2: Assessment of the skid resistance of a road pavement surface by the use of dynamic measuring systems* standard. Wet surface friction was evaluated, therefore the water supply tank had to be mounted on a towing vehicle. A continuous dynamic evaluation of longitudinal friction coefficient was performed with average measurement speed of 65 km/h. The device measures friction performance by a fixed slip principle. The measurement output is friction coefficient evaluated for 10 meters long section.

Texture measurements were performed by a high-speed laser profilometer Hawkeye 2000 (Figure 4.2b). It is a vehicle-installed profiler system for continuous monitoring of pavement properties with measurement and data processing unit. The measurement unit is equipped with five lasers distributed on a specific distance along the beam. The lasers enable longitudinal high precision linear scanning of road surfaces in the direction of travel. This measurement system enables the characterization of several pavement performance indicators: International Roughness Index (IRI), Rut Depth, texture parameters Mean Profile Depth (MPD) and Sensor Measured Texture Depth (SMTD). The system is equipped with a video camera producing high resolution video frames, Garmin GPS system, accelerometers for the real-time speed and distance calculations and an interactive real-time data acquisition software Onlooker Live. Data processing is performed by a specialized inbuilt data analysis software Processing Toolkit, which enables the calculation and visualization of collected data (Hawkeye 2000 Manual, 2015). Hawkeye 2000 system enables continuous dataset collection without the traffic disruption, as it operates under normal driving speeds and has no additional requirements for the data acquisition procedure. It requires a driver and another operator for the data collection and analysis. The system is not suitable for the single-spot texture measurements as the indicators are calculated for a specified processing interval of 10 meters. Texture measurements were performed following the EN ISO 13473-1: *Characterization of pavement texture by use of surface profiles – Part 1: Determination of Mean Profile Depth* standard.



Figure 4.2. Data collection devices: friction measurement device (a) and texture measurement device (b)

4.2. Data analysis

The highway sections were selected from the existing database of friction and texture data before the pavement rehabilitation program, collected as a part of a routine pavement performance assessment procedures performed by road authority Croatian highways. The database contained friction measurements for 100 m long sections expressed as LFC. The corresponding texture values were expressed as MPD. Friction and texture data were measured on selected highway sections characterized by a critical friction performance indicator before the pavement rehabilitation procedure. The threshold value for a critical friction performance indicator LFC (longitudinal friction coefficient) was $LFC \leq 0.46$, adopted as the lower limit value of performance indicator classification grade “Satisfactory”, following the defined grades in the COST 354 Action Final report. The 100 m sections were marked as measurement positions and the measured friction and texture performance after the pavement rehabilitation procedure were expressed for the same positions as the mean values of measurements. Overall, 105 positions were evaluated for friction and texture data (Figure 4.3).

Friction values increased after the rehabilitation procedure on all positions, in average for approximately 50% (Figure 4.3a). Friction values were generally lower for passing lane before the rehabilitation and slightly higher after the rehabilitation. All evaluated positions obtained LFC higher than the threshold value after the rehabilitation. Pavement texture didn't follow the same trend as the friction values (Figure 4.3b). A better performance was recorded for passing lane before the surface remediation. In general, pavement performance increased after the rehabilitation, but not for all inspected positions. Some positions in driving lane obtained lower texture values after the rehabilitation. The increase rate was lower in comparison to friction, in

average approximately 20%. All measured texture values expressed as performance indicator MPD were higher than the texture threshold defined in the COST 354 Action Final report, $MPD \geq 0.68$ for a satisfactory texture performance.

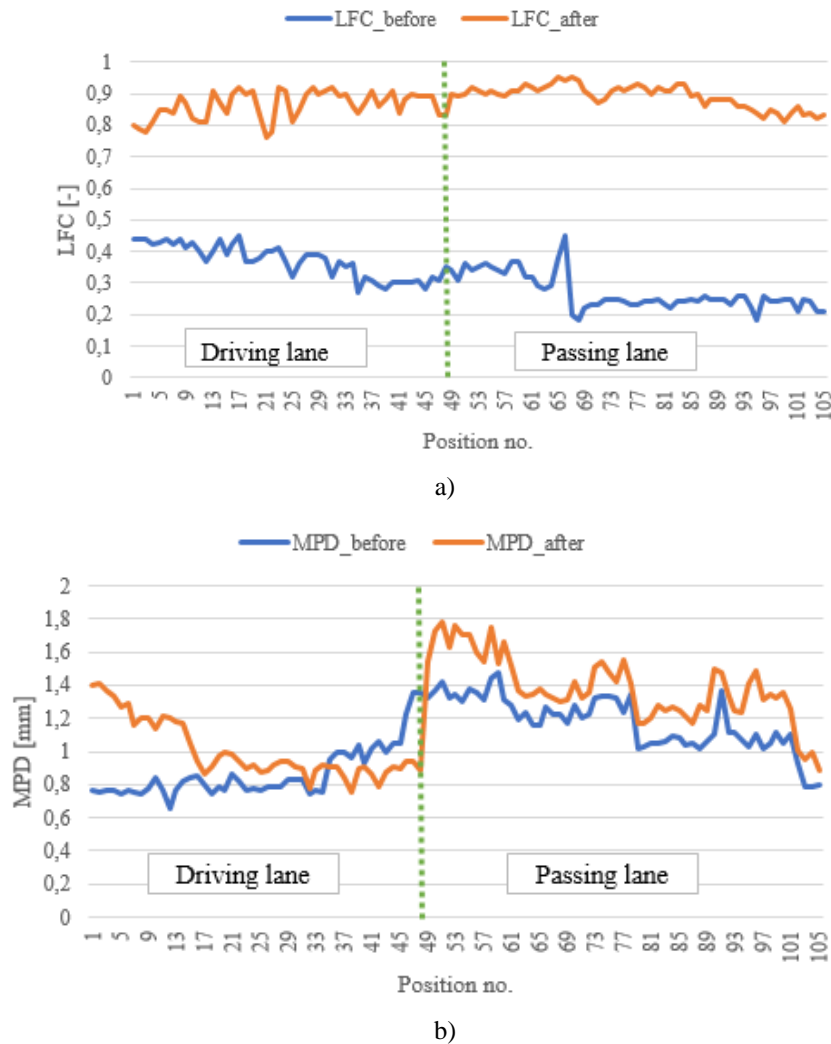


Figure 4.3. Friction (a) and texture (b) measurement results compared before and after the pavement rehabilitation

To investigate the correlation between friction and texture data, a Pearson's correlation test was performed with obtained correlation coefficient of 0.302 (Table 4.1). A scatterplot of texture and friction data confirmed the obtained correlation analysis result, indicating no significant correlation between the texture and friction values (Figure 4.4).

Table 4.1 Correlation analyses results for different dataset size

Observed dataset	Pearson's correlation coefficient	Significance (p-value < 0.05)
Full dataset	0.302	< 0.0001
Before pavement rehabilitation	-0.447	< 0.0001
After pavement rehabilitation	0.218	0.026

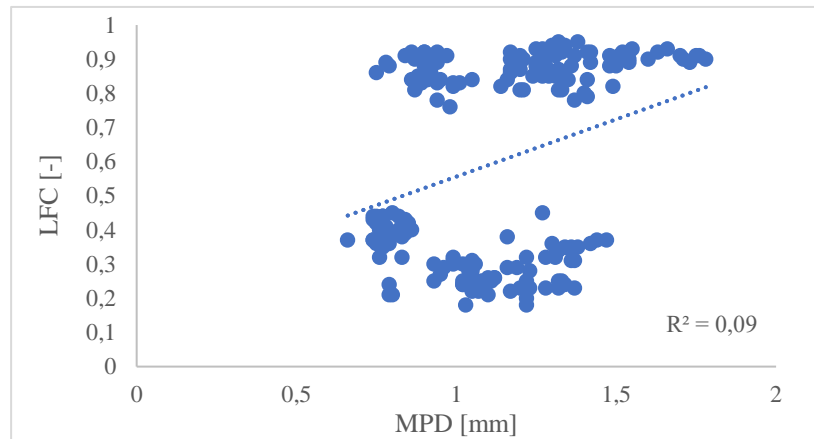


Figure 4.4. Scatterplot of texture and friction data for all measurement results

The scatterplot showed two data clusters, one for the LFC values below the threshold performance indicator value and one for the LFC values measured after the rehabilitation measure. Data was therefore further analysed with respect to different friction performance – before and after the pavement rehabilitation. Correlation analyses were again performed with Pearson’s correlation coefficient as the output (Table 4.1). A negative correlation was observed for texture and friction values collected before the rehabilitation, while the obtained correlation coefficient for the texture and friction data collected after the pavement treatment was even lower than for the whole dataset.

The dataset was down sampled to a lower project level analysis, investigating the correlation between the texture and friction values measured on separate lanes. The dataset collected on driving lane was not observed, as the texture values showed inconsistent behavior (Figure 4.3). The scatter plots for texture and friction data collected on passing lane before and after the pavement rehabilitation are presented in Figure 4.5. The obtained Pearson’s correlation coefficients for passing lane data before and after the rehabilitation were 0.566 and 0.40, respectively.

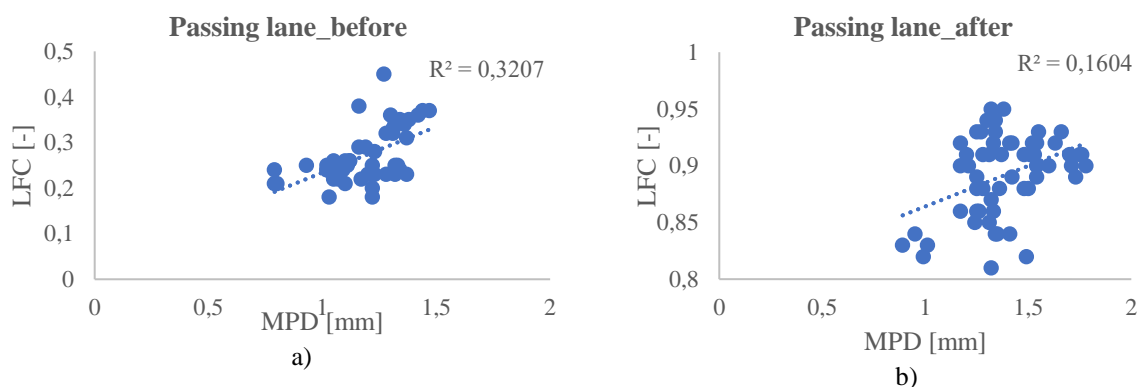


Figure 4.5. Scatter plots for MPD and LFC values for passing lane, before (a) and after (b) the rehabilitation procedure

4.3. Discussion

The performed analyses of dataset obtained by traditional measurement methods showed no significant correlation between texture and friction performance indicators. Both data collection devices operated on high-speeds, therefore it can be assumed that the micro-texture effect on friction performance was not taken into account as an influencing factor to the friction performance. The characteristic texture and friction performance indicators were determined for a single position as the mean of measured values for a 100 m long section. Averaging of measured values on such long sections could discriminate the actual relationship between texture and friction derived from the measured values for a defined measurement or processing interval. Friction measurements were performed under wet surface conditions, so the effect of water presence on the texture morphology cannot be excluded.

By reducing the size of dataset sample and dividing the data from the full dataset to the dataset collected on a specific lane for a certain pavement performance indicator threshold, the obtained correlations were better. The obtained results were in a good agreement with several previous research exploring texture-friction relationship by simple empirical models, where no significant correlation between traditionally evaluated texture and friction indicators was observed (Basu & Chowdhury, 2017; Chou et al., 2017; G. Yang et al., 2018). A similar procedure of dataset down sampling was performed in a research by Islam et al., 2018, where more significant correlation was obtained for smaller and focused dataset.

The results of preliminary analysis motivated further research of texture-friction relationship. To be able to provide a more reliable prediction of pavement friction performance from the texture features, a more detailed description of roughness-related properties is needed. In recent two decades advanced methods based on remote sensing technologies are used for pavement texture characterization, as described in Chapter 3. Further research in this thesis was focused on the development of photogrammetry-based methodology for texture roughness characterization by non-standard parameters, presented in Chapter 5.

5. Methodology development for pavement texture data analysis

To investigate the applicability of advanced methodology for pavement texture roughness characterization described in Chapter 3, a photogrammetry-based method for 3D texture data acquisition was utilized in this research. Photogrammetry method was selected due to the existing expertise previously applied to larger scale problems of coastal morphology monitoring and landslide analysis (Ružić et al., 2014, 2015; Pajalić et al., 2021; Tadić et al., 2022). The first research goal in the methodology development was to investigate if the available photogrammetry equipment was adequate for analysis of pavement texture roughness features from the created 3D digital surface models (DSM). The results of this research were published in a paper by Pranjic & Deluka-Tibljaš, 2022. The proposed texture data acquisition method was evaluated by performance testing of different acquisition settings and the resulting DSM properties. The determined texture roughness features were evaluated for different resolutions of the created DSM, resulting in a proposal for the optimal data acquisition and analysis procedure. The proposed method was verified by performance comparison with another photogrammetry-based method and a 3D laser scanning device.

5.1. Photogrammetry method applicability for pavement texture characterization

The investigation of photogrammetry method applicability was performed on a laboratory produced asphalt specimen. The specimen's surface roughness properties were evaluated by standard low-speed friction measurement with pendulum device (EN 13036-4). Photogrammetry method performance was investigated for two data acquisition procedures, different for the relative position of the photographic equipment to the analysed specimen. The data acquisition procedure and properties of created DSM for each method were compared to select the optimal method. The DSM resulting from the selected method was analyzed in terms of texture roughness parameters, correlated to the measured friction performance. Following sections provide a detailed description of performed procedures. The results of this research were published in Pranjić & Deluka-Tibljaš, 2022.

5.1.1. Asphalt specimen properties and friction performance evaluation

The investigated asphalt specimen was produced by a roller compaction device (Controls Group, model 77-PV41C05, 2014) following the procedure defined in EN 12697-33: *Bituminous mixtures – Test methods for hot mix asphalt – Part 33: Specimen prepared by roller compactor*. The selected asphalt mixture for specimen preparation was dense-graded Hot Mix Asphalt (HMA) surface layer, commonly used on heavy trafficked roads such as motorways, primary roads or urban high-speed roads (bypasses) in Croatia. Mixture properties relevant for the friction performance are given in Table 5.1. Volumetric and mechanical properties of the asphalt mixture were not inspected prior to the specimen production.

Table 5.1 Asphalt mixture properties for the produced asphalt specimen

Asphalt mixture type	HMA
Mixture gradation	Dense-graded
Aggregate type	Eruptive (Fužinski Benkovac)
Maximum aggregate grain size	11 mm
Bitumen type	BIT 50/70
Bitumen amount	5.5%

The produced specimen was rectangular, 300 mm wide and 400 mm long. The compaction energy and target specimen density settings applied in the production procedure resulted with

a final specimen thickness of 40 mm. Figure 5.1 shows the roller compaction device and resulting asphalt specimen.

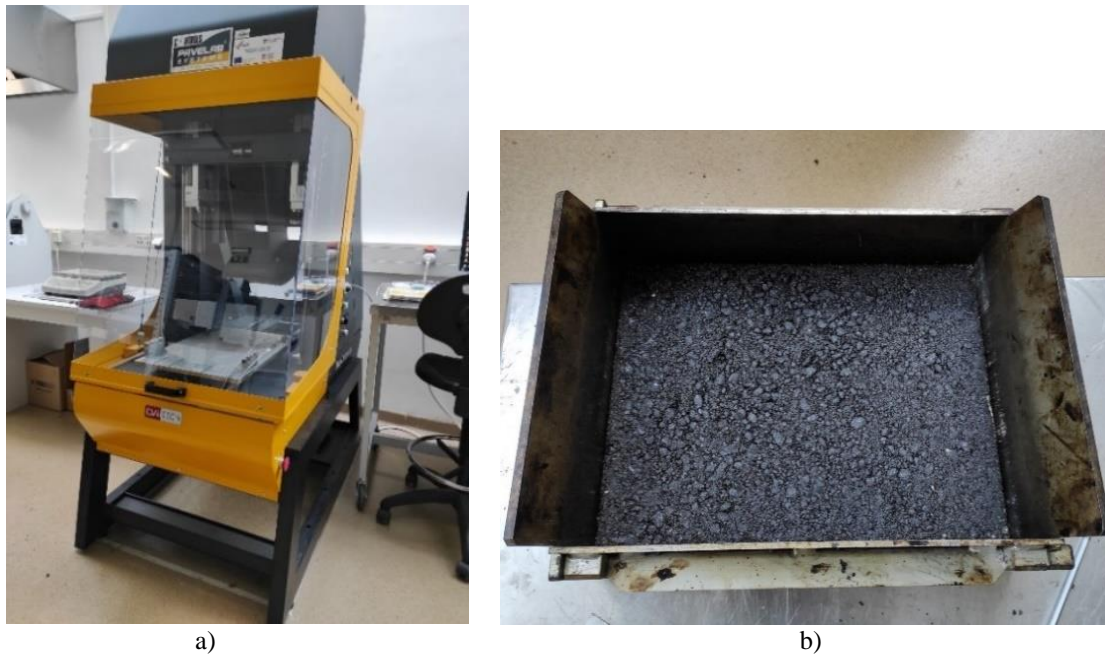


Figure 5.1 Roller compaction device (a) and produced rectangular specimen in a mold (b), Transportation laboratory Faculty of Civil engineering Rijeka, 2021

Friction measurements were performed several days after the specimen production. Friction performance was measured by a standard stationary low-speed friction measurement device Skid Resistance Tester – SRT (Controls Group, model PV0190/E, 2014), presented in Figure 5.2a. SRT device measures frictional performance of the inspected surface as the resistance to sliding motion of the pendulum arm provided by the surface roughness. The operating principle, measurement procedure and interpretation of measurement results are given in EN ISO 13036-4. Friction was evaluated on produced asphalt specimen by four SRT measurements, performed on four smaller rectangular sections of the specimen's surface (Figure 5.2b). The dimensions of each section were selected to satisfy the required sliding length of $125 \text{ mm} \pm 1 \text{ mm}$ for the SRT procedure. The sections were marked as I - IV, and friction performance was determined for each section as an average of five consecutive SRT readings. The test was performed without wetting the specimen surface to exclude the effect of water on the friction performance. The obtained SRT results (Table 5.2) showed a high friction performance of the inspected specimen, resulting from the following specimen properties and test conditions. The specimen was produced from asphalt mixture with nominally good frictional properties and the surface was not worn out, since it was not exposed to any kind of polishing procedure. The test was

performed in dry surface conditions, for which it can be presumed that the measured friction values would be higher in comparison to wet surface conditions.

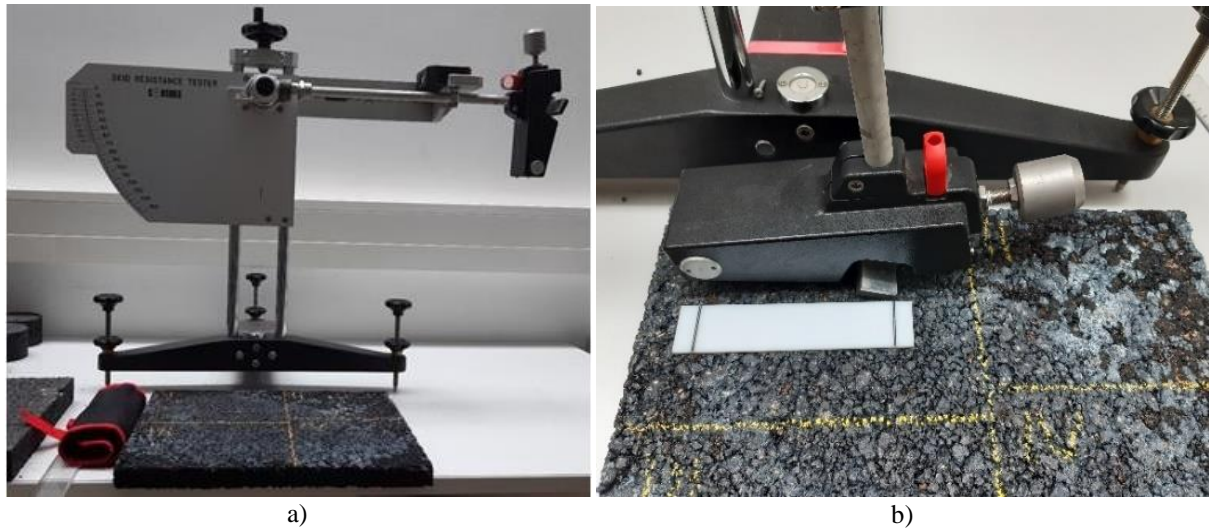


Figure 5.2. SRT low-speed friction measurement device(a) and friction measurement assembly on produced asphalt specimen (b)

Table 5.2. Friction performance of asphalt specimen evaluated by SRT measurements

Section no.	SRT measurement [-]					SRT mean [-]
	1	2	3	4	5	
I	75	75	76	77	76	75.8
II	79	77	79	79	77	78.2
III	84	84	83	84	83	83.6
IV	89	90	90	92	90	90.2

5.1.2. Selection of data acquisition procedure

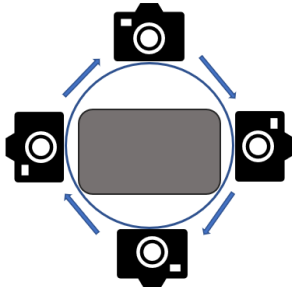
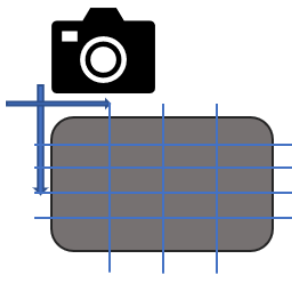
Photogrammetry method applicability for the pavement texture analysis was first investigated by two different data acquisition methods. The difference between two tested methods was the relative camera position to the asphalt specimen. The same photographic equipment was used in both methods, with characteristics specified in Table 5.3. Prior to the data acquisition procedure, the specimen was mounted on a fixed stand, brushed to remove any loose aggregate grains or other debris and sprayed with an antireflective agents, to remove the light reflection effect caused by surface layer bitumen.

Table 5.3. Photographic equipment specifications

Photographic equipment	Nikon D500 DSLR single lense digital camera + height-adjustable tripod
Camera resolution	20.9 Mpix
Camera lens focal length	11-20 mm
Aperture	f/1.8
ISO	100

The two data acquisition procedures were named *Turntable* and *Ortho*, with respect to the relative camera position during the image acquisition process. In *Turntable* procedure, the camera was moving around the specimen in a circular motion on several different heights. In *Ortho* procedure, camera was moving horizontally and vertically over the specimen on a fixed height (Table 5.4).

Table 5.4. A schematic representation of camera movement for *Turntable* and *Ortho* image acquisition mode and images of performed data acquisition process with two different methods

Data acquisition mode	Turntable	Ortho
Relative camera position (schematic)		
Image of data acquisition procedure		

In *Turntable* mode, the specimen's surface images were captured by camera rotation for 25° for each image on three different heights and camera angles. The height and angle adjustments were made so the captured image contained the entire specimen surface. For each camera height 15 images were acquired so overall, 45 images were captured with the *Turntable* data acquisition method. In *Ortho* mode 2, the camera was translated in horizontal and vertical directions at a fixed height, capturing orthogonal specimen surface images. Each captured image represented only a portion of the entire specimen surface. The consecutive images overlapped by approximately 60% side overlap and 80% forward overlap. 20 surface images were captured in the orthogonal camera position: five images along the specimen length in four rows and four images along the specimen width in five columns. Images were captured in RAW format in both acquisition procedures, so the image information collected in the data acquisition process and stored in a pixel was preserved in the original form. The RAW images were optimized for its brightness and contrast settings to obtain the high quality images for further data processing and stored in TIFF format with pixel size $4.45 \times 4.45 \mu\text{m}$, containing all the data acquired from the camera sensor. The stored images were prepared for the surface reconstruction procedure performed by a specialized photogrammetry software *Agisoft Metashape*.

Agisoft Metashape (v.1.5 Pro, Agisoft LLC, St. Petersburg, Russia) is an advanced stand-alone software for the creation of 3D digital models of objects captured on still images. It enables the fully automatic object reconstruction process from the arbitrary images taken from random positions, with a condition that the object is visible on at least two images. The reconstruction workflow for any object of interest contains four main stages: camera alignment, sparse point cloud adjustments, dense point cloud creation and surface reconstruction. Each stage results in an object that can be analyzed according to the demands of the reconstruction procedure and the final expected outcome. The reconstruction process is automated and the user defined inputs are captured images and reconstruction parameters set prior to the initiation of the reconstruction process, whose values depend on the desired outcomes. In this research phase, the settings were defined from the automatic software recommendations, as the functional and performance assessment of the *Metashape* created models was not analyzed thoroughly. This was done later in the performance optimization procedure, described in section 5.2. A simplified *Metashape* workflow for the creation of a digital model is given in Figure 5.3.

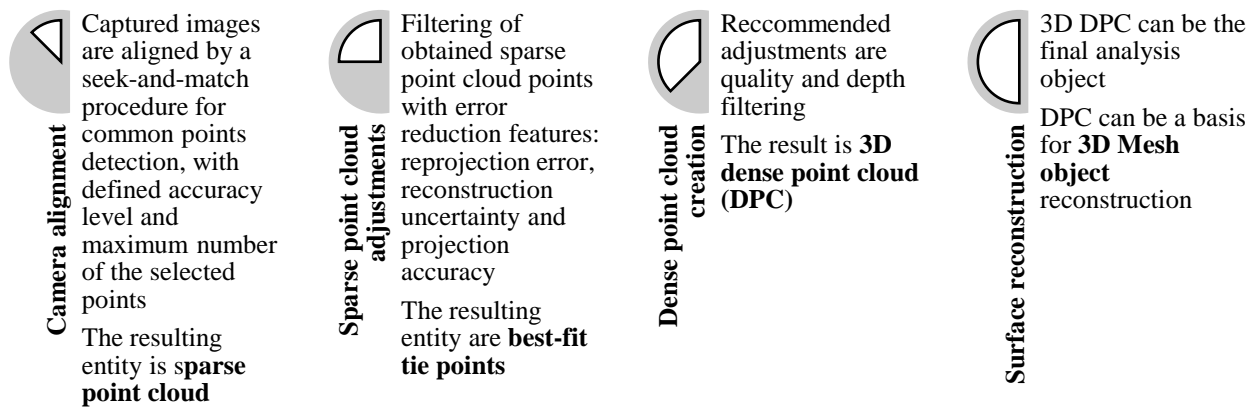


Figure 5.3. Agisoft Metashape workflow scheme for 3D object reconstruction from photogrammetry-based data acquisition method

The resulting digital models' properties can be inspected from the *Metashape* report document, where the properties of each reconstruction stage are presented. Table 5.5 compares the results from the generated reports for models created with *Turntable* and *Ortho* data acquisition procedure.

Table 5.5. Resulting DSM properties for two data acquisition modes (from generated Agisoft Metashape Processing reports)

Image acquisition mode	<i>Turntable</i>	<i>Ortho</i>
Tie points	21,533	5,423
RMS reprojection error	0.598153 pixel	0.549274 pixel
Max reprojection error	4.51687 pixel	3.65751 pixel
Average tie point multiplicity	5.28681	4.87589
Depth maps processing time	25 minutes 10seconds	4 minutes 3 seconds
Point cloud generation time	28 minutes 38 seconds	2 minutes 23 seconds
Number of points	25,648,555	5,945,252
Model reconstruction time	5 minutes 54 seconds	4 minutes 15 seconds

To evaluate the performance of two different data acquisition procedures, the acquisition procedure proces and the properties of resulting digital models were compared. The adjustments of different camera heights and corresponding angles to capture the specimen surface were more time consuming than the translation of camera along the horizontal and vertical specimen axes. In *Ortho* mode, the camera was fixed at a certain height. The image acquisition procedure was less susceptible to uncertainties and lower quality of captured images in comparison to

Turntable mode, where camera heights, angles and positions were changing during the rotation around the specimen. By observing the resulting DSM properties in Table 5.5, it can be seen that the *Turntable* produced a larger number of tie points from the alignment procedure due to the larger number of acquired images. Consequently, the processing time and DPC generation time is longer and the number of points in the final DPC is five times larger than for the *Ortho* mode. The values of reprojection errors (RMS and Max) are in favour to *Ortho* mode, despite the significantly smaller amount of data available for the model reconstruction. From the obtained DSM properties and the image acquisition process analysis, the *Ortho* mode was selected as having better performance. Further analyses were done on DSM produced by *Ortho* data acquisition mode.

5.1.3. Surface roughness characterization for created digital surface model (DSM)

The DPC entity created from the *Ortho* image acquisition mode consisted of approximately 6×10^6 points. The final result of the reconstruction procedure was a 3D mesh object, created from the DPC with 1.25×10^3 points/cm³ density (Figure 5.4 a, c). The mesh object's elements are faces, describing its 3D geometry. Mesh models enable a more realistic description of surface depths in comparison to point cloud objects. This model consisted of 1.19×10^6 faces. The mesh DSM was further analysed to investigate the surface roughness features for pavement texture characterization.

The analysis of DSM was done in *Cloud Compare* (v 2.11.3 (Anoia), 2021) an open-source software for 3D point cloud and mesh processing and analysis. The resulting mesh was imported to *Cloud Compare* (CC) and subjected to the initial leveling, scaling and filtering operations. Leveling was performed by adjusting the object's plane to be parallel to the horizontal plane. Scaling was performed so the digital model units correspond to the millimeters. Filtering was performed to remove the data outliers falling outside the surface model and threshold values of macro-texture level. The final step was surface segmentation. It was done by selecting the central part of the model and removing all the peripheral parts that might have some redundant data due to the weaker model performance on the edges. The final mesh object was sampled to dense point cloud object to obtain the surface morphology data in a form of 3D point coordinates (Figure 5.4 b, d). The mesh sampling was done by selecting the maximum possible number of points to describe the model's geometry. The resulting DPC was created with 1.5×10^6 points, having 2.041×10^3 points/cm³ density.

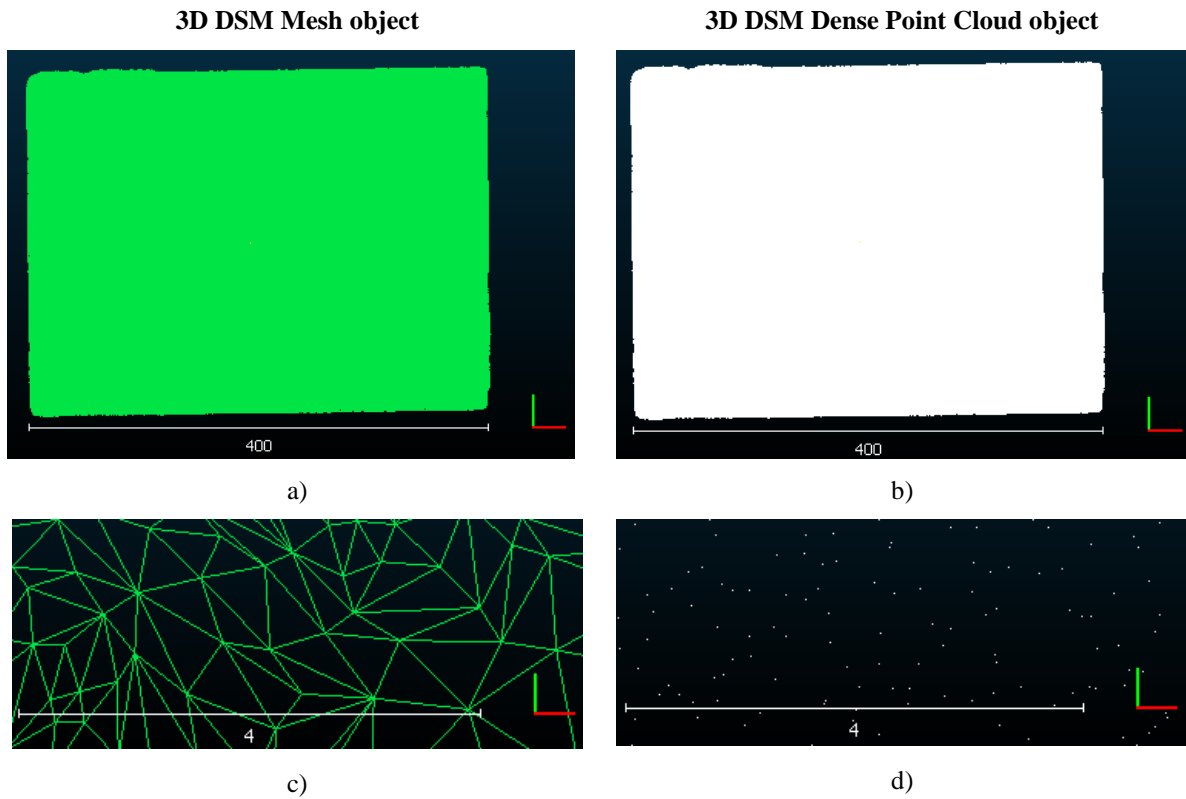


Figure 5.4. 3D Mesh object (a) and a close-up of mesh structure (c) and 3D DPC object (b) and a close-up of DPC structure (d) in millimeters

The DPC was divided in four sections, corresponding to the sections where the frictional performance was evaluated, as described in section 5.1.1. A central part of each smaller section was extracted as a separate DPC with dimensions corresponding to the SRT sliding area of approximately 100 cm^2 . From each DPC section, five surface profiles were segmented out to calculate the standard profile-related texture indicator MPD (Figure 5.5). The segmented profiles' length was 100 mm, corresponding to the profile baseline length defined in EN ISO 13473-1 for MPD calculation. Profiles were segmented for each 15 mm of the surface. Overall, twenty profiles were extracted from the four sections. The extracted profiles consisted of approximately 4,500 points. The average profile's horizontal resolution was 45 points/mm. Each point was defined with x and z coordinate, corresponding to the profile's length and height values.

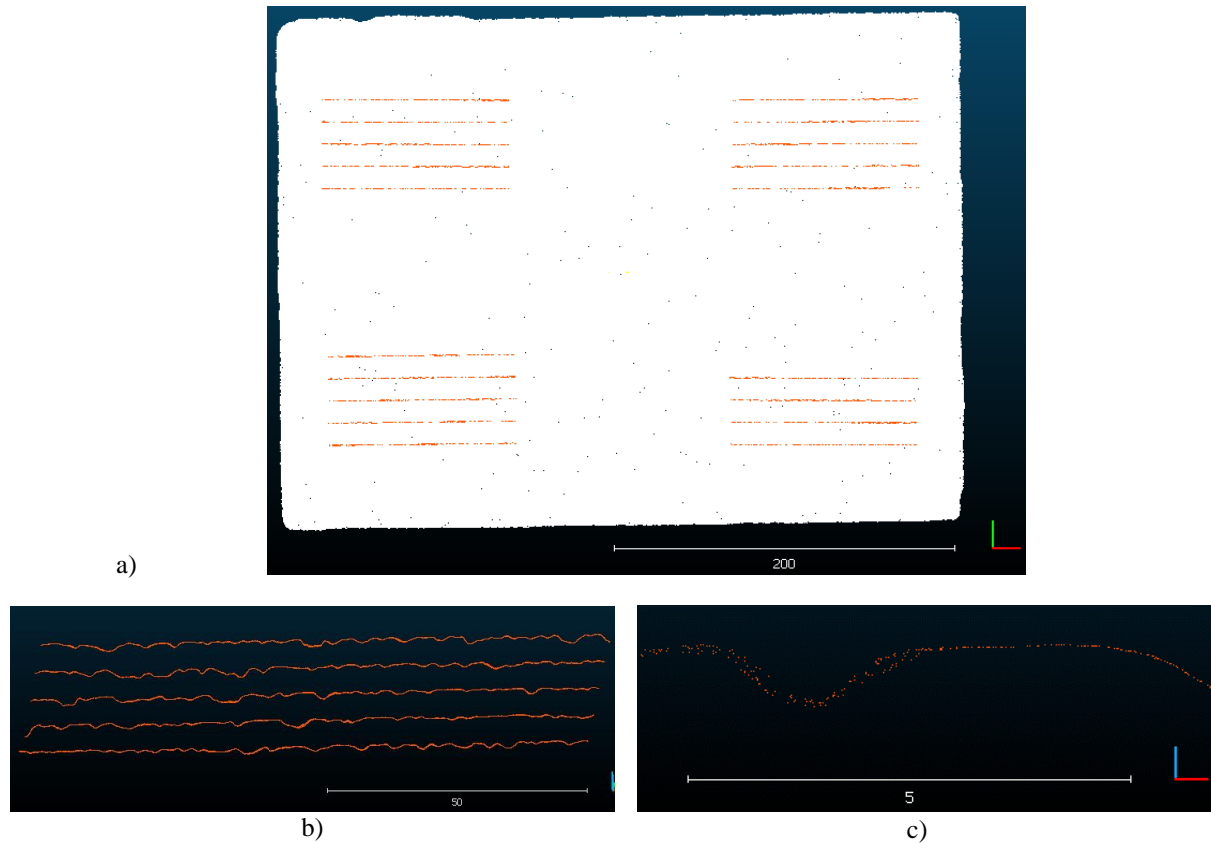


Figure 5.5. Segmented profiles' position on DPC model (a) and profile close-up for one section (b) and one profile (c)

To compare the profile-related parameter MPD with the measured friction performance, the calculated MPD values for each profile were averaged to represent the surface-related MPD. The correlation analysis was performed for surface-related MPD and SRT values (Table 5.6). Additional texture parameters were evaluated from the profiles, corresponding to the profile-related amplitude parameters defined in EN ISO 21920-2 and previously described in Chapter 3: arithmetic mean height P_a , root mean square height P_q , total height P_t , skewness P_{sk} and kurtosis P_{ku} . Selected non-standard parameters values calculated for each section were averaged to represent the surface-related feature and to be comparable with the standard texture parameter MPD and measured friction performance SRT determined for each section. Correlation analysis was performed for standard texture parameter MPD and non-standard parameters listed before, with results presented in Table 5.6.

The obtained Pearson's correlation coefficients indicate a significant relationship between the measured friction performance and texture parameters calculated from the profiles extracted from the DSM. SRT highly correlated with MPD. The calculated non-standard texture parameters showed a very strong correlation to the MPD. The obtained result agrees with the previous research conclusions where photogrammetry methods were utilized for pavement

surface roughness characterization, presented in Chapter 3. Parameters P_a , P_t and P_q obtained a positive correlation to the MPD, while P_{sk} and P_{ku} showed a strong but negative correlation to the MPD. The highest positive correlation coefficient value between friction and non-standard texture parameter was obtained for P_q and the lowest positive correlation was for the P_t parameter.

Table 5.6. Pearson's correlation coefficients for analysed profile-related texture parameters and measured friction

	SRT	MPD	P_a	P_t	P_q	P_{sk}	P_{ku}
SRT	1						
MPD	0.807	1					
P_a	0.706	0.978	1				
P_t	0.699	0.983	0.969	1			
P_q	0.728	0.988	0.998	0.981	1		
P_{sk}	-0.770	-0.928	-0.845	-0.941	-0.876	1	
P_{ku}	-0.751	-0.935	-0.861	-0.953	-0.890	0.999	1

The $P_{sk} > 0$ value indicates the predominance of the surface peaks, while negative values of P_{sk} indicate the prevailing valley structure. The P_{ku} parameter describes the “flatness” of the profile height in a way that $P_{ku} > 3$ values indicate sharper peaks and/or valleys on the analyzed surface and $P_{ku} < 3$ are representing smaller texture height variations (Li et al., 2016). P_{sk} can be used to characterize quantitatively the surface texture profile contour shape and indicate the texture capacity (Chen et al., 2022). The results from recent studies analyzing the effect of P_{sk} and P_{ku} parameters on surface friction performance are ambiguous: some researchers didn't find any significant relation of these parameters to the friction (Zuniga-Garcia & Prozzi, 2019), some of them found a positive and significant correlation for both parameters (Huyan et al., 2020; Ji et al., 2022) while others reported a positive correlation for the P_{sk} parameter and negative correlation with the P_{ku} parameter (Song, 2022).

The obtained results provided a promising potential for pavement texture characterization from the DSM obtained by photogrammetry method. The comparison of two different data acquisition setups showed that the *Ortho* mode produced a DSM with better performance for a smaller number of acquired images and simpler acquisition procedure. Therefore, the *Ortho* mode was adopted for further application in research. Both investigated methods fall within the close-range photogrammetry range, as the distance between the camera lens and the specimen's surface was within one meter. The adopted *Ortho* mode for image acquisition was named Close-

Range Orthogonal Photogrammetry method – CROP and it will be addressed by this acronym further in the text.

5.2. CROP method performance testing

To investigate the performance of CROP method for surface data acquisition and digital representation of texture roughness features, four DSMs were created as a result of different photographic equipment used for the data acquisition. The same digital camera Nikon D500 was used with four different camera lenses. The adopted camera settings remained equal for all four equipment setups: aperture f/4.0, shutter speed 1/10 s, ISO 100, white balance manually selected and selected color profile Nikon standard. The properties of each setup are given in Table 5.7. Different setups were named Mode 1 – Mode 4.

Table 5.7. Camera lens properties for different CROP method data acquisition equipment

CROP acquisition mode	Mode 1	Mode 2	Mode 3	Mode 4
Lens type	Tokina SD 11-20, f2.8 (if) DX.	Tokina SD 11-20, f2.8 (if) DX.	AF Nikkor 50 mm f1.8 D	AF-S Micro Nikkor 105 mm f2.8 G
Focal length	11 mm	20 mm	50 mm	105 mm
Camera height	300 mm	300 mm	500 mm	700 mm

The performance was tested on the same asphalt specimen as described in section 5.1. To improve the resulting DSM performance, twelve Metashape-related markers were generated. The markers enable precise object scaling with respect to the known target distance (Over et al., 2021). The markers were grouped in a line of three, where the distance between two consecutive markers in a line was set to be 88.50 mm (Figure 5.6a). The markers were arranged around a smaller surface portion, marked with a 3D printed frame with inner dimensions 150×150 mm². A smaller surface section was selected to reduce the amount of data and consequently the time for the 3D model reconstruction procedure. The dimensions were selected with respect to the skidding length of the SRT device for a future comparison of texture roughness features to the friction performance and to be able to extract a full length profile for MPD evaluation, corresponding to 100 mm. Previous research showed that average values of pavement texture roughness parameters can be evaluated with high reliability if the pavement texture evaluation area was larger than 80×80 mm² (Sha et al., 2021), therefore the selected inner frame dimensions correspond to this condition.

5.2.1. Image acquisition and DSM creation

The image acquisition procedure followed the same camera translation scheme as described in section 5.1.2 for *Ortho* mode. For each Mode, the camera height was adjusted by a tripod and all the images were acquired from the same height (Figure 5.6b). The images were captured by following a grid marked on the reference frame, with 60% side overlap and 80% forward overlap. For each Mode, 25 images were acquired – five more than for the „original“ *Ortho* mode described in section 5.1. Images were captured in RAW format to preserve the full information stored in a pixel and pre-processed in Nikon Capture NX-D software by white balance and lens corrections, without any geometry corrections. The processed images were exported in 16-bit TIFF format, compatible with the *Metashape* software.

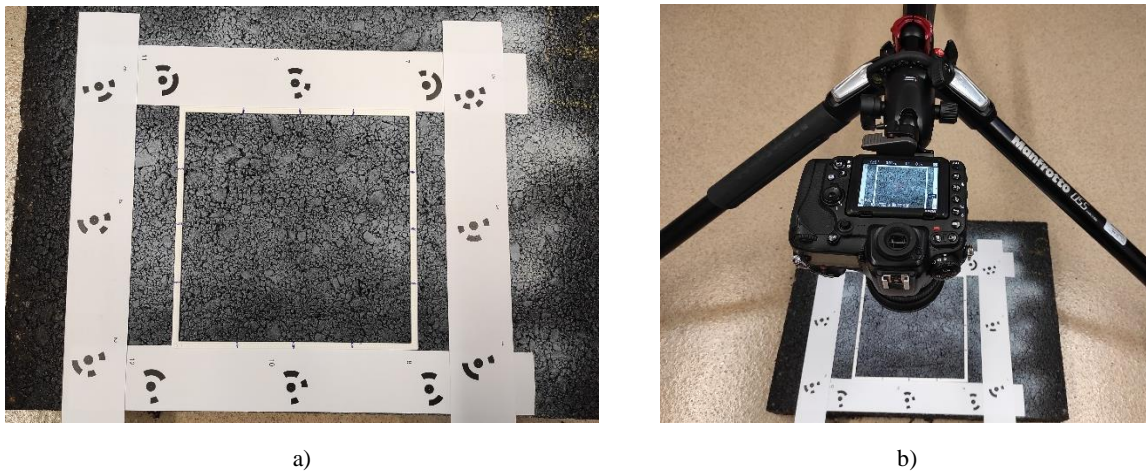


Figure 5.6. *Metashape* markers arrangement(a) and image acquisition procedure example(b)

The DSMs were created in *Metashape* for every data acquisition Mode with the same alignment procedure settings applied: Accuracy set to high, Key point limit set to 40,000, Tie point limit set to 4,000. High accuracy setting provides more accurate camera position estimations and enables the usage of original size images. The limit values set for key point and tie point represent the upper limit value of feature points and matching points respectively, that should be considered on each image during the alignment procedure. These specific values are selected as recommended to satisfy the demands of performance optimization and avoid the possibility of reducing the quality of the resulting model (*Metashape* User Manual, v1.5 Professional Edition, 2019). The result of the alignment procedure is a sparse point cloud (SPC) entity. The SPC entity is further filtered to exclude the points that do not fall within the defined threshold values. For this purpose, three error reduction features were adjusted to select and remove the “outliers” or low-quality tie points, based on the camera geometry of the images (Over et al., 2021). With application of such features, the intention is to produce a high-quality tie points set

and more accurate final model. The quality assessment features for the selection of high-quality tie points are reconstruction uncertainty, projection accuracy and reprojection error.

Reconstruction uncertainty removes the points resulting from poor geometric camera relations, whose removal reduces the noise and disables the influence of the points with large uncertainty to the points delivered from good camera geometry. The reconstruction accuracy value is gradually selected starting from the target value of 10 and increasing towards the maximum of 50% selected tie points to be removed in the filtering procedure. The optimization of reconstruction accuracy value is performed by evaluation of the reprojection error value (in pixels), where smaller value indicates better performance. The projection accuracy filter selects the points that were assigned with poor match accuracy by the software matching algorithm. The performance measure of this error reduction feature is the measure of Mean Key Point Size (in pixels). Smaller values indicate a better precision of key point location in the image. Again, the value is gradually selected, starting from level 1 of projection accuracy, which represents the highest possible accuracy. The amount of removed points should not exceed 50%, as for the reconstruction accuracy metric. Reprojection error is the final point filtering procedure, which sorts out the tie points that are resulting from false matching procedure. A higher value of reprojection error indicates weaker estimation of the original point location in its projection after the alignment procedure. Reprojection error is optimized by evaluating the obtained RMS reprojection error (in pixels), where smaller value indicates better performance. A sufficient level of model optimization is reached when the RMS reprojection error is approximately 0.3 pixels (Over et al., 2021). This value was set as a threshold for reconstruction uncertainty and reprojection error metrics in the performance evaluation of all four DSM produced by different Modes.

The values of the error metrics were gradually selected to filter out 10% of the original tie points used for the SPC creation having weakest performance for all four Modes, so the comparison between the DSM performance can be made. For each step of the point removal procedure, the accuracy for the remaining tie point set was updated and the optimization procedure was repeated. With the final set of best-fit tie points for all four Modes, the creation of a DPC object was initiated. The reconstruction procedure started with the quality adjustment set to ultra-high, providing more detailed and accurate geometry of the reconstructed object. Another adjustable feature in the DPC creation is depth filtering. For the analysis of texture details in small scale such as pavement surfaces, the recommended setting for the depth filtering is mild (Over et al.,

2021). In this way, the applied filtering doesn't exclude the details of the analysed object as outliers and won't reduce the sharpness of an object in focus. When all the reconstruction parameters were defined, the 3D DPC model was created. In this research, the reconstruction process was defined with equal settings for all four Modes so the comparison between the resulting DPCs can be made, regardless of the differences in the data acquisition process.

5.2.2. Resulting DSM properties

To evaluate the performance of the created DSMs, a comparative analysis of key features reported in the *Metashape* Processing report was done. The Processing report contains the information related to the image acquisition process such as number of images, number of markers, image resolution and pixel size, the alignment procedure properties with error metrics, the resulting objects - DPC and mesh features and the data related to the computational process, such as memory usage or processing time. Each report is specific for a corresponding model and by comparing some of the features provided in the report, the model with superior performance can be selected. The aim of this analysis was to evaluate the DSM features different for the generated models and to select the one with the best performance with respect to the analysed parameters.

The analysed properties were grouped into three sections, each one describing a specific step of the 3D model reconstruction and the properties of resulting entity. The first section contained the alignment procedure properties, including error metrics RMS reprojection error and Mean Key Point Size value for the projection accuracy assessment and the resulting SPC properties. In the second section, the reconstruction properties were provided and the last section observed the properties of the resulting DPC and mesh objects.

From the SPC properties obtained for all four data acquisition modes presented in Table 5.8 it can be seen that the Mode 4 DSM obtained the smallest values of RMS Reprojection Error within the defined threshold value. The Reprojection Error parameter for Mode 1 is almost three times higher. The value of Mean Key Point Size is also the smallest for Mode 4. The parameters describing the computational complexity of the reconstruction procedure (computational time and file size) obtained the highest values for Mode 4. The properties of resulting 3D entities are different for all four analyzed acquisition modes. The Mode 1 model obtained the highest number of points in the DPC entity and the smallest number of faces in the mesh entity. Mode 4 acquisition procedure resulted in the DPC with the smallest number of points and largest number of mesh elements.

Table 5.8. DSM properties for models generated from different data acquisition procedures (from Metashape Processing Reports generated for the created DSMs, 2022)

		Acquisition Mode	Mode 1	Mode 2	Mode 3	Mode 4	
Alignment procedure properties	Sparse Point Cloud Properties	Nr. Of Points (original)	13,312	20,749	19,332	28,062	
		Tie Points (filtered)	11,478	18,585	17,201	26,227	
		Projections	85,001	87,138	88,996	99,325	
		RMS Reprojection Error	0.629319 pix	0.562486 pix	0.307105 pix	0.230675 pix	
		Mean Key Point Size value	3.28669 pix	3.43472 pix	2.51834 pix	2.32783 pix	
	Alignment parameters	Accuracy	High				
		Key Point Limit	40000				
		Tie Point Limit	4000				
		Matching Time	17 s	18s	21 s	21 s	
		Matching Memory Usage	233.09 MB	208.63 MB	187.89 MB	206.35 MB	
		Alignment Time	2 s	3 s	4 s	13 s	
	Reconstruction parameters properties	Depth Maps parameters	Quality	Ultra High			
			Processing Time	12 min 26 s	10 min 32 s	9 min 47 s	7 min 27 s
Memory Usage			4.58 GB	4.57 GB	4.25 GB	4.32 GB	
File Size			834.68 MB	751.92 MB	670.48 MB	618.29 MB	
Reconstruction parameters		Source Data	Depth Maps				
		Processing Time	6 min 46 s	7 min 32 s	8 min 51 s	10 min 37 s	
		Memory Usage	10.55 GB	10.27 GB	10.12 GB	10.16 GB	
Resulting 3D model entity properties	DPC properties	Nr. Of Points	4.50E+08	3.68E+08	3.07E+08	2.48E+08	
	Mesh properties	Nr. of Faces	1.37E+06	4.40E+06	6.35E+06	1.25E+07	

5.2.3. Surface roughness features analysis

The DSMs created by four different data acquisition Modes were subjected to roughness features analysis to determine if the resulting texture parameters differ significantly. The analyses were performed on DPC objects resulting from the reconstruction procedure in *Metashape*. The DPC models were imported in the *Cloud Compare* software and subjected to pre-processing: leveling to horizontal position and scaling to correspond the millimeters units. Afterwards, the DPCs were aligned by a point picking algorithm, where three points on the reference object and the corresponding points on the objects to be aligned were selected (Figure 5.7). The selected reference object was Mode 3 DPC. The other three DPCs were aligned with respect to the reference points defined on the Mode 3 DPC. The alignment procedure was controlled by a RMS error value, whose threshold was set to be $< 10\%$.

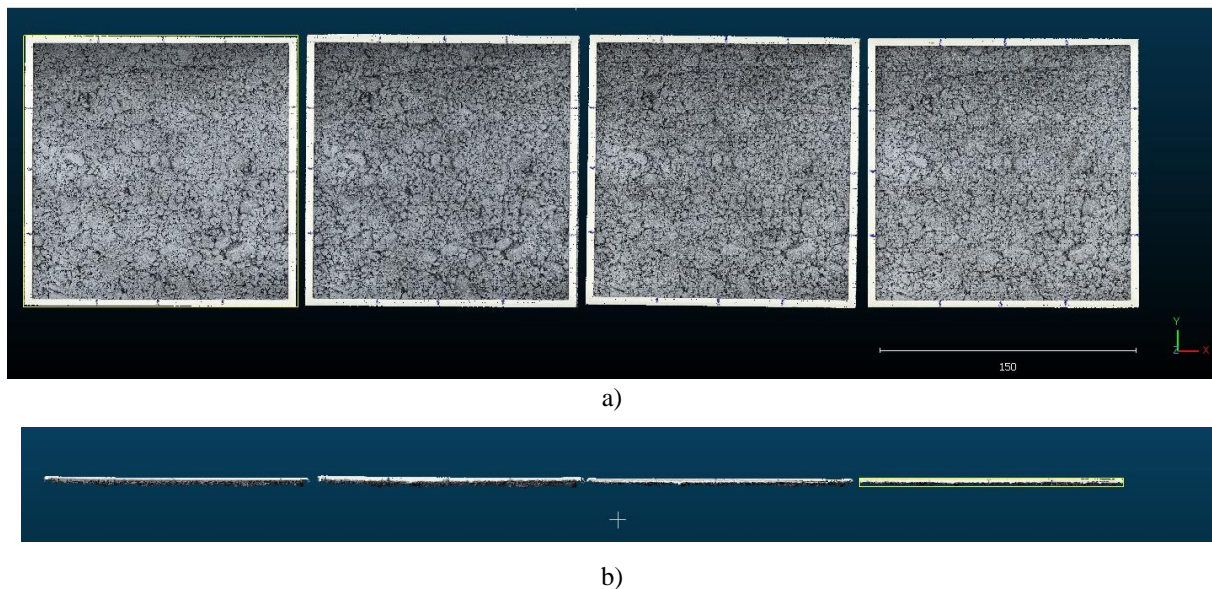


Figure 5.7. DPC alignment procedure in *Cloud Compare*: aerial view (a) and side view (b)

5.2.3.1. DPC properties and profile extraction settings optimization

When the DPCs were aligned with $RMS < 10\%$, they were subjected to segmentation to investigate the geometrical features of the resulting profiles. For each DPC, three 100 mm long sections were extracted from a central surface area at the same position at a distance of 37 millimetres, corresponding to the grid markings on the reference frame (Figure 5.8). The sections were extracted as DPCs, representing surface profiles at the selected positions. This procedure required the definition of the extracted section thickness, i.e. the width of a DPC section from which the profile will be generated. The selected section thickness depends on the density of the DPC, where in general the DPCs with higher point density require smaller section thicknesses. Larger section thickness will include larger number of points. In case when the

section thickness is too narrow for a given DPC density, the resulting profile will consist of an insufficient number of sparsely distributed points and the roughness features won't be described precisely enough or realistic. Such a profile will be discontinuous and a significant number of points should be extrapolated to represent a profile. On the opposite, if the section thickness is too wide for a given DPC density, specific profile segments will contain points with different height coordinates for the same x-coordinate value, resulting in a noisy dataset which should be interpolated to be able to obtain a linear profile. Such data wouldn't represent a profile but a surface section, which leads to 3D instead of 2D analysis.

Two different section thicknesses were defined in the extraction procedure to investigate the optimal thickness for a specific model, 0.01 mm and 0.005 mm for all extracted sections. This value represents the width of the extracted surface segment in y direction. Larger value of section thickness would imply a smaller precision and possibly generate a redundant point dataset describing surface and not profile features. Smaller section thickness implies smaller number of data points for the description of a surface profile. This would decrease the computational demands and enable the profile representation without the possible data redundancy present for larger section thickness.

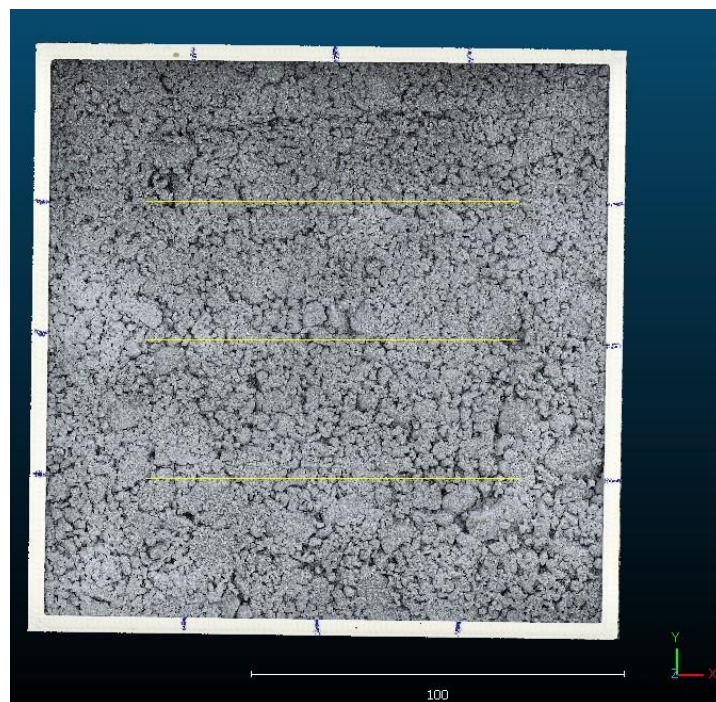


Figure 5.8. Aligned DPCs and the position of extracted sections

Table 5.9 shows the number of points in each extracted section and average horizontal resolution calculated for different section thickness settings for all four DPCs. The number of

points in a profile was significantly smaller for profile section thickness of 0.005 mm and the values of average horizontal resolution are higher for this section thickness property. The average horizontal resolution (point-to-point distance in x direction) was the smallest for the Mode 1 DPC resulting profiles. This is in coincidence with the number of points in DPCs from which the sections were extracted, so it was expected that the Mode 1 resulting profiles would have the largest number of points.

Table 5.9. Number of points in extracted sections for DPCs obtained from different data acquisition modes and resulting horizontal resolution of profiles

DPC Mode	Mode 1	Mode 2	Mode 3	Mode 4
Point density [pts/cm ³]	2.5 E+06	2.02 E+06	2.56E+06	1.96E+06
section thickness 0.01 mm				
Profile 1	17,548	13,742	11,833	9,865
Profile 2	18,583	14,485	12,666	10,585
Profile 3	17,923	14,485	12,316	10,214
average horizontal resolution [mm]	0.0057	0.0073	0.0084	0.0101
section thickness 0.005 mm				
Profile 1	8,857	7,126	5,885	5,000
Profile 2	8,733	7,356	6,430	5,277
Profile 3	8,889	7,164	6,067	4,986
average horizontal resolution [mm]	0.0113	0.0570	0.0733	0.0752

The average horizontal resolution value was calculated to investigate the methods' capability of capturing relevant surface wavelengths in micro-texture and macro-texture range. For both section thicknesses, the obtained values were below the macro-texture lower limit value. As the micro-texture doesn't have a lower limit value, the section thickness setting providing smaller resolution values is preferable as it captures micro-texture more in detail. From Table 5.9 it can be seen that the average horizontal resolution values obtained for the section thickness of 0.01 mm are in general smaller than the ones obtained for section thickness of 0.005 mm. Moreover, they are all below 0.01 mm except the Mode 4 profile resolution which indicates the sub-millimeter precision of the obtained profile data. A comparison of profile's resolution with different section thicknesses is given in Figure 5.9. Roughness features were further analysed on profiles extracted with section thickness of 0.01 mm.

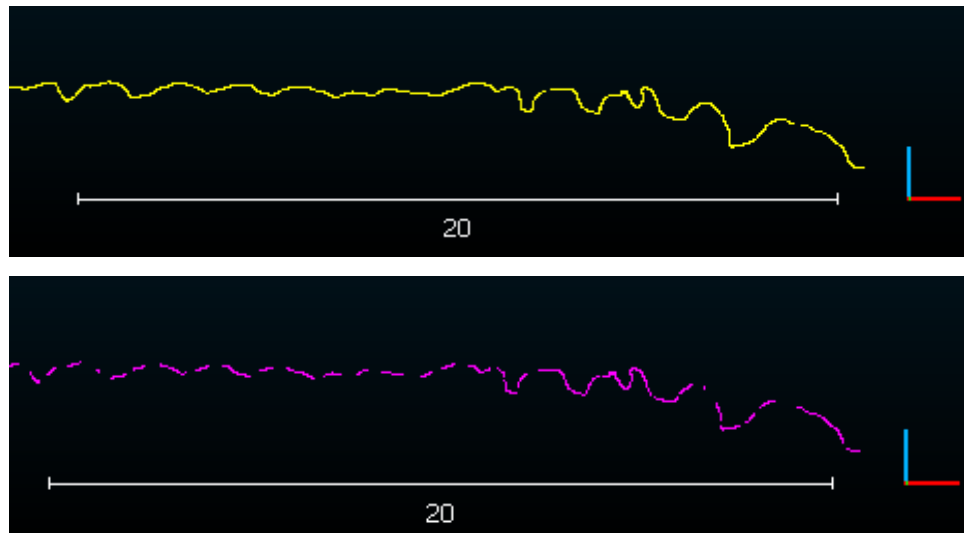


Figure 5.9. An example of profile portion segmented from the DPC with two different section thicknesses: section thickness 0.01 mm (upper) and section thickness 0.005 (lower)

5.2.3.2. Profile geometry and roughness analysis

To perform a comparative profile data analysis, the original profile data was corrected to have the same absolute x coordinate of the first profile point, $x = 0$. Height coordinates were adjusted with respect to the calculated mean height value for a given profile so they fluctuate around the mean level equal to zero. The corrected profiles were plotted to evaluate the profile geometry for different data acquisition methods. The profile plots obtained from Mode 1 and Mode 2 surface models showed that the extracted profiles have a convex form. The profiles obtained from Mode 3 showed a minor deviation from the horizontal plane, resulting from the manual procedure of DPC alignment in CC software. The profiles extracted from Mode 4 DPC were perfectly horizontal (Figure 5.10).

A difference in the surface roughness description was also observed for extracted profiles. A smaller portion of overlapped profiles was observed, where it can be seen that the roughness representation from Mode 1 and Mode 2 profiles is different than for the Mode 3 and Mode 4 profiles (Figure 5.11). The roughness on smaller scale (i.e. micro-texture) is captured more in detail with the Mode 3 and Mode 4 resulting profiles. The differences in profiles' geometry are due to the convex form of the profiles from Mode 1 and Mode 2 and the precision tolerance in the DPC overlapping procedure.

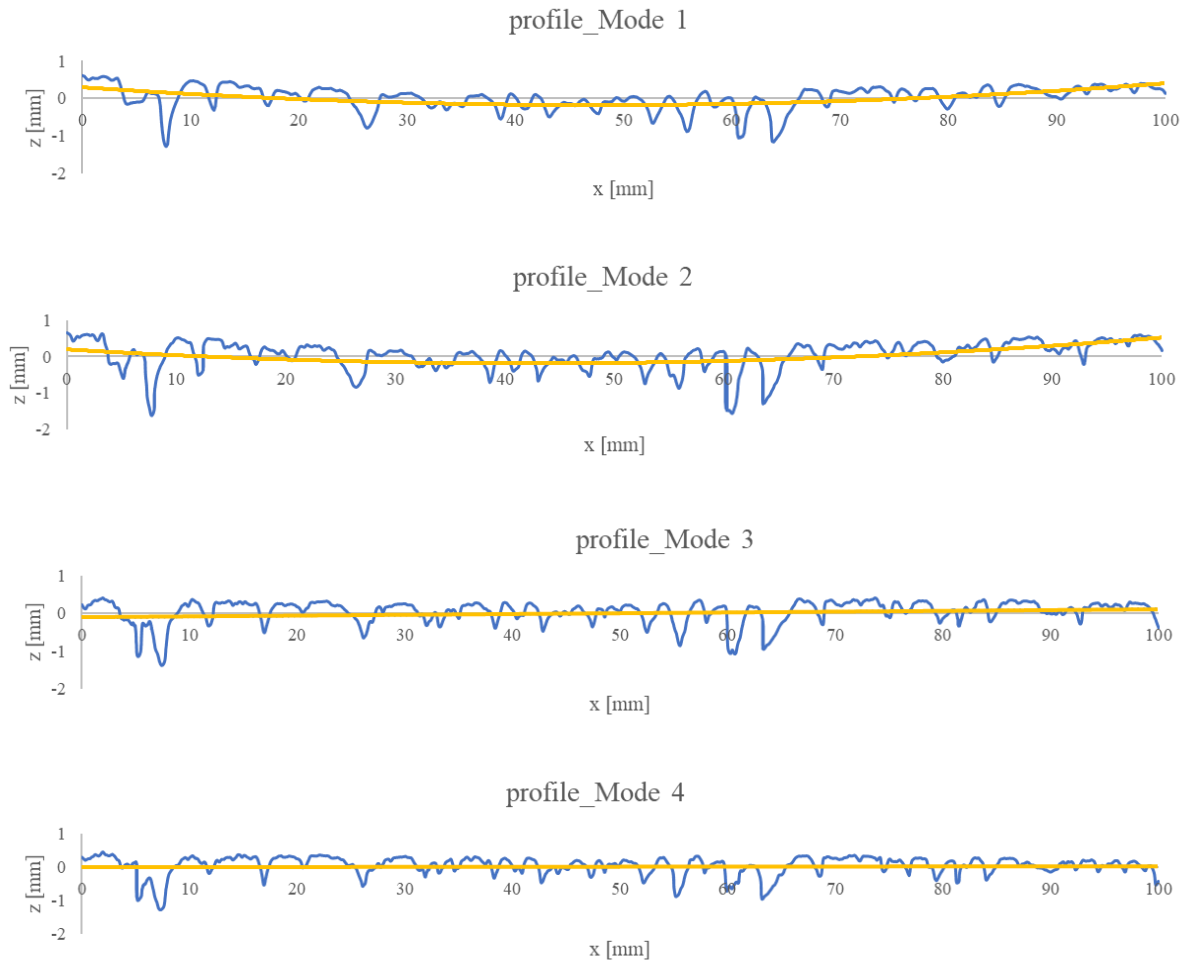


Figure 5.10. Comparison of profile geometry for different data acquisition modes

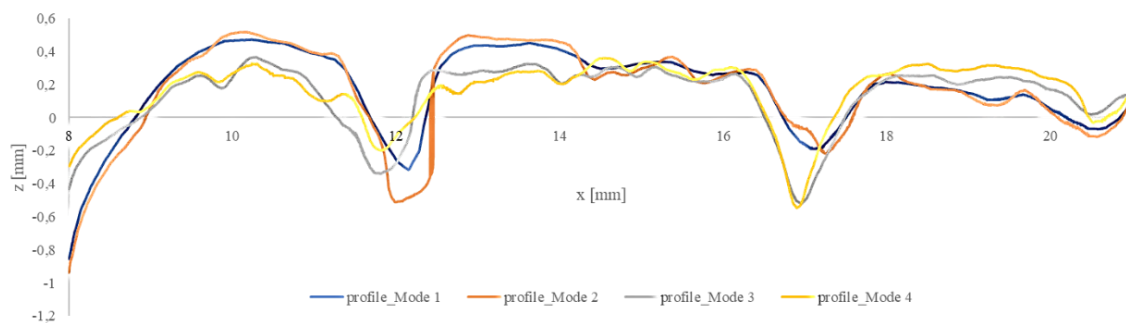


Figure 5.11. Comparison of profiles' roughness representation for different data acquisition modes

Further analysis of the characteristic texture parameters was performed only for the profiles extracted from the DPCs generated by Mode 3 and Mode 4 acquisition methods. The other two methods were excluded as the profiles extracted from the resulting surfaces showed a geometry distortion which could affect the values of the texture parameters. These profiles would have to be subjected to additional adjustments and filtering of original data points, requiring additional

time for data analysis and a possible unrealistic relation to the surface frictional performance. Surface roughness features were captured more in detail by Mode 3 and Mode 4 acquisition methods, therefore they were found to be more suitable for the inclusion of micro-texture effect on the texture roughness characteristics.

5.2.3.3. Comparison of texture parameters values

DSMs produced by Mode 3 and Mode 4 were further analyzed by additional profile segmentation from which the selected texture parameters were calculated. The purpose of this analysis was to investigate the difference in the texture parameters values derived from the DSMs obtained by different data acquisition methods. To acquire the best possible overlap between the DSMs, additional alignment was performed following the same procedure as described in section 4.2.3. From the aligned DSMs, ten sections were segmented with section thickness of 0.01 mm and 100 mm length, representing the surface profiles (Figure 5.12).

Extracted profiles' coordinates were corrected to start from $x = 0$ and to have the height values fluctuating around mean height value equal to zero. The corrected profiles were saved as .csv files and imported to *MountainsMap* software (version Lab Premium 9.0, Digital Surf, 2023) for surface and profile texture analysis by roughness parameters defined in EN ISO 21920-2 and EN ISO 25178-2 standards. *MountainsMap* enables the calculation of texture parameters on roughness and waviness level separately, by applying the Gaussian filters with corresponding threshold levels. This feature enables the exclusion of the micro-texture or macro-texture effect on the profile roughness properties prior to the calculation of selected parameters. The software contains all the profile-related and surface-related texture parameters described in Chapter 3 for the characterization of any surface roughness performance on the selected roughness scale.

This research focused on the evaluation of the profile features on both friction-relevant texture scales. Therefore, the selected texture parameters were calculated on the primary profiles so none of the texture levels was excluded from the analysis. Prior to the parameters calculation, the profiles were subjected to automatic leveling to remove any remaining vertical slope from the obtained profiles and filtered with a Gaussian S-filter to remove the small lateral scale profile components below 2.5 μm . In this way, the profiles were de-noised and the points within the defined method precision range of 0.01 millimeters were still preserved.

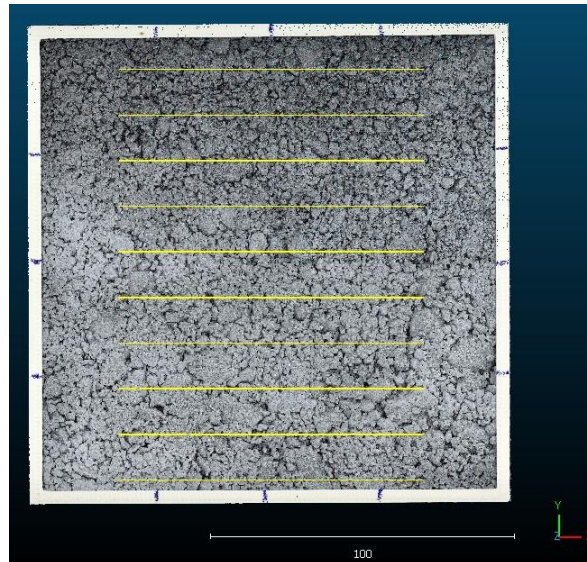


Figure 5.12. Aligned DPCs from Mode 3 and Mode 4 and marked positions of ten sections for profiles extraction

The profile-related texture parameters evaluated by *MountainsMap* software were selected from the amplitude group and feature group: arithmetic mean absolute height P_a , root mean square height P_q , total height P_t , mean height P_z , maximum peak height P_{pt} and maximum valley depth P_{vt} and mean height of profile element P_c . The traditional pavement profile-related parameters MPD and ETD were also evaluated for the inspected profiles, calculated in *Microsoft Excel* for the leveled and filtered profiles according to EN ISO 13473-1. The calculated profile parameters values are given in Table 5.10. An example of profile plots for two different data acquisition modes after the profile adjustments in *MountainsMap* software is given in Figure 5.13.

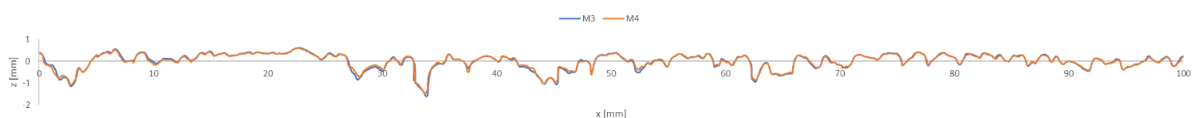


Figure 5.13. Profile P9 geometry extracted from Mode 3 and Mode 4 data acquisition modes

To address the difference between the texture parameters calculated from the same profiles extracted from different data acquisition modes, the mean absolute difference was calculated for parameters' pairs (Table 5.11). For most of the analysed parameters, the calculated mean absolute difference was $\leq 5\%$. The exceptions were the parameters P_t (total height), P_{vt} (max. valley depth) and P_z (mean height), amongst which the parameter P_t showed the greatest mean absolute difference of 16% between the values determined for Mode 3 and Mode 4 profiles. The values of standard texture parameters MPD and ETD showed low variations in the mean difference values with 2% and 1%, respectively.

Table 5.10. Profile-related parameters extracted from DSMs from Mode 3 (M3) and Mode 4 (M4) data acquisition setup

Profile no.	Mode no.	Profile parameters EN ISO 21920-2 [mm]							Profile parameters EN ISO 13473-1 [mm]	
		Pa	Pq	Pt	Ppt	Pvt	Pz	Pc	MPD	ETD
1	M3	0.151	0.194	1.040	0.337	0.703	0.869	0.513	0.296	0.436
	M4	0.160	0.205	1.161	0.296	0.865	0.971	0.551	0.270	0.416
2	M3	0.211	0.283	2.191	0.426	1.765	1.189	0.725	0.391	0.513
	M4	0.205	0.277	2.100	0.393	1.707	1.186	0.721	0.367	0.493
3	M3	0.242	0.334	2.191	0.467	1.724	1.387	0.897	0.436	0.549
	M4	0.226	0.312	2.062	0.444	1.617	1.322	0.830	0.418	0.534
4	M3	0.155	0.202	1.190	0.294	0.896	0.937	0.490	0.288	0.430
	M4	0.160	0.217	1.368	0.292	1.076	1.048	0.495	0.282	0.426
5	M3	0.259	0.338	2.067	0.471	1.596	1.185	0.894	0.433	0.546
	M4	0.251	0.327	2.010	0.485	1.525	1.156	0.892	0.435	0.548
6	M3	0.269	0.389	2.358	0.531	1.826	1.393	0.849	0.474	0.579
	M4	0.262	0.371	2.182	0.472	1.710	1.318	0.819	0.456	0.565
7	M3	0.293	0.408	2.419	0.491	1.928	1.545	1.088	0.458	0.566
	M4	0.283	0.390	2.405	0.497	1.908	1.514	0.999	0.449	0.559
8	M3	0.355	0.517	2.757	0.731	2.026	1.468	0.999	0.544	0.635
	M4	0.340	0.495	2.498	0.666	1.832	1.367	0.887	0.499	0.599
9	M3	0.271	0.355	2.221	0.613	1.607	1.513	0.810	0.517	0.613
	M4	0.257	0.336	2.062	0.595	1.467	1.422	0.767	0.499	0.599
10	M3	0.225	0.276	1.360	0.447	0.914	1.110	0.692	0.428	0.543
	M4	0.233	0.295	1.737	0.467	1.270	1.253	0.778	0.446	0.557

Table 5.11. Mean absolute difference for profile-related parameters for Mode 3 and Mode 4 (Table 5.10) and average value $MAD_{average}$ for each calculated parameter

Profile no.	1	2	3	4	5	6	7	8	9	10	$MAD_{average}$ [%]
	Mean absolute difference (MAD) for parameters calculated for M3 and M4 profiles										
Pa	0.009	0.007	0.017	0.005	0.009	0.006	0.011	0.015	0.014	0.008	1%
Pq	0.011	0.006	0.023	0.015	0.011	0.018	0.018	0.022	0.019	0.019	2%
Pt	0.121	0.091	0.129	0.178	0.057	0.176	0.014	0.259	0.159	0.377	16%
Ppt	0.041	0.034	0.023	0.002	0.014	0.059	0.007	0.065	0.018	0.021	3%
Pvt	0.162	0.058	0.107	0.180	0.071	0.116	0.020	0.194	0.140	0.356	14%
Pz	0.102	0.003	0.065	0.111	0.029	0.075	0.031	0.101	0.091	0.143	8%
Pc	0.038	0.004	0.067	0.005	0.001	0.031	0.089	0.112	0.043	0.086	5%
MPD	0.026	0.024	0.018	0.006	0.002	0.018	0.008	0.044	0.017	0.018	2%
ETD	0.021	0.019	0.014	0.005	0.002	0.015	0.007	0.036	0.014	0.015	1%

The profile parameters values were subjected for descriptive statistical analysis to evaluate the variation between the obtained values from different DSMs. In this way, profile-related analysis was extended to surface-related analysis by calculation of mean values for profile-related parameters as the surface roughness representations. This was done only for the parameters describing an overall roughness feature, while the parameters describing an extreme profile feature total height P_t , maximum peak height P_{pt} and maximum valley depth P_{vt} were not included in this analysis. The results of performed analyses are given in Table 5.12. In general, profiles extracted from Mode 4 DSM have lower variability of calculated mean parameters evaluated by variability statistics values: standard deviation, variance and coefficient of variation. The highest values of standard deviation and variance were obtained for parameters P_z and P_c , while the average roughness parameter P_a obtained the smallest variation in case of both data acquisition modes. The mean parameters' values calculated for all ten profiles are slightly higher for the Mode 3 DSM.

The effect of the number of extracted profiles was evaluated by comparing the mean values of six roughness parameters, separately for even and odd profiles and for the total number of profiles. Statistical variability indicators standard deviation σ , variance σ^2 and coefficient of variation CV were calculated and the obtained results are given in Table 5.13. From the obtained results it can be seen that the number of profiles or profile spacing doesn't have a significant effect for the estimation of overall surface-related texture parameters as the variability measures are low. Generally, the parameters values calculated for the profiles extracted from two different data acquisition modes were not significantly different, as the average absolute difference between the calculated mean parameters' values in Table 5.13. was 0.01 mm.

By observing the properties of DSMs created by Mode 3 and Mode 4 data acquisition setups, the resulting point density and profile resolution for the optimal section thickness of 0.01 mm, Mode 3 performed better. The calculation of profile-related parameters and the results of statistical analyses for the parameters determined from Mode 3 and Mode 4 profiles showed that there was no significant difference between the obtained values. From the results of the performed comparative analyses between the DSMs performance, the mode selected for further application was the Mode 3. By comparing the DPCs created by Mode 3 and Mode 4, former has approximately 60 million points more and thus provides a more detailed representation of the analyzed surface. The selected data acquisition method verification is described in the next section 5.3.

Table 5.12. Calculated descriptive statistics for profiles extracted from Mode 3 and Mode 4 DSM

Profile parameter	M3					M4				
	Mean [mm]	Range [mm]	σ [mm]	σ^2 [mm ²]	CV [%]	Mean [mm]	Range [mm]	σ [mm]	σ^2 [mm ²]	CV [%]
Pa	0.243	0.204	0.058	0.003	0.240	0.237	0.180	0.052	0.003	0.22
Pq	0.329	0.323	0.092	0.008	0.280	0.322	0.290	0.080	0.006	0.25
Pz	1.259	0.676	0.226	0.051	0.180	1.256	0.543	0.159	0.025	0.13
Pc	0.796	0.598	0.184	0.034	0.231	0.774	0.504	0.146	0.021	0.19
MPD	0.426	0.256	0.079	0.006	0.186	0.412	0.230	0.077	0.006	0.19
ETD	0.541	0.205	0.064	0.004	0.117	0.530	0.184	0.062	0.003	0.12

Table 5.13. Calculation of mean parameters values for a different number of profiles for both data acquisition setups

Mean value [mm]	M3 _{all} profiles	M4 _{all} profiles	M3 even profiles	M3 odd profiles	M4 even profiles	M4 odd profiles	Mean [mm]	σ [mm]	σ^2 [mm ²]	CV [%]
Pa	0.243	0.237	0.243	0.243	0.240	0.235	0.241	0.002	0.000	0.98
Pq	0.329	0.322	0.333	0.326	0.331	0.314	0.328	0.004	0.000	1.20
Pz	1.259	1.256	1.219	1.230	1.234	1.277	1.254	0.027	0.001	2.17
Pc	0.796	0.774	0.751	0.840	0.740	0.808	0.780	0.036	0.001	4.57
MPD	0.426	0.412	0.425	0.428	0.410	0.414	0.420	0.007	0.000	1.79
ETD	0.541	0.530	0.540	0.542	0.528	0.531	0.532	0.006	0.000	1.12

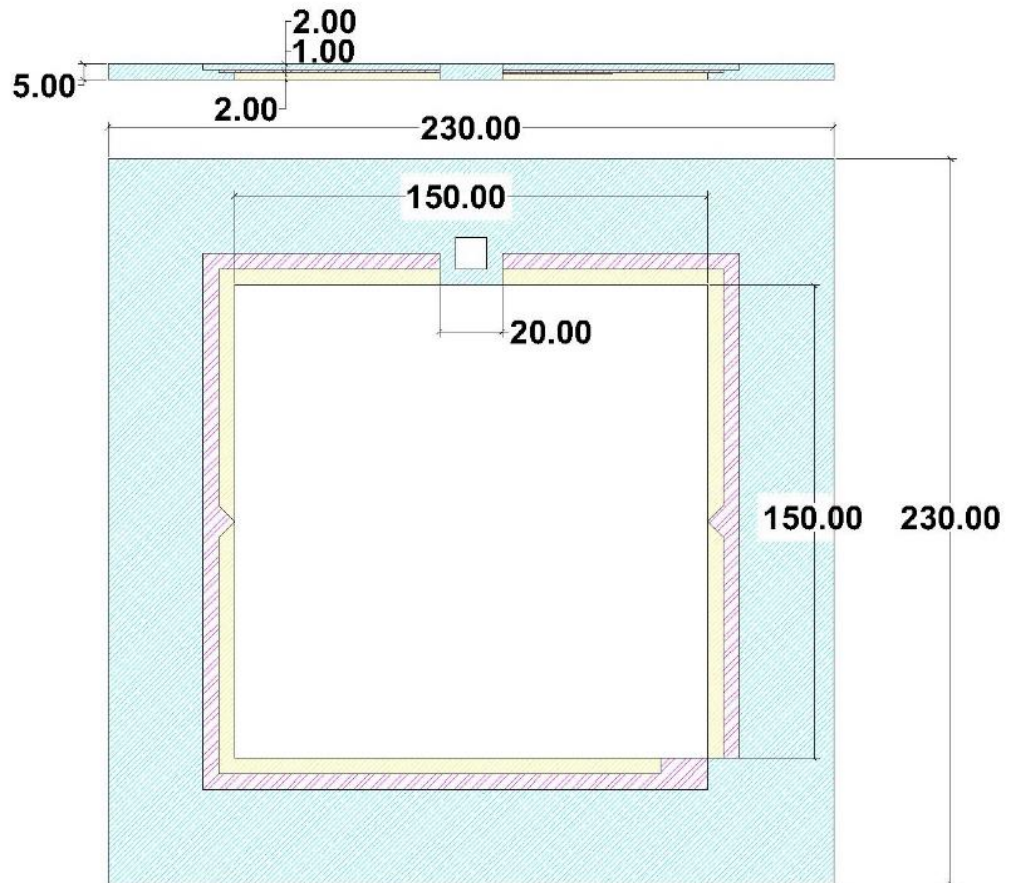
5.3. Verification of the proposed CROP method

The established CROP method for pavement texture data acquisition was evaluated by comparing the method's performance with two similar data acquisition methods: 3D laser scanning method and photogrammetry method utilizing a specialized photogrammetric camera. The aim of this analysis was to investigate the accuracy of the proposed method and to determine the extent of the micro-texture range that could be investigated by the CROP method. Accuracy is an important feature of DSM models created by photogrammetry-based methods and used for measurements on various scales (Sapirstein, 2016). Adequate CROP method's accuracy is the precondition for a realistic reconstruction of surface morphology from which the texture parameters relevant for friction performance can be determined. The accuracy of created DSMs described in section 5.2 was based on *Metashape* markers arranged around the analysed surface and later evaluated by

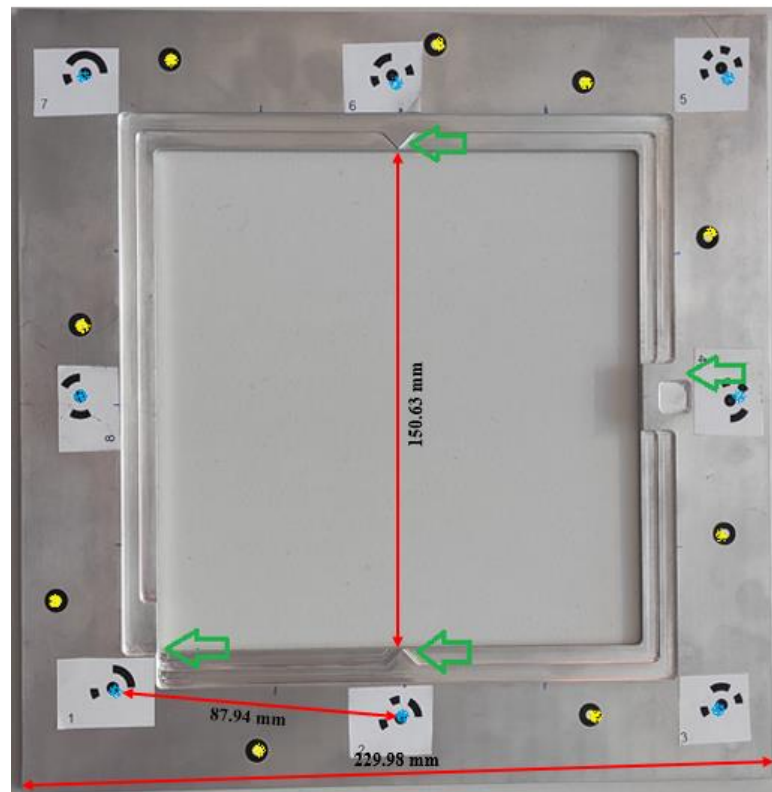
error metrics. The analyses showed that DSM created by Mode 3 acquisition setup obtained the lowest value of error metrics, therefore it was adopted for further accuracy analysis.

The verification was performed on a reference object, a custom-designed 3D frame constructed by using a CNC milling machine, intended for precise cutting of CAD-designed objects (Figure 5.14). The selected material for the frame construction was aluminium because it is a solid, lightweight material, doesn't deform and can be precisely cut. The design dimensions of the reference frame were defined as $230 \times 230 \text{ mm}^2$ for the outer edge and $150 \times 150 \text{ mm}^2$ for the inner edge, selected to correspond to the dimensions of the pavement surface area analysed in section 4.2 (Figure 5.14a). The maximum frame thickness was 5 mm on the outer frame edge. The inner edge of the frame was designed to have three different thicknesses: 2 mm for the outer steps (marked blue and yellow) and 1 mm for the middle step (marked magenta). Several reference shapes were designed on the frame to enable precise determination of frame dimensions and to ease the selection of the reference points on the frame (marked green in Figure 5.14b). Two triangular shaped objects were designed in the middle of the inner frame height and at the lower inner corner for a precise dimension measurement. A square shaped object on the upper edge of the frame was designed for the determination of the frame orientation.

The frame was referenced by two different sets of markers: one for the 3D laser scanning data acquisition method (marked yellow in Figure 5.14b) and one for the photogrammetry methods data acquisition (marked blue in Figure 5.14b). The markers were utilized for the alignment and model calibration in the DSM creation procedure. Laser scanner markers were randomly distributed to cover the entire frame surface, while photogrammetry markers were positioned on approximately equal distances close to the inner edge of the frame. The distance between the photogrammetry markers 1 and 2 (lower left corner and the adjacent right) was a reference distance for alignment procedure. This distance on the frame was measured with a digital calliper and recorded as 87.94 mm. The dimensions of the produced reference frame were slightly different than the design dimensions. The reason is the precision of the CNC milling machine, however the inner frame dimensions showed an acceptable deviation from the original design of 0.63 mm measured between two reference objects on the frame.



a)



b)

Figure 5.14. CAD design for the reference frame (a) and the produced reference frame with attached markers prior to the data acquisition procedure (b)

5.3.1. 3D laser scanning procedure and the resulting DSM properties

3D laser scanning data acquisition was performed by a high precision ATOS III Triple Scan 3D optical measurement system (*Center for Advanced Computing and Modelling, University of Rijeka*) (Figure 5.15). The scanner enables a precise 3D object scan, capturing point spacing up to 0.01 mm precision, exported as a surface model convertible to a 3D Mesh or a DPC object (Li et al., 2017). The equipment is fast, robust and flexible in terms of scale adjustment with respect to the size or precision demands of the analysed object. It is considered as a benchmark equipment for the geometrical features analyses of scanned objects (Eiríksson et al., 2016). DSMs produced by photogrammetry methods are commonly compared to the laser scanning produced DSMs for the evaluation of method's accuracy (Sapirstein, 2016).

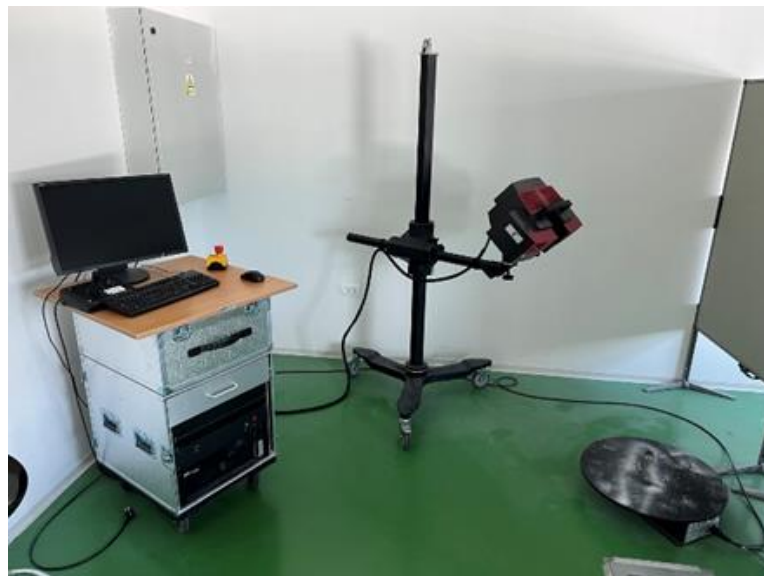


Figure 5.15. ATOS III Triple Scan laser scanning system assembly, Centre for advanced modelling and calculations, University of Rijeka, 2022

The reference frame was scanned by ATOS III Triple Scan and stored as a 3D mesh object with 2.5×10^5 faces (Figure 5.16. a,b). The mesh model was further processed in *Cloud Compare* software by following the procedure described in the previous section: alignment to a horizontal plane and scaling to correspond the dimensions in millimeters. The processed mesh object was sampled to a DPC object with approximately 51×10^3 points/cm³ density (Figure 5.16 c,d).

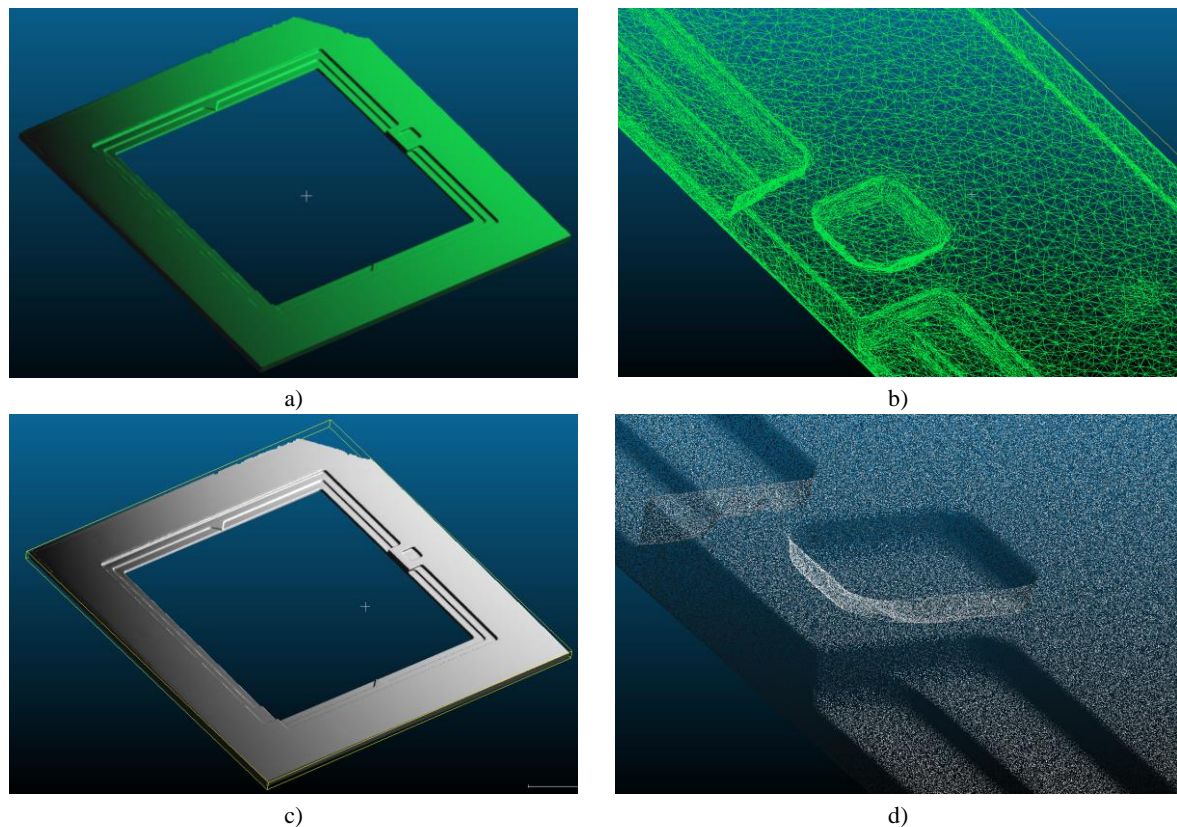


Figure 5.16. A DSM of 3D laser scanning result object: Mesh (a,b) and DPC (c,d)

The accuracy of the DSM was evaluated by control measurements on the actual frame. The plane dimensions were determined for selected characteristic points (Figure 5.17a). The calculated absolute difference between the measurements on actual frame and 3D DSM resulting from 3D scanning procedure were within 0.01 mm, except the outer frame dimension which obtained larger dimension deviations (Table 5.14). The DSM height accuracy was validated on a DSM cross section where the characteristic heights were measured (Figure 5.17b). The cross section was extracted at the central position of the frame where the thickness was measured on different positions (Figure 5.17c, d). Calculated absolute differences between the measured values on the frame and DSM objects were up to 0.03 mm (Table 5.15).

Table 5.14. Calculated absolute differences between the plane dimensions determined on frame and DSM created from 3D laser scanning procedure

Dimension	Length on frame [mm]	Length on DSM [mm]	Absolute difference [mm]
A	150.63	150.62	0.01
B	19.55	19.54	0.01
C	99.53	99.52	0.01
D	229.98	229.91	0.07

Table 5.15. Calculated absolute differences between the height dimensions determined on frame and DSM created from 3D laser scanning procedure

Position	Height on frame [mm]	Height on DSM [mm]	Absolute difference [mm]
1	4.77	4.75	0.02
2	2.83	2.85	0.02
3	1.84	1.86	0.02
4	4.79	4.82	0.03
5	4.88	4.85	0.03

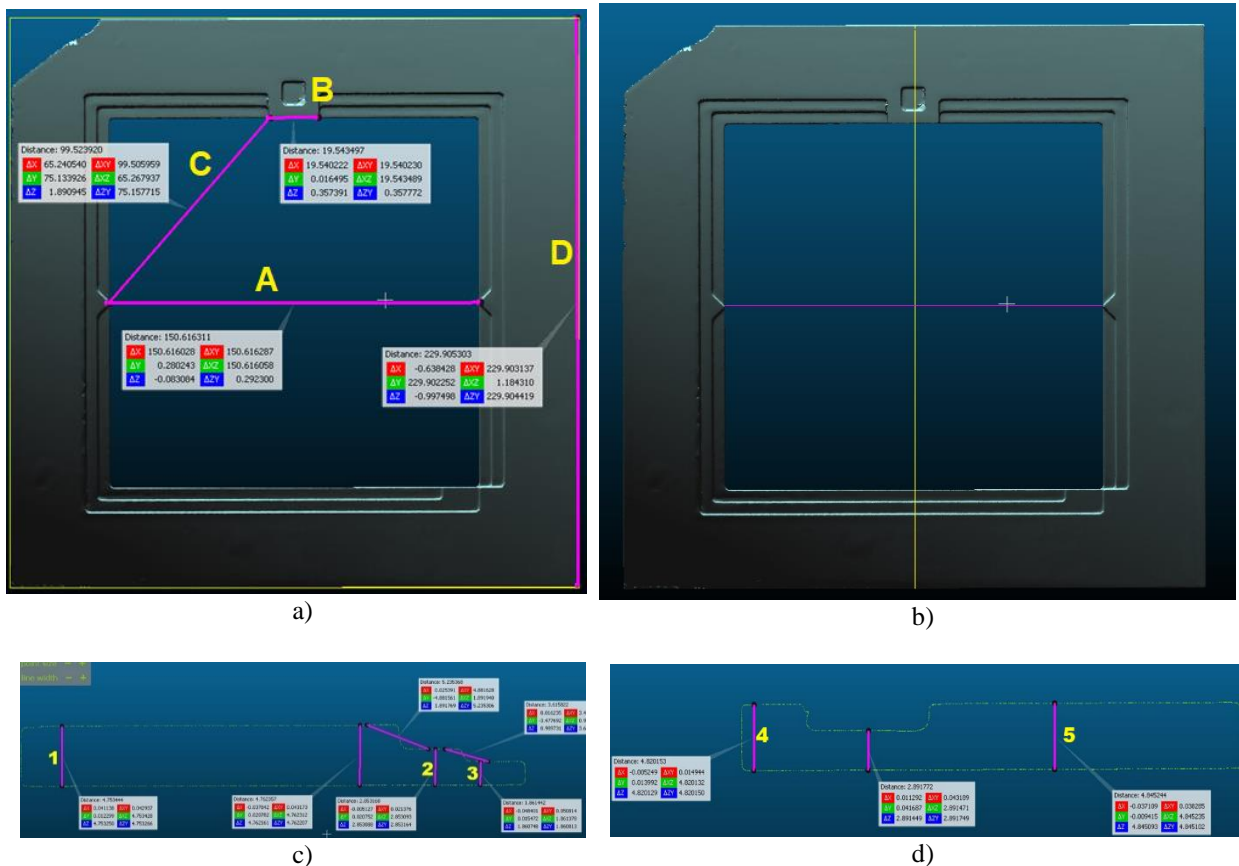


Figure 5.17. Dimensions (a, b) and height measurement positions (c, d) on DSM selected for the comparison with the measurements on actual frame, determined with respect to the reference frame objects for precise measurements

5.3.2. Photogrammetry procedure and resulting DSM properties

Photogrammetry-based data acquisition procedure was performed with two different cameras: professional photogrammetry camera Canon 5D Mark III with 20 mm lens and previously used Nikon D500 with 50 mm lens. The data acquisition followed the same procedure as described in section 4.2. The camera settings were set to a standard mode with automatic brightness and contrast adjustments, light sensitivity set to ISO 100 and aperture size f/4.0. A trial image was taken for each equipment setup before the data acquisition was prompted to manually adjust the brightness and contrast camera settings if necessary. The selected camera properties and image acquisition settings specific for both performed procedures are listed in Table 5.16.

The image acquisition was performed on asphalt specimen to obtain a better contrast between the reference frame and environment (Figure 5.18). This was important for later frame extraction, which was done more precisely for sharp boundary between the smooth frame edge and rough pavement surface. If the frame was photographed on a smoother surface, the frame edge wouldn't be so emphasized. To disable the light reflection effect, the frame was sprayed with an antireflective agents. The images were captured by translating the camera across the target surface with respect to the defined grid, without changing the camera height or angle. The camera heights were specific for each acquisition procedure, selected as the closest possible focus distance specific for each camera that still provides sharp images of captured surface. Images were taken consecutively, starting from upper left corner and moving horizontally towards the opposite corner with standard 60% side and 80% forward overlap. The images were taken in five rows and the inspected surface was covered by 25 images. One additional image was taken at 370 mm height for Canon Mode to capture the whole reference frame. The same was done for the Nikon Mode with camera height adjusted to 650 mm. In this way, the conditions for the calibration procedure were enhanced so the resulting model could be more precise.

Table 5.16. Properties of different photogrammetry acquisition devices

	Acquisition Mode	CROP Canon	CROP Nikon
Camera Settings and Image Capture Design	Camera Model	Canon EOS 5D Mark III 22Mpix	Nikon D500 20 Mpix
	Lens Type	EF 20 mm f2.8 USM	AF Nikkor 50 mm f1.8 D
	Focal Length	20 mm	50 mm
	Aperture	f/4.0	f/4.0
	Shutter Speed	1/15 s	1/20 s
	ISO	100	100
	Camera Height	250 mm	500 mm (650 mm)
	Camera Angle	0°	0°
	Nr.of Images	25	25
	Nr. Of Markers	8	8
	Camera resolution	5760x3840	5568x3712
	Pixel Size	6.44 x 6.44 μm	4.31 x 4.31 μm

The DSM reconstruction in *Metashape* was done by applying the same settings as described in section 5.2. In this way, a comparison between the specific features of all three DPC's could be made, regardless of the differences in the data acquisition process. The properties of DSMs extracted from the *Metashape* Processing report are given in Table 5.17. Besides the previously analysed DSM properties in section 5.2., the residual error vector properties were plotted for both DSMs. For the residual error vectors shorter than 1 pixel which do not follow a certain pattern, a DSM is considered as a valid representation of the actual object (Over J., et al, 2021).

Another property was evaluated, related to the scale control obtained by reference markers and evaluated by the calculated error in distance between two markers. From the DSM properties in Table 5.17, it can be seen that Nikon Mode DSM satisfied the residual error vector condition and obtained smaller value of scale control error.

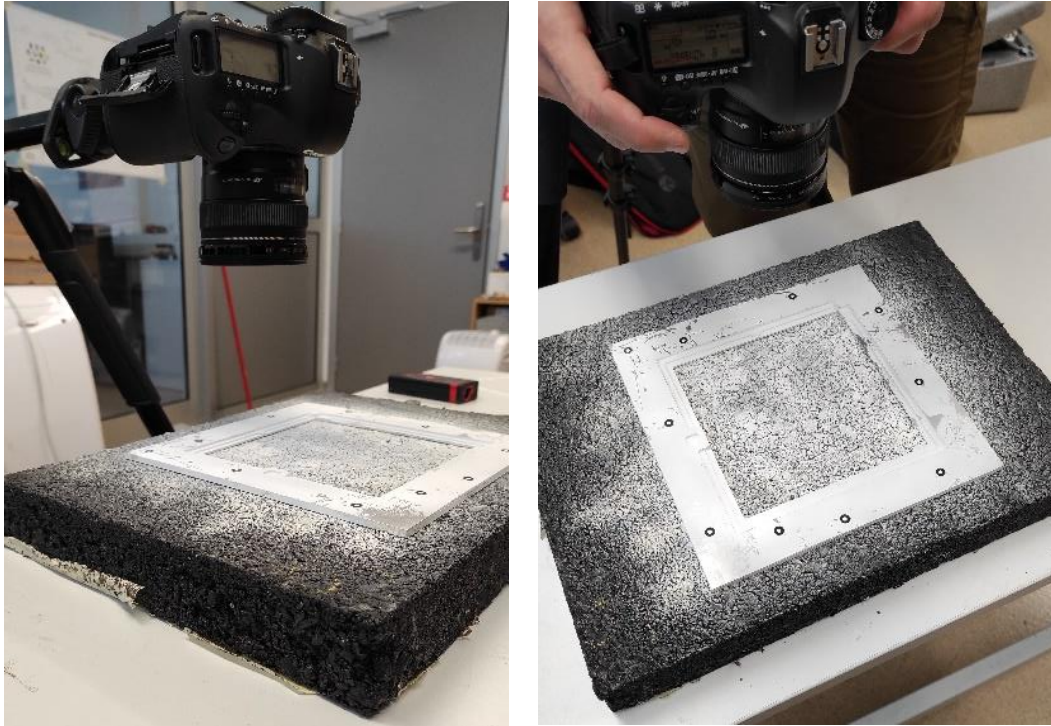
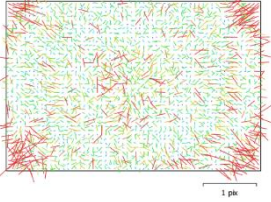
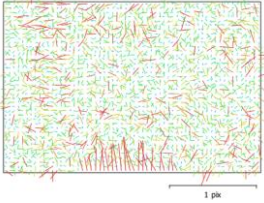


Figure 5.18. CROP procedure performed for reference frame DSM acquisition

The Nikon mode DSM obtained lower values of the observed error metrics RMS reprojection error and Mean Key Point Size. It obtained higher point density and higher number of points in the DPC. It was computationally more demanding than the Canon Mode DSM, with longer overall processing time for all reconstruction phases and required more memory.

Table 5.17. Resulting photogrammetry 3D DSMs properties, Metashape Processing reports

	Acquisition Mode	<i>CROP Canon</i>	<i>CROP Nikon</i>
Scale control	Error in distance (Marker 1-Marker 2) [m]	5.23822 E-05	6.4795 E-05
Image residuals			
Sparse Point Cloud Properties	Point density	438 pts/mm ²	981 pts/mm ²
	Nr. Of Points	17,201	23,244
	Tie Points	9,790	15,905
	Projections	52,397	77,809
	RMS Reprojection Error	0.368194 pix	0.30455 pix
	Max Reprojection Error	2.11893 pix	1.40683 pix
	Mean Key Point Size	2.77345 pix	2.49148 pix
Alignment parameters	Accuracy	High	High
	Key Point Limit	40,000	40,000
	Tie Point Limit	4,000	4,000
	Matching Time	2 min 48 s	37 s
	Matching Memory Usage	292.68 MB	287.68 MB
	Alignment Time	5 s	13 s
	Alignment Memory Usage	34.38 MB	108.17 MB
Depth Maps parameters	Quality	Ultra High	Ultra High
	Processing Time	13 min 33 s	10 min 30s
	Memory Usage	5.29 GB	5.23 GB
	File Size	865.24 MB	769.30 MB
DPC properties	Nr. Of Points	2.81E+07	6.81E+07
	Processing time	11 min 17 s	11 min 59 s
Model reconstruction parameters	Processing Time	19 min 16 s	46 min 9 s
	Memory Usage	9.82 GB	14.98 GB
Mesh model properties	Nr. of Faces	1.51E+07	3.43E+07

The DSMs created by two photogrammetry methods were compared to the reference DSM created from the 3D laser scanning procedure. The aim of this analysis was to inspect which of the CROP created models is more accurate in comparison to the reference DSM created by a benchmark method. The comparison was done by applying the DPC alignment procedure in *Cloud Compare* software. Three points were selected for the alignment (Figure 5.19). The selected points were the specific reference points on the frame: two of the points are the peaks of the triangles in the middle of the frame length (R0 and R1), and another one is on the peak in the lower right corner of the inner frame (R2). These points were chosen as easily recognizable on both objects so the alignment could be done more precisely. The points on the reference DPC were defined by the same coordinates for the performed alignments. For the CROP models, the corresponding points were slightly different for each alignment procedure, since the number of points in each DPC was different and it was not possible to select the exact same points. However, the points were selected to have as close as possible coordinates to the alignment points defined on the reference frame. When the reference points were selected on the frame to be aligned, the alignment procedure was performed until the calculated RMS error value for the obtained alignment was below the threshold value, set to $\text{RMS} < 10\%$ or 0.1.

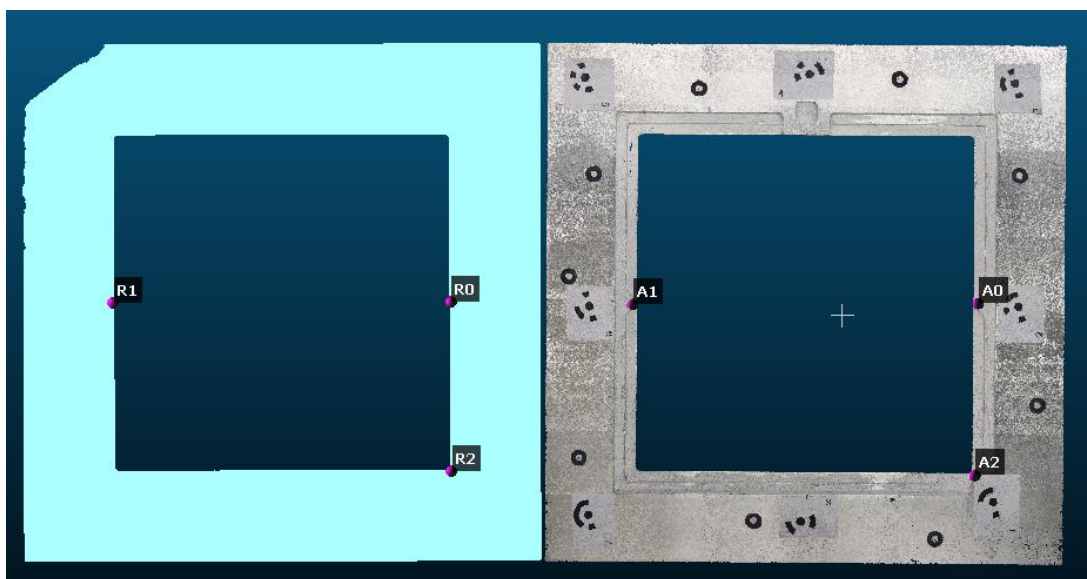


Figure 5.19. Reference DPC (left) and DPC to be aligned (right) with marked alignment points

After the alignment procedure, an algorithm for the calculation of cloud-to-cloud distances (C2C) was utilized to determine which DPC obtained better coincidence with the reference DPC. The *Cloud Compare* software calculates the distances by using „nearest neighbor distance“ algorithm, which calculates the euclidean distance between two points subjected to comparison (one in reference DPC and the corresponding nearest neighbour in the compared DPC). This method enables simple, fast and direct distance estimation between the points (Lague et al., 2013).

A threshold value of maximum distance can be defined, so the true distances greater than this value won't be computed but replaced by the threshold value itself. A threshold value of maximum distance between the compared DPC's was set to 1 mm. The reason was the data acquisition procedure by 3D laser scanner, in which the frame was attached to an arm holding the frame in the air. The upper left corner of the frame was not reconstructed in the DSM creation, as can be seen in Figure 5.16a, c. The C2C algorithm could not converge to a solution if the threshold value was below 1 mm, because the distance between the aligned DPCs in the upper left corner would be infinite (as the reference DPC doesn't contain these points).

After the C2C distance was calculated, obtained values were represented as the resulting color scale scalar field on the DPC compared to the reference frame. The corresponding histograms where calculated C2C distances were grouped into classes with range 0.05 mm were generated as a result (Figure 5.20). Each C2C distance class is presented with a different color and the height of each class resembles the number of DPC points falling within that specific class. The blue color marked the smallest calculated C2C distances (below 0.05 mm) and red color marked the distances closest to the defined threshold (> 0.95 mm). From the scalar field in Figure 5.20 for both aligned DSMs, it can be seen that the upper left corner is fully red, as the C2C distance exceeds the threshold value in this DSM area since there were no reference points for the comparison.

From the obtained results it can be observed that both DPCs have a better performance on the inner edge of the frame, with higher concentration of blue and green colored C2C distances. The resulting histograms were not directly comparable, as they described different number of points. To be able to compare the performance of each DPC, the percentage of points falling within the upper range classes with C2C distances < 0.5 mm was calculated for both DSMs (Table 5.18), with number of points falling in a certain class was approximated from the histograms.

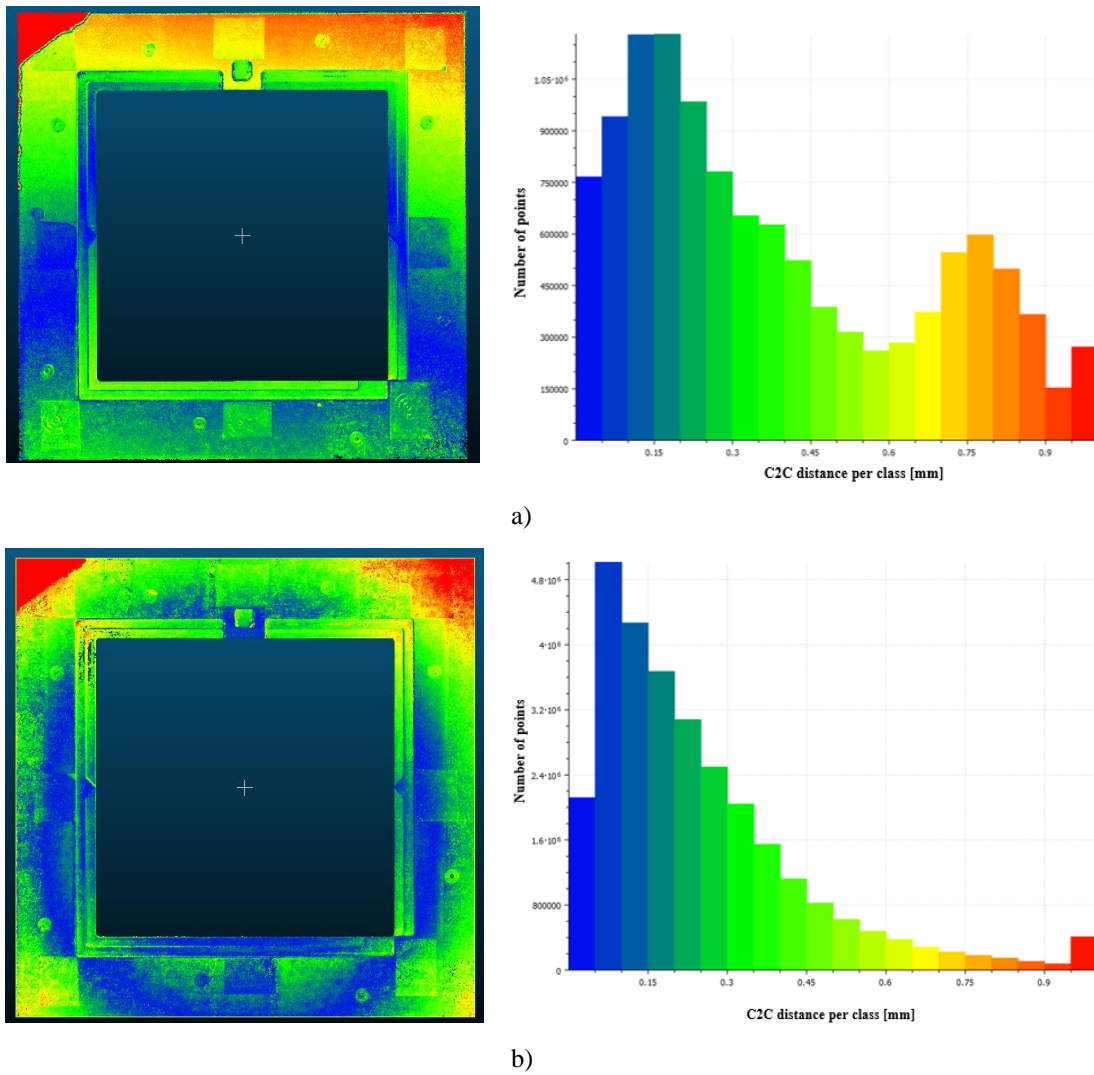


Figure 5.20. Color scale scalar field of C2C distances for DPC of the reference frame and corresponding histograms for Canon Mode (a) and Nikon Mode (b) DSM

Table 5.18. Calculated C2C distance ranges and percentage of DPC points falling within each distance range for C2C distance < 0.5 mm

C2C distance ranges [mm]	number of points		percentage of points [%]	
	Canon Mode	Nikon Mode	Canon Mode	Nikon Mode
0-0.05	760,000	2,100,000	6.50	7.22
0.05-0.1	930,000	5,000,000	7.95	17.18
0.1-0.15	1,250,000	4,250,000	10.68	14.60
0.15-0.2	1,250,000	3,600,000	10.68	12.37
0.2-0.25	975,000	2,800,000	8.33	9.62
0.25-0.3	770,000	2,500,000	6.58	8.59
0.3-0.35	650,000	2,100,000	5.56	7.22
0.35-0.4	625,000	1,550,000	5.34	5.33
0.4-0.45	525,000	1,100,000	4.49	3.78
0.45-0.5	375,000	600,000	3.21	2.06

A graphical representation of calculated percentages for each data acquisition mode is presented in Figure 5.21. It can be seen that Nikon Mode DPC obtained larger number of points within lower C2C distance ranges, indicating better coincidence with the reference DPC.

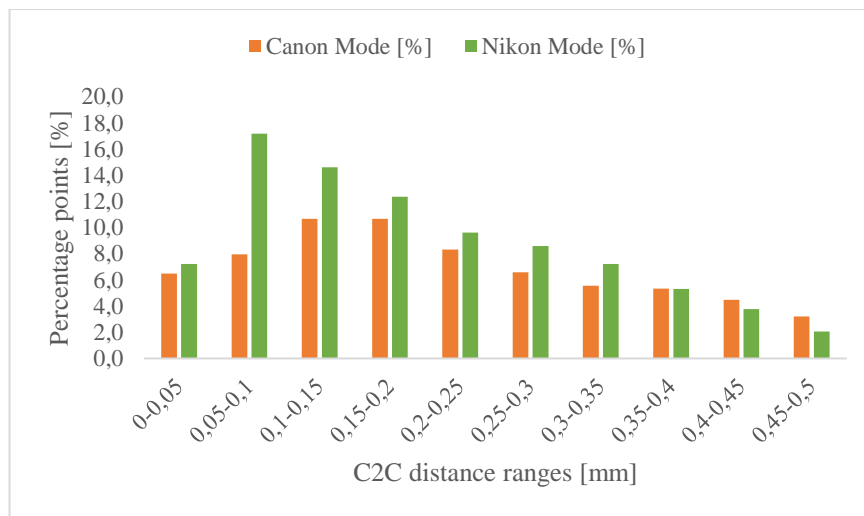


Figure 5.21. Percentage points (%) falling within C2C distance ranges < 0.5 mm for DPCs created by two different data acquisition setups

Aligned DPCs were compared with respect to the height distances between the reference DPC and the photogrammetry produced DPC on the same cross section positions as in Figure 5.17c, d. The measured values of point-to-point distance with respect to the reference DPC in selected positions are given in Table 5.19, indicating better coincidence between Nikon Mode DPC and reference DPC.

Table 5.19. Measured point-to-point distances on selected positions for both aligned DPCs and reference frame DSM

Position	Point-to-point distance for Reference DPC versus Canon DPC [mm]	Point-to-point distance for Reference DPC versus Nikon DPC [mm]
1	0.20	0.15
2	0.32	0.12
3	0.42	0.07
4	0.66	0.12
5	0.69	0.11

Additional performance evaluation was done by comparing the distances measured on the reference DPC and actual frame with those determined on the Nikon Mode DPC (Figure 5.22). The absolute difference between measured values on Nikon Mode DPC and actual frame were similar to the absolute differences obtained for the reference DPC, except for the outer frame edge

(dimension D), where the absolute difference was much larger than for the reference DPC (Table 5.20).

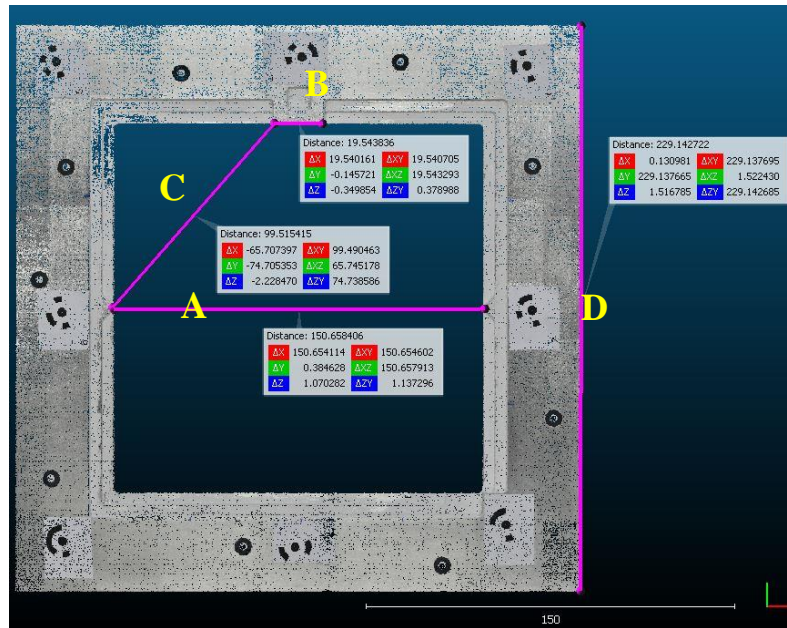


Figure 5.22. Distance measurements on Nikon Mode DPC

Table 5.20. Comparison of absolute differences between actual measurements on reference frame and distance measurements on DSMs created with different data acquisition methods (3D laser scanning and photogrammetry)

Dimension	Length on frame [mm]	Length on Nikon Mode DPC [mm]	Absolute difference for 3D scanner DPC [mm]	Absolute difference for Nikon Mode DPC [mm]
A	150.63	150.66	0.01	0.03
B	19.55	19.54	0.01	0.01
C	99.53	99.52	0.01	0.01
D	229.98	229.14	0.07	0.84

Height values were evaluated on Nikon Mode DPC and compared to the actual height values on the reference frame, defined by the thickness of the frame steps on upper and lower frame edge (Figure 5.23). The actual height values and measured values from the Nikon Mode DPC differ in sub-millimeter range values, with better model performance closer to the inner frame edge (Table 5.21).

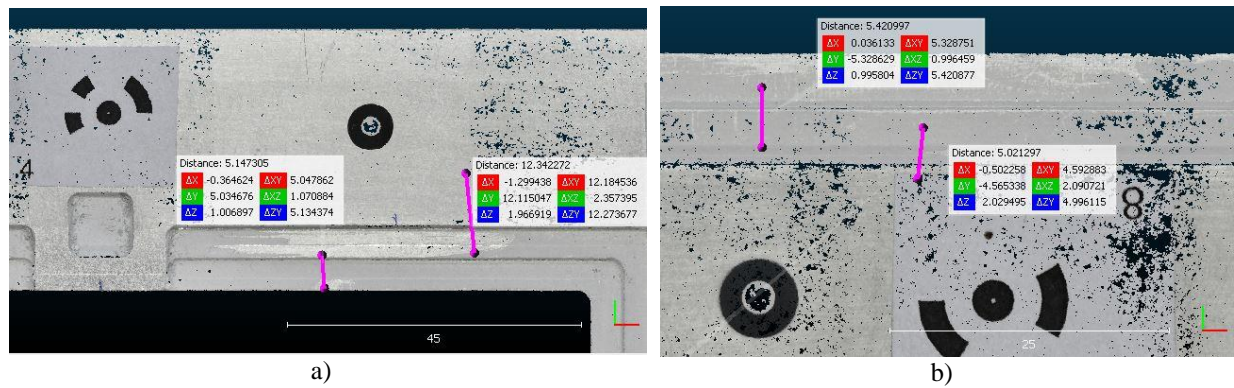


Figure 5.23. Measured heights (Δz coordinate) for upper (a) and lower (b) edge of reference frame DPC crated by Nikon Mode

Table 5.21. Comparison of frame thicknesses measured on actual frame and DPC frame created by Nikon Mode CROP method

Actual height on reference frame [mm]	Measured height on DPC of reference frame [mm]	Absolute height difference [mm]
1.00	1.01	0.01
2.00	1.97	0.03
1.00	0.995	0.005
2.00	2.03	0.03

5.4. Discussion

The proposed photogrammetry-based method for pavement texture data acquisition provides 3D digital surface representation from images captured at the same height orthogonally to the surface. Therefore, the method is named CROP – Close Range Orthogonal Photogrammetry. In comparison to the photogrammetry method where the images were captured under different angles, the CROP method showed better performance in terms of DSM reconstruction error metrics, despite the smaller amount of points forming the DPC object. The applicability of the method for pavement texture data analysis was shown by calculating several texture-related roughness parameters and comparing them to the measured friction performance of the same surface. The obtained correlation coefficient of 0.807 indicated a significant relationship between texture performance indicator MPD calculated from the DSM and friction expressed as SRT value. The results are in good agreement with previous research where texture-friction relationship was investigated by texture parameters derived from DSM obtained by photogrammetry methods (D. Chen, 2020; Huyan et al., 2020; Kogbara et al., 2018; Y. Wang et al., 2019). This motivated further analysis and optimization of CROP method.

To investigate the CROP method performance for different types of photographic equipment, four different camera lenses were used for image acquisition and creation of DSMs.

The resulting DSMs properties were analysed and compared by selected error metrics, digital model's properties and resulting texture features. Two methods were excluded as they resulted in a distorted geometry of captured surface, providing a concave-shaped profile. The acquisition mode using 50 mm lens showed the best performance in terms of resulting DSM properties, therefore it was selected for further analysis and data acquisition. The performed analyses also served for the selection of optimal section thickness and number of profiles segmented from the DPC surface representation. A comparison between two different section thicknesses for profile data segmentation showed that optimal profile representation by data points is obtained for defined section thickness of 0.01 mm. The calculation of selected profile-related roughness parameters showed that the number of profiles or profile spacing does not have a significant effect for the determination of a mean value of overall roughness parameter, calculated from the extracted profiles. The selected profile's spacing defined for further analyses was 10 mm between each profile segmented from a single surface.

To verify the proposed CROP method for accuracy, two data acquisition setups with same image acquisition procedure and different photographic equipment were tested. Their performance was compared to the benchmark method for 3D data acquisition and reconstruction, a high precision 3D laser scanner system. The benchmark method accuracy was evaluated by comparing the selected dimensions of a reference object to the measurements of DSM created from laser scanning procedure. The obtained differences in plane dimensions and height differences were on submillimeter range, with the highest difference value for the outer edge of the frame of 0.07 mm. Therefore, the created reference frame DSM was defined as suitable for the analysis of pavement texture morphology on whole macro-texture level and to some extent of the micro-texture level.

The comparison of two DSMs created by application of CROP method for data acquisition was performed by analysis of resulting DSM properties in terms of error measures RMS reprojection error and Mean Key Point size, number of points generated in the DPC and number of elements in the Mesh object resulting from the DSM creation. The analysis showed that the model produced by Nikon Mode CROP method obtained better properties, with lower values of error metrics and more detailed representation of the reference object in both DPC and Mesh entity, having higher number of DSM elements (faces and points). Both DPCs were subjected to a performance comparison with the DSM produced by benchmark method, whose accuracy was previously determined. The Nikon Mode showed better performance by having higher amount of points with

smaller C2C distances: Nikon Mode DPC obtained 87.97% points with C2C distance below 0.5 mm and Canon Mode DPC obtained 69.32% points with C2C distance below 0.5 mm.

Previous research utilizing photogrammetry methods where the accuracy of the proposed data acquisition method was verified is very sparse. J. Chen et al., 2019 validated the proposed close-range photogrammetry method by calculating selected texture parameters MTD and root mean square roughness (RMSR) on the DSM obtained by CRP on three pavement surfaces, where texture was evaluated by sand patch test and laser scanning device. The obtained error metrics and correlation analyses for texture parameters evaluated by different data acquisition methods showed good performance of the proposed CRP method with relative errors below 5% and $R^2 = 0.995$ for measured versus calculated MTD. Authors Tian et al., 2020 compared the performance of photogrammetry-based method for pavement texture analysis with a conventional laser texture scanner and showed that the MPD values calculated from the DSMs differ from the values obtained by traditional measurements by an average of 4%. To evaluate the accuracy of the proposed method, they calculated the RMS reprojection error for the created model, which was 1.550 pixels. In comparison to the obtained RMS reprojection error of 0.301 for the DSM created in this research by CROP method, this value is approximately five times higher. Medeiros et al., 2021 designed a calibration plate with different heights and evaluated the proposed photogrammetry-based method performance by comparing the CAD design measures with the dimensions measured on the DSM. The accuracy was reported as percent error between the CAD and DSM dimensions, equal to 4.2%. The method was additionally validated by calculating the texture surface roughness parameters on DSMs obtained from the photogrammetry method and laser scanning method, with calculated errors expressed as percent difference below 15%. The created calibration plate was not used in the texture data acquisition procedure, so it was not possible to perform the method validation simultaneously during the data collection.

The method verification procedure performed in this research was applied to an independent object with strictly defined dimensions in CAD design, which showed minor deviations from the dimensions measured on the actual object, all below 0.1 mm. The verification was not related to pavement-surface morphology or traditional texture performance evaluation methods. In this way the uncertainties stemming from the measurement procedure or complex surface morphology were avoided. The absolute difference values obtained for the comparison of actual dimensions and CROP DSM dimensions were all below 0.05 mm, except the outer edge of the reference frame where the difference was 0.84 mm. However, as the reference frame will be used for the pavement texture analysis on surface within the inner edge of the frame, this deviation was found to be irrelevant.

The design of the reference frame used for the verification of the CROP method enables the simultaneous texture data acquisition and accuracy evaluation. This means that the accuracy of the CROP method can be checked for every created DSM, consisting of both reference object and pavement surface. This reduces the potential risk of DSM accuracy reduction due to the image acquisition procedure deficiencies, caused by manual operating. The proposed and verified CROP method for data acquisition was further used to collect the texture data used for the development of friction prediction model, described in Chapter 6.

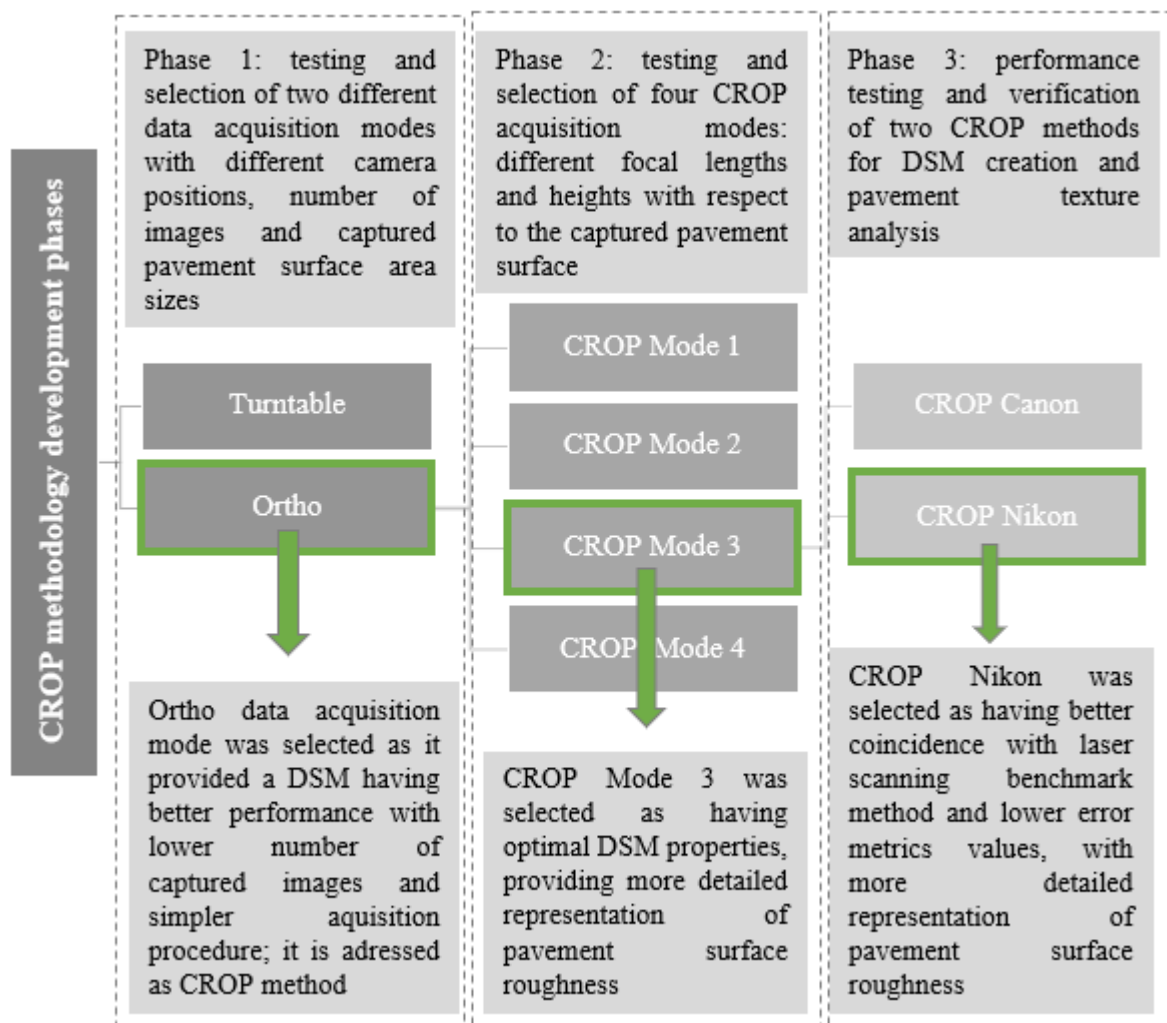


Figure 5.24 A schematic summary of procedures performed in the CROP methodology development and verification

6. Development of a friction performance prediction model

The main research aim of this thesis is the development of a reliable friction performance prediction model based on non-standard pavement texture parameters. In this Chapter, the methodology that was originally developed and verified in laboratory conditions was applied for texture data acquisition on road pavement surfaces. This Chapter provides the results of the CROP method application for field investigation of non-standard pavement texture parameters and development of a friction performance prediction model. The procedures for friction and texture data collection, texture data processing and analysis, prediction models' establishment, optimization and proposed models' validation are presented in a schematic summary in Figure 6.1.

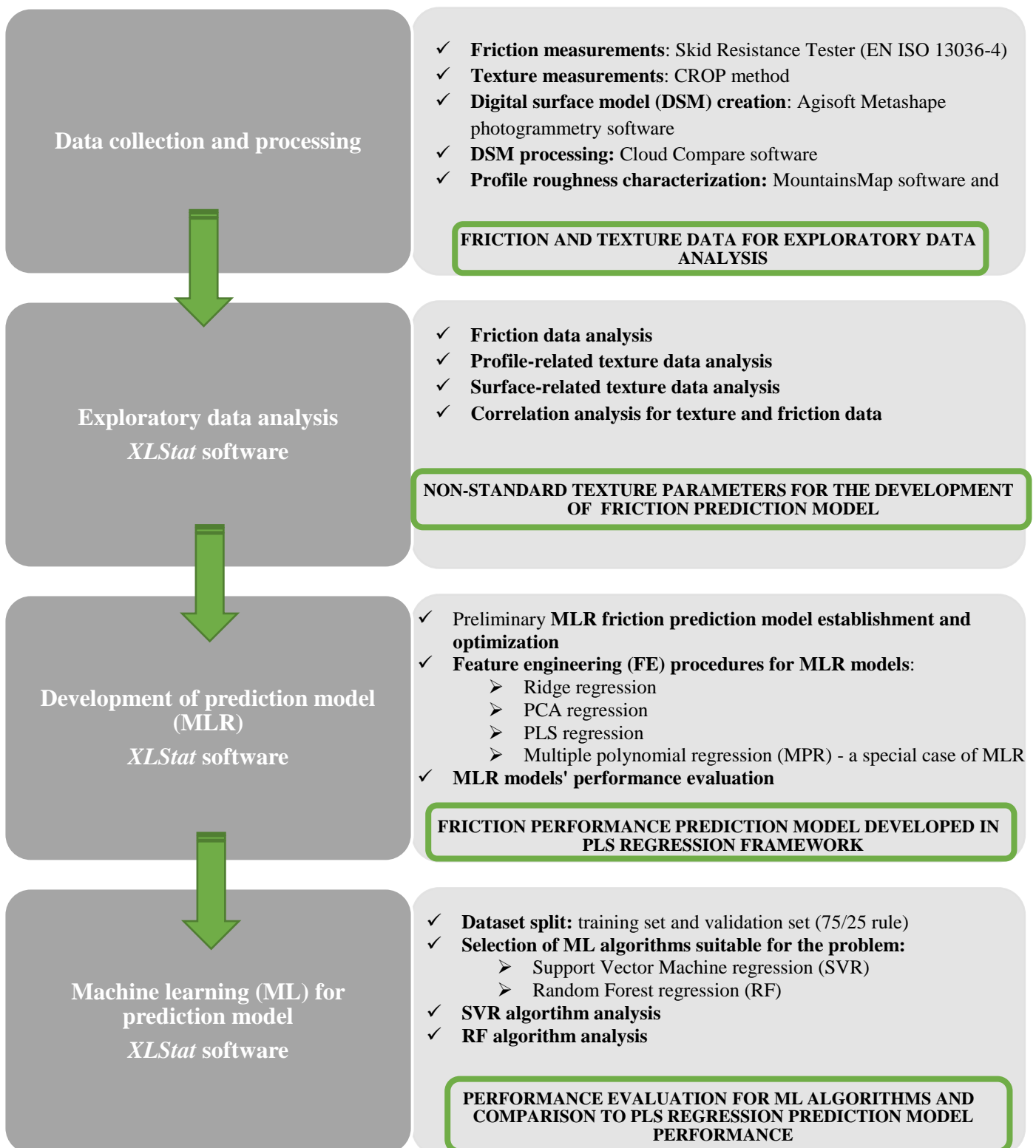


Figure 6.1 A schematic overview of performed procedures and used tools in the friction prediction model establishment

6.1. Application of CROP method - field investigation

An advanced method for pavement texture data collection and analysis – CROP method, was developed and verified in laboratory conditions on produced asphalt specimens which were not exposed to any external influencing factors affecting the friction performance. The established CROP method showed to be suitable for the analysis of full range of macro-texture and micro-texture up to 0.01 mm, corresponding to the achieved average horizontal resolution of profiles extracted from the DSM of analysed pavement surface. The accuracy of the verified CROP method was confirmed for the analysis of texture roughness features on submillimeter range, accounting for the whole macro-texture range and micro-texture range up to 0.05 mm. CROP method was further applied to field investigation of texture and friction relationship as described further in this Chapter.

Pavement friction and texture data was collected on twenty different asphalt pavement surfaces in use (Figure 6.2). Eleven surfaces were selected on secondary urban traffic network on roads located in City of Rijeka residential area (marked blue). The selected roads were either collector or interzonal, with following characteristics: design speed 30-50 km/h (lower speed is characteristic for interzonal road type), no intensive heavy vehicle traffic, high frequency of non-motorized traffic users, non-semaphorized intersections and presence of parking areas in the road profile. The other nine surfaces were selected on a low trafficked parking area in City of Rijeka University Campus (marked yellow), used as a service area for the delivery vehicles for the nearby Campus facilities.

The aim was to investigate the possibility of surface frictional performance prediction based only on the texture parameters derived from the digital surface models created by CROP method for texture data acquisition. The surfaces were selected without the prior knowledge of asphalt mixture properties, pavement age or traffic load. The environmental impacts were excluded by performing the measurements under similar weather conditions: moderate air temperatures between 15°C and 20°C and no precipitation. Friction and texture data collection was performed on the same day, with no time delay. First, the friction was measured on selected surfaces by a standard low-speed device. The procedure is described in the following section. Afterwards, the texture data was collected by established CROP method, as described in Chapter 5.

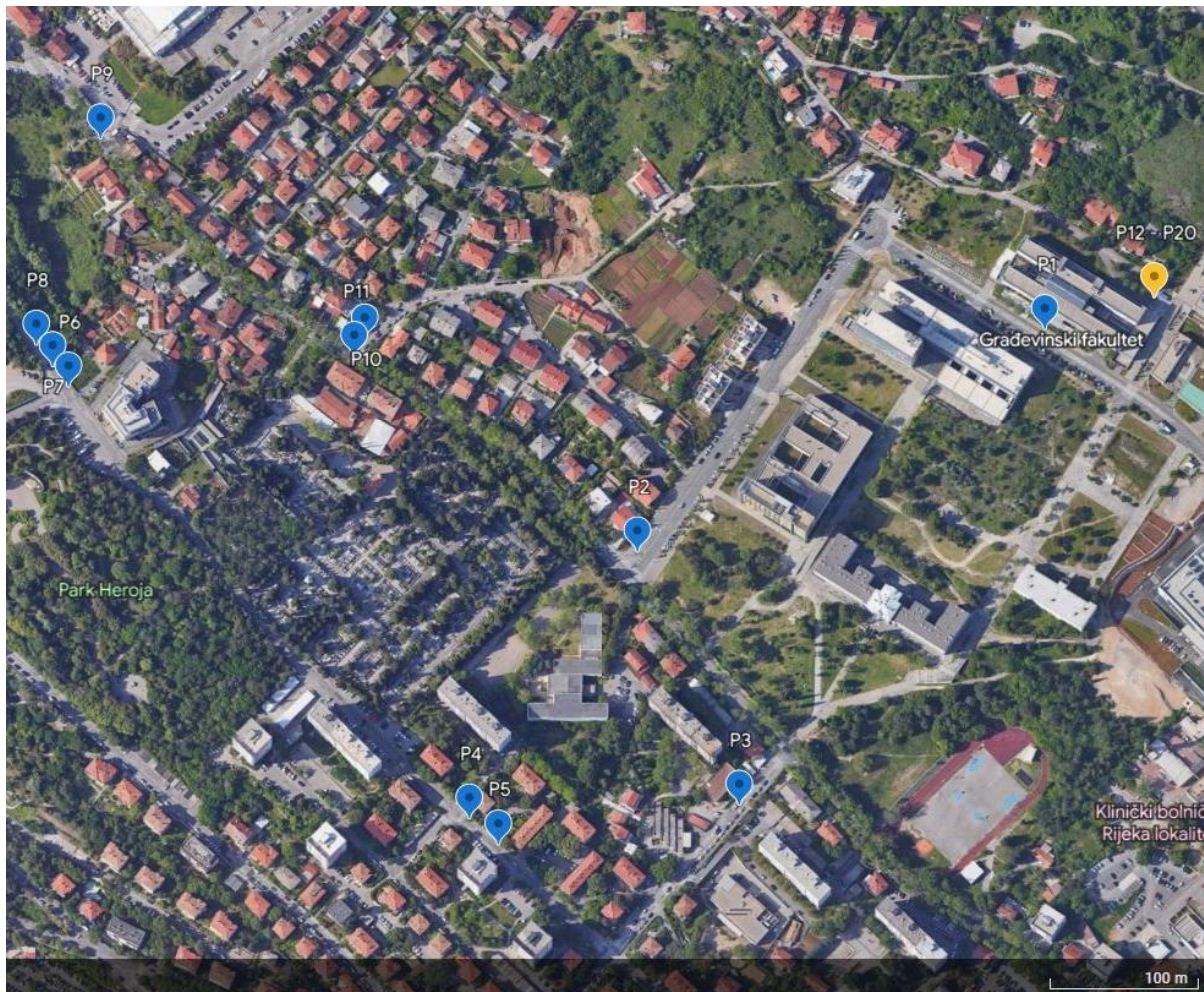


Figure 6.2 Map of sites where friction and texture data were collected. Blue marked sites are located on urban road network, yellow marked site is the position of parking area (Google Earth, 2023)

6.1.1. Friction data collection

Before the friction measurements, surfaces were visually examined to check for any large texture irregularities which could significantly affect the friction performance. They were cleaned with a brush so the loose particles, dust or other type of debris potentially present on the surface are removed and thus eliminated as an influencing parameter in frictional performance of the pavement surface. Friction measurements were performed without the presence of water. This was done to exclude the hydrodynamic effect of water film to the pavement frictional performance as one of influencing parameters and to investigate the prediction model performance in comparison to similar empirical models, where the water effect was not excluded.

Water effect is usually observed in numerical prediction models by including the viscous hydroplaning mechanisms in the friction numerical model (Kienle et al., 2020). In the existing empirical research of texture-friction relationship with texture features derived from the photogrammetry-based methods, the proposed friction prediction models established from the wet

friction measurements where the water effect was not excluded obtained no significant correlation between texture parameters and measured friction in general (Kogbara et al., 2018; Medeiros et al., 2021; Y. Wang et al., 2019). Research studies where the friction was evaluated without the water presence (D. Chen, 2020; Huyan et al., 2020) resulted in texture-friction prediction models with better performance in comparison to the ones including the effect of water.

The surface friction data was collected by a pendulum device SRT, following the procedure defined in EN ISO 13036-4: *Road and airfield surface characteristics – Test methods – Part 4: Method for measurement of slip/skid resistance of a surface: The pendulum test*. For each surface, five consecutive measurements were performed and the corresponding surface SRT value was calculated as the mean of all five measurements. The measured area was marked so the texture data can be collected on the same surface. The size of the measured surface was 125 mm x 75 mm, corresponding to the sliding length of the pendulum rubber and the rubber slider width (Figure 6.3). The area of the measured surfaces was approximately 100 cm². The results of friction measurements are given in Table 6.1.

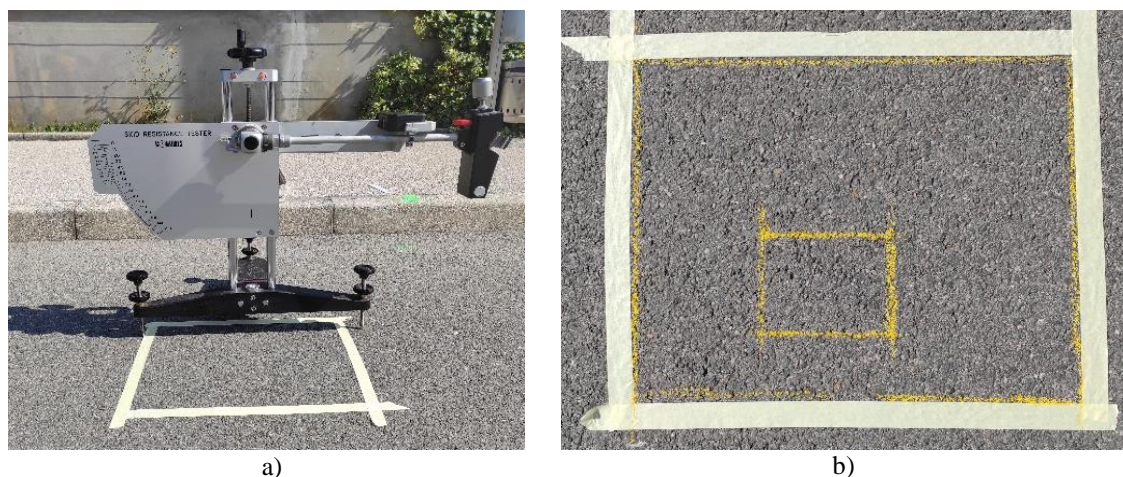


Figure 6.3 Friction measurement assembly with SRT pendulum (a) and close-up of an example of measured pavement surface (b), 2023

The measured SRT values range was from SRT = 68.4, determined for surface no. 3 located on straight road section to SRT = 103.2, determined for surface no. 17 located on parking area. All the measured values were higher than the threshold value of $SRT \geq 55$ defined by Croatian national regulation for the corresponding road category (*Tehnički propis za asfaltne kolnike*, 2021.). Such good frictional performance of measured surfaces could be due to the dry surface measurement conditions, as the SRT threshold value is defined for wet surface measurements. High friction performance on surfaces located on the parking was caused by a low rate of surface wear, since the area is not frequently utilized.

Table 6.1 Measured values of SRT on all investigated sites and mean calculated SRT values

Surface no.	Measured SRT [°]					SRT_mean [°]
	SRT1	SRT2	SRT3	SRT4	SRT5	
1	84	85	85	85	86	85
2	85	85	85	85	86	85.2
3	66	68	68	70	70	68.4
4	67	70	70	70	70	69.4
5	80	79	80	80	80	79.8
6	79	79	79	79	79	79
7	78	78	78	77	77	77.6
8	85	85	86	85	86	85.4
9	80	82	81	80	80	80.6
10	70	70	69	70	72	70.2
11	83	84	85	84	83	83.8
12	90	92	91	90	91	90.8
13	93	94	94	94	93	93.6
14	89	89	89	89	90	89.2
15	89	90	91	90	90	90
16	94	94	94	95	95	94.4
17	104	103	103	103	103	103.2
18	98	97	99	99	99	98.4
19	90	91	92	92	92	91.4
20	89	88	87	88	88	88

6.1.2. Texture data collection and determination of surface texture parameters

Texture data was collected and processed by applying the developed CROP methodology, elaborated in Chapter 5. The precision and accuracy of the digital surface model (DSM) were assured in the data collection procedure by using the created reference frame. The reference frame was positioned to cover the whole area of the marked surface previously measured by SRT. Each surface was captured by 25 consecutive and overlapping images, with two additional images of the upper and lower half of the reference frame for the improvement of the alignment procedure in the model creation process. An example of image acquisition setup is given in Figure 6.4.

The acquired surface images were imported to *Agisoft Metashape* software to generate the corresponding 3D DSMs by semi-automatic procedure, where the input settings for the alignment procedure and model build-up were adopted from the established CROP method optimization

procedure. The resulting DSMs were exported as 3D mesh objects and further processed in *Cloud Compare* software.



Figure 6.4 Texture data acquisition procedure by CROP methodology, 2023

Each DPC was sectioned by profiles, with profile-to-profile distance set to 10 mm and section length of 100 mm, so the standard profile-based texture parameters MPD and ETD could be determined from the profiles for the later comparison with the non-standard texture parameters. The thickness of the DPC section from which the profiles were generated was set to be 0.01 mm, corresponding to the optimal thickness obtained in the previous analyses. In this way, the resulting profiles contained 7000 points on average and the horizontal resolution requirement equal to or less than the defined model precision of 0.01 mm was satisfied. For each surface, nine profiles with the previously defined section settings were generated. A total of 180 profiles was sectioned from all analyzed surfaces.

Prior to the calculation of the profile-related texture parameters, the extracted profiles were pre-processed by relative coordinates correction of the profile points so that each profile starts with a point $(0, z_0)$ and ends with $(100, z_n)$ for n profile points, where 0 and 100 are x-coordinate values and z_0 and z_n are corresponding heights in the first and the last profile point. The profile slope was suppressed by leveling the profile heights to a mean height value z_{mean} . Afterwards, the corrected profiles were imported to *Mountains Map* software for profile data analysis. The profiles were

first filtered by a Gaussian S-filter with threshold value of $2.5 \mu\text{m}$ to remove noisy data irrelevant for texture properties analysis due to the DSM target accuracy of 0.01 mm . To remove any remaining profile slope resulting from the manual leveling procedure of the surfaces performed in *Cloud Compare* software, profiles were once again leveled to the horizontal plane.

The calculation of the texture parameters was performed on primary profiles, with respect to the EN ISO 21920-2 Standard. In this way, neither micro- or macro-texture data was excluded from the profile's performance analysis. The selected texture parameters are listed in Table 6.2. The parameters were evaluated with respect to the full profile length or the evaluation length l_e and the section lengths l_s , which are basically segments of full profile length divided by the characteristic profile heights $z(x)$. The division of evaluation length to section lengths is usually performed by profile peak heights, in a way that one section length contains two adjacent profile peaks and one pit. Some of the texture parameters were evaluated with respect to the profile elements, corresponding to the portions of profile between two consecutive points where profile height is equal to the mean profile height (if the mean height of the profile is zero, then the profile elements are defined as profile portions between two points with $z = 0$). They are described by their width in horizontal direction X_s and height in vertical direction Z_t . A graphical representation of profile characteristic geometric features relevant for the calculation of texture parameters is presented in Figure 6.5. Traditional texture characterization parameters related to the profile features, MPD and ETD, were calculated manually according to EN ISO 13473-1 standard in *Microsoft Excel* software.

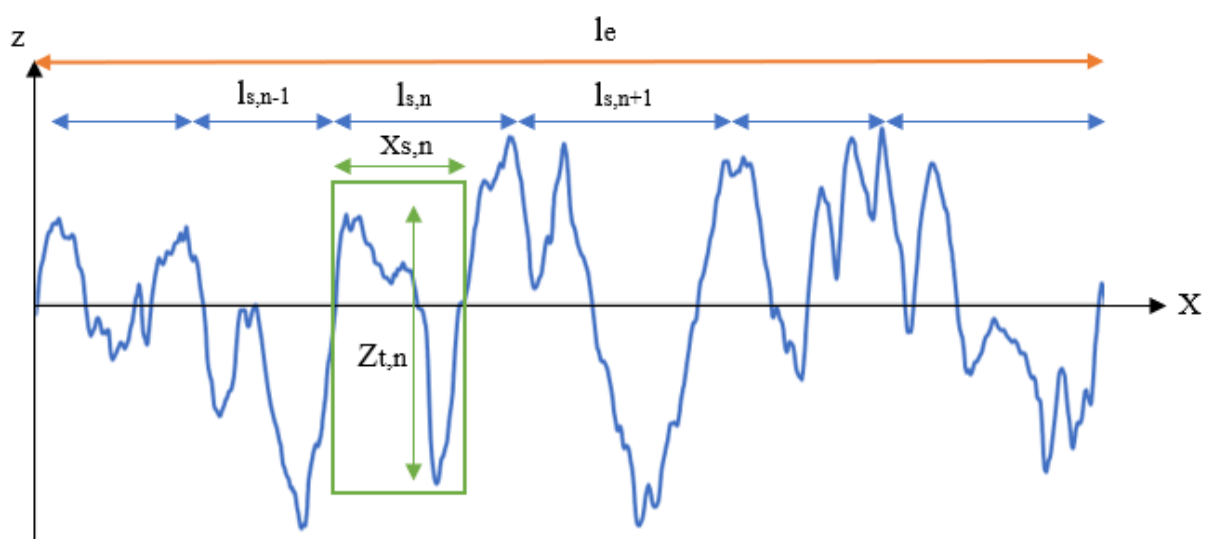


Figure 6.5 Characteristic profile geometry dimensions: l_e is profile evaluation length, l_s is n -th profile section length, X_s is profile element width and Z_t is profile element height

Table 6.2. Profile-related texture parameters calculated for the surface properties analysis

Profile texture parameter	Description	Calculation expression
P_a – arithmetic mean height [mm]	arithmetic mean of absolute ordinate values on the evaluation length l_e	$P_a = \frac{1}{l_e} \int_0^{l_e} z(x) dx$
P_q – root mean square height [mm]	Square root of the mean square of the ordinate values on the evaluation length l_e	$P_q = \sqrt{\frac{1}{l_e} \int_0^{l_e} z^2(x) dx}$
P_z – maximum height [mm]	Mean value of the per section sum of largest peak height and pit depth for all section lengths	$P_z = \frac{1}{n_{sc}} \sum_{n=1}^{n_{sc}} (\max(z_{ph,j}) + \max(z_{vd,k}))$ $j \in N_{p,i} = \{j = 1, 2, \dots, n_p (i - 1)l_{sc} \leq x_j \leq il_{sc}\}$ $k \in N_{v,i} = \{k = 1, 2, \dots, n_v (i - 1)l_{sc} \leq x_k \leq il_{sc}\}$
P_t – total height [mm]	Sum of the largest height and largest depth on the evaluation length l_e	$P_t = \max(z(x)) - \min(z(x))$ $x \in X, X = \{x \in R 0 \leq x \leq l_e\}$
P_{pt} – maximum peak height [mm]	Largest peak height of all section lengths l_s	$P_{pt} = \max(z_{ph,j}), j = 1, \dots, n_p$
P_{vt} – maximum pit depth [mm]	Largest pit depth of all section lengths l_s	$P_{vt} = \max(z_{vd,j}), j = 1, \dots, n_p$
P_{sk} - skewness	Quotient of the mean cube value of the ordinate values and P_q cube value	$P_{sk} = \frac{1}{P_q^3} \frac{1}{l_e} \int_0^{l_e} z^3(x) dx$
P_{ku} - kurtosis	Quotient of the mean quartic value of the ordinate values and fourth power P_q value	$P_{ku} = \frac{1}{P_q^4} \frac{1}{l_e} \int_0^{l_e} z^4(x) dx$
P_c – mean profile element height [mm]	Mean value of profile element heights Z_t for a total number of profile elements (n_{pe})	$P_c = \frac{1}{n_{pe}} \sum_{i=1}^{n_{pe}} Z_{t,i}$
P_{cx} – maximum profile element height [mm]	Maximum value of profile element heights Z_t for a total number of profile elements (n_{pe})	$P_{cx} = \max Z_{t,i} \quad i = 1, \dots, n_{pe}$
P_{sm} – mean profile element spacing [mm]	Mean value of profile elements spacing (X_s) for a total number of profile elements (n_{pe})	$P_{sm} = \frac{1}{n_{pe}} \sum_{i=1}^{n_{pe}} X_{s,i}$
P_{smx} – maximum profile element spacing [mm]	Maximum profile elements spacing on the evaluation length	$P_{smx} = \max X_{s,i} \quad i = 1, \dots, n_{pe}$
MPD – mean profile depth [mm]	Average value of profile depth over a specified baseline (profile evaluation length) divided into two equal lengths, for which peak heights are determined (z_1 and z_2)	$MPD = \frac{\max z_1 + \max z_2}{2} - z_{mean}$
ETD – estimated texture depth [mm]	Estimation of texture depth from the calculated mean profile depth (MPD)	$ETD = 0.2 \text{ mm} + 0.8 \text{ MPD}$

Besides the overall roughness parameters analysed in previous Chapter 5, some additional roughness parameters were selected for surface roughness description. Profile skewness P_{sk} and steepness (kurtosis) P_{ku} were selected as a measure of profile amplitudes distribution and profile flatness, respectively. They showed a strong negative correlation with the traditional texture indicator MPD in the analysis described in section 5.1. and they were selected to corroborate this relationship. Three new profile feature parameters were considered for the texture characterization: maximum height of profile elements P_{cx} and mean and maximum width of profile elements P_{sm} and P_{smx} .

The selected profile-related texture parameters were separated into two groups, following their physical meaning for the profile roughness characterization: overall roughness characteristic parameters and extreme roughness characteristic parameters. The first group contained the parameters calculated as mean values with respect to a certain profile feature – profile evaluation length, section length or profile element number. The second group consisted of profile-related parameters evaluated as a maximum or minimum value of the profile height or length feature. Therefore, profile-related parameters P_a , P_q , P_z , P_{sk} , P_{ku} , P_{sm} and P_c were characterized as overall roughness parameters and parameters P_t , P_{pt} , P_{vt} , P_{smx} and P_{cx} were characterized as extreme roughness parameters. The traditional texture descriptors MPD and ETD were also categorized as overall roughness parameters, as they are evaluated as mean value on profile evaluation length. The selected texture parameters were calculated for all the extracted profiles and they were further used as the input data in the EDA procedure.

6.2. Exploratory data analysis (EDA)

The exploratory data analysis (EDA) was performed on mean values of measured friction performance and profile-related roughness parameters obtained by *Microsoft Excel* and *Mountains Map* software. The EDA was performed in *XLStat* software for statistical data analysis.

6.2.1. Friction data analysis

The mean values of measured friction performance for all the investigated surfaces was tested for normality by Shapiro-Wilk test (Mohd Razali & Bee Wah, 2011). The obtained p-value of 0.793 indicated that the friction dataset follows a normal distribution, being significantly higher than the p-value significance of 0.05. The generated Q-Q normal probability plot and histogram of SRT values confirmed the normal distribution of the friction data (Figure 6.6).

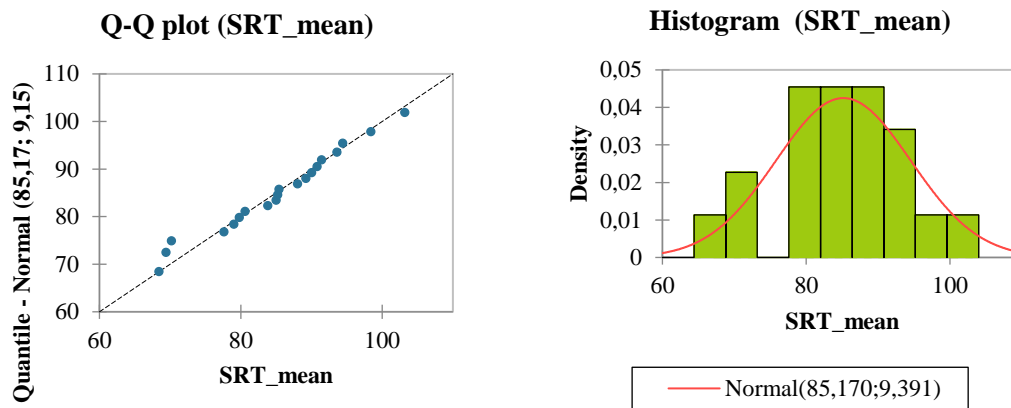


Figure 6.6 Q-Q normal probability plot (left) and histogram of SRT mean values (right) showing normal data distribution

6.2.2. Profile-related texture data analysis

The calculated profile-related texture parameters were first analyzed to investigate the relation between the non-standard texture parameters and texture performance descriptors used for the traditional evaluation of pavement surface friction performance. Afterwards, for each inspected surface corresponding profiles parameters were analyzed to define how to relate them to the surface texture performance. The analysis was oriented on the quantification of the parameters variability among the profile dataset describing a single surface, resulting in surface-related texture parameters used as input data in the process of friction prediction model development.

Profile-related data analysis was performed on the entire texture dataset, consisting of 180 profiles extracted from the created digital surface models. The aim was to determine the texture data distribution type and the relationship between the texture parameters in general. The conclusions resulting from the profile data analysis were used as a guidance in the process of friction prediction model definition.

The calculated profile-related texture parameters were analyzed by normality test to investigate the data distribution type. The performed Shapiro-Wilk test results showed that none of the parameters is distributed normally, therefore additional distribution testing was performed. The results are given in Table 6.3, where for each parameter the best fit data distribution is provided together with the obtained p-value indicating the significance and resulting histogram.

Table 6.3. Profile-related texture parameters distribution fitting. None of the parameters follows the normal distribution, most parameters are skewed to the left

Texture parameter	Shapiro-Wilk p-value	Distribution fitting	p-value	Histogram
Pa	<0.0001	Arcsine	1.000	
Pq	<0.0001	Log-normal	0.385	
Pz	<0.0001	Fisher-Tippett (2)	0.866	
Pt	<0.0001	Log-normal	0.500	
Ppt	<0.0001	GEV	0.361	

Pvt	<0.0001	Log-normal	0.486	
Psk	<0.0001	Beta4	0.173	
Pku	<0.0001	Log-normal	0.007	
Pc	<0.0001	Log-normal	0.928	
Pcx	<0.0001	Log-normal	0.674	

Psm	<0.0001	Fisher-Tippett (2)	0.570	<p>Histogram (Psm) Density vs Psm. The x-axis ranges from 0 to 30, and the y-axis (Density) ranges from 0 to 0.15. The distribution is unimodal and slightly right-skewed, peaking around Psm = 10.</p>
Psmx	<0.0001	Chi-square	0.578	<p>Histogram (Psmx) Density vs Psmx. The x-axis ranges from 0 to 50, and the y-axis (Density) ranges from 0 to 0.08. The distribution is unimodal and right-skewed, peaking around Psmx = 10.</p>
MPD	<0.0001	Log-normal	0.253	<p>Histogram (MPD) Density vs MPD. The x-axis ranges from 0 to 2, and the y-axis (Density) ranges from 0 to 2. The distribution is unimodal and right-skewed, peaking around MPD = 0.7.</p>
ETD	<0.0001	GEV	0.109	<p>Histogram (ETD) Density vs ETD. The x-axis ranges from 0 to 2, and the y-axis (Density) ranges from 0 to 3. The distribution is unimodal and right-skewed, peaking around ETD = 0.7.</p>

The correlation test was performed to analyze the relation between the selected texture parameters. As the parameters showed to be non-normally distributed and therefore the condition for the Pearson's correlation test wasn't satisfied, a non-parametric Kendall's correlation test was performed (Akoglu, 2018). This test measures the strength of the monotonic relationship between the two variables, which is not necessarily linear. The test result can be evaluated the same way as the Pearson's correlation – the strength of the relation increases if the correlation coefficient is closer to +/-1, where positive sign indicates a positive relationship and negative sign shows a negative trend between the two confronted variables. No specific interpretation of Kendall's correlation coefficient strength was found in the literature for the analysis of the experimentally obtained data. In a review paper by Akoglu, 2018, a comparison of different correlation

coefficients strength was given where it can be seen that the interpretation of the obtained values varies for different disciplines (psychology, medicine and politics). Kendall's correlation test results could be compared to the Spearman's test results as both are non-parametric tests observing non-normal data. Authors Fredricks & Nelsen, 2007 investigated the relationship between these two statistics and found that the ratio between Pearson's and Kendall's correlation coefficients is approximately 3/2, meaning that the correlation strength observed by Kendall's test is stronger for lower obtained values of correlation coefficient. By considering the values provided by Akoglu, 2018 and conclusions of the research by Fredricks and Nielsen, 2007, the threshold value for Kendall's correlation coefficient adopted in this analysis was set to be 0.4 for an indication of a moderate relationship between the observed parameters. The values of correlation coefficient above 0.6 were defined to be indicative of a strong relationship between the variables. The correlation analysis results are presented as matrices of Kendall's correlation coefficients and p-values, given in Table 6.4.

The obtained results showed that all texture parameters correlate significantly, with exception of parameters P_{sk} , P_{ku} , P_{sm} and P_{smx} . Profile skewness and kurtosis parameters P_{sk} and P_{ku} obtained weak and negative correlation coefficients with all the other parameters. The P_{sm} and P_{smx} parameters describing profile characteristics in horizontal direction showed a weak connection to other parameters, with positive correlation coefficients below 0.3. The perfect correlation obtained for MPD and ETD parameters was expected as they are linearly related by an equation defined in EN ISO 13473-1. Therefore, ETD was excluded from the further analysis as it showed equal correlation coefficient values as the MPD parameter for all the non-standard parameters.

By comparing the correlation coefficients obtained for non-standard texture parameters versus traditional parameter MPD, it can be observed that the P_{pt} parameter representing the peak profile height obtained the best correlation with coefficient of 0.879 to MPD and P_{vt} parameter related to the peak valley depth had the weakest correlation to MPD with coefficient of 0.518. Other non-standard parameters obtained a correlation coefficient with the MPD higher than 0.6.

Table 6.4. Kendall's correlation coefficient matrix for profile-related texture parameters. Values in bold are statistically significant with p-value below $\alpha = 0.05$

	P_q	P_{sk}	P_{ku}	P_t	P_{pt}	P_{vt}	P_z	P_a	P_{sm}	P_{smx}	P_c	P_{cx}	MPD
P_q	1												
P_{sk}	-0.202	1											
P_{ku}	-0.198	-0.416	1										
P_t	0.827	-0.269	-0.055	1									
P_{pt}	0.674	0.043	-0.308	0.655	1								
P_{vt}	0.726	-0.403	0.047	0.837	0.495	1							
P_z	0.835	-0.174	-0.194	0.792	0.679	0.692	1						
P_a	0.932	-0.158	-0.261	0.769	0.684	0.673	0.818	1					
P_{sm}	0.247	-0.198	0.098	0.268	0.176	0.292	0.168	0.225	1				
P_{smx}	0.190	-0.118	0.001	0.212	0.168	0.220	0.105	0.179	0.486	1			
P_c	0.834	-0.226	-0.152	0.802	0.634	0.735	0.817	0.808	0.300	0.186	1		
P_{cx}	0.792	-0.271	-0.057	0.840	0.604	0.789	0.753	0.742	0.259	0.227	0.787	1	
MPD	0.713	0.031	-0.319	0.670	0.879	0.518	0.722	0.728	0.173	0.135	0.673	0.620	1
ETD	0.713	0.031	-0.319	0.670	0.879	0.518	0.722	0.728	0.173	0.135	0.673	0.620	1

6.2.3. Surface – related texture parameters

To relate the profile-related texture parameters to the measured surface friction performance, they had to be converted to surface-related parameters. The initial idea was to average the overall roughness profile-related parameters values and adopt the mean parameters values as surface-related parameters. However, this procedure could be performed only if the surfaces were homogenous. The established criterion for the homogeneity classification of the surface was defined through the threshold value of a selected variability measure applied to the overall roughness profile parameter P_a in the following way. If all the profiles extracted from a single surface satisfied the defined variability measure threshold value for the surface-related parameter P_a , then the surface was classified as homogenous and the calculated mean values of the other overall roughness parameters P_q , P_z and P_c could be adopted as surface-related. The same rule was applied for the calculation of surface-related MPD and ETD texture indicators. The extreme roughness parameters P_t , P_{pt} , P_{vt} and P_{cx} were attributed to the corresponding surfaces as the extreme values from all the profiles belonging to the same surface, since the averaging could reduce the influence that extreme roughness parameters might have to the friction performance.

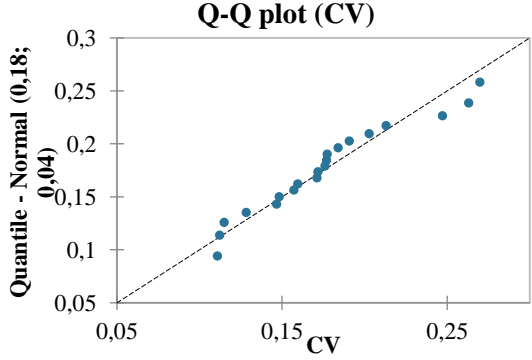
The analyzed variability measure applied to P_a parameter values was the coefficient of variation (CV), also known as relative standard deviation - a unitless relative measure of variability,

indicating the ratio between the standard deviation σ and the mean value μ of a dataset (Botta-Dukát, 2023),

$$CV = \frac{\sigma}{\mu}$$

CV enables the comparison of the variability between multiple datasets, therefore it was selected as the most appropriate variability measure for the analysis of the homogeneity of the texture parameters. Since there exists no universal pre-defined threshold value for the CV, it was determined by analyzing the values obtained for the inspected surfaces (Jalilibal et al., 2021). The calculated CVs were tested for normal distribution by Shapiro-Wilk normality test. The obtained p-value of 0.212 was higher than the significance $\alpha = 0.05$, thus confirming the normality of the CV dataset. A Q-Q normal probability plot for CV and descriptive statistics results are shown in Table 6.5.

Table 6.5. CV (%) statistics for mean values of overall roughness parameter P_a determined for all observed surfaces

Statistic	CV [%]	CV Q-Q normal probability plot
Minimum	11%	
Maximum	27%	
Range	16%	
1st Quartile	15%	
Median	17%	
3rd Quartile	19%	
Mean	17.6%	
Standard deviation	4.5%	

The 3rd quartile value of the CV was estimated to 19% and it was set to be the threshold value for dataset homogeneity characterization. This means that if the variability between the calculated P_a values for each profile extracted from the same surface was equal to or less than 19%, the surface homogeneity condition was satisfied. Otherwise, the surface would be categorized as non-homogenous and additional analysis would be required. Table 6.6 provides an overview of calculated mean values and coefficient of variation for profile parameter P_a for all analyzed surfaces. Five surfaces obtained CV higher than the established threshold value: surfaces P4, P6, P7, P15 and P20. These surfaces were further analyzed to investigate if there is a potential profile outlier in the dataset, and more importantly, could this outlier be excluded to obtain more homogenous profiles for the surface representation.

Table 6.6. Calculated P_a parameter mean values for all surfaces, corresponding CV (%) and surface classification according to the CV value

Surface	P_a , mean [mm]	CV [%]	Surface type
P1	0.194	18%	Homogenous
P2	0.320	16%	Homogenous
P3	0.133	16%	Homogenous
P4	0.351	21%	Non-homogenous
P5	0.256	15%	Homogenous
P6	0.350	26%	Non-homogenous
P7	0.233	25%	Non-homogenous
P8	0.203	17%	Homogenous
P9	0.294	17%	Homogenous
P10	0.100	18%	Homogenous
P11	0.271	12%	Homogenous
P12	0.702	19%	Homogenous
P13	0.298	11%	Homogenous
P14	0.272	18%	Homogenous
P15	0.448	27%	Non-homogenous
P16	0.686	15%	Homogenous
P17	0.772	11%	Homogenous
P18	0.447	13%	Homogenous
P19	0.229	18%	Homogenous
P20	0.307	20%	Non-homogenous

Before the outlier tests were performed, the data distribution was inspected on the surfaces categorized as non-homogenous. The performed Shapiro-Wilk normality test showed that the P_a parameter is distributed normally when observed for a single surface with p-values higher than the significance $\alpha = 0.05$ for all the inspected surfaces, therefore an outlier test applicable for normal data distribution could be exploited. For this purpose, a Z-score test was used as a measure of a single observation divergence from the mean value of the dataset from which it was extracted (Aggarwal et al., 2015). The test statistic is calculated by subtracting the actual data point value x from the sample X by the mean value of the dataset μ_X and dividing the result with the standard deviation of the dataset σ_X ,

$$Z = \frac{X - \mu_X}{\sigma_X}$$

The threshold value for Z-score is determined by the interval where 95% of the observed values in a sample fall into and the rest 5% values are higher or lower than this interval. For normally distributed data, the 95% interval is defined with approximately 2 standard deviations from the mean, so the threshold value range for the Z-score can be calculated as

$$Z_{critical,x} = \mu_x \pm 2 \times \sigma_x$$

If the result was higher than the critical value of Z-score, it was considered to be an outlier. The results of Z-score test performed for all five non-homogenous surfaces showed that only surface P6 was found to have an outlier profile (Table 6.7). However, as the obtained CV for the P6 surface was not the highest in the dataset and there were two other surfaces with similar CV values (P7 and P15), an additional custom outlier test was performed on the selected surfaces.

Table 6.7. Z-score outlier test results for non-homogenous surfaces

Surface	Z-score test results	Surface	Z-score test results
P4		P6	
P20			

For each non-homogenous surface, the minimum, maximum and mean P_a parameter values were calculated from the corresponding profiles. Afterwards, absolute differences between the mean value and minimum and maximum values were calculated and assigned to be an outlier detection method, where the profile having higher absolute difference was selected as a potential outlier. By calculating the absolute difference value for all non-homogenous surfaces, four of them obtained highest absolute difference for maximum profile parameter value and one surface obtained it for the minimum profile parameter value.

The potential outlier profiles values of extreme roughness texture parameters were compared to the maximum values of these parameters obtained for the corresponding surfaces. If the potential outlier profile did not contain a maximum value of any of the extreme roughness parameters P_t , P_{pt} , P_{vt} and/or P_{cx} with respect to the maximum surface values, it was excluded as an outlier profile. On the contrary, if the observed profile was characterized by an extreme value, additional analysis was performed. This was done because excluding a profile with extreme roughness parameter could have an impact on the prediction model for friction performance if this parameter would be a part of the model. The selection criterion was based on the difference between the extreme roughness parameter value of the observed profile and the next highest parameter value in the surface dataset. The threshold value for the absolute difference was set to be 0.1 mm. If the absolute difference between the two peak roughness parameters was below 0.1 mm, this would confirm that the profile can be excluded as an outlier as it would not significantly affect the prediction of friction performance due to a very similar peak parameter value in the remaining dataset. If the difference was higher, this profile would not be excluded from the surface dataset. The surfaces P4 and P15 contained profiles that were finally excluded as the outliers since they did not contain any extreme value of the peak roughness parameters. The other three surfaces P6, P7 and P20 were additionally analyzed and classified since the selected outlier profile contained extreme values of observed parameters. The results of the performed outlier analysis are presented in Table 6.8.

The additional outlier analysis showed that surfaces P7 and P20 do have an outlier profile with a significantly higher value of peak roughness parameter in comparison to the next highest parameter value obtained for another profile (Table 6.9). Therefore, they were not excluded and the surfaces were categorized as non-homogenous. For the surfaces whose profiles were excluded as the outliers from the dataset (P4, P6 and P15), the mean values of overall roughness parameters were re-calculated as the representation of a homogenous surface roughness feature. Surface P6 obtained satisfactory value of CV after the threshold profile was excluded, while surfaces P4 and

P15 still scored CV higher than the established threshold value. Therefore, they were also categorized as a non-homogeneous surface.

Table 6.8 Outlier profiles analysis by extreme roughness texture parameters

Surface	P4	P6	P7	P15	P20
$P_{a, \text{Min}}$	0.237	0.224	0.142	0.305	0.189
$P_{a, \text{Max}}$	0.472	0.553	0.338	0.657	0.389
$P_{a, \text{Mean}}$	0.351	0.350	0.233	0.448	0.307
abs difference	0.121	0.203	0.106	0.208	0.118
Potential outlier profile	p8	p9	p8	p1	p4
$P_{t, \text{profile}}$	2.655	3.548	2.108	3.079	1.341
$P_{pt, \text{profile}}$	0.865	0.905	0.654	1.335	0.611
$P_{vt, \text{profile}}$	1.790	2.643	1.454	1.744	0.729
$P_{cx, \text{profile}}$	2.655	3.548	2.108	2.694	1.163
$P_{t \text{ max, surface}}$	3.413	3.548	2.122	3.768	2.353
$P_{pt \text{ max, surface}}$	0.900	0.905	0.728	1.342	1.026
$P_{vt \text{ max, surface}}$	2.662	2.868	1.454	2.427	1.471
$P_{cx \text{ max, surface}}$	3.204	3.548	2.108	3.510	2.103
outlier	yes	no- additional analysis	no- additional analysis	yes	no- additional analysis

Table 6.9. Results of additional outlier analysis performed for non-homogenous surfaces

Surface	Category	P_t [mm]	P_{pt} [mm]	P_{vt} [mm]	P_{cx} [mm]
P6	outlier profile extreme roughness parameter value	3.548	0.905	2.643	3.548
	absolute difference with the next highest parameter value	0.060	0.040	-	0.070
P7	outlier profile extreme roughness parameter value	2.108	0.654	1.454	2.108
	absolute difference with the next highest parameter value	-	-	0.030	0.120
P20	outlier profile extreme roughness parameter value	1.341	0.611	0.729	1.163
	absolute difference with the next highest parameter value	0.140	0.030	-	-

The descriptive statistics results for the remaining overall roughness parameters P_{sk} and P_{ku} and P_{sm} calculated for the surfaces showed a high variability of values in comparison to the other overall roughness parameters. The values range was significantly wider than for the other determined parameters, especially for the P_{sm} and P_{ku} parameters (Figure 6.7). It was concluded

that in general, the mean values of the profile-related parameters P_{sk} , P_{ku} and P_{sm} could not be a genuine representation of the surface features. Therefore, they were excluded from the further analysis and the procedure of the friction prediction model establishment. Similarly, a comparison of mean range of values for the extreme roughness parameters pointed out that P_{smx} has a significantly wider range of values within a surface than the other extreme roughness parameters, therefore it would be difficult to determine the representative value for a surface.

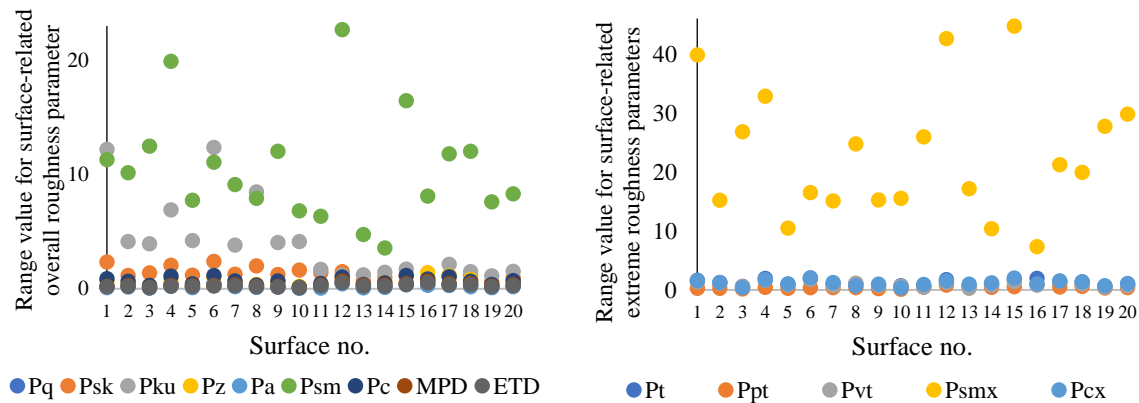


Figure 6.7 Range values for surface-related overall roughness parameters (left) and extreme roughness parameters (right).

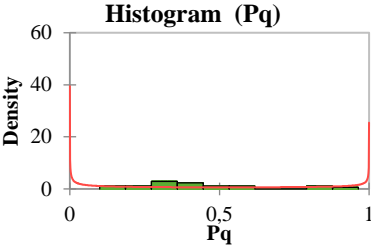
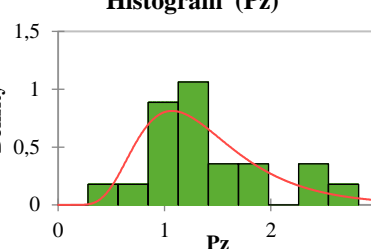
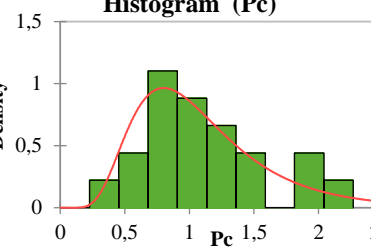
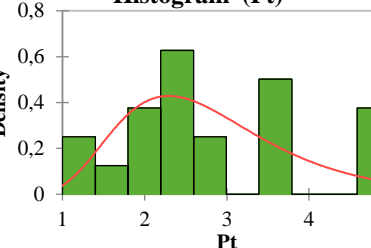
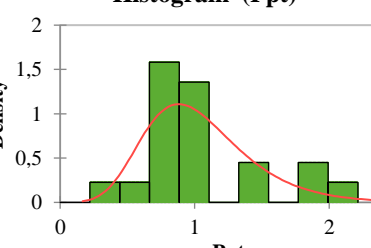
The final surface-related parameters dataset included the mean values of the overall roughness parameters P_a , P_q , P_z and P_c and the maximum values of extreme roughness parameters P_t , P_{pt} , P_{vt} and P_{cx} calculated from the profiles extracted from the corresponding surfaces (Table 6.10). The standard texture descriptor MPD was also included in the surface dataset. The final surface texture parameters dataset was tested for distribution type (Table 6.11). Similar to the profile-related data distribution analysis, the obtained results showed that the surface-related parameters were also non-normally distributed. In comparison to the distribution type defined for profile-related parameters, it can be seen that not all of the parameters exhibit the same distribution type for their surface equivalents.

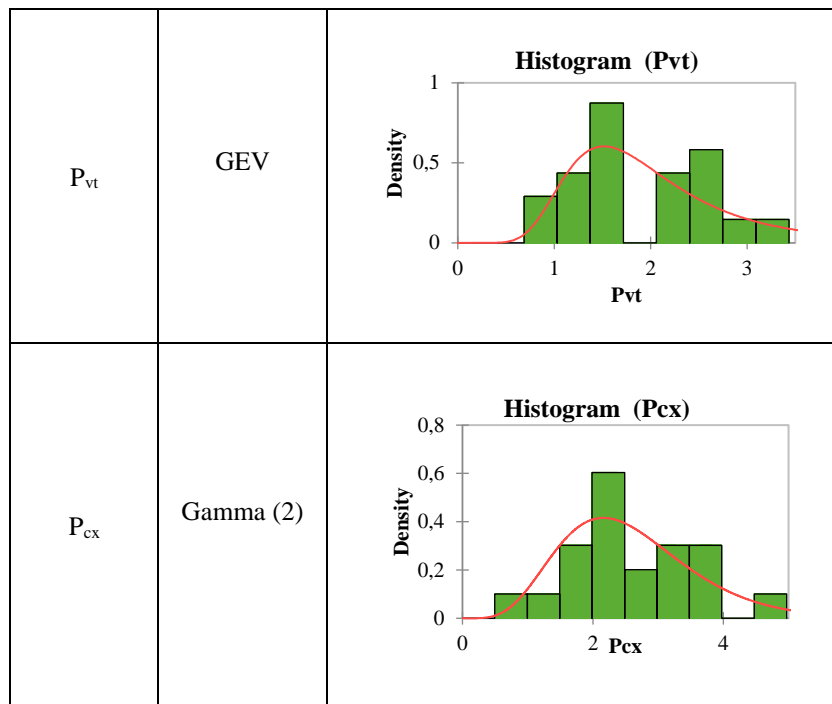
Table 6.10. Surface-related texture parameters: final dataset

Surface	SRT _{mean}	Pa	Pq	Pz	Pc	Pt	Ppt	Pvt	Pcx	MPD
P1	85.0	0.194	0.269	1.044	0.843	2.950	0.805	2.145	2.572	0.564
P2	85.2	0.320	0.424	1.454	1.149	2.896	0.871	2.181	2.684	0.709
P3	68.4	0.133	0.171	0.665	0.466	1.324	0.472	0.928	1.102	0.354
P4	69.4	0.336	0.461	1.347	1.248	3.413	0.900	2.662	3.204	0.596
P5	79.8	0.256	0.325	1.103	0.852	2.392	0.820	1.710	2.118	0.606
P6	79.0	0.325	0.449	1.542	1.268	3.485	0.864	2.868	3.478	0.560
P7	77.6	0.233	0.298	0.942	0.748	2.122	0.729	1.454	2.108	0.539
P8	85.4	0.203	0.262	0.861	0.644	2.150	0.879	1.654	1.564	0.546
P9	80.6	0.294	0.374	1.195	0.952	2.342	0.923	1.623	2.258	0.7395
P10	70.2	0.100	0.132	0.448	0.317	1.225	0.413	0.845	0.828	0.314
P11	83.8	0.271	0.352	1.158	0.903	2.099	1.012	1.307	1.896	0.696
P12	90.8	0.702	0.843	2.263	1.979	4.607	1.962	2.708	3.927	1.390
P13	93.6	0.298	0.366	1.302	0.924	2.200	1.089	1.125	2.200	0.743
P14	89.2	0.272	0.343	1.282	0.916	2.421	1.064	1.532	2.343	0.709
P15	90.0	0.448	0.559	1.755	1.469	3.768	1.342	2.427	3.510	0.948
P16	94.4	0.686	0.824	2.498	2.008	4.886	2.113	2.446	3.889	1.412
P17	103.2	0.772	0.954	2.724	2.169	4.871	1.885	3.334	4.871	1.480
P18	98.4	0.447	0.556	1.806	1.407	3.425	1.503	2.202	3.150	1.012
P19	91.4	0.229	0.293	1.001	0.729	1.795	0.827	1.064	1.686	0.606
P20	88.0	0.307	0.386	1.398	1.002	2.353	1.026	1.471	2.103	0.704

Table 6.11. Surface-related parameters distribution for the final surface texture dataset

Surface-related texture parameter	Distribution type	Histogram
Pa	Arcsine	

P_q	Arcsine	
P_z	Log-normal	
P_c	Log-normal	
P_t	Log-normal	
P_{pt}	GEV	



6.2.4. Correlation analysis

To investigate the correlation between the surface-related texture parameters and measured friction performance expressed in SRT values, scatter plots were generated for each pair of texture parameters and friction measurement (Figure 6.8). The ETD parameter was not observed as it showed a perfect linear relationship with the MPD, as was previously concluded. The scatterplots showed that there exists a monotonic and positive relationship between the measured friction performance and observed texture parameters. However, none of the scatterplots was indicative of a significant linear relationship between the observed variables. The range of obtained coefficients of determination for non-standard parameters related to SRT friction values was from $R^2 = 0.146$ for parameter P_{vt} to $R^2 = 0.587$ for P_{pt} parameter.

Since the texture parameters showed to be non-normally distributed and there was no indication of a significant linear relationship, Kendall's correlation test was applied as a measure of the strength of the monotonic and non-linear relationship between the texture parameters and friction performance. The resulting Kendall's correlation coefficients matrix is given in Table 6.12. All the parameters showed statistical significance for the texture-friction correlation with p-values below 0.05 (marked bold), except the P_{vt} parameter.

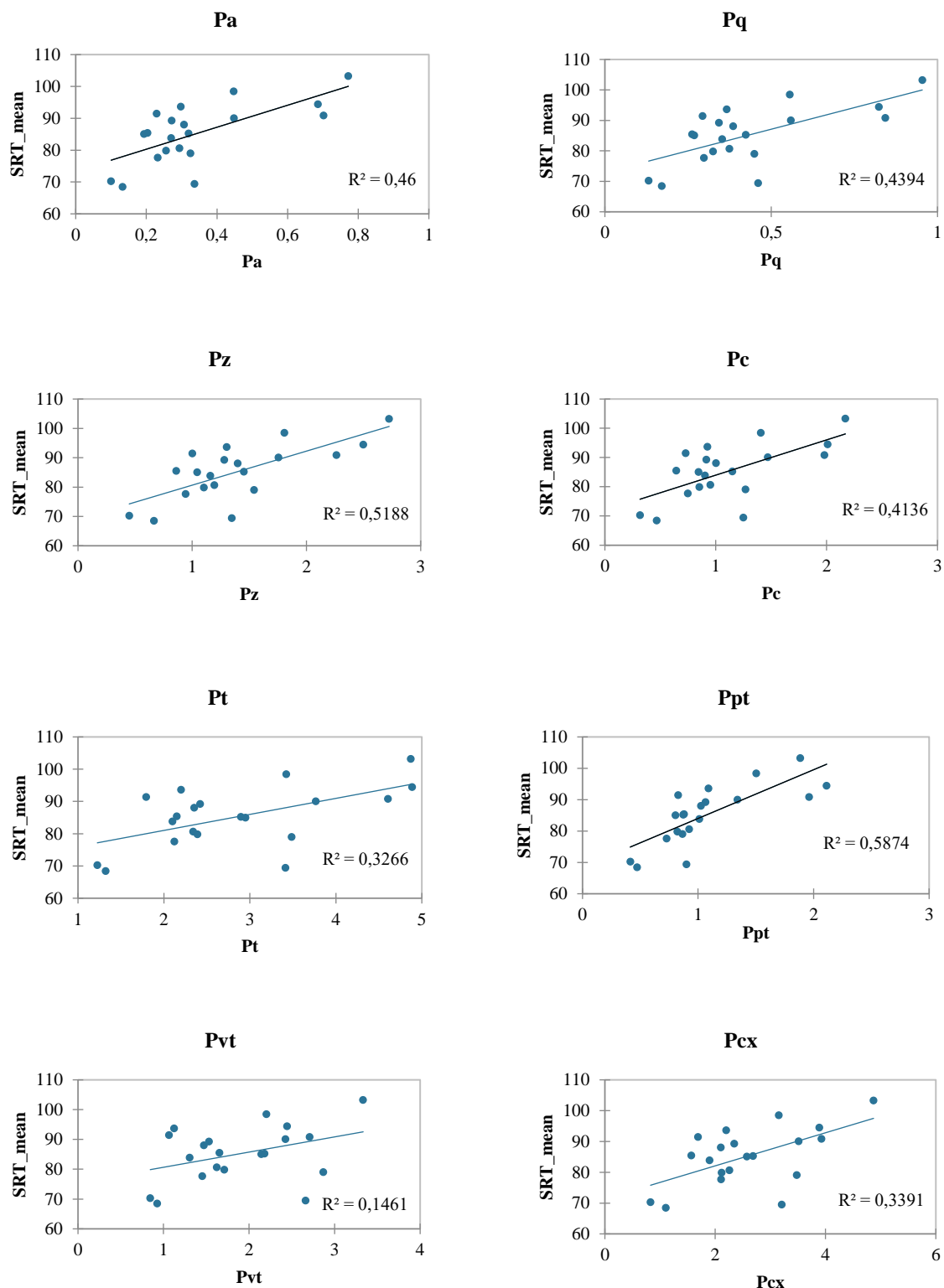


Figure 6.8 Scatter plots for surface-related non-standard texture parameters versus measured friction performance expressed in SRT

By comparing the obtained values of Kendall's correlation coefficient to the previously established threshold values of moderate relationship of 0.4 and significant relationship of 0.6, it can be seen that, among the statistically significant variables, four non-standard texture parameters

showed a moderate to strong correlation: P_a , P_z , P_c and P_{pt} . Three parameters were weakly correlated to the measured friction performance: P_q , P_t and P_{cx} . The highest correlation coefficient of 0.653 was observed for P_{pt} parameter, while the weakest strength was observed for P_t and P_{cx} parameters with correlation coefficient of 0.358. All the non-standard texture parameters showed to be significantly correlated to each other and to have at least a moderate correlation to the traditional MPD parameter, with the highest value obtained for P_{pt} parameter and lowest value for P_{vt} parameter.

Table 6.12 Kendall's correlation coefficient matrix for surface-related texture parameters and friction. Values in bold are statistically significant. Values higher than 0.4 are indication of a moderate relationship and values higher than 0.6 are indication of a strong relationship

	P_q	P_a	P_z	P_c	P_t	P_{pt}	P_{vt}	P_{cx}	MPD	SRT_mean
P_q	1									
P_a	0.968	1								
P_z	0.884	0.895	1							
P_c	0.947	0.937	0.937	1						
P_t	0.737	0.726	0.747	0.789	1					
P_{pt}	0.632	0.663	0.684	0.642	0.537	1				
P_{vt}	0.632	0.621	0.600	0.663	0.811	0.368	1			
P_{cx}	0.779	0.768	0.768	0.811	0.874	0.516	0.789	1		
MPD	0.684	0.695	0.758	0.716	0.547	0.800	0.442	0.589	1	
SRT_mean	0.389	0.421	0.484	0.421	0.358	0.653	0.232	0.358	0.663	1

Traditional texture indicator MPD showed a moderate linear relationship with the SRT friction value with $R^2 = 0.592$ and a significant correlation with Kendall's coefficient of 0.66. Therefore, a basic prediction model with MPD as an explanatory variable and SRT as the output was fitted with a linear regression (Figure 6.9). The selected goodness of fit statistics of the prediction model was root mean squared error (RMSE), representing the square root of average squared error between the measured values Y_i and model output values $Y_{i, \text{hat}}$ for n number of observations,

$$RMSE = \sqrt{\frac{1}{n} \sum_{i=1}^n (Y_i - \hat{Y}_i)^2}$$

The analysis of variance (ANOVA) and sum of squares analysis showed that the established basic prediction model was statistically significant with the obtained value of $RMSE = 6.162$ with obtained R^2 value of 0.592.

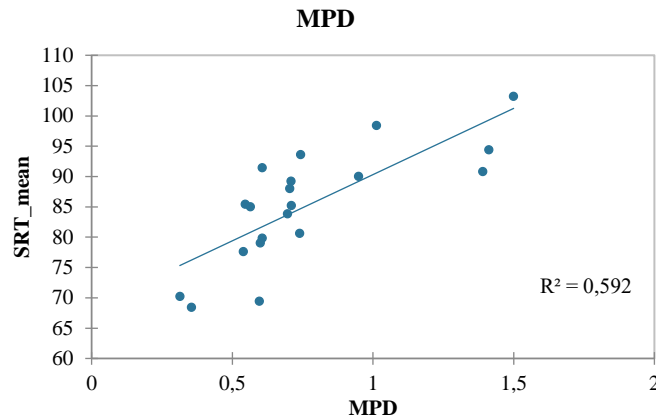


Figure 6.9 Linear regression fit for traditional texture parameter MPD versus friction expressed as SRT

The results of the correlation analysis highlighted four non-standard texture parameters that are statistically significant and have a moderate to strong relation to the friction performance: P_a , P_z , P_c and P_{pt} . These parameters will be accounted for in the pursuit for the friction prediction model development and the research hypotheses confirmation.

6.3. Multiple linear regression (MLR) models

The prediction model for friction performance investigated in this research was based on surface-related non-standard texture parameters obtained from the DSM created by the established CROP methodology for texture data acquisition and analysis. EDA of texture properties evaluated through selected non-standard texture parameters showed some peculiarities of the texture dataset:

- Non-standard parameters do not follow a normal distribution in the observed dataset
- Non-standard parameters are significantly correlated to each other
- Non-standard parameters are correlated to the standard texture descriptor MPD to a certain extent
- Non-standard parameters show a positive monotonic and non-linear relationship with the measured friction performance in moderate to strong range of correlation coefficients values

The listed properties were utilized as guidelines in the procedure of the prediction model establishment via regression analysis framework, as described in the following sections. First, a simple multiple linear regression (MLR) was used for the prediction model establishment showing better performance than the simple LR model with MPD as a single texture indicator. However, the obtained model statistics indicated the need of feature engineering (FE) procedures applied to the model input data to overcome the issues of MLR analysis framework. Several regression-

based methods for the prediction model development were tested. The performance of each proposed model was evaluated by the selected error metric, root mean squared error (RMSE). The models were validated on a test dataset, selected as 25% of the whole dataset to derive the final conclusions about the models' performance.

6.3.1. Basic multiple linear regression (MLR) model

The relationship between the texture parameters and friction performance was first investigated by using multiple linear regression (MLR) analysis. MLR is a statistical data analysis technique that utilizes more than one independent variable for the prediction of the single dependent variable (Permai & Tanty, 2018; Uyanık & Güler, 2013), formulated as

$$Y = \beta_0 + \beta_1 X_1 + \dots + \beta_n X_n + e$$

Where Y is dependent variable, β_i are model parameters, X_i are independent variables and e is error term.

Where Y is dependent variable, b_i are model parameters, X_i are independent variables and e is error term.

To perform the multiple regression analysis, the following assumptions of linear regression should be satisfied (Korstanje, 2021): independence of observations in the data collection process, usage of all relevant explanatory or independent variables, linear relationship between the independent and dependent variables, no multicollinearity in the independent variables dataset, normal distribution of the model residuals, constant error along the dependent variable values or homoscedasticity and no correlation between the independent variables and the error term of the model.

For the texture dataset investigated in this research, the first assumption was clearly satisfied, as the data was collected on different surfaces which had no mutual dependence. The texture parameters that showed statistical significance in the previously performed correlation analysis between the measured friction performance and texture dataset were selected for further analysis, therefore the second assumption was also satisfied. The linear relationship assumption was violated, since the texture parameters showed monotonic non-linear correlation with the friction, with coefficients of determination below 0.6 for linear regression plotted on scatterplots in Figure 5.9. However, the dataset was subjected to multiple linear regression analysis to investigate if the combination of several non-standard texture parameters could yield a better prediction of friction performance.

The initial analysis was performed for the entire dataset, including all four selected non-standard texture parameters in the prediction model establishment. The model statistics showed that the lowest RMSE of the model was obtained when the parameter P_a was excluded as the independent variable. The resulting adjusted R^2 for the model based on the remaining three parameters P_z , P_c and P_{pt} was 0.762. In comparison to the R^2 obtained for the linear regression with MPD and SRT, this value was higher which indicated that the friction could be predicted better if more than one texture parameter was included in the model. The sum of squares analysis results pointed out the statistical insignificance of parameter P_{pt} in the model, with p-value higher than the defined significance level. Therefore, it was excluded as the independent variable and the model was redefined. The second iteration of the MLR model with the remaining parameters P_z and P_c as the independent variables resulted in slightly lower adjusted R^2 of 0.720 and higher RMSE in comparison to the previous model (Table 6.13).

Table 6.13. MLR models performance comparison

Regression model	Model parameters	R^2 (adjusted)	RMSE [-]
LR	MPD	0.592	6.162
MLR_V1	P_z, P_c, P_{pt}	0.762	4.581
MLR_V2	P_z, P_c	0.720	4.970

One of the assumptions of the MLR analysis is the absence of collinearity between the independent variables. The correlation analysis showed that the non-standard texture parameters are strongly related, which could affect the reliability of a prediction model if the collinear variables were used as explanatory variables. The most common multicollinearity detection statistic is the Variance Inflation Factor - VIF (Daoud, 2018). Even though no strict threshold value exists for the VIF indication of the multicollinearity, a general observation is that if $VIF > 10$, there exists a strong correlation among the independent variables (Yoo et al., 2014). If the VIF is over the threshold value, it will cause the increase of standard errors of the independent variables and inflation of their variances. Multicollinearity causes unreliable prediction models due to the overlapping effect of the independent variables which are in fact, not independent. Therefore, it is hard to define what is the unique contribution of each independent variable to the response variable modelled by the prediction model. The obtained VIF values for the prediction model with texture parameters that showed to be statistically significant were exceeding the defined threshold value, thus clearly indicating that there is a multicollinearity issue for the independent variables of the model (Table 6.14).

Table 6.14. VIF scores for 1st and 2nd iteration of MLR model

MLR Model	Model parameters	VIF scores for explanatory variables		
		Pz	Pc	Ppt
V1	Pz, Pc, Ppt	60.581	65.305	15.243
V2	Pz, Pc	47.653		n.a.

The normality distribution of MLR model residuals was observed by performing Shapiro-Wilk test and generating Q-Q plot for the residuals. As the obtained p-value of the Shapiro-Wilk test was higher than the p-value of significance and Q-Q residual plot (Figure 6.10a) followed the straight line, both methods confirmed that the residuals were normally distributed, therefore this assumption was not violated. The homoscedascity assumption was checked by a scatter plot of standardized residuals versus model predictions (Figure 6.10b) showing no specific pattern, therefore there was no evident relationship between the residuals and the predictions and the homoscedascity could be confirmed. The assumption of absence of correlation of the independent variables with the error term of the model was checked by scatter plots of each independent variable versus model residuals (Figures 6.10c, d). There was no clear correlation evident in any of the scatter plots, therefore this assumption was also not violated.

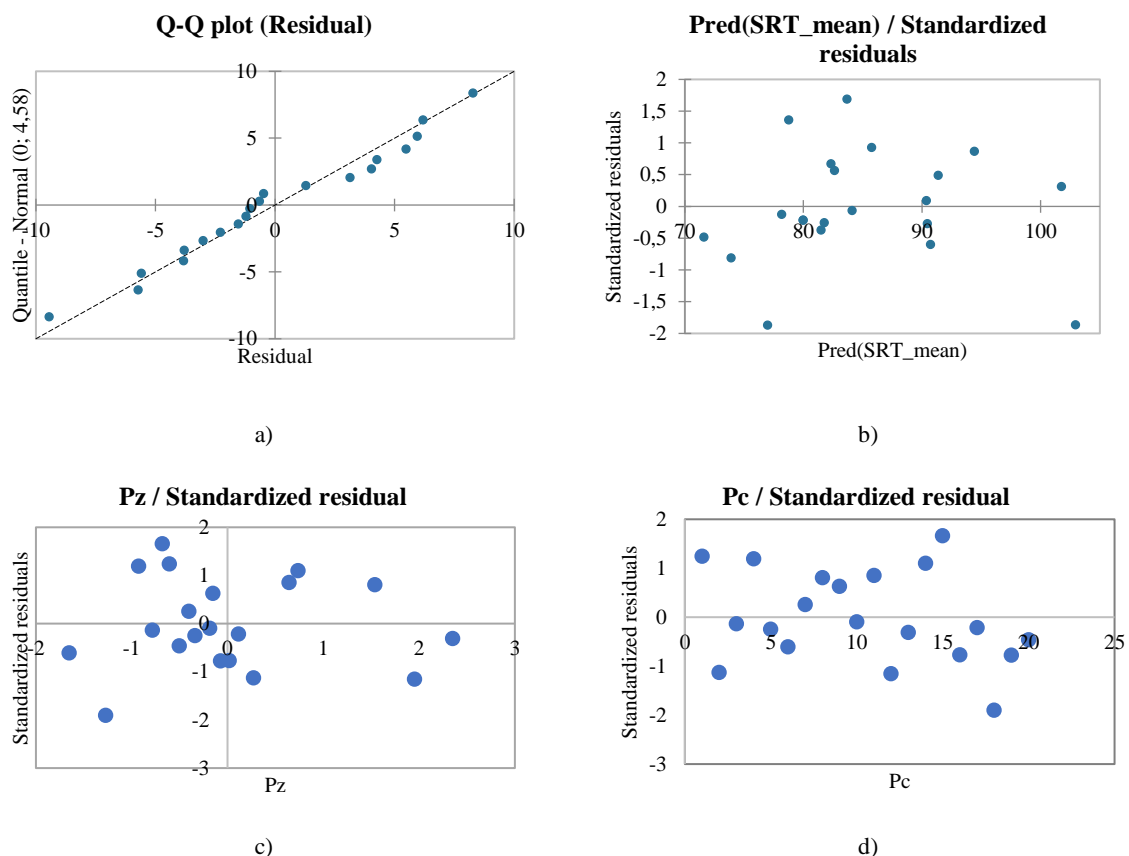


Figure 6.10 Confirmations of MLR assumptions: normally distributed residuals (a), homoscedascity (b), no correlation between explanatory variable Pz and residuals (c) and Pc and residuals (9d)

A summary of MLR analysis assumptions is presented in Table 6.15. Even though no significant linear relationship was observed in the correlation analysis between each texture parameter with the friction, a linear combination of more than one texture parameter explored in MLR resulted in an R^2 value higher than the R^2 values obtained for single texture parameter versus friction, including both standard and non-standard parameters. However, the MLR assumption of no collinear variables was violated, which compromises the reliability of the prediction model. Therefore, feature engineering (FE) procedures were performed to resolve the multicollinearity issue and continue the prediction model development in the regression framework analysis.

Table 6.15. MLR assumptions overview and evaluation for the texture dataset

MLR assumption	Condition satisfied
Data independence	YES
Relevance of explanatory variables	YES
Linear relationship between IV's and DV	YES (to some extent)
No multicollinearity in IV's	NO
Normally distributed residuals	YES
Homoscedascity	YES
No correlation between IV's and residuals	YES

6.3.2. Feature engineering (FE) procedures

The multicollinearity problem has been studied in many scientific disciplines and there are several effects on the prediction model if the independent variables are correlated: increased standard error estimate, confidence intervals widening, increase of test insignificance, mixed effect of independent variables to the regression coefficients which causes wrong coefficients signs, instability of the defined models detected by a significant change of regression coefficient when the model input is slightly changed etc. (Yoo et al., 2014).

To address the multicollinearity and improve the multiple linear regression model, there exists several solutions. The simplest approach would be to remove the highly correlated independent variables if they are not significant for the prediction model (Schreiber-Gregory, 2018). However, if all the independent variables are important and they provide different types of information relevant for the study objective, neither of them should be excluded from the prediction.

Another possible solution for the multicollinearity issue is the usage of regularization methods, which generalize models by adding a penalty term to all the model coefficients except the intercept and constrain the coefficients estimates towards zero, thus significantly reducing their variance (James et al., 2021). Two most common regularization methods are LASSO (Least Absolute

Shrinkage and Selection Operator) regression or L1 and Ridge regression or L2 (Schreiber-Gregory, 2018.). The difference between these two regularization techniques is that the LASSO regression tends to remove the coefficients for which the penalty term λ is too large and thus performs a variable selection procedure, where some of the important independent variables could be excluded from the model (Melkumova & Shatskikh, 2017). As most of the texture parameters showed to be statistically significant (Table 6.12), none of them was to be excluded a priori in the FE procedures, therefore LASSO regression was rejected as a possible approach. Ridge regression, on the other hand, doesn't remove any of the coefficients but reduces the variances of the coefficients estimates and therefore it is more appropriate for the multicollinearity issue where all the independent variables are significant for the prediction model (Schreiber-Gregory, 2018.).

In LASSO regression, the penalty term λ is introduced in the loss function defined by residual sum of squares (RSS) through the absolute value of the model coefficients β_j ,

$$RSS = \sum_{i=1}^n (Y_i - \sum_{j=1}^p X_{ij}\beta_j)^2 + \lambda \sum_{j=1}^p |\beta_j|$$

In Ridge regression, the penalty term λ is introduced through a squared coefficient value β_j^2 to the error function,

$$RSS = \sum_{i=1}^n (Y_i - \sum_{j=1}^p X_{ij}\beta_j)^2 + \lambda \sum_{j=1}^p \beta_j^2$$

where Y_i is the actual value of the dependent variable, $X_{ij}\beta_j$ is the predicted value of the dependent variable calculated from the independent variables X_{ij} and corresponding coefficients β_j .

In Ridge regression, the magnitude of λ regularizes the reduction of the variance. If the value is too small (close to zero), there would be no difference between the loss function with and without the penalty term, which would converge to the standard form of MLR. On the other hand, if the value is too large, the penalty term might have too much influence on the model prediction and cause an under-fit issue. Therefore, it is important to adequately select the λ value to obtain the optimal fit of the prediction model. In Schreiber-Gregory, 2018. RMSE was selected as a metric for the optimization of penalty parameter. By introducing the penalty term in the residual sum of squares, the coefficients b_j initially determined by the MLR exhibit a size constraint, which disables the high variance among them and consequently, eliminates the multicollinearity issue (Hastie et al., 2009).

Another solution for the multicollinearity issue could be by introducing the dimensionality reduction techniques, such as Principal Component Analysis (PCA) or Partial Least Squares (PLS) regression (Hastie et al., 2009). The key feature of such procedures is to remove the highly correlated independent variables by creating one or more composite variables from the original independent variables and use them in the prediction model (Maitra and Yan, 2008). In the PCA method, the independent variables are combined linearly into principal components, new predictors for the model definition which are not collinear and therefore, do not cause the multicollinearity problem (Gwelo, 2019). Each principal component is a result of transformation of the original independent variables matrix by spectral decomposition, which creates eigen values and corresponding eigen vectors. The number of resulting principal components is equal to the number of eigen values of the decomposed data matrix, where several first principal components describe the majority of the original independent variables variance, measured by the magnitude of the resulting eigen values (Maitra and Yan, 2008.). In this way, the problem dimension is reduced from the n number of original independent variables to k number of principal components, selected by the number of eigen values that dominantly describe the data variance (usually 90% or more). If the eigen value corresponding to a principal component is higher than 1, this principal component is considered as significant for the further analysis and prediction model setup (Joshi & Patil, 2020). After the new set of independent variables is defined from the selected principal components satisfying the above-mentioned criterion, they are used for the definition of a new prediction model based on multiple regression analysis.

The Partial Least Squares (PLS) method is addressed as a more efficient method for the dimensionality reduction in comparison to PCA method when it comes to multiple linear regression analysis with a number of highly correlated independent variables (Liu et al., 2022). PLS differs from the PCA method for considering not only the interaction of the independent variables with each other, but also their relationship with the dependent variable in the creation of the new composite variables. The goal of the PLS regression method is to find the linear combination of independent variable coefficients which would maximize the covariance between the predictors and dependent variable (Maitra & Yan, 2008). The new variables are called latent variables (LV) or components (t) and they are weighted by the coefficients which are iteratively calculated to obtain the maximum covariance. These variables weights (w) identify not only the importance of each original independent variable to the new LV, but also the contribution they have to the dependent variable, measured by the covariance magnitude. This is why PLS is found to be more appropriate than the PCA when the research aim is to find which combination of highly correlated independent variables best predicts the model output. The number of LV's is usually

lower than the number of original independent variables and they are not collinear, therefore the multicollinearity issue is resolved. The final model equation is defined with original independent variables weighted by the coefficients that resulted from the PLS regression algorithm, which iteratively maximizes the covariance between the predictors and the outcome variable.

To address the multicollinearity issue in the initial MLR prediction model, the described FE procedures were applied to the same dataset used for the initial MLR analysis: four non-standard texture parameters as independent variables and one dependent variable, i.e. friction performance expressed in SRT. Every method was additionally optimized to obtain the best model performance. Prior to the model build-up, the independent variables were standardized (with $\mu = 0$ and $\text{Var} = 1$), since none of the applied methods was scale invariant. The analyses were performed in *XLSTAT* software (Addinsoft, 2023) for statistical analysis.

Table 6.16 provides an overview of the prediction models established within the MLR framework as a result of different FE procedures which showed the best performance after the applied optimization procedures. For each observed regression model framework, a short comment in the last column of the table is given as an indication of performed optimization procedures, which are in detail described further in the text. The statistics of each final optimized model was obtained by dividing the dataset into training and validation set, where the validation set was chosen randomly from the total number of observations as 25% of the dataset.

Table 6.16. An overview of optimized regression models' performance statistics and comparison to the initial MLR prediction model

Regression model	Texture parameters (independent variables)	Final model equation	R ² (adjusted)	Comments
MLR	Pz, Pc	$\text{SRT} = 85.17 + 36.6094 \text{ Pz} - 30.3366 \text{ Pc}$	0.720	Multicollinearity issue
Ridge regression	Pz, Ppt	$\text{SRT} = 83.928 + 3.762 \text{ Pz} + 2.899 \text{ Ppt}$	0.768	Outlier detection and optimization of penalty parameter λ
PCA Regression	PC1 (Pa, Pz, Pc, Ppt)	$\text{SRT} = 85.9865 + 1.670 \text{ Pa} + 1.672 \text{ Pz} + 1.668 \text{ Pc} + 1.533 \text{ Ppt}$	0.617	Outlier detection and optimization of principal components (PC) number in the model
PLS regression	Pz, Ppt	$\text{SRT} = 85.4377 + 3.9748 \text{ Pz} + 3.93478 \text{ Ppt}$	0.784	Outlier detection and optimization of number of explanatory variables in the model

6.3.2.1. Ridge regression

Ridge regression was first applied to the entire dataset, including all four non-standard texture parameters as explanatory variables. As the goal of Ridge regression is to minimize the model coefficients and thus reduce their variance and multicollinearity, the penalty parameter λ has to be adequately selected. To avoid manual tuning of the λ value in search of its optimum, a k-fold cross validation method was applied (Hastie et al., 2009). In this method, a k number of equal folds is created and the dataset is equally divided in each of the created folds. For each k-fold, the rest of the folds is used as a training set of the model, and the error of the prediction model is calculated by comparing the predicted values with the values stored in that same k-fold. The selected number of folds k is typically 5 or 10, but it can be assigned differently. For Ridge regression applied to the whole dataset with k values equal to 5 and 10, the model statistics are provided in Table 6.17. It can be seen that the adjusted R^2 value and RMSE value is lower when the penalty parameter is determined by 5-fold cross-validation.

Table 6.17. Model statistics for Ridge regression with parameter λ optimized by k-fold cross-validation method

k-fold cross validation	Penalty parameter λ	Adjusted R^2	RMSE [-]
k = 5	0.6873	0.684	4.741
k = 10	0.5464	0.600	5.028

The residuals of the superior resulting model were tested for outliers since their presence could affect the model's performance. A Z-score test was applied because the residuals were normally distributed, with one detected outlier. After the outlier was removed from the dataset, another iteration of Ridge regression was performed (V1), resulting in improvement of the test statistics R^2 and RMSE (Table 6.18). By observing the model coefficients, it can be seen that two of them obtained negative sign. This is not in coincidence with the results of initial correlation analysis, presented in section 6.2.4, where all the parameters showed a positive relation to the friction performance, regardless of the correlation strength (Figure 6.8). Therefore, Ridge regression was further optimized by excluding the parameters P_a and P_c as explanatory variables in the model, as they were related to negative model coefficients. The final Ridge regression model V2 showed an improvement in model statistics in comparison to the earlier iteration, with both positive coefficients associated with the parameters P_z and P_{pt} .

Table 6.18. Optimization of Ridge regression by removing the explanatory variables with negative sign of model parameters

Ridge regression model version	Penalty parameter λ	Adjusted R ²	Model equation	RMSE [-]
V1	0.68	0.694	SRT = 86.358 – 1.107 Pa + 3.468 Pz – 1.207 Pc + 5.590 Ppt	4.604
V2	0.812	0.768	SRT = 83.928 + 3.762 Pz + 2.899 Ppt	4.442

6.3.2.2. PCA regression

Being a dimensionality reduction technique, PCA delivers new explanatory variables which can be used to fit a MLR prediction model. These new variables called principal components (PC) are derived as a linear combination of original variables, thus reducing the number of model parameters. All the PCs are orthogonal, which eliminates the multicollinearity problem. The number of PCs can be defined by cross-validation for a large number of generated PCs (Hastie et al., 2009) or by selecting only those PCs which explain the highest amount of variability (Lafi & Kaneene, 1992). The latter criterion was used in this analysis by exploring the cumulative variability of the calculated PCs and the eigen values determined for each PC. For eigen values close to zero, the corresponding PC could cause a collinearity issue in the prediction model, therefore it should be excluded from the model definition (Lafi and Kaneene, 1992).

The performed PCA results are presented in Table 6.19, where it can be seen that the first two PCs explain the most of the data variability, especially the PC1. The calculated eigen values indicate that the PC3 and PC4 should be excluded as they are almost equal to zero. Furthermore, the percent contribution of each original independent variable, i.e. texture parameter, showed that all four parameters contribute almost equally to the PC1, while parameter P_{pt} contributes significantly more to the PC2 in comparison to other three parameters.

Table 6.19. Principal components analysis results for dimensionality reduction by selecting the explanatory variables with the most significant contribution to the “new” model inputs defined as principal components (PC’s)

	PC1	PC2	PC3	PC4
Eigen value	3.736	0.232	0.024	0.008
Variability [%]	93.403	5.796	0.603	0.197
Pa contribution [%]	26.033	5.744	53.127	15.066
Pz contribution [%]	26.054	5.889	46.703	21.355
Pc contribution [%]	25.969	10.661	0.168	63.201
Ppt contribution [%]	21.944	77.676	0.002	0.378

By using calculated factor loadings for each original variable, the principal components PC1 and PC2 were defined and used as new explanatory variables in the MLR framework as

$$PC1 = 0,986 P_a + 0,987 P_z + 0,985 P_c + 0,905 P_{pt}$$

$$PC2 = -0,116 P_a - 0,117 P_z - 0,157 P_c + 0,424 P_{pt}$$

The MLR model defined with PC1 and PC2 as independent variables was no longer having the multicollinearity issue, as VIF values were slightly higher than 1. The obtained model performance statistics are presented in Table 6.20. The final model equation was derived by subtracting the obtained model parameters with the factor loadings of the original independent variables used for the definition of the PCs. From the model equation, it can be seen that three parameters have a negative sign which is contradictory to the initial correlation analysis. Therefore, the second iteration of the PCA regression model was tested, where only the most influential PC was observed as the independent variable. This model was defined within the LR framework, having only one independent variable.

The residuals for model versions V1 and V2 were tested for normality distribution and confirmed by Q-Q normal probability plots (Figure 6.11a, b). Z-score tests were performed to check if there are any outliers in the dataset (Figure 6.11c, d). For the first model version there was no Z-score exceeding the threshold value of 2 for normally distributed data, but for the model with only PC1 as explanatory variable, an outlier occurred and another model iteration was performed, without the outlier. The final PCA regression model V2.1 showed to have better goodness of fit statistics in comparison to the previous two models and more importantly, the model parameters were not negative which was in coincidence with the physical meaning of texture parameters contribution to the friction performance.

Table 6.20. PCA regression model optimization by analysis of model parameters values

PCA regression model version	Model variables	VIF	(Adjusted) R ²	Model equation	RMSE [-]
V1	PC1, PC2	1.040	0.569	SRT = 85.170 - 1.217 Pa - 1.239 Pz - 2.186 Pc + 11.402 Ppt	6.164
V2	PC1	n.a.	0.503	SRT = 85.17 + 1.679 Pa + 1.681 Pz + 1.676 Pc + 1.541 Ppt	6.798
V2.1	PC1	n.a.	0.667	SRT = 85.8609 + 1.8917 Pa + 1.8937 Pz + 1.8898 Pc + 1.7363 Ppt	5.757

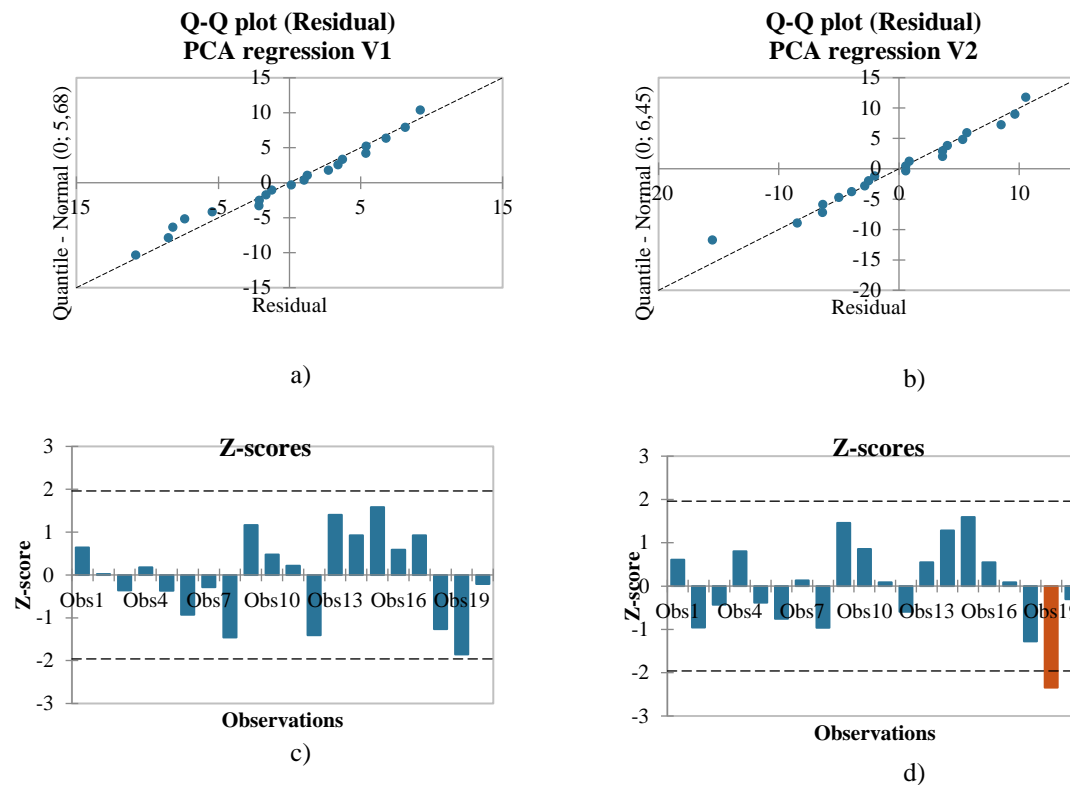


Figure 6.11 Normal distribution of residuals confirmed by Q-Q plots for PCA regression models V1 (a) and V2 (b) and outlier test Z-score for PCA V1 (c) and PCA V2 (d) regression models

6.3.2.3. PLS regression

PLS regression is an alternative to PCA regression which also reduces the number of components or independent variables in the model, but unlike PCA which combines only the independent variables, PLS uses the power of correlation between the explanatory variables and the model outcome to optimize the model parameters (James et al., 2021). The PLS components are calculated by weighing the LR coefficients between each explanatory and dependent variable and assigning the highest weights to the first component. The next component is calculated by taking the residuals of the first model iteration and using them as weights for the next model iteration etc. The number of components is chosen similarly to the PCA components selection. The most common method for components selection is leave-one-out (LOO) cross-validation (James et al. 2021). This method is similar to the k-fold cross-validation, with k number of folds equal to the number of observations n. The validation set contains only one observation (leave-one-out) and the model is fit to all the other observations. The test errors are calculated for each validation set and averaged as the cross-validation estimate of means squared error.

PLS regression analysis was first performed for the whole dataset, resulting in one component which contained all four texture parameters characterized by Variable Importance in the Projection scores (VIP scores). These scores indicate the importance of each independent variable

in the definition of a PLS component, where VIP score > 1 represents a highly influential variable and VIP score < 0.8 indicates that the variable has no significant influence on the component build-up (Tran et al., 2014). Two of the parameters obtained VIP score > 1 , P_{pt} and P_z and the other two parameters' VIP score was also significantly high, just slightly below 1 (Figure 6.12). The model residuals were tested for normality and outliers, with Q-Q plot and Z-score results provided in Figure 6.13. It can be seen that the dataset contained one outlier which was removed for the second iteration of PLS regression model. The second version of PLS regression model showed improvements in the goodness of fit statistics and once again, P_{pt} and P_z parameters obtained VIP score > 1 . To explore if the PLS regression model could obtain better performance, the final iteration was performed for these two parameters only. The obtained goodness of fit statistics was significantly improved when the PLS regression model was defined by the two parameters scoring VIP > 1 . The obtained model statistics for all three PLS regression model iterations are presented in Table 6.21.

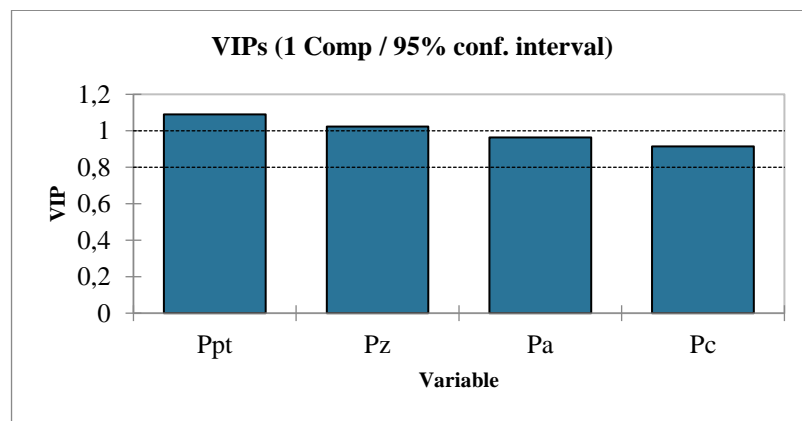


Figure 6.12 VIP scores for parameters Pa, Pz, Pc and Ppt used for the creation of PLS regression component

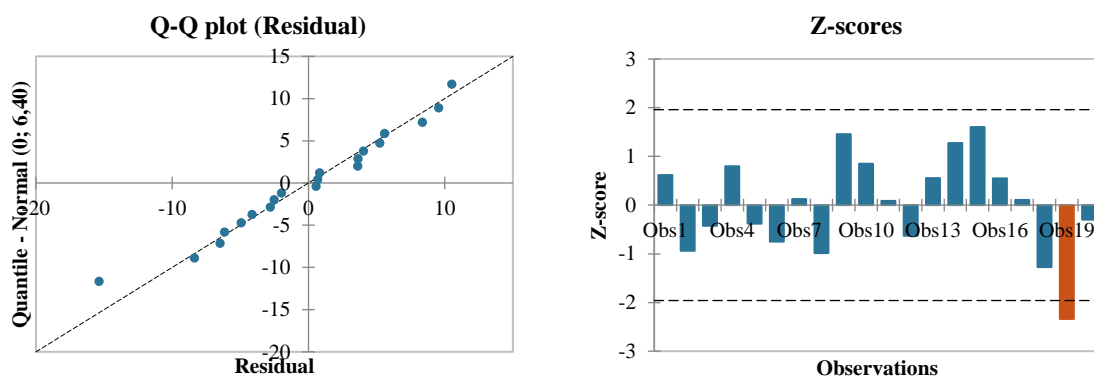


Figure 6.13 Normal probability Q-Q plot and Z-score test for the PLS regression model V1

Table 6.21. Summary statistics of PLS regression models optimized by number of explanatory variables in the PLS component based on VIP score and outlier test of model residuals

PLS regression model version	Model parameters	Adjusted R ²	Model equation	RMSE [-]
V1	Pa, Pz, Pc, Ppt	0.510	SRT = 85.17 + 1.6005 Pa + 1.6997 Pz + 1.5177 Pc + 1.8086 Ppt	6.571
V2	Pa, Pz, Pc, Ppt	0.594	SRT = 85.9813 + 1.5896 Pa + 1.6786 Pz + 1.5778 Pc + 1.7203 Ppt	5.646
V3	Pz, Ppt	0.784	SRT = 85.4377 + 3.9748 Pz + 3.93478 Ppt	4.412

6.3.3. Multiple polynomial regression (MPR)

Polynomial regression is a special case of linear regression, used for the description of a non-linear relationship between the exploratory variables x_i and the output variable y_i , defined as

$$y_i = \beta_0 + \beta_1 x_i + \beta_2 x_i^2 + \dots + \beta_n x_i^n + \epsilon$$

where β_i are the model parameters, n is the polynomial degree and ϵ is the error term (James et al., 2021). The nonlinearity stems from the definition of independent variables, which can be quadratic or higher order expansions of the original variables, or a combination of two (or more) variables obtained by multiplication, or any other non-linear function (Hastie et al., 2009). The coefficients of the independent variables remain linear and by redefining the original independent variables to a new set of independent variables, the model equation becomes linear again and can be explored in the MLR analysis framework. The independent variables of the MPR model should also satisfy the assumption of the absence of multicollinearity and the model errors should be homoscedastic and normally distributed (Ostertagová, 2012).

The original independent variables can be transformed by means of a so-called basis function which can be of any form. The most common are the polynomial functions, logarithmic or power functions and nonlinear functions applied separately to non-overlapping regions of the original independent variable – piecewise-polynomials and splines (Hastie et al., 2009). The selection of the proper basis function mainly depends on the dataset characteristic and the nature of the problem to be solved. To address the goodness of fit of the selected function, the resulting prediction model can be evaluated by common fitting metric such as MSE.

Polynomial regression requires the definition of a polynomial of n -th degree. The most common are 2nd and 3rd degree polynomials, since higher degree polynomials could cause data over-fitting, especially for the limited dataset size (James et al., 2021). By over-fitting the model, the predictive performance decreases as it becomes hyper-sensitive to changes in the input dataset.

The number of independent variables exponentially increases with the increase of the polynomial degree, making the regression model more complex and less intuitive.

To investigate the applicability of a polynomial regression for the establishment of a friction prediction model from selected texture parameters, a polynomial of the 2nd order was defined as a linear basis expansion function. To avoid the multicollinearity between the original independent variables, an alternative set of independent variables was used for the creation of the polynomial regression model, i.e. the principal components PC1 and PC2 defined earlier in the MLR optimization analysis. The polynomial equation defined for the regression model was

$$SRT = \beta_0 + \beta_1 PC_1 + \beta_2 PC_1^2 + \beta_3 PC_2 + \beta_4 PC_2^2 + \beta_5 PC_1 PC_2 + \epsilon$$

with six $\beta_i, i = 0, \dots, 5$ model parameters. For a higher 3rd degree polynomial, the equation would have ten parameters which would significantly increase the complexity of a model.

As for the models observed in the linear regression framework, the normality distribution and outlier tests were performed for the residuals, showing there is one outlier observation (Figure 6.14). By removing the outlier and performing the MPR analysis on the updated dataset, the model’s goodness of fit statistics increased (Table 6.22). The statistics of the final version of MPR model were obtained for the dataset divided into training and validation set, following the same rule as for the previously tested models in MLR framework.

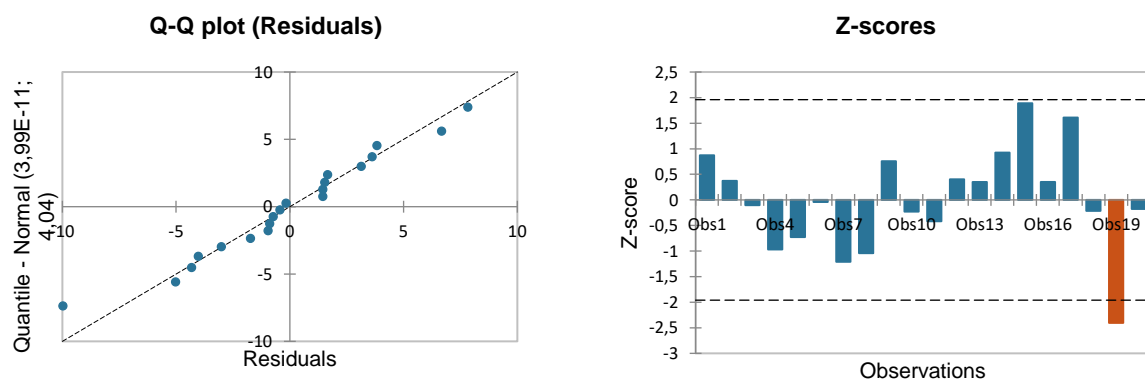


Figure 6.14 Normal probability plot for MPR model residuals and Z-score test of outliers, showing one outlier in the dataset

Table 6.22. Resulting error metrics for the MPR model iterations: V1 is the model containing the outlier detected with the Z-score test, V2 is the model without the outlier in the dataset

MPR model version	RMSE [-]
V1	4.830
V2	3.038

The final equation of the MPR model is defined as

$$SRT = 87.7987 + 1.7916 PC1 - 0.2636 PC1^2 + 29.6636 PC2 + 14.0581 PC2^2 + 0.3410 PC1 PC2$$

If the principal components were expressed as original independent variables, i.e. texture parameters P_a , P_z , P_c and P_{pt} , the model equation would be

$$SRT = 87.7987 - 1.6745 P_a - 1.7023 P_z - 2.8925 P_c + 14.1988 P_{pt} - 0.1061 P_a^2 - 0.1037 P_z^2 + 0.0380 P_c^2 + 2.4423 P_{pt}^2 - 0.1051 P_a P_z - 0.0528 P_a P_c - 0.7841 P_a P_{pt} - 0.0509 P_z P_c - 0.7901 P_z P_{pt} - 1.0284 P_c P_{pt}$$

6.4. Discussion

The optimization of different models by feature engineering procedures resulted in four multiple linear regression models and one multiple polynomial regression model. To address the performance of all the optimized prediction models developed in the regression framework, the models were evaluated by the resulting error metric root mean squared error (RMSE),

$$RMSE = \sqrt{\frac{1}{n} \sum_{i=1}^n (y_i - y_{i,pred})^2}$$

where y_i is the observed value, $y_{i,pred}$ is the value obtained by the prediction model and n is the number of observations.

This error metric is evaluated from the mean squared error (MSE), which squares the residuals of the prediction model and provides an average value for the tested dataset. MSE is therefore expressed in the squared unit of the model outcome, which may be difficult to interpret (Trevisan, 2022). Therefore, the square root value of MSE, the RMSE metric, provides the error measure in the same units as the value predicted by the model and it is more intuitive for the model error estimation. An alternative error metric would be the mean absolute error (MAE), which measures the absolute distance between the observed values and the predicted values,

$$MAE = \frac{1}{n} \sum_{i=1}^n |y_i - y_{i,pred}|$$

By comparing the formulae for RMSE and MAE it can be concluded that RMSE squares the distance between the actual and predicted value, giving more weight to larger distances, i.e. potential outliers. MAE assigns the same weight to all error terms by observing their absolute values and thus it is less sensitive to the outliers (Chai & Draxler, 2014). RMSE is more suitable

for normally distributed errors, which is one of the linear regression assumptions followed in this research. On the other hands, MAE is more suitable if the errors are uniformly distributed. Therefore, the RMSE was selected as more robust and reliable error evaluation method.

The resulting error metric RMSE evaluated on the optimized prediction models with dataset division into training and validation set by following the rule 75/25 is given in a model summary Table 6.23. It can be seen that the smallest value of error metric was obtained for MPR regression model, RMSE = 3.038 and the highest RMSE = 5.757 was obtained for the PCA regression model. Ridge regression and PLS regression obtained similar RMSE values, with prediction models accounting for two texture parameters.

Table 6.23. A summary of the models' error metric RMSE, model input variables and the resulting model equations observed in the optimized MLR framework

Regression model	Non-standard texture parameters (explanatory variables)	Model equation	RMSE (with validation dataset) [-]
Ridge	Maximum height (P_z) Maximum peak profile height (P_{pt})	$SRT = 83.928 + 3.762 P_z + 2.899 P_{pt}$	4.442
PCA	Arithmetic mean height (P_a) Maximum height (P_z) Mean profile element height (P_c) Maximum peak profile height (P_{pt})	$SRT = 85.8609 + 1.8917 P_a + 1.8937 P_z + 1.8898 P_c + 1.7363 P_{pt}$	5.757
PLS	Maximum height (P_z) Maximum peak profile height (P_{pt})	$SRT = 85.4377 + 3.9748 P_z + 3.93478 P_{pt}$	4.412
MPR	Arithmetic mean height (P_a) Maximum height (P_z) Mean profile element height (P_c) Maximum peak profile height (P_{pt})	$SRT = 87.7987 - 1.6745 P_a - 1.7023 P_z - 2.8925 P_c + 14.1988 P_{pt} - 0.1061 P_a^2 - 0.1037 P_z^2 + 0.0380 P_c^2 + 2.4423 P_{pt}^2 - 0.1051 P_a P_z - 0.0528 P_a P_c - 0.7841 P_a P_{pt} - 0.0509 P_z P_c - 0.7901 P_z P_{pt} - 1.0284 P_c P_{pt}$	3.038

By comparing the Ridge, PCA and PLS regression models it can be seen that the PLS model obtained the smallest error metric RMSE. The result coincides with the fact that the PLS regression accounts for the relationship between both independent and dependent variables and finds the model parameters by selecting the most significant component, which is iteratively calculated from the combination of the most weighted correlation coefficients between the independent variables and dependent variable. PCA regression obtained the smallest value of R^2 and highest RMSE for the prediction model, which was not surprising since the principal

components created by PCA and used for the MLR/LR model establishment do not account for the relationship between the dependent variable with the independent variables. The optimized Ridge regression model was defined with two parameters, P_z and P_{pt} . The other two parameters were associated with negative model coefficients, which is contradictory to the initial observations of the texture-friction relationship given in Figure 5.9. This is another advantage of PLS regression, which resulted in all positive model parameters in the second iteration, where all the independent variables were accounted for regardless of the VIP score.

Despite the fact that the MPR model scored the lowest value of error metric, it is the most complex model with fourteen (14) predictors defined by a single texture parameter, squared texture parameter or a multiplication of two different texture parameters. By analyzing the MPR model coefficients it can be seen that some of them are relatively small in comparison to the others, for example the parameter associated with the squared value of P_c equal to 0.038 or the parameters corresponding to $P_a P_c$ equal to 0.0528 and $P_z P_c$ equal to 0.059. Removing the independent variables associated to the model parameters with smaller values would reduce the model complexity, but it could also impact the model's predictive strength. Further optimization of the MPR model wasn't performed in this research.

When a prediction model is established from the experimental observations, not only model statistics but also the physical meaning of model parameters should be observed for the selection of an optimal prediction model (Ahammed & Tighe, 2008). Therefore, the PLS regression model with two parameters P_z and P_{pt} can be adopted as the optimal model for prediction of friction performance based on the non-standard texture parameters. In comparison to the model statistics of the initial simple linear regression model for friction performance prediction based on the traditional texture parameter MPD, the PLS regression model performed better with the RMSE = 4.412 and adjusted $R^2 = 0.784$ (Table 6.24).

Table 6.24. Comparison of models' performance: initial linear regression model with MPD as explanatory variable and optimized PLS regression model with two non-standard texture parameters as explanatory variables

Model	Model Parameters	R^2 (adjusted)	RMSE [-]
LR	MPD	0.592	6.162
PLS regression	P_z, P_{pt}	0.784	4.412

6.5. Machine learning methods for friction prediction model development

The friction performance prediction models investigated in the previous section rely on the assumptions of the linear regression framework. The original texture data collected by the CROP

methodology had to be adjusted by feature engineering procedures so it could satisfy the LR assumptions and become suitable for the selected analysis framework. Some of the advantages of the LR framework are its simplicity in model establishment and interpretation and good performance even for the limited dataset size (Hastie et al., 2009). The LR framework best describes the dataset in which independent variables are linearly correlated to the dependent variable. It is a parametric method, which means that the prediction model is defined by a function $f(X)$ which is assumed to be linear. The function is defined by the parameters β and the goal of LR is to find the parameters values in a way that the prediction error is minimized (James et al., 2021). For parametric methods, the data distribution is assumed prior to the definition of prediction model. In case of linearity assumption, the input data should be normally distributed, as well as the errors of the model. The EDA of the original texture dataset described in section 6.2. had to be performed to investigate the appropriateness of the dataset for the LR framework. The adjustments of the original data were done by FE procedures, resulting in exclusion of some input variables as they did not satisfy the LR framework assumptions, even though they might contribute significantly to the prediction of the outcome and thus improve the prediction model performance.

An alternative way to establish the prediction model without the prior assumption of its functional form or data distribution type would be by applying the non-parametric methods (James et al., 2021). These methods do not assume any specific function for which the dataset is fitted, but seek for the closest estimate of a fit function in a wide range of functional shapes. The result is a flexible but complex function with many model parameters. However, the flexibility of non-parametric methods for prediction model establishment might result in data overfitting in case where the dataset has a limited size because the prediction model function could also account for outliers and noise in the dataset.

The results obtained via the LR framework showed that the friction performance can be predicted from the selected texture parameters to a certain extent. However, the true relationship between the texture parameters and the friction performance is showed to be non-linear. This is why some additional non-parametric methods for prediction model establishment were investigated in this research as a potential improvement of the prediction model.

Prediction models developed by non-parametric generalized additive models (GAM) are an extension of the multiple polynomial regression explored in section 6.3.3. The non-linear relationship between each explanatory variable and the model outcome can be defined with a smooth and non-parametric function and the contribution of each defined function is added

together for an overall model performance evaluation (James et al., 2021). The selection of a function which describes the relationship between the explanatory variable and the response is done by the scatterplot smoother, which is any smooth function that fits the dataset the best and minimizes the error term of the model (Hastie et al., 2009). GAM does not require the FE of the model input data to extract or adapt the predictors to satisfy some characteristic conditions, as for the parametric methods explored in previous sections. However, in case when there is many predictor variables in the model, the additivity of the GAM approach might result in a very complex and non-intuitive model and some more important relations could be lost among the others. Alternatively, the predictors could be manually selected, but this would again require FE procedures which would reduce the flexibility of the GAM approach (Hastie et al., 2009).

To preserve the flexibility of non-parametric methods for prediction model establishment, machine learning (ML) algorithms are used as the so-called “off-the-shelf methods”, where no significant EDA or FE has to be done on the original dataset prior to the model setup (Hastie et al., 2009). ML algorithms are supervised learning methods, building a prediction model from explanatory variables and the model outcome as the model input data (Cano-Ortiz et al., 2022). ML uses statistics theory to develop prediction models with the main goal to make an inference from a given data sample (Alpaydin, 2014). The goal of ML algorithm is to provide the generalization of an observed problem based on the input dataset by optimizing the model parameters and provide a reliable model estimates (Marcelino et al., 2017). In ML methods, model parameters are called hyper-parameters and they are defined prior to the model setup. Each ML algorithm has a set of specific hyper-parameters and their definition largely affects the model performance. Therefore, hyper-parameters are iteratively adjusted or tuned to provide the ML model with the most reliable model estimates. The hyper-parameter tuning procedure is performed by different cross-validation strategies, again depending on the ML algorithm used for the prediction model establishment.

ML algorithms learn from the input data through a knowledge extraction procedure, where a rule (or a model) is learnt based on the properties of the model input dataset (Alpaydin, 2014). Therefore, larger dataset will enable the algorithm more examples of different behavior and consequently result with more reliable prediction model (Pruksawan et al., 2019). In case when the data collected in experimental research is limited in size, the prediction models based on a ML algorithm might be more susceptible to errors and fail to produce reliable estimators.

The applicability of ML for the development of a friction performance prediction model was tested by two different algorithms: Support Vector Machine (SVM) regression and Random

Forest (RF) regression. The SVM algorithm was developed and introduced in 1992 by authors Boser, Guyon and Vapnik as a classification method based on kernels, smoothing functions which separate (classify) the data and further extended to the regression problems applicable for a limited dataset size (Rivas-Perea et al., 2013). The applicability of this ML algorithm to a small dataset and the similarity to linear regression principle were the main motivation for its selection in this research.

The RF regression is an ensemble ML algorithm which combines many decision trees, which are a set of hierarchically organized conditions applied successively from the root to the leaf of each tree element (Gupta et al., 2022). The decision trees are built from a random subset of data and features evaluated by the defined conditions by bootstrapping method. Bootstrapping is a specific statistical-based method where a random subset of the original dataset is selected and extracted, but also simultaneously replaced in the original dataset. In this way, multiple random datasets are created for the model training, increasing its robustness. Another RF characteristic is selection of random feature subset for each decision tree. This means that each decision tree is regressed by different selected dataset features, which reduces the correlation between the decision trees and improves the model performance. In RF regression algorithm, the final model prediction is derived as an average of the predictions made by decision trees constructed in the forest.

Additionally, the RF algorithm provides the variable importance measurements in the context of the contribution strength of each explanatory variable to the model outcome (Zhan et al., 2021). This approach is similar to the PLS regression VIP scores, observed in the LR framework. RF algorithm was selected for several reasons. It was found to be suitable for a small sample size problem due to the bootstrapping method for the creation and randomization of a training dataset. The RF property of randomization of the model features is useful for the problems with collinear input variables present in this research. Finally, the result of RF algorithm could be compared to the PLS regression results in the evaluation of the contribution of each texture parameter to the friction performance.

The feasibility of the ML algorithms application for the prediction of pavement frictional performance stems from the complexity and non-linearity of friction phenomenon, dependent on many versatile influential factors. In the last few years, different ML algorithms were utilized for the prediction of friction performance with some examples given in Table 6.25. However, the usage of ML methods for pavement performance prediction and monitoring is still relatively new and there is still no wide application in the pavement management (Cano-Ortiz et al., 2022).

Table 6.25. An overview of ML algorithms, dataset properties and results utilized for the establishment of a friction performance prediction model

Authors	ML algorithms	Model input data	Dataset size	Results
Panahandeh et al., 2017	SVM (classification), Artificial Neural Network (classification)	Measured friction data (historical), Climatic conditions	9281 friction measurements (from November 2015 to October 2016)	Friction performance is evaluated through a classification to slippery or non-slippery based on the predicted friction coefficient, the ANN algorithm provides more stable results for a variety of conditions
Yang et al., 2018	Convolutional Neural Network (CNN)	Raw macro-texture profiles	504 000 pairs of texture and friction data	Obtained model accuracy was 96.85% for training dataset, 88.92% for validation dataset and 88.37% for test set for the prediction of friction levels
Zhan et al., 2020	Deep Residual Network DNN for classification	2D spectrograms of texture data obtained by FFT of profile data and corresponding friction measure	33 600 texture profiles paired to the friction measurements	Classification accuracy of 91.3% for the predicted friction level from the DNN based on texture spectrogram data
Zhan et al., 2021	RF	14 parameters grouped into Aggregate type, Traffic load (AADT), Pavement condition and Climatic conditions variable groups	179 datasets containing relevant parameters	Obtained value of $R^2=0.79$ for friction prediction model, variable importance analysis pointed out the most influential properties of aggregates for the friction performance
Hu et al., 2022	Light Gradient Boosting Machine algorithm (tree-based)	10 macro-texture parameters extracted from two types of asphalt mixture specimens with different gradation (AC and OGFC)	200 groups of texture dataset	Obtained $R^2 = 0.98$ for training set and $R^2 = 0.93$ for test set when predicting pavement friction by LightGBM method; in comparison to other ML algorithms (RF, SVR and XGboost) the proposed algorithm had superior performance

6.5.1. Application of Support Vector Regression (SVR) algorithm

SVR algorithm is an adjustment of the original SVM algorithm developed for binary classification problems to the prediction of numerical outputs (Rodríguez-Pérez & Bajorath, 2022). The quantitative predictions of SVR model are derived by projecting the training dataset into a pre-defined feature space. Afterwards, a regression function is fitted to the projected data as a linear

hyper-plane. If the input data is non-linear, the SVR algorithm applies additional transformations of the original input variables to account for the non-linearity in the dataset and thus maps them in a higher-dimension feature space where linear regression could be applicable. The transformation of original variables to higher-dimension feature spaces is done by kernel functions. A so-called “kernel trick” has a dominant effect when SVR is used for the prediction model establishment. When it is not possible to obtain a linear model for the data in a given input space X , the “kernel trick” maps the data to a higher-dimension space H where linear model could be possible. The most used kernel functions are linear kernel, polynomial kernel, Gaussian and RBF kernel (James et al., 2021; Rodriguez-Perez and Bajorath, 2022).

To address the errors in the SVR algorithm, a so-called ε -insensitive tube is defined as a penalization criterion, where all data values falling outside the ε -tube are the support vectors. SVR regression function is of a form

$$y = \langle w, x \rangle + b$$

where y is the prediction, x is the input data vector, w is the weight vector and b is the bias (Figure 6.15). The width of the ε -tube has to be selected by specifying the distance from the hyperplane defined by the SVR function in a way that all the predictions falling outside the defined width are penalized and categorized as support vectors. This is why ε -tube width is an important hyper-parameter of the SVR algorithm.

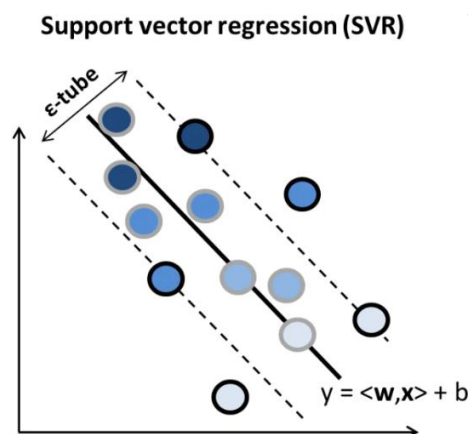


Figure 6.15 SVR with linear kernel and ε -tube width, all datapoints outside the ε -tube width are support vectors (Rodriguez-Perez and Bajorath, 2022)

Another important hyper-parameter is the regularization parameter C , which controls the relaxation of margin maximization and thus balances model performance by accounting for complexity and accuracy (Rodriguez-Perez and Bajorath, 2022). In general, any value of C from 0.001 to 1000 can be selected for the SVR algorithm, where a large C value might lead to

overfitting by a complex model and a small C value could cause model under-fit and low complexity. The value of hyper-parameter C is usually optimized by cross-validation methods.

The performance of SVR algorithm for the development of a friction prediction model was tested by defining the input dataset, model hyper-parameters ϵ and C and linear kernel function. Since the ML algorithms are in general non-parametric methods, the dataset contained all calculated texture parameters regardless of the previous EDA results and performed FE procedures. The dataset was divided to training and validation set, following the 75/25 rule as for the linear regression framework. The optimization of the SVR algorithm was performed by k-fold cross validation with $k = 5$ folds. The selection of an optimal model was performed by comparison of the resulting error metric RMSE and accuracy expressed in percentage obtained for training and validation set for different values of hyper-parameters. The data analysis by SVR ML algorithm was performed in *XLStat* software. The obtained results are presented in Table 6.26.

Table 6.26. SVR algorithm hyper-parameters optimization and the resulting statistics of the friction prediction model

SVR algorithm	C hyper-parameter	ϵ -tube hyper-parameter	Accuracy training set	RMSE training set [-]	Accuracy validation set	RMSE validation set [-]
SVR_auto	1	0.1	65.2 %	5.3136	55.5 %	5.7030
SVR_V1	0.1	0.1	38.0 %	6.5534	50.5 %	7.8754
SVR_V2	100	0.1	85.5 %	3.2373	60.5 %	6.5586
SVR_V3	200	0.1	86.4 %	3.0508	51.1 %	7.8332
SVR_V4	250	0.1	85.5 %	3.5488	76.3 %	4.0728
SVR_V5	300	0.1	88.8 %	3.0732	33.8 %	9.2353
SVR_V6	250	1	47.4 %	5.9165	79.9 %	5.1248
SVR_V7	250	0.01	89.4 %	3.2938	34.6 %	5.9028
SVR_V8	250	0.001	85.6 %	3.5058	57.0 %	4.3996

The first iteration was performed for generic values of hyper-parameters C and ϵ selected in the data analysis software. From the Table 25 it can be seen that the model obtained better accuracy for a larger value of C hyper-parameter in comparison to the initial value for both training and validation dataset. The RMSE value decreased for both datasets if the C hyper-parameter was larger than the selected initial value. Further optimization of C hyper-parameter resulted in the best model performance for $C = 250$.

The tuning of hyper-parameter ϵ was performed for the optimal value of hyper-parameter $C = 250$. By selecting different ϵ values, the model performance metrics showed that the optimal value

of ε -tube width is 0.1, for which the validation set observed the smallest RMSE error metric and the obtained accuracy is slightly lower than for the next iteration.

6.5.2. Application of Random Forest (RF) regression algorithm

The RF algorithm is based on the bootstrap aggregation or bagging, which is a reduction technique for handling variance of the estimated prediction function (Hastie et al., 2009). The algorithm seeks for the variance reduction by random selection of input variables in the tree-growing process, which contributes to the reduction of the correlation between them. Random forest consists of a specified number of decision trees, holding noisy and complex data interaction structures (Figure 6.16). Each regression tree is fitted to each bootstrap sample, which is randomly selected from the original training dataset and replaced (Segura et al., 2022). The regression tree grows by binary partitioning of the input variables randomly selected from the overall dataset, with defined decision criterion. Usually, it is defined through the minimization of residual sum of square (RSS) of the resulting tree. The partition process is repeated for the next small set of input variables and the data is further split in an iterative procedure which is limited by the RSS threshold or by a limited number of trees, maximum depth of each tree in the forest or other stopping condition (James et al., 2021).

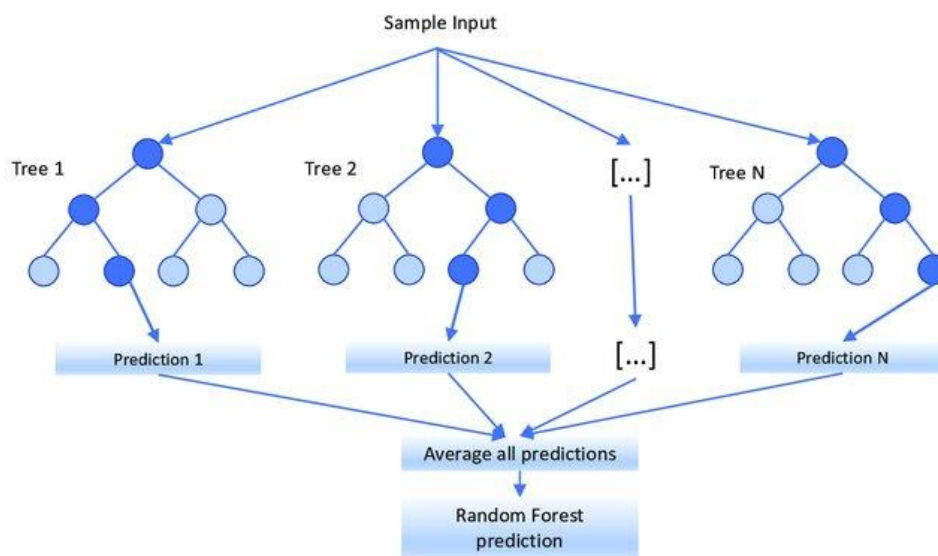


Figure 6.16 RF regression algorithm- a schematic diagram (Segura et al., 2022)

There are two important hyper-parameters for the RF algorithm: number of bagging samples and number of trees. Number of bagging iterations can be limited to the number of bootstrap samples. A recommendation for RF regression is given as $m = 2/3 p$, where m is number of bootstrap samples and p is number of the original data samples (Hastie et al., 2009). However, in practical applications the hyper-parameter value largely depends on the problem and therefore it is tuned

to provide the best model performance, where a smaller value of m may be particularly useful when there is a large number of correlated predictors (James et al., 2021).

The number of trees is not universally recommended but depends on the size of the dataset, number of input variables and nature of the problem (James et al., 2021). The best way to optimize the number of trees for a specific problem is to monitor the stabilization of the out-of-bag (OOB) sample error estimate, which can be characterized as a cross-validation method for RF algorithm, similar to the k -fold cross validation in the SVR algorithm. The random forest predictor is calculated for each observation z as an average of the trees corresponding to bootstrap samples which did not contain the z sample. Generally speaking, an increase in number of trees can significantly improve the prediction accuracy (James et al., 2021).

The performance of RF algorithm was tested for the development of a friction prediction model was tested by defining the input dataset, model hyper-parameters bagging sample size and number of trees in the forest in *XLStat* software. Again, as for the SVR algorithm, the dataset included all the calculated texture parameters and it was divided to training and validation sample as 75/25 ratio. The initial value of bagging sample size hyper-parameter was set to be 7, following the recommendation of bagging size equal to $2/3$ of the original sample size. The number of trees was set to be maximum to investigate which number of trees stabilizes the OOB sample error estimate. Figure 6.17 shows that the optimal number of trees would be approximately 110, therefore this value was adopted for further algorithm optimization.

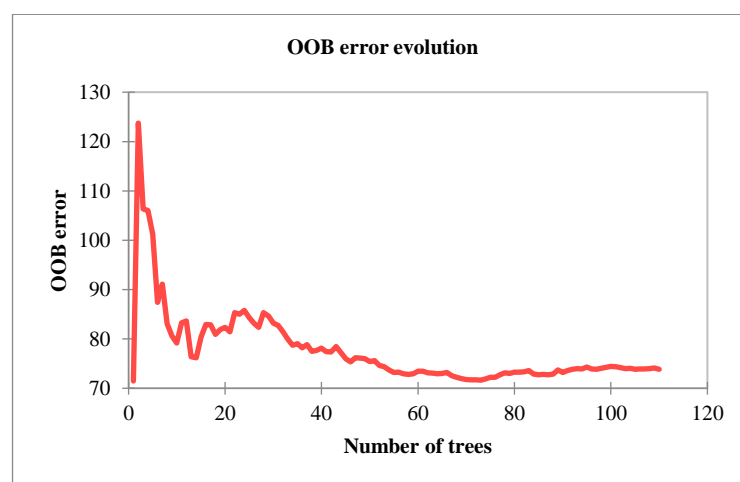


Figure 6.17 Stabilization of OOB sample error estimate used for the optimization of number of trees in the forest, *XL Stat 2023*

The size of bagging sample for an optimal number of trees was tested to assess the model performance via selected error metric for the validation sample, which was again RMSE. From

the results presented in Table 6.27 it can be concluded that the best performance of the RF model is obtained if the number of bagging samples was set to be between 7 and 10.

Table 6.27. Estimated error metric RMSE for different size of bagging sample of the RF algorithm

Bagging sample size	RMSE (Validation set) [-]
5	8.1585
7	5.6540
10	5.7546
12	8.2848

As already mentioned, RF algorithm measures the contribution of each explanatory variable in the dataset. Figure 6.18 shows the assigned variable importance to all the texture parameters included in the dataset, where it can be seen that the most important variables are Ppt and Pz, while the variables assigned with a “negative” importance to the prediction model performance are Pvt and Pcx. The results coincide well with the PLS regression analysis VIP scores, but also with the initial correlation analysis between the surface-related texture parameters and friction performance. To investigate the RF model performance if only the most important variables are accounted in the dataset, another algorithm iteration was performed with the model hyper-parameter bagging sample size set to 8. In comparison to the optimized sample size RF algorithm which accounted for all the texture parameters, this one showed better performance (Table 6.28).

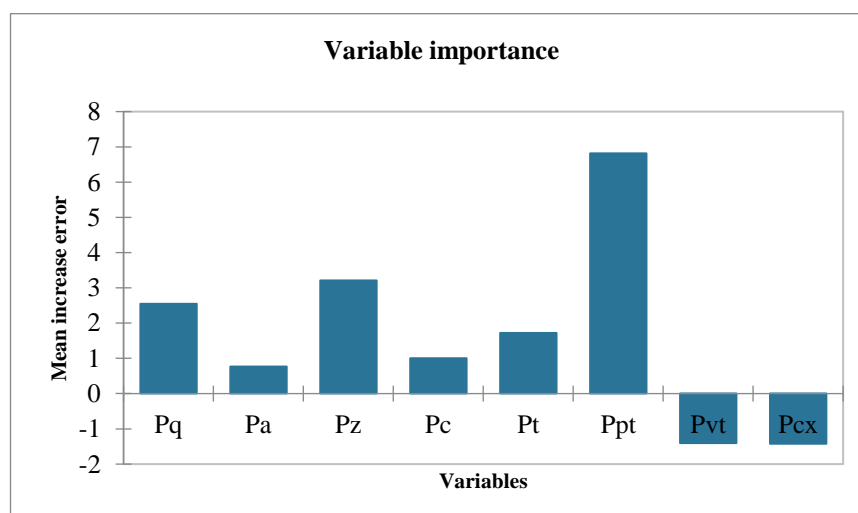


Figure 6.18 Variable importance evaluation for the optimized RF algorithm

Table 6.28. Evaluation of RF model performance for different input dataset

RF algorithm	Model input dataset	Number of trees	Bagging sample size	RMSE (Validation sample) [-]
V1	Pa, Pq, Pz, Pc, Pt, Ppt, Pvt, Pcx	110	8	4.6119
V2	Pz, Ppt			3.4237

6.5.3. Discussion

By comparing the error metric RMSE obtained for the two optimized ML algorithms explored in this research, it can be concluded that the performance of the RF algorithm is superior as the resulting error metric is lower. This conclusion follows the results of the performed research utilizing RF algorithm for pavement friction prediction by authors Zhan et al., 2021. It is also in agreement with the findings from the PLS regression analysis, where the same two texture parameters were selected as the most important for the friction prediction model establishment. However, the obtained results have to be taken with caution. The results of similar research exploring the ML framework for the friction prediction model establishment were training the model with a significantly larger dataset than the one explored in this thesis. Moreover, a recent research concluded that the power of the friction prediction model based only on texture-related parameters is significantly improved if some other influential parameters, such as aggregate characteristics and traffic volume were included in the RF regression framework (Yu et al., 2023).

The resulting error metric of the optimized RF prediction model is smaller in comparison to the RMSE of the optimized PLS regression model, which could lead to the conclusion that the ML framework gives best predictive power of pavement friction model based on non-standard texture parameters. However, the PLS regression model is established on the LR framework, which is more suitable for limited dataset size than the ML algorithms.

7. Conclusions and further research perspectives

In this chapter a summary of obtained research results is presented and discussed, with a special attention to the novelty and the scientific contribution of the performed research. The limitations of the research are also discussed. The chapter is concluded with the questions that have emerged from the conducted research and obtained results, and some future research perspectives.

7.1. Discussion of the overall research results

The main research aim of this thesis was the development of a pavement friction prediction model from the non-standard texture-related roughness parameters. The non-standard parameters cannot be determined from the traditional texture evaluation methods, therefore an advanced method based on remote sensing technology had to be developed and utilized for alternative texture roughness characterization.

Analyses of existing research in the field overviewed in Chapter 2 showed that research resulted in different empirical models with more or less successful prediction of friction performance. These models were uniquely classified into simple and complex empirical models, based on the number of influencing parameters they accounted for the friction prediction. The preliminary research described in Chapter 4 was done to investigate if the traditional friction measurement methods can be replaced by texture measurements resulting in a texture indicator that could predict the friction performance of a pavement in a reliable way (Pranjić et al., 2020). The performance of prediction model resulting from the preliminary research was weak, as the obtained correlation between friction and texture was not significant. Friction and texture values did not show an equal trend and varied significantly for the measured locations. The results indicated that the generalization of the friction prediction from the texture measurements regardless of the inspected location is not possible if only one texture indicator was used for the model establishment. The result was partially in agreement with previous research where only one texture indicator was observed for the friction prediction model establishment, as presented in Chapter 2.

Due to the described findings, this research direction was abandoned. In the next research phase advanced methods for texture characterization were explored as a possible solution for a better understanding of texture-friction relationship.

The first step was to establish a method for pavement surface data collection, which enables accurate roughness representation in relevant texture scales. Analyses of recent research in the field showed that photogrammetry is a well known remote sensing technology for pavement texture analysis, utilized in the last two decades for a detailed characterization of roughness properties in 2D and 3D, i.e. for profile-related or surface-related texture parameters. A similar technology is 3D laser scanning, which in comparison to the photogrammetry equipment requires high-end laser scanners for data acquisition.

Photogrammetry method was selected because of the existing expertise for large-scale civil engineering problems. The photogrammetry-based method utilized in this thesis for the analysis of texture roughness properties was developed for small-scale problems and named Close-Range Orthogonal Photogrammetry method – CROP. The method name stems from the special case of photogrammetry used, related to image acquisition from a close distance with camera positioned orthogonally to the inspected surface. Pavement surface images were captured by a single digital camera, representing an off-the-shelf device for data collection. Captured images were used for the creation of 3D digital surface model, from which the roughness features could be extracted and analysed with respect to their effect on the frictional performance. Texture roughness features were analysed in 2D framework to be comparable to the traditional texture indicator Mean Profile Depth (MPD). The calculated profile-related parameters were converted to surface-related properties and compared to the measured friction performance, showing a promising potential for texture-friction relationship establishment by using CROP method for texture data acquisition.

CROP method developed in this research was subjected to an extensive optimization and verification procedure. This included the investigation of optimal data acquisition procedure and equipment setup, which was not performed in any other similar research overviewed in Chapter 3.

Two different methods for data acquisition were explored and compared, using same photographic equipment in different ways for texture data acquisition: *Turntable* and *Ortho*. The latter showed better performance in terms of quality of the reconstructed digital surface model and simplicity of the data acquisition procedure. Four camera lenses were tested for image acquisition and creation of digital models, whose performance was compared and evaluated by selected error metrics and properties of reconstructed digital model. Following the data acquisition procedure optimization, a unique workflow for texture roughness features analysis was defined (Figure 7.1). The optimized CROP method produced DSM with resolution within sub-millimeter range, making it suitable for the analysis of macro-texture effects in the full level range and micro-texture effect to a limited range of values up to 0.01 mm.

The obtained accuracy of CROP method verified by a benchmark procedure for 3D data acquisition on sub-millimeter scales was 0.05 mm. To verify the CROP method, a custom made reference frame was created and digitalized by 3D laser scanning and CROP method with two different cameras. The verification was done on a CAD designed object with known dimensions. This enabled a direct comparison of the corresponding dimensions on the digital models created by laser scanning procedure and CROP method. In comparison to similar research utilizing

photogrammetry-based method for texture surface reconstruction where the verification was done by comparison to a traditional measurement method (J. Chen et al., 2019; Tian et al., 2020), the effects of measurement method uncertainties were excluded. The verification procedure showed that the CROP method does not produce digital surface models with such high level of accuracy as the 3D laser scanner for the entire model's surface. The deviations of the plane dimensions and height differences were larger on the model margins. However, as the reference frame was also created for pavement surface data acquisition, the model anomalies on the outer frame edges were not considered as relevant for the method performance in data collection as the observed pavement surface was in the central part of the reference frame.

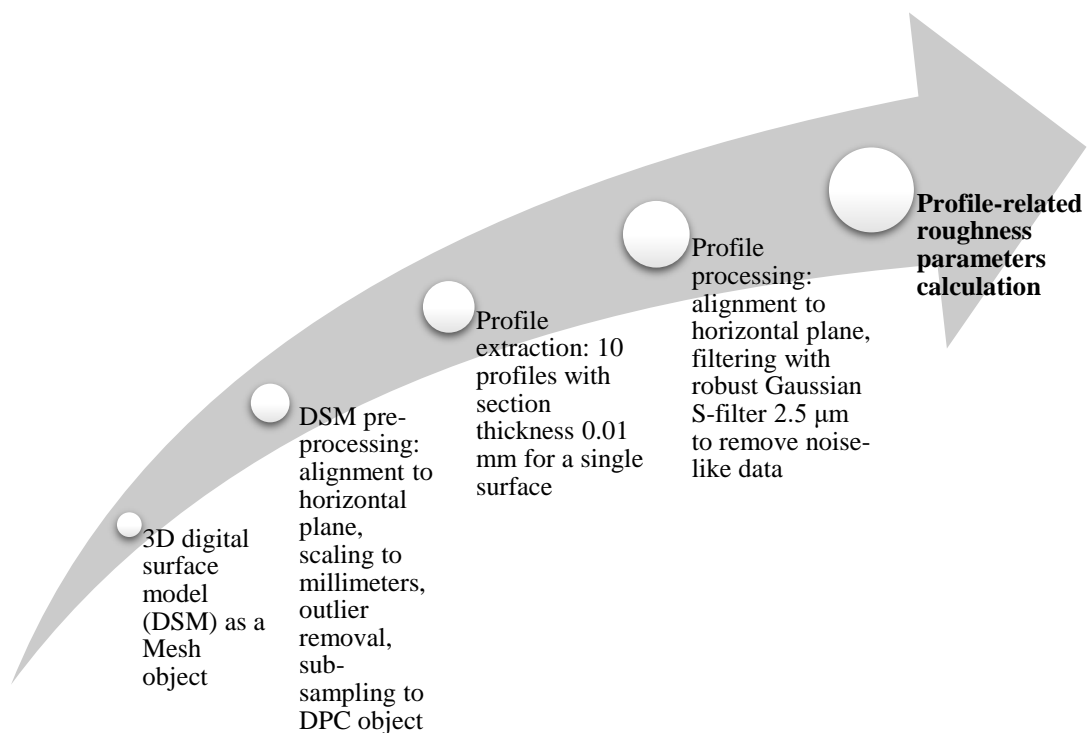


Figure 7.1 A schematic overview of performed workflow for texture data processing for the calculation and analysis of profile-related roughness parameters

Considering the texture data acquisition and analysis, the drawback of the established CROP method is an excessive amount of time necessary to derive texture roughness characterization in comparison to traditional pavement texture evaluation methods, where texture parameters are directly exported after the measurement. The data collection procedure is manual, requiring an experienced technician in the field of photogrammetry. The reconstruction of digital surface model from acquired images requires time and efficient computational equipment, as well as a good knowledge and operating experience with the photogrammetry software. The quality of resulting DSM depends on the pre-processing adjustments in the software, selected manually to reduce the error metrics analysed in Chapter 4. The resulting RMS reprojection error value for the

optimized CROP method model of 0.3 was marginally acceptable value, following the recommendations given in (Over et al., 2021). A digital surface model with higher accuracy could be obtained for further fine-tuning of input pre-processing parameters.

The friction prediction model was developed in regression analysis framework, accounting for the texture roughness parameters determined on primary profiles, without the scale separation to micro- and macro-texture level. The selected texture parameters were determined from profile representations of analysed surfaces and converted to surface-related parameters to be comparable to the friction performance determined on the same surfaces. An extensive exploratory data analysis was performed to investigate the properties of calculated roughness parameters related to profile and surface morphology and to select only those parameters representative for the establishment of a friction prediction model. Profile-related parameters were converted to their surface equivalents by accounting for the variability in the profile data and excluding the profiles which showed an outlier character. Figure 7.2. summarizes the performed procedures in the friction prediction model establishment.

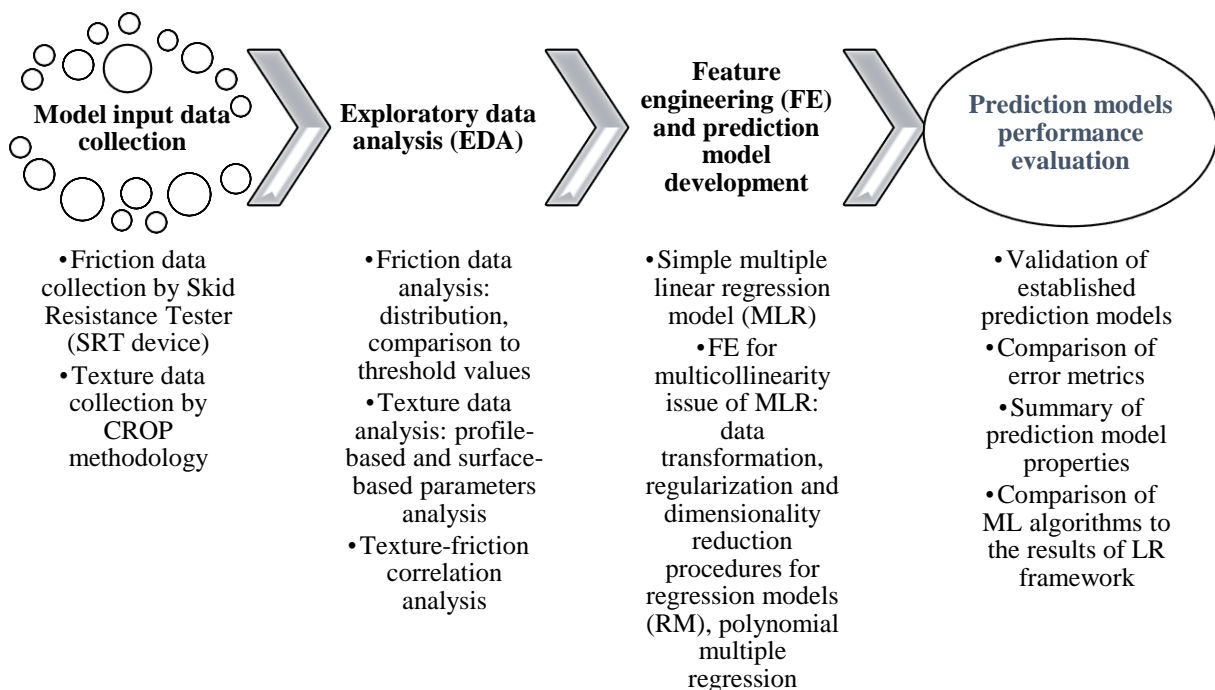


Figure 7.2 A graphical summary of data analysis procedures in the process of friction prediction model establishment

The initial friction prediction model was defined for traditional texture roughness indicator, Mean Profile Depth. This model showed a moderate correlation with the measured friction performance expressed in Skid Resistance Test number in range from $SRT = 68.4$ to $SRT = 103.2$, with $R^2 = 0.592$ and $RMSE = 6.162$. The obtained result was comparable to previous research results where Mean Profile Depth derived from pavement digital surface models was correlated to measured

friction performance (Čelko et al., 2016; Wang et al., 2019). Furthermore, the obtained texture-friction relationship was significantly higher in comparison to the results obtained in the preliminary research described in Chapter 4, where no significant relationship was observed between texture and friction indicators.

As the aim of this research was to establish a friction prediction model from non-standard texture parameters, a multiple linear regression model was defined accounting for those that showed the most significant effect to friction in the exploratory data analysis: Mean average roughness P_a , Maximum height P_z , Mean profile element height P_c and Maximum peak profile height P_{pt} , calculated according to EN ISO 21920-2: *Geometrical product specifications (GPS) — Surface texture: Profile — Part 2: Terms, definitions and surface texture parameters*. The obtained regression statistic was higher in comparison to the initial prediction model, with $R^2 = 0.762$ and $RMSE = 4.581$.

The model had to be additionally processed to satisfy the linear regression framework by feature engineering procedures, applied to remove the multicollinearity issue for the predictor variables – texture parameters. The final model was established in regression framework by performing partial least squares (PLS) feature engineering procedure. The PLS regression algorithm accounted for the influence of all four texture parameters on the friction performance and sorted out the two most influential parameters: one amplitude parameter - Maximum height P_z and one feature parameter – Maximum peak profile height P_{pt} . The resulting model statistics were $R^2 = 0.784$ and $RMSE = 4.412$, indicating better performance of the friction prediction model in comparison to initial linear regression model accounting for traditional texture parameter Mean Profile Depth.

Previous research utilizing the photogrammetry-based method for texture data assessment resulted in lower friction prediction model performance (El Gendy et al., 2011; Kogbara et al., 2018; Mahboob Kanafi et al., 2015; Medeiros et al., 2021) and similar or better model performance for a complex data acquisition procedure consisting of multiple cameras, additional light sources and fixed platforms applicable only for laboratory measurements (D. Chen, 2020; Huyan et al., 2020; Wang et al., 2019). Some of the friction prediction models developed from texture parameters derived from pavement digital surface models resulting from 3D laser scanning procedure showed weaker or similar performance to the model developed in this thesis (Alhasan et al., 2018; Čelko et al., 2016; Hu et al., 2016; Q. J. Li et al., 2020; Q. J. Li et al., 2017) and some performed much better with very high predictive power (Kováč et al., 2021; L. Li et al., 2016). High-performance models utilized surface-related parameters determined directly from the

pavement surface morphology as model predictors, mostly by applying laser scanning technology. The precision of 3D laser scanners for texture data acquisition is better in comparison to photogrammetry method, as was showed in the verification procedure. However, laser scanners are high-end data collection equipment, less available than digital cameras utilized in photogrammetry methods. Texture data acquisition procedure established in this research is simple and easily repeatable, utilizes a single digital camera and a reusable reference frame for the precise and accurate digital surface model reconstruction. It is applicable for laboratory and field measurements and the inspected pavement surface area is sufficiently large to be comparable to traditional texture volumetric measurements and low-speed friction evaluation.

7.2. Research limitations

This research was limited to analysis of pavement texture morphology influence to friction performance of asphalt pavements. In comparison to some complex empirical friction prediction models overviewed in Chapter 2, where other influencing parameters were accounted for the prediction model establishment, the performance of the prediction model developed in this thesis was weaker. The dataset used for the prediction model establishment was obtained from twenty pavement surfaces with unknown properties, except for the friction performance measured with low-speed pendulum device Skid Resistance Tester. The measured friction values were in a range from $SRT = 68.4$ to $SRT = 103.2$ and above the threshold level for friction performance defined in Croatian regulations. A larger number of investigated surfaces with wider range of friction measurement values, together with the inclusion of other influencing parameters related to pavement surface properties such as aggregate type or mixture design and gradation might contribute to establishment of a prediction model with better predictive power.

Selected non-standard texture parameters utilized as predictors in the model were derived from profiles extracted from DSMs and converted to surface-related parameters to be comparable to the surface's friction performance. Surface roughness representation expressed in surface-related parameters derived from their profile equivalents is just an approximation and doesn't reflect true surface roughness characteristics. Profile-related parameters were selected so they could be compared to the traditional profile-related texture parameter Mean Profile Depth (MPD). However, a friction prediction model which accounts for true surface-related parameters calculated from the surfaces would be more realistic representation of pavement texture effect to the friction performance.

7.3. Final conclusions

The performed research focused on the establishment of a friction prediction model from the non-standard texture parameters, derived from the advanced method for texture characterization. A novel method for texture data acquisition, called Close-Range Orthogonal Photogrammetry - CROP method was developed and verified for accuracy by comparing the performance of resulting digital surface model with the properties of digital surface model created by a benchmark remote sensing technology 3D laser scanner. Texture roughness features were represented on full scale of macro-texture wavelength and amplitude range and micro-texture scale larger than 0.01 mm. A procedure for texture data processing and analysis by specialized softwares was established. A set of profile-related texture parameters, describing roughness features on both relevant texture scales was obtained from digital surface models of pavement surface.

Selected texture parameters were utilized for the establishment of a friction prediction model by application of feature engineering procedures. This was a novel approach for the development of a friction performance prediction model in regression framework, based on uniquely derived non-standard texture parameters that showed to be the most significant with respect to the applied regression algorithms. The resulting model was defined within the partial least squares (PLS) regression method. This method selected the most significant texture parameters with the highest influence on friction performance: amplitude parameter Maximum height P_z and feature parameter Maximum peak profile height, P_{pt} . Maximum height (P_z) parameter describes an overall roughness property and Maximum peak profile height (P_{pt}) is a description of extreme roughness property of a pavement surface. The established model's performance for the prediction of pavement frictional characteristics was superior in comparison to the prediction model defined by a single traditional texture indicator Mean Profile Depth (MPD). It showed better performance in comparison to prediction models developed in previously performed similar research.

The results obtained in this research confirmed the research hypotheses defined in Chapter 1, proving that:

H1: Close-range photogrammetry based method is suitable for the determination of non-standard pavement texture parameters.

H2: Non-standard texture parameters enable a more detailed description of surface roughness properties related to the pavement friction performance in comparison to traditional texture descriptors.

H3: Non-standard texture parameters can be used for the definition of a friction prediction model which is more reliable in comparison to the prediction models defined from traditional texture indicators.

In this way, the defined research goals were accomplished and the main research aim was reached.

7.4. Future research perspectives

In recent few years, research community dealing with pavement friction prediction models' development started utilizing machine learning framework, with superior results in comparison to the traditional approach for friction prediction, mostly based on regression analysis. The main premise of all performed research is a large dataset. The final section of Chapter 6 introduced two machine learning (ML) algorithms as a possible framework for friction prediction model development. The preliminary results of ML algorithm implementation showed a good performance for both tested methods, with obtained RMSE values lower from the error metric of the established prediction model in classical regression framework. However, the available dataset is too small for the implementation of ML algorithms which would provide reliable results.

By summarizing the results obtained in this thesis research, the highlighted research limitations and current research trends, some future research perspectives are defined as the conclusion of this Chapter:

- CROP method automation for fast, precise and accurate data acquisition
- Further optimization of DSM reconstruction procedure by adjustment of alignment procedure inputs to obtain a DSM with smaller RMS reprojection error value, which implies higher model accuracy
- Texture data analysis extension to 3D surface-related roughness features determined from surface morphology
- Wider range of measured pavement friction values
- Further development of friction prediction model in regression framework by including other pavement texture related influencing parameters, such as asphalt mixture properties relevant for friction performance
- Implementation of ML framework for the development of more robust prediction model on a larger dataset

List of Figures

- Figure 1.1 A schematic overview of research activities performed in this thesis
- Figure 2.1. Definition of friction coefficient μ as a ratio between tangential friction force (T) and Normal force (F)
- Figure 2.2. Difference between static, sliding and rolling friction
- Figure 2.3. Difference between contact area for smooth contact (left) and rough contact (right)
- Figure 2.4. The effect of magnification level on the contacting interface and the distribution of the stress function defined in Persson's contact theory (Persson, 2001)
- Figure 2.5. Pavement friction phenomenon and forces in the system (from Hall et al., 2009)
- Figure 2.6. Adhesion and hysteresis mechanisms of pavement friction on dry (a,c) and wet (b,d) pavement surfaces (from Fwa, 2021)
- Figure 2.7. Slip ratio versus pavement friction performance (Hall et al., 2009)
- Figure 2.8. The effect of different texture levels on the slip ratio (Yu et al., 2020)
- Figure 2.9. Friction measurement devices with different operating principles: (i) pendulum-based devices, (ii) single-spot dynamic friction testers, (iii) locked wheel dynamic testers, (iv) fixed slip dynamic testers, (v) variable slip dynamic testers, (vi) sideways force testers (Rajaei et al., 2016)
- Figure 2.10. TYROSAFE project analysis of friction national policies (Nitsche & Spielhofer, 2009)
- Figure 2.11. Friction prediction models – a schematic overview
- Figure 3.1. An example of full-length profile
- Figure 3.2 Characteristic profile-related texture dimensions
- Figure 3.3. Texture classification by PIARC with four texture levels and different reference lengths of a pavement at which they are relevant (Hall et al., 2009)
- Figure 3.4. Texture levels according to the PIARC categorization and the specific effect on the pavement surface-vehicle interaction (Hall et al., 2009)
- Figure 3.5. The combined effects of micro-texture and macro-texture on friction performance for an increase in vehicle speed (Hall et al., 2009)
- Figure 3.6. Micro-texture level of pavement surface roughness (Kotek&Kovac, 2015)
- Figure 3.7. Macro-texture of different asphalt mixtures on laboratory samples: a) dense-graded mixture HMA, b) gap-graded mixture SMA, c) porous mixture PA (author's images, 2023)
- Figure 3.8. The physical meaning of MPD profile-related texture parameter (Kovač et al., 2015)
- Figure 3.9. Characteristic horizontal and vertical dimensions for profile roughness analysis according to EN ISO 21920-2
- Figure 3.10. Profile-related texture roughness parameters from EN ISO 21920-2

Figure 3.11. Surface-related texture roughness characterization from EN ISO 25178-2

Figure 3.12. Fractal nature of rough surfaces with an increase of fractal dimension D_f , (https://www.wikiwand.com/en/Fractal_dimension, accessed 19.5.2023)

Figure 3.13. PSD function of different asphalt pavement types (Deng et al., 2021)

Figure 4.1 The measured highway section A4, junction Popovec – Sveta Helena (Analiza vrijednosti makroteksture i hvatljivosti na definiranim dionicama autocesta..., - Izvještaj, 2019)

Figure 4.2. Data collection devices: friction measurement device (a) and texture measurement device (b)

Figure 4.3. Friction (a) and texture (b) measurement results compared before and after the pavement rehabilitation

Figure 4.4. Scatterplot of texture and friction data for all measurement results

Figure 4.5. Scatter plots for MPD and LFC values for passing lane, before (a) and after (b) the rehabilitation procedure

Figure 5.1 Roller compaction device (a) and produced rectangular specimen in a mold (b), Transportation laboratory Faculty of Civil engineering Rijeka, 2021

Figure 5.2. SRT low-speed friction measurement device(a) and friction measurement assembly on produced asphalt specimen (b)

Figure 5.3. Agisoft Metashape workflow scheme for 3D object reconstruction from photogrammetry-based data acquisition method

Figure 5.4. 3D Mesh object (a) and a close-up of mesh structure (c) and 3D DPC object (b) and a close-up of DPC structure (d) in millimeters

Figure 5.5. Segmented profiles' position on DPC model (a) and profile close-up for one section (b) and one profile (c)

Figure 5.6. Metashape markers arrangement(a) and image acquisition procedure example(b)

Figure 5.7. DPC alignment procedure in Cloud Compare: aerial view (a) and side view (b)

Figure 5.8. Aligned DPCs and the position of extracted sections

Figure 5.9. An example of profile portion segmented from the DPC with two different section thicknesses: section thickness 0.01 mm (upper) and section thickness 0.005 (lower)

Figure 5.10. Comparison of profile geometry for different data acquisition modes

Figure 5.11. Comparison of profiles' roughness representation for different data acquisition modes

Figure 5.12. Aligned DPCs from Mode 3 and Mode 4 and marked positions of ten sections for profiles extraction

Figure 5.13. Profile P9 geometry extracted from Mode 3 and Mode 4 data acquisition modes

Figure 5.14. CAD design for the reference frame (a) and the produced reference frame with attached markers prior to the data acquisition procedure (b)

Figure 5.15. ATOS III Triple Scan laser scanning system assembly, Centre for advanced modelling and calculations, University of Rijeka, 2022

Figure 5.16. A DSM of 3D laser scanning result object: Mesh (a,b) and DPC (c,d)

Figure 5.17. Dimensions (a, b) and height measurement positions (c, d) on DSM selected for the comparison with the measurements on actual frame, determined with respect to the reference frame objects for precise measurements

Figure 5.18. CROP procedure performed for reference frame DSM acquisition

Figure 5.19. Reference DPC (left) and DPC to be aligned (right) with marked alignment points

Figure 5.20. Color scale scalar field of C2C distances for DPC of the reference frame and corresponding histograms for Canon Mode (a) and Nikon Mode (b) DSM

Figure 5.21. Percentage points (%) falling within C2C distance ranges < 0.5 mm for DPCs created by two different data acquisition setups

Figure 5.22. Distance measurements on Nikon Mode DPC

Figure 5.23. Measured heights (Δz coordinate) for upper (a) and lower (b) edge of reference frame DPC created by Nikon Mode

Figure 5.24 A schematic summary of procedures performed in the CROP methodology development and verification

Figure 6.1 A schematic overview of performed procedures and used tools in the friction prediction model establishment

Figure 6.2 Map of sites where friction and texture data were collected. Blue marked sites are located on urban road network, yellow marked site is the position of parking area (Google Earth, 2023)

Figure 6.3 Friction measurement assembly with SRT pendulum (a) and close-up of an example of measured pavement surface (b), 2023

Figure 6.4 Texture data acquisition procedure by CROP methodology, 2023

Figure 6.5 Characteristic profile geometry dimensions: l_e is profile evaluation length, l_s is n -th profile section length, X_s is profile element width and Z_t is profile element height

Figure 6.6 Q-Q normal probability plot (left) and histogram of SRT mean values (right) showing normal data distribution

Figure 6.7 Range values for surface-related overall roughness parameters (left) and extreme roughness parameters (right).

Figure 6.8 Scatter plots for surface-related non-standard texture parameters versus measured friction performance expressed in SRT

Figure 6.9 Linear regression fit for traditional texture parameter MPD versus friction expressed as SRT

Figure 6.10 Confirmations of MLR assumptions: normally distributed residuals (a), homoscedascity (b), no correlation between explanatory variable Pz and residuals (c) and Pc and residuals (9d)

Figure 6.11 Normal distribution of residuals confirmed by Q-Q plots for PCA regression models V1 (a) and V2 (b) and outlier test Z-score for PCA V1 (c) and PCA V2 (d) regression models

Figure 6.12 VIP scores for parameters Pa, Pz, Pc and Ppt used for the creation of PLS regression component

Figure 6.13 Normal probability Q-Q plot and Z-score test for the PLS regression model V1

Figure 6.14 Normal probability plot for MPR model residuals and Z-score test of outliers, showing one outlier in the dataset

Figure 6.15 SVR with linear kernel and ϵ -tube width, all datapoints outside the ϵ -tube width are support vectors (Rodriguez-Perez and Bajorath, 2022)

Figure 6.16 RF regression algorithm- a schematic diagram (Segura et al., 2022)

Figure 6.17 Stabilization of OOB sample error estimate used for the optimization of number of trees in the forest, XL Stat 2023

Figure 6.18 Variable importance evaluation for the optimized RF algorithm

Figure 7.1 A schematic overview of performed workflow for texture data processing for the calculation and analysis of profile-related roughness parameters

Figure 7.2 A graphical summary of data analysis procedures in the process of friction prediction model establishment

List of Tables

- Table 2.1. A summary of the positive and negative effects of the key influencing parameters for pavement friction performance
- Table 2.2. An overview of friction measurement devices used in Europe (Andriejauskas et al., 2014)
- Table 2.3. Required friction levels in some EU countries (Wallman and Astrom, 2001; Litzka et al., 2008)
- Table 2.4. Threshold friction levels in non-EU countries (Hall et al., 2009)
- Table 2.5. Proposed transfer functions for the friction Technical Parameters analyzed in COST 354 Action (Litzka et al., 2008)
- Table 2.6. Performance Index grades for friction determined by two different measurement devices and resulting Technical Parameters SFC and LFC, (Litzka et al., 2008)
- Table 2.7. National policies of friction and texture monitoring for ROSANNE project participating countries (Goubert et al., 2014)
- Table 2.8 Friction performance requirements for newly built roads - acceptance criterion (Tehnički propis za asfaltne kolnike, 2021)
- Table 2.9. Friction performance requirements at the end of warranty period for different aggregate types in asphalt mixture (Tehnički propis za asfaltne kolnike, 2021)
- Table 2.10. Examples of FEM application for numerical modelling of pavement friction phenomenon
- Table 2.11. Overview of empirical friction prediction models with texture emphasized as the main predictor for friction performance
- Table 3.1 Pavement texture levels and classification with respect to the wavelengths and amplitudes and the effect on the pavement-vehicle interaction phenomenon
- Table 3.2. Positive and negative effects of asphalt mixture properties on the pavement macro-texture
- Table 3.3. Volumetric contact methods for macro-texture characterization
- Table 3.4. Properties of profilometric devices for pavement texture characterization (EN ISO 13473-3)
- Table 3.5. Summary of macro-texture evaluation in European countries for road authorities decision making policies and data analysis (Aavik et al., 2013)
- Table 3.6. Macro-texture performance indicator values expressed in MPD, (Litzka et al., 2008)
- Table 3.7. Threshold values for macro-texture performance assessment in Croatia (Technical specification for asphalt pavements, 2021)

Table 3.8. Macro-texture prediction models based on asphalt mixture properties

Table 3.9. Research results exploiting photogrammetry method for pavement texture characterization and analysis

Table 3.10. Research results for pavement texture roughness features analysis by 3D laser scanning methods for data acquisition

Table 4.1 Correlation analyses results for different dataset size

Table 5.1 Asphalt mixture properties for the produced asphalt specimen

Table 5.2. Friction performance of asphalt specimen evaluated by SRT measurements

Table 5.3. Photographic equipment specifications

Table 5.4. A schematic representation of camera movement for Turntable and Ortho image acquisition mode and images of performed data acquisition process with two different methods

Table 5.5. Resulting DSM properties for two data acquisition modes (from generated Agisoft Metashape Processing reports)

Table 5.6. Pearson's correlation coefficients for analysed profile-related texture parameters and measured friction

Table 5.7. Camera lens properties for different CROP method data acquisition equipment

Table 5.8. DSM properties for models generated from different data acquisition procedures (from Metashape Processing Reports generated for the created DSMs, 2022)

Table 5.9. Number of points in extracted sections for DPCs obtained from different data acquisition modes and resulting horizontal resolution of profiles

Table 5.10. Profile-related parameters extracted from DSMs from Mode 3 (M3) and Mode 4 (M4) data acquisition setup

Table 5.11. Mean absolute difference for profile-related parameters for Mode 3 and Mode 4 (Table 5.10) and average value $MAD_{average}$ for each calculated parameter

Table 5.12. Calculated descriptive statistics for profiles extracted from Mode 3 and Mode 4 DSM

Table 5.13. Calculation of mean parameters values for a different number of profiles for both data acquisition setups

Table 5.14. Calculated absolute differences between the plane dimensions determined on frame and DSM created from 3D laser scanning procedure

Table 5.15. Calculated absolute differences between the height dimensions determined on frame and DSM created from 3D laser scanning procedure

Table 5.16. Properties of different photogrammetry acquisition devices

Table 5.17. Resulting photogrammetry 3D DSMs properties, Metashape Processing reports

Table 5.18. Calculated C2C distance ranges and percentage of DPC points falling within each distance range for C2C distance < 0.5 mm

Table 5.19. Measured point-to-point distances on selected positions for both aligned DPCs and reference frame DSM

Table 5.20. Comparison of absolute differences between actual measurements on reference frame and distance measurements on DSMs created with different data acquisition methods (3D laser scanning and photogrammetry)

Table 5.21. Comparison of frame thicknesses measured on actual frame and DPC frame created by Nikon Mode CROP method

Table 6.1 Measured values of SRT on all investigated sites and mean calculated SRT values

Table 6.2. Profile-related texture parameters calculated for the surface properties analysis

Table 6.3. Profile-related texture parameters distribution fitting. None of the parameters follows the normal distribution, most parameters are skewed to the left

Table 6.4. Kendall's correlation coefficient matrix for profile-related texture parameters. Values in bold are statistically significant with p-value below $\alpha=0.05$

Table 6.5. CV (%) statistics for mean values of overall roughness parameter Pa determined for all observed surfaces

Table 6.6. Calculated Pa parameter mean values for all surfaces, corresponding CV (%) and surface classification according to the CV value

Table 6.7. Z-score outlier test results for non-homogenous surfaces

Table 6.8 Outlier profiles analysis by extreme roughness texture parameters

Table 6.9. Results of additional outlier analysis performed for non-homogenous surfaces

Table 6.10. Surface-related texture parameters: final dataset

Table 6.11. Surface-related parameters distribution for the final surface texture dataset

Table 6.12 Kendall's correlation coefficient matrix for surface-related texture parameters and friction. Values in bold are statistically significant. Values higher than 0.4 are indication of a moderate relationship and values higher than 0.6 are indication of a strong relationship

Table 6.13. MLR models performance comparison

Table 6.14. VIF scores for 1st and 2nd iteration of MLR model

Table 6.15. MLR assumptions overview and evaluation for the texture dataset

Table 6.16. An overview of optimized regression models' performance statistics and comparison to the initial MLR prediction model

Table 6.17. Model statistics for Ridge regression with parameter λ optimized by k-fold cross-validation method

Table 6.18. Optimization of Ridge regression by removing the explanatory variables with negative sign of model parameters

Table 6.19. Principal components analysis results for dimensionality reduction by selecting the explanatory variables with the most significant contribution to the “new” model inputs defined as principal components (PC’s)

Table 6.20. PCA regression model optimization by analysis of model parameters values

Table 6.21. Summary statistics of PLS regression models optimized by number of explanatory variables in the PLS component based on VIP score and outlier test of model residuals

Table 6.22. Resulting error metrics for the MPR model iterations: V1 is the model containing the outlier detected with the Z-score test, V2 is the model without the outlier in the dataset

Table 6.23. A summary of the models’ error metric RMSE, model input variables and the resulting model equations observed in the optimized MLR framework

Table 6.24. Comparison of models’ performance: initial linear regression model with MPD as explanatory variable and optimized PLS regression model with two non-standard texture parameters as explanatory variables

Table 6.25. An overview of ML algorithms, dataset properties and results utilized for the establishment of a friction performance prediction model

Table 6.26. SVR algorithm hyper-parameters optimization and the resulting statistics of the friction prediction model

Table 6.27. Estimated error metric RMSE for different size of bagging sample of the RF algorithm

Table 6.28. Evaluation of RF model performance for different input dataset

References

- Ahamed, M. A., & Tighe, S. L. (2008). Statistical modeling in pavement management do the models make sense? *Transportation Research Record*, 2084, 3–10.
<https://doi.org/10.3141/2084-01>
- Ahamed, M. A., & Tighe, S. L. (2012). Asphalt pavements surface texture and skid resistance - Exploring the reality. *Canadian Journal of Civil Engineering*, 39(1), 1–9.
<https://doi.org/10.1139/L11-109>
- Alamdarlo, M. N., & Hesami, S. (2018). Optimization of the photometric stereo method for measuring pavement texture properties. *Measurement: Journal of the International Measurement Confederation*, 127, 406–413.
<https://doi.org/10.1016/j.measurement.2018.05.109>
- Al-Assi, M., & Kassem, E. (2017). Evaluation of adhesion and hysteresis friction of rubber-pavement system. *Applied Sciences (Switzerland)*, 7(10). <https://doi.org/10.3390/app7101029>
- Al-Assi, M., Kassem, E., & Nielsen, R. (2020). Using Close-Range Photogrammetry to Measure Pavement Texture Characteristics and Predict Pavement Friction. *Transportation Research Record*, 2674(10), 794–805. <https://doi.org/10.1177/0361198120936650>
- Alauddin Ahmed, M., & Tighe, S. L. (2010). Effect of Short-term and Long-term Weather on Pavement Surface Friction. *International Journal of Pavement Research and Technology* (Vol. 3, Issue 6).
- Alhasan, A., Smadi, O., Bou-Saab, G., Hernandez, N., & Cochran, E. (2018). Pavement Friction Modeling using Texture Measurements and Pendulum Skid Tester. *Transportation Research Record*, 2672(40), 440–451. <https://doi.org/10.1177/0361198118774165>
- Alpaydin, E. (2014). Introduction to Machine Learning 3rd Edition. *The MIT Press*.
[https://dl.matlabyard.com/siavash/ML/Book/Ethem%20Alpaydin-Introduction%20to%20Machine%20Learning-The%20MIT%20Press%20\(2014\).pdf](https://dl.matlabyard.com/siavash/ML/Book/Ethem%20Alpaydin-Introduction%20to%20Machine%20Learning-The%20MIT%20Press%20(2014).pdf)
- Andriejauskas, T., Vorobjovas, V., & Mielonas, V. (2014). Evaluation of skid resistance characteristics and measurement methods. *9th International Conference on Environmental Engineering, ICEE 2014*. <https://doi.org/10.3846/enviro.2014.141>
- Araujo, V. M. C., Bessa, I. S., & Castelo Branco, V. T. F. (2015). Measuring skid resistance of hot mix asphalt using the aggregate image measurement system (AIMS). *Construction and Building Materials*, 98, 476–481. <https://doi.org/10.1016/j.conbuildmat.2015.08.117>
- Asi, I. M. (2007). Evaluating skid resistance of different asphalt concrete mixes. *Building and Environment*, 42(1), 325–329. <https://doi.org/10.1016/j.buildenv.2005.08.020>

- Barazzetti, L., & Scaioni, M. (2010). Development and implementation of image-based algorithms for measurement of deformations in material testing. *Sensors*, *10*(8), 7469–7495. <https://doi.org/10.3390/s100807469>
- Barber, J. R. (2018). *Solid Mechanics and Its Applications Contact Mechanics*, Springer, <http://www.springer.com/series/6557>
- Basu, A., & Chowdhury, R. (2017). The Effect of Surface Texture on Skid Resistance of Asphalt Pavements. *International Journal of Innovative Research and Advanced Studies (IJIRAS)*, *4* (2), <https://www.semanticscholar.org/paper/The-Effect-Of-Surface-Texture-On-Skid-Resistance-Of-Chowdhury/18f00a87aa11ee2e4e14baca2b1700ce31c75931>
- Bilten o sigurnosti cestovnog prometa 2021. (2022). *Ministarstvo unutarnjih poslova Republike Hrvatske*. https://mup.gov.hr/UserDocsImages/statistika/2022/Bilten_o_sigurnosti_cestovnog_prometa_2021.pdf
- Birkner, C., Adesiyun, A., Greene, M., Conter, M., Schmidt, B., Sandberg, U., Scharnigg, K., & Haider, M. (2016). ROSANNE Project Final Summary Report. <https://www.rosanne-project.eu/documents?id=7299#>
- Bitelli, G., Simone, A., Girardi, F., & Lantieri, C. (2012). Laser scanning on road pavements: A new approach for characterizing surface texture. *Sensors (Switzerland)*, *12*(7), 9110–9128. <https://doi.org/10.3390/s120709110>
- Bonari, J., & Paggi, M. (2020). Viscoelastic effects during tangential contact analyzed by a novel finite element approach with embedded interface profiles. *Lubricants*, *8*(12), 1–15. <https://doi.org/10.3390/lubricants8120107>
- Bonari, J., Marulli, M. R., Hagemeyer, N., Mayr, M., Popp, A., & Paggi, M. (2020). A multi-scale FEM-BEM formulation for contact mechanics between rough surfaces. *Computational Mechanics*, *65*(3), 731–749. <https://doi.org/10.1007/s00466-019-01791-3>
- Bonari, J., Paggi, M., & Dini, D. (2022). A new finite element paradigm to solve contact problems with roughness. *International Journal of Solids and Structures*, *253*, 111643, <https://doi.org/10.1016/j.ijsolstr.2022.111643>
- Bonari, J., Paggi, M., & Reinoso, J. (2021). A framework for the analysis of fully coupled normal and tangential contact problems with complex interfaces. *Finite Elements in Analysis and Design*, *196*. <https://doi.org/10.1016/j.finel.2021.103605>
- Bugnicourt, R., Sainsot, P., Lesaffre, N., Lubrecht, A., Bugnicourt, R., Sainsot, P., Lesaffre, N., & Lubrecht, A. A. (2017). Transient frictionless contact of a rough rigid surface on a

viscoelastic half-space. *Tribology International*, Elsevier.

<https://doi.org/10.1016/j.triboint.2017.01.032>

Callai, S. C., De Rose, M., Tataranni, P., Makoundou, C., Sangiorgi, C., & Vaiana, R. (2022).

Microsurfacing Pavement Solutions with Alternative Aggregates and Binders: A Full Surface Texture Characterization. *Coatings*, 12(12). <https://doi.org/10.3390/coatings12121905>

Cano-Ortiz, S., Pascual-Muñoz, P., & Castro-Fresno, D. (2022). Machine learning algorithms for monitoring pavement performance. In *Automation in Construction* (Vol. 139). Elsevier B.V. <https://doi.org/10.1016/j.autcon.2022.104309>

Cantisani, G., D'Andrea, A., Di Mascio, P., & Loprencipe, G. (2016). Reliance of pavement texture characteristics on mix-design and compaction process. In *RILEM Bookseries* (Vol. 11, pp. 271–281). Kluwer Academic Publishers. https://doi.org/10.1007/978-94-017-7342-3_22

Canudas-De-Wit, C., Tsiotras, P., Velenis, E., Basset, M., & Gissinger, G. (2003). Dynamic Friction Models for Road/Tire Longitudinal Interaction. *Vehicle System Dynamics*, 39(3), 189-226, DOI: 10.1076/vesd.39.3.189.14152

CEN/TS 13036-2: Road and airfield surface characteristics – Test methods – Part 2: Assessment of the skid resistance of a road pavement surface by the use of dynamic measuring systems, *HZN*, 2011

Chai, T., & Draxler, R. R. (2014). Root mean square error (RMSE) or mean absolute error (MAE)? *Geosci. Model Dev. Discuss*, 7, 1525–1534. <https://doi.org/10.5194/gmdd-7-1525-2014>

Chen, B., Xiong, C., Li, W., He, J., & Zhang, X. (2021). Assessing surface texture features of asphalt pavement based on three-dimensional laser scanning technology. *Buildings*, 11(12). <https://doi.org/10.3390/buildings11120623>

Chen, D. (2020). Evaluating asphalt pavement surface texture using 3D digital imaging. *International Journal of Pavement Engineering*, 21(4), 416–427. <https://doi.org/10.1080/10298436.2018.1483503>

Chen, D., Roohi Sefidmazgi, N., & Bahia, H. (2015). Exploring the feasibility of evaluating asphalt pavement surface macro-texture using image-based texture analysis method. *Road Materials and Pavement Design*, 16(2), 405–420. <https://doi.org/10.1080/14680629.2015.1016547>

Chen, J., Huang, X., Zheng, B., Zhao, R., Liu, X., Cao, Q., & Zhu, S. (2019). Real-time identification system of asphalt pavement texture based on the close-range photogrammetry. *Construction and Building Materials*, 226, 910–919. <https://doi.org/10.1016/j.conbuildmat.2019.07.321>

- Chen, J.-S., Sun, Y.-C., Liao, M.-C., Chien, ;, Huang, C., & Tsou, K.-W. (2013). *Evaluation of Permeable Friction Course Mixes with Various Binders and Additives*.
[https://doi.org/10.1061/\(ASCE\)MT](https://doi.org/10.1061/(ASCE)MT)
- Chen, S., Liu, X., Luo, H., Yu, J., Chen, F., Zhang, Y., Ma, T., & Huang, X. (2022). A state-of-the-art review of asphalt pavement surface texture and its measurement techniques. *Journal of Road Engineering*, 2(2), 156–180. <https://doi.org/10.1016/j.jreng.2022.05.003>
- Chou, C. P., Lee, C. C., Chen, A. C., & Wu, C. Y. (2017). Using a constructive pavement texture index for skid resistance screening. *International Journal of Pavement Research and Technology*, 10(4), 360–368. <https://doi.org/10.1016/j.ijprt.2017.05.002>
- Ciavarella, M., Greenwood, J. A., & Paggi, M. (2008). Inclusion of “interaction” in the Greenwood and Williamson contact theory. *Wear*, 265(5–6), 729–734.
<https://doi.org/10.1016/j.wear.2008.01.019>
- Čelko, J., Kováč, M., & Kotek, P. (2016). Analysis of the Pavement Surface Texture by 3D Scanner. *Transportation Research Procedia*, 14, 2994–3003.
<https://doi.org/10.1016/j.trpro.2016.05.434>
- D’Apuzzo, M., Evangelisti, A., & Nicolosi, V. (2012). Preliminary Findings for a Prediction Model of Road Surface Macrotecture. *Procedia - Social and Behavioral Sciences*, 53, 1109–1118. <https://doi.org/10.1016/j.sbspro.2012.09.960>
- Daoud, J. I. (2018). Multicollinearity and Regression Analysis. *Journal of Physics: Conference Series*, 949(1). <https://doi.org/10.1088/1742-6596/949/1/012009>
- Dell’Acqua, G., De Luca, M., & Lamberti, R. (2011). Indirect skid resistance measurement for porous asphalt pavement management. *Transportation Research Record*, 2205, 147–154.
<https://doi.org/10.3141/2205-19>
- Deng, Q., Zhan, Y., Liu, C., Qiu, Y., & Zhang, A. (2021). Multiscale power spectrum analysis of 3D surface texture for prediction of asphalt pavement friction. *Construction and Building Materials*, 293. <https://doi.org/10.1016/j.conbuildmat.2021.123506>
- Descantes, Y., & Hamard, E. (2015). Parameters influencing the polished stone value (PSV) of road surface aggregates. *Construction and Building Materials*, 100, 246–254.
<https://doi.org/10.1016/j.conbuildmat.2015.10.002>
- Do, M. T., Tang, Z., Kane, M., & de Larrard, F. (2009). Evolution of road-surface skid-resistance and texture due to polishing. *Wear*, 266(5–6), 574–577.
<https://doi.org/10.1016/j.wear.2008.04.060>

- Dunford, A. M., Parry, A. R., Shipway, P. H., & Viner, H. E. (2012). Three-dimensional characterisation of surface texture for road stones undergoing simulated traffic wear. *Wear*, 292–293, 188–196. <https://doi.org/10.1016/j.wear.2012.05.010>
- Edl, M., Mizerák, M., & Trojan, J. (2018). 3D laser scanners: history and applications. *Acta Simulatio*, 4(4), 1–5. <https://doi.org/10.22306/asim.v4i4.54>
- Edmondson, V., Woodward, J., Lim, M., Kane, M., Martin, J., & Shyha, I. (2019). Improved non-contact 3D field and processing techniques to achieve macrotexture characterisation of pavements. *Construction and Building Materials*, 227. <https://doi.org/10.1016/j.conbuildmat.2019.116693>
- Eiríksson, E. R., Wilm, J., Pedersen, D. B., & Aanæs, H. (2016). Precision and accuracy parameters in structured light 3D scanning. *The International Archives of the Photogrammetry, Remote Sensing and Spatial Information Sciences*, XL-5/W8, 7–15. <https://doi.org/10.5194/isprs-archives-xl-5-w8-7-2016>
- El Gendy, A., Shalaby, A., Saleh, M., & Flintsch, G. W. (2011). Stereo-vision applications to reconstruct the 3D texture of pavement surface. *International Journal of Pavement Engineering*, 12(3), 263–273. <https://doi.org/10.1080/10298436.2010.546858>
- Elunai, R., Chandran, V., & Gallagher, E. (2011). Asphalt concrete surfaces macrotexture determination from still images. *IEEE Transactions on Intelligent Transportation Systems*, 12(3), 857–869. <https://doi.org/10.1109/TITS.2011.2116784>
- Elunai, R., Chandran, V., & Mabukwa, P. (2010). Digital image processing techniques for pavement macro-texture analysis. *Proceedings of the 24th ARRB Conference: Building on 50 Years of Road Transport Research, ARRB Group Ltd., Sebel Hotel, Melbourne, Vic, Pp. 1-5*. <https://eprints.qut.edu.au/40770/>
- EN 13036-4: Road and airfield surface characteristics – Test methods – Part 4: Method for measurement of slip/skid resistance of a surface: The pendulum test, *HZN*, 2012
- EN ISO 13473-1: Characterization of pavement texture by use of surface profiles – Part 1: Determination of Mean Profile Depth, *HZN*, 2004
- EN 13036-1: Road and airfield surface characteristics – Test methods – Part 1: Measurement of pavement surface macrotexture depth using a volumetric patch technique, *HZN*, 2011
- EN ISO 13473-3: Characterization of pavement texture by use of surface profiles — Part 3: Specification and classification of profilometers, *HZN*, 2005
- EN ISO 21920-2: Geometrical product specifications (GPS) — Surface texture: Profile — Part 2: Terms, definitions and surface texture parameters, *HZN*, 2022

- EN ISO 25178-2: Geometrical product specifications (GPS) — Surface texture: Areal — Part 2: Terms, definitions and surface texture parameters, *HZN*, 2014
- EN 12697-33: Bituminous mixtures – Test methods for hot mix asphalt – Part 33: Specimen prepared by roller compactor, *HZN*, 2008
- Ergun, M., Iyınam, S., & Iyınam, A. F. (2005). Prediction of road surface friction coefficient using only macro- and microtexture measurements. *Journal of Transportation Engineering*, *131*(4), 311–319. [https://doi.org/10.1061/\(ASCE\)0733-947X\(2005\)131:4\(311\)](https://doi.org/10.1061/(ASCE)0733-947X(2005)131:4(311))
- Florková, Z., & Komačka, J. (2015). Usage of microscope method for detection of aggregate microtexture. *Procedia Engineering*, *111*, 209–214. <https://doi.org/10.1016/j.proeng.2015.07.078>
- Fwa, T. F. (2017). Skid resistance determination for pavement management and wet-weather road safety. *International Journal of Transportation Science and Technology*, *6*(3), 217–227. <https://doi.org/10.1016/j.ijst.2017.08.001>
- Fwa, T. F. (2021). Determination and prediction of pavement skid resistance—connecting research and practice. *Journal of Road Engineering*, *1*, 43–62. <https://doi.org/10.1016/j.jreng.2021.12.001>
- Gendy, A. El, & Shalaby, A. (2007). *Mean Profile Depth of Pavement Surface Macrotecture Using Photometric Stereo Techniques*. <https://doi.org/10.1061/ASCE0733-947X2007133:7433>
- Genovese, A., Farroni, F., Papangelo, A., & Ciavarella, M. (2019). A discussion on present theories of rubber friction, with particular reference to different possible choices of arbitrary roughness cutoff parameters. *Lubricants*, *7*(10). <https://doi.org/10.3390/lubricants7100085>
- Gonzalez-Jorge, H., Solla, M., Armesto, J., & Arias, P. (2012). Novel method to determine laser scanner accuracy for applications in civil engineering. *Optica Applicata*, *42*(1), 43–53. <https://doi.org/10.5277/oa120104>
- Goubert, L., Do, M. T., Bergiers, A., Karisson, R., & Sandberg, U. (2014). ROSANNE Project Deliverable D4.1, 2014, <https://www.rosanne-project.eu/documents?id=7299#>
- Gupta, S., Saluja, K., Goyal, A., Vajpayee, A., & Tiwari, V. (2022). Comparing the performance of machine learning algorithms using estimated accuracy. *Measurement: Sensors*, *24*. <https://doi.org/10.1016/j.measen.2022.100432>
- Gwelo, A. S. (2019). Principal components to overcome multicollinearity problem. *Oradea Journal of Business and Economics*, University of Oradea, Faculty of Economics, *4*(1), 79-91, <https://ideas.repec.org/a/ora/jrojbe/v4y2019i1p79-91.html>.

- Haider, M., & Conter, M. (2010). TYROSAFE Project Final Summary Report. <http://tyrosafe.fehrl.org>
- Hall, J. W., Smith, K. L., Titus-Glover, L., Wambold, J. C., Yager, T. J., & Rado, Z. (2009). Guide for Pavement Friction, National Cooperative Highway Research Program, *The National Academies Press*, <https://doi.org/10.17226/23038>.
- Han, J., Hong, K., & Kim, S. (2012). Application of a Photogrammetric System for Monitoring Civil Engineering Structures, www.intechopen.com
- Harcarik, M., & Jankovych, R. (2016). Relationship between values of profile and areal surface texture parameters. *MM Science Journal*, 2016, 1659–1662. https://doi.org/10.17973/MMSJ.2016_12_2016206
- Hartikainen, L., Petry, F., & Westermann, S. (2014). Frequency-wise correlation of the power spectral density of asphalt surface roughness and tire wet friction. *Wear*, 317(1–2), 111–119. <https://doi.org/10.1016/j.wear.2014.05.017>
- Hastie, T., Tibshirani, R., & Friedman, J. (2009), The Elements of Statistical Learning 2nd edition, *Springer*, <https://hastie.su.domains/Papers/ESLII.pdf>
- Heinrich, G., & Klüppel, M. (2008). Rubber friction, tread deformation and tire traction. *Wear*, 265(7–8), 1052–1060. <https://doi.org/10.1016/j.wear.2008.02.016>
- Hou, Y., Wang, X., Sun, W., & Wang, L. (2018). A multiscale DEM-FEM approach to investigate the tire–pavement friction. *International Journal of Pavement Engineering*, 19(5), 399–406. <https://doi.org/10.1080/10298436.2017.1402596>
- Hu, L., Yun, D., Liu, Z., Du, S., Zhang, Z., & Bao, Y. (2016). Effect of three-dimensional macrotexture characteristics on dynamic frictional coefficient of asphalt pavement surface. *Construction and Building Materials*, 126, 720–729. <https://doi.org/10.1016/j.conbuildmat.2016.09.088>
- Hu, L., Yun, D., Liu, Z., Du, S., Zhang, Z., & Bao, Y. (2016). Effect of three-dimensional macrotexture characteristics on dynamic frictional coefficient of asphalt pavement surface. *Construction and Building Materials*, 126, 720–729. <https://doi.org/10.1016/j.conbuildmat.2016.09.088>
- Hu, Y., Sun, Z., Han, Y., Li, W., & Pei, L. (2022). Evaluate Pavement Skid Resistance Performance Based on Bayesian-LightGBM Using 3D Surface Macrotexture Data. *Materials*, 15(15). <https://doi.org/10.3390/ma15155275>
- Huang, C. (2010). Texture characteristics of unpolished and polished aggregate surfaces. *Tribology International*, 43(1–2), 188–196. <https://doi.org/10.1016/j.triboint.2009.05.024>

- Huang, C., & Huang, X. (2014). Effects of pavement texture on pavement friction: a review. In *Int. J. Vehicle Design*, 65, 3
- Huang, W., Liu, C., Guo, W., & Wei, Y. (2022). A Surface Texture Prediction Model Based on RIOHTrack Asphalt Pavement Testing Data. *Applied Sciences (Switzerland)*, 12(20). <https://doi.org/10.3390/app122010539>
- Huyan, J., Li, W., Tighe, S., Sun, Z., & Sun, H. (2020). Quantitative Analysis of Macrotecture of Asphalt Concrete Pavement Surface Based on 3D Data. *Transportation Research Record*, 2674(8), 732–744. <https://doi.org/10.1177/0361198120920269>
- Hyun, S., Pei, L., Molinari, J.-F., & Robbins, M. O. (2004). Finite-element analysis of contact between elastic self-affine surfaces, *Phys Rev E Stat Nonlin Soft Matter Phys*, 70(2):026117, doi: 10.1103/PhysRevE.70.026117
- Islam, S., Hossain, M., & Miller, R. (2019). Evaluation of pavement surface texture at the network level. *Nondestructive Testing and Evaluation*, 34(1), 87–98. <https://doi.org/10.1080/10589759.2018.1554067>
- Iuele, T. (2016). Road surface micro- and macrotecture evolution in relation to asphalt mix composition, *Proceedings of the International Conference on Advanced Materials and Engineering Structural Technology (ICAMEST 2015), China*, DOI: 10.1201/b20958-92
- Jacobs, T. D. B., Junge, T., & Pastewka, L. (2017). Quantitative characterization of surface topography using spectral analysis. In *Surface Topography: Metrology and Properties* (Vol. 5, Issue 1). IOP Publishing Ltd. <https://doi.org/10.1088/2051-672X/aa51f8>
- James, G., Witten, D., Hastie, T., & Tibshirani, R. (2021). An Introduction to Statistical Learning with Applications in R, 2nd edition, *Springer*, https://hastie.su.domains/ISLR2/ISLRv2_website.pdf
- James, M. R., Chandler, J. H., Eltner, A., Fraser, C., Miller, P. E., Mills, J. P., Noble, T., Robson, S., & Lane, S. N. (2019). Guidelines on the use of structure-from-motion photogrammetry in geomorphic research. *Earth Surface Processes and Landforms*, 44(10), 2081–2084. <https://doi.org/10.1002/esp.4637>
- Ji, J., Ren, W., Jiang, T., Dong, Y., Hou, Y., & Li, H. (2022). Establishment and Analysis of the Relationship Model between Macro-Texture and Skid Resistance Performance of Asphalt Pavement. *Coatings*, 12(10). <https://doi.org/10.3390/coatings12101464>
- Joshi, K., & Patil, B. (2020). Prediction of Surface Roughness by Machine Vision using Principal Components based Regression Analysis. *Procedia Computer Science*, 167, 382–391. <https://doi.org/10.1016/j.procs.2020.03.242>

- Kargah-Ostadi, N., & Howard, A. (2015). Monitoring Pavement Surface Macrotexture and Friction: Case Study. *Transportation Research Record*, 2525(1), 111–117.
<https://doi.org/10.3141/2525-12>
- Khasawneh, M. A., Liang, R. Y., & Street, S. M. (2012). Temperature Effect on Frictional Properties of HMA at Different Polishing Stages. In *Jordan Journal of Civil Engineering* (Vol. 6, Issue 1).
- Kienle, R., Ressel, W., Götz, T., & Weise, M. (2020). The influence of road surface texture on the skid resistance under wet conditions. *Proceedings of the Institution of Mechanical Engineers, Part J: Journal of Engineering Tribology*, 234(3), 313–319.
<https://doi.org/10.1177/1350650117753995>
- Kogbara, R. B., Masad, E. A., Kassem, E., Scarpas, A., & Anupam, K. (2016). A state-of-the-art review of parameters influencing measurement and modeling of skid resistance of asphalt pavements. In *Construction and Building Materials* (Vol. 114, pp. 602–617). Elsevier Ltd.
<https://doi.org/10.1016/j.conbuildmat.2016.04.002>
- Kogbara, R. B., Masad, E. A., Woodward, D., & Millar, P. (2018). Relating surface texture parameters from close range photogrammetry to Grip-Tester pavement friction measurements. *Construction and Building Materials*, 166, 227–240.
<https://doi.org/10.1016/j.conbuildmat.2018.01.102>
- Kokkalis, A. G. [, & Panagouli, O. K. [. (1998). Fractal Evaluation of Pavement Skid Resistance Variations. I :Surface Wetting. *Chaos\ Solitons + Fractals*, 8.
- Korstanje, J. (2021), Assumptions of linear regression, *Towards data science*,
<https://towardsdatascience.com/assumptions-of-linear-regression-fdb71ebeaa8b>
- Kotek, P., & Kováč, M. (2015). Comparison of valuation of skid resistance of pavements by two device with standard methods. *Procedia Engineering*, 111, 436–443.
<https://doi.org/10.1016/j.proeng.2015.07.113>
- Kouchaki, S., Roshani, H., Prozzi, J. A., Garcia, N. Z., & Hernandez, J. B. (2018). Field Investigation of Relationship between Pavement Surface Texture and Friction. *Transportation Research Record*, 2672(40), 395–407. <https://doi.org/10.1177/0361198118777384>
- Kováč, M., Brna, M., & Decký, M. (2021). *Pavement Friction Prediction Using 3D Texture Parameters*. 11, 1180. <https://doi.org/10.3390/coatings11>
- Kumar, A., & Gupta, A. (2021). Review of Factors Controlling Skid Resistance at Tire-Pavement Interface. In *Advances in Civil Engineering* (Vol. 2021). Hindawi Limited.
<https://doi.org/10.1155/2021/2733054>

- Lafi, S. Q., & Kaneene, J. B. (1992). An explanation of the use of principal-components analysis to detect and correct for multicollinearity. In *Preventive Veterinary Medicine* (Vol. 13).
- Lague, D., Brodu, N., & Leroux, J. (2013). Accurate 3D comparison of complex topography with terrestrial laser scanner : application to the Rangitikei canyon (N-Z), *ISPRS Journal of Photogrammetry and Remote Sensing*, 82, 10-26, <https://doi.org/10.1016/j.isprsjprs.2013.04.009>
- Li, L., Wang, K. C. P., & Li, Q. J. (2016). Geometric texture indicators for safety on AC pavements with 1 mm 3D laser texture data. *International Journal of Pavement Research and Technology*, 9(1), 49–62. <https://doi.org/10.1016/j.ijprt.2016.01.004>
- Li, Q. (Joshua), Yang, G., Wang, K. C. P., Zhan, Y. (Jason), & Wang, C. (2017). Novel Macro- and Microtexture Indicators for Pavement Friction by Using High-Resolution Three-Dimensional Surface Data. *Transportation Research Record*, 2641(1), 164–176. <https://doi.org/10.3141/2641-19>
- Li, Q. J., Zhan, Y., Yang, G., & Wang, K. C. P. (2020). Pavement skid resistance as a function of pavement surface and aggregate texture properties. *International Journal of Pavement Engineering*, 21(10), 1159–1169. <https://doi.org/10.1080/10298436.2018.1525489>
- Litzka, J., Leben, B., La Torre, F., Weninger-Vycudil, A., Antunes, M., Kokot, D., Mladenovic, G., Brittain, S., & Viner, H. (2008). *COST Action 354 Performance Indicators for Road Pavements Final Project Report*. www.cost.esf.org
- Liu, C., Zhang, X., Nguyen, T. T., Liu, J., Wu, T., Lee, E., & Tu, X. M. (2022). Partial least squares regression and principal component analysis: Similarity and differences between two popular variable reduction approaches. In *General Psychiatry* (Vol. 35, Issue 1). BMJ Publishing Group. <https://doi.org/10.1136/gpsych-2021-100662>
- Liu, J., Guan, B., Chen, H., Liu, K., Xiong, R., & Xie, C. (2020). Dynamic model of polished stone value attenuation in coarse aggregate. *Materials*, 13(8). <https://doi.org/10.3390/MA13081875>
- Liu, X., Cao, Q., Wang, H., Chen, J., & Huang, X. (2019). Evaluation of Vehicle Braking Performance on Wet Pavement Surface using an Integrated Tire-Vehicle Modeling Approach. *Transportation Research Record*, 2673(3), 295–307. <https://doi.org/10.1177/0361198119832886>
- Lorenz, B. (2012). Contact mechanics and friction of elastic solids on hard and rough substrates. *Hochschulbibliothek Rheinisch-Westfälische Technischen Hochschule Aachen*, https://user.fz-juelich.de/record/21170/files/Schlusseltech_37.pdf?version=1

- Lorenz, B., Oh, Y. R., Nam, S. K., Jeon, S. H., & Persson, B. N. J. (2015). Rubber friction on road surfaces: Experiment and theory for low sliding speeds. *Journal of Chemical Physics*, *142*(19). <https://doi.org/10.1063/1.4919221>
- Lorenz, B., Persson, B. N. J., Dieluweit, S., & Tada, T. (2011). Rubber friction: Comparison of theory with experiment. *European Physical Journal E*, *34*(12). <https://doi.org/10.1140/epje/i2011-11129-1>
- Luan, B. Q., Hyun, S., Molinari, J. F., Bernstein, N., & Robbins, M. O. (2006). Multiscale modeling of two-dimensional contacts. *Physical Review E - Statistical, Nonlinear, and Soft Matter Physics*, *74*(4). <https://doi.org/10.1103/PhysRevE.74.046710>
- Luhmann, T., Robson, S., Kyle, S., & Harley, I. (2006). *Close Range Photogrammetry*. <http://www.tiespl.com/sites/default/files/pdfebook/Full%20page%20Html%20interface/pdf/Photogrammetry.pdf>
- Ma, Z., & Liu, S. (2018). A review of 3D reconstruction techniques in civil engineering and their applications. In *Advanced Engineering Informatics* (Vol. 37, pp. 163–174). Elsevier Ltd. <https://doi.org/10.1016/j.aei.2018.05.005>
- Maas, H. G., & Hampel, U. (2006). Programmetric techniques in civil engineering material testing and structure monitoring. *Photogrammetric Engineering and Remote Sensing*, *72*(1), 39–45. <https://doi.org/10.14358/PERS.72.1.39>
- Mahboob Kanafi, M., & Tuononen, A. J. (2017). Top topography surface roughness power spectrum for pavement friction evaluation. *Tribology International*, *107*, 240–249. <https://doi.org/10.1016/j.triboint.2016.11.038>
- Mahboob Kanafi, M., Kuosmanen, A., Pellinen, T. K., & Tuononen, A. J. (2015). Macro-and micro-texture evolution of road pavements and correlation with friction. *International Journal of Pavement Engineering*, *16*(2), 168–179. <https://doi.org/10.1080/10298436.2014.937715>
- Maitra, S., & Yan, J. (2008). Principle Component Analysis and Partial Least Squares--Two Dimension Reduction Techniques for Regression. <https://www.semanticscholar.org/paper/Principle-Component-Analysis-and-Partial-Least-Two-Maitra-Yan/8276a0c6d57335a18547776fcfa7be639c13b822#cited-papers>
- Marcelino, P., de Lurdes Antunes, M., Fortunato, E., & Gomes, M. C. (2017). Machine learning for pavement friction prediction using scikit-learn. *Lecture Notes in Computer Science (Including Subseries Lecture Notes in Artificial Intelligence and Lecture Notes in Bioinformatics)*, *10423 LNAI*, 331–342. https://doi.org/10.1007/978-3-319-65340-2_28

Mataei, B., Moghadas Nejad, F., Zahedi, M., & Zakeri, H. (2018). Evaluation of pavement surface drainage using an automated image acquisition and processing system. *Automation in Construction*, 86, 240–255. <https://doi.org/10.1016/j.autcon.2017.11.010>

Mathavan, S., Kamal, K., & Rahman, M. (2015). A Review of Three-Dimensional Imaging Technologies for Pavement Distress Detection and Measurements. *IEEE Transactions on Intelligent Transportation Systems*, 16(5), 2353–2362.

<https://doi.org/10.1109/TITS.2015.2428655>

Matlack, G. R., Horn, A., Aldo, A., Walubita, L. F., Naik, B., & Khoury, I. (2023). Measuring surface texture of in-service asphalt pavement: evaluation of two proposed hand-portable methods. *Road Materials and Pavement Design*, 24(2), 592–608.

<https://doi.org/10.1080/14680629.2021.2009902>

McQuaid, G., Millar, P., & Woodward, D. (2014). *A comparison of techniques to determine surface texture data*.

https://www.academia.edu/48773458/A_comparison_of_techniques_to_determine_surface_texture_data

Medeiros, M., Babadopulos, L., Maia, R., & Castelo Branco, V. (2021). 3D pavement macrotexture parameters from close range photogrammetry. *International Journal of Pavement Engineering*. <https://doi.org/10.1080/10298436.2021.2020784>

Meegoda, J. N., & Gao, S. (2015). Evaluation of pavement skid resistance using high speed texture measurement. *Journal of Traffic and Transportation Engineering (English Edition)*, 2(6), 382–390. <https://doi.org/10.1016/j.jtte.2015.09.001>

Melkumova, L. E., & Shatskikh, S. Y. (2017). Comparing Ridge and LASSO estimators for data analysis. *Procedia Engineering*, 201, 746–755.

<https://doi.org/10.1016/j.proeng.2017.09.615>

Metashape User Manual, v1.5 Professional Edition (2019), Agisoft Metashape LLC, Russia

Miao, Y., Li, J., Zheng, X., & Wang, L. (2016). Field investigation of skid resistance degradation of asphalt pavement during early service Skid resistance degradation of asphalt pavement. *International Journal of Pavement Research and Technology*, 9(4), 313–320.

<https://doi.org/10.1016/j.ijprt.2016.08.005>

Miao, Y., Wu, J., Hou, Y., Wang, L., Yu, W., & Wang, S. (2019). Study on asphalt pavement surface texture degradation using 3-D image processing techniques and entropy theory.

Entropy, 21(2). <https://doi.org/10.3390/e21020208>

Nacionalni plan sigurnosti cestovnog prometa Republike Hrvatske za razdoblje 2021. – 2030.. (2021). https://mup.gov.hr/UserDocsImages/2022/06/NPSCP_hr_web.pdf

- Nataadmadja, A. D., Do, M. T., Wilson, D. J., & Costello, S. B. (2015). Quantifying aggregate microtexture with respect to wear-Case of New Zealand aggregates. *Wear*, 332–333, 907–917. <https://doi.org/10.1016/j.wear.2014.11.028>
- Nguyen, V. T., & Hwu, C. (2019). Boundary element method for two-dimensional frictional contact problems of anisotropic elastic solids. *Engineering Analysis with Boundary Elements*, 108, 49–59. <https://doi.org/10.1016/j.enganabound.2019.08.010>
- Nitsche, P., & Spielhofer, R. (2009). *TYROSAFE Project Deliverable D06*. <http://tyrosafe.fehrl.org>
- Ostertagová, E. (2012). Modelling using polynomial regression. *Procedia Engineering*, 48, 500–506. <https://doi.org/10.1016/j.proeng.2012.09.545>
- Over, J. S., Ritchie, A. C., Kranenburg, C. J., Brown, J. A., Buscombe, D., Noble, T., Sherwood, C. R., Warrick, J., & Wernette, P. (2021). *Processing Coastal Imagery With Agisoft Metashape Professional Edition, Version 1.6-Structure From Motion Workflow Documentation*.
- Paggi, M., & Hills, D. (2020). *International Centre for Mechanical Sciences CISM International Centre for Mechanical Sciences Courses and Lectures 593 Modeling and Simulation of Tribological Problems in Technology*. <http://www.springer.com/series/76>
- Pajalić, S., Peranić, J., Maksimović, S., Čeh, N., Jagodnik, V., & Arbanas, Ž. (2021). Monitoring and data analysis in small-scale landslide physical model. *Applied Sciences (Switzerland)*, 11(11). <https://doi.org/10.3390/app111115040>
- Panahandeh, G., Ek, E., & Mohammadiha, M. (2017). Road Friction Estimation for Connected Vehicles using Supervised Machine Learning. *2017 IEEE Intelligent Vehicles Symposium (IV)*.
- Pawłowicz, J. A., Szafranko, E., & Harasymiuk, J. (2018). 3D laser scanning in civil engineering - Measurements of volume of earth masses. *IOP Conference Series: Materials Science and Engineering*, 324(1). <https://doi.org/10.1088/1757-899X/324/1/012005>
- Pawlus, P., Reizer, R., & Wieczorowski, M. (2021). Functional importance of surface texture parameters. In *Materials* (Vol. 14, Issue 18). MDPI. <https://doi.org/10.3390/ma14185326>
- Peng, Li, Zhan, Wang, & Yang. (2019). Finite Element Method-Based Skid Resistance Simulation Using In-Situ 3D Pavement Surface Texture and Friction Data. *Materials*, 12(23), 3821. <https://doi.org/10.3390/ma12233821>
- Pérez-Acebo, H., Gonzalo-Orden, H., & Rojí, E. (2019). Skid resistance prediction for new two-lane roads. *Proceedings of the Institution of Civil Engineers: Transport*, 172(5), 264–273. <https://doi.org/10.1680/jtran.17.00045>

- Permai, S. D., & Tanty, H. (2018). Linear regression model using bayesian approach for energy performance of residential building. *Procedia Computer Science*, 135, 671–677. <https://doi.org/10.1016/j.procs.2018.08.219>
- Persson, B. N. J. (2001). Theory of rubber friction and contact mechanics. *Journal of Chemical Physics*, 115(8), 3840–3861. <https://doi.org/10.1063/1.1388626>
- Persson, B. N. J. (2006). Contact mechanics for randomly rough surfaces. In *Surface Science Reports* (Vol. 61, Issue 4, pp. 201–227). <https://doi.org/10.1016/j.surfrep.2006.04.001>
- Persson, B. N. J., Albohr, O., Tartaglino, U., Volokitin, A. I., & Tosatti, E. (2005). On the nature of surface roughness with application to contact mechanics, sealing, rubber friction and adhesion. In *Journal of Physics Condensed Matter* (Vol. 17, Issue 1). <https://doi.org/10.1088/0953-8984/17/1/R01>
- Pikelj, K., Ružić, I., James, M. R., & Ilic, S. (2018). *Structure-from-Motion (SfM) monitoring of nourished gravel beaches in Croatia*. 561–564. <https://doi.org/10.1680/cmsb.63174.0561>
- Pomoni, M., Plati, C., Loizos, A., & Yannis, G. (2020). Investigation of pavement skid resistance and macrotexture on a long-term basis. *International Journal of Pavement Engineering*, 1–10. <https://doi.org/10.1080/10298436.2020.1788029>
- Popov, V. L. (2010). *Contact Mechanics and Friction*. <https://doi.org/10.1007/978-3-642-10803-7>
- Pranjić, I., & Deluka-Tibljaš, A. (2022). Pavement Texture–Friction Relationship Establishment via Image Analysis Methods. *Materials*, 15(3). <https://doi.org/10.3390/ma15030846>
- Pranjić, I., Deluka-Tibljaš, A., Cuculić, M., & Šurdonja, S. (2020). Influence of pavement surface macrotexture on pavement skid resistance. *Transportation Research Procedia*, 45, 747–754. <https://doi.org/10.1016/j.trpro.2020.02.102>
- Pranjić, I., Deluka-Tibljaš, A. (2019) Analiza vrijednosti makroteksture i hvatljivosti na definiranim dionicama autocesta A3 i A4 nakon hrapavljenja površine kolnika-Izveštaj, *Građevinski fakultet u Rijeci*, elaborat PB106
- Praticò, F. G., & Briante, P. G. (2020). Prediction of surface texture for better performance of friction courses. *Construction and Building Materials*, 230. <https://doi.org/10.1016/j.conbuildmat.2019.116991>
- Praticò, F. G., & Vaiana, R. (2013). A study on volumetric versus surface properties of wearing courses. *Construction and Building Materials*, 38, 766–775. <https://doi.org/10.1016/j.conbuildmat.2012.09.021>

- Praticò, F. G., Vaiana, R., & Iuele, T. (2015). Macrotexture modeling and experimental validation for pavement surface treatments. *Construction and Building Materials*, 95, 658–666. <https://doi.org/10.1016/j.conbuildmat.2015.07.061>
- Pratico, F. G., Vaiana, R., Moro, A., & Iuele, T. (2010). HMA composition vs surface characteristics: Issues and perspectives to optimise road asset management. *ICTi2010*. <https://www.researchgate.net/publication/260390447>
- Pravilnik o aktivnostima i postupcima za poboljšanje sigurnosti cestovne infrastrukture i reviziji cestovne sigurnosti (2022), *NN 55/2022-739*, https://narodne-novine.nn.hr/clanci/sluzbeni/2022_05_55_739.html
- Pravilnik o aktivnostima poboljšanja sigurnosti TEM cesta (2013), *NN 74/2013-1485*, https://narodne-novine.nn.hr/clanci/sluzbeni/2013_06_74_1485.html
- Pravilnik o održavanju cesta (2014), *NN 90/2014-1826*, https://narodne-novine.nn.hr/clanci/sluzbeni/2014_07_90_1826.html
- Pruksawan, S., Lambard, G., Samitsu, S., Sodeyama, K., & Naito, M. (2019). Prediction and optimization of epoxy adhesive strength from a small dataset through active learning. *Science and Technology of Advanced Materials*, 20(1), 1010–1021. <https://doi.org/10.1080/14686996.2019.1673670>
- Putignano, C., & Carbone, G. (2014). A review of boundary elements methodologies for elastic and viscoelastic rough contact mechanics. *Physical Mesomechanics*, 17(4), 321–333. <https://doi.org/10.1134/S1029959914040092>
- Puzzo, L., Loprencipe, G., Tozzo, C., & D'Andrea, A. (2017). Three-dimensional survey method of pavement texture using photographic equipment. *Measurement: Journal of the International Measurement Confederation*, 111, 146–157. <https://doi.org/10.1016/j.measurement.2017.07.040>
- Rajaei, Shabnam, Chatti, Karim, Dargazany, & Roozbeh. (2016). A review: Pavement Surface Micro-texture and its contribution to Surface Friction. *Proceedings of Transportation Research Board 96th Annual Meeting*, 17-06773, <https://trid.trb.org/view/1439716>
- Renaud, C., Feng, Z.-Q., Renaud -Zhi-, C., & Feng, Q. (2005). *Modeling of contact problems by boundary element and finite element methods*. <https://hal.archives-ouvertes.fr/hal-01509006>
- Rezaei, A., & Masad, E. (2013). Experimental-based model for predicting the skid resistance of asphalt pavements. *International Journal of Pavement Engineering*, 14(1), 24–35. <https://doi.org/10.1080/10298436.2011.643793>

- Rezaei, A., Hoyt, D., & Martin, A. (2011). Simple laboratory method for measuring pavement macrotexture. *Transportation Research Record*, 2227, 146–152. <https://doi.org/10.3141/2227-16>
- Rivas-Perea, P., Cota-Ruiz, J., Chaparro, D. G., Venzor, J. A. P., Carreón, A. Q., & Rosiles, J. G. (2013). Support Vector Machines for Regression: A Succinct Review of Large-Scale and Linear Programming Formulations. *International Journal of Intelligence Science*, 03(01), 5–14. <https://doi.org/10.4236/ijis.2013.31002>
- Rodríguez-Pérez, R., & Bajorath, J. (2022). Evolution of Support Vector Machine and Regression Modeling in Chemoinformatics and Drug Discovery. *Journal of Computer-Aided Molecular Design*, 36(5), 355–362. <https://doi.org/10.1007/s10822-022-00442-9>
- Roh, Y.-S., & Rhee, I. (2006). Application of Fractal Theory to Various Surfaces, *International Journal of Concrete Structures and Materials*, 18, 23-28
- Ružić, I., Marović, I., Benac, Č., & Ilić, S. (2014). Coastal cliff geometry derived from structure-from-motion photogrammetry at Stara Baška, Krk Island, Croatia. *Geo-Marine Letters*, 34(6), 555–565. <https://doi.org/10.1007/s00367-014-0380-4>
- Ružić, I., Marović, I., Benac, Č., & Ilić, S. (2015). A stability assessment of coastal cliffs using digital imagery. *Acta Geotechnica Slovenica*.
<https://www.researchgate.net/publication/287814408>
- Sansoni, G., Trebeschi, M., & Docchio, F. (2009). State-of-the-art and applications of 3D imaging sensors in industry, cultural heritage, medicine, and criminal investigation. In *Sensors* (Vol. 9, Issue 1, pp. 568–601). <https://doi.org/10.3390/s90100568>
- Sapirstein, P. (2016). Accurate measurement with photogrammetry at large sites. *Journal of Archaeological Science*, 66, 137–145. <https://doi.org/10.1016/j.jas.2016.01.002>
- Schreiber-Gregory, D. N. (2018). Ridge Regression and multicollinearity: An in-depth review. *Model Assisted Statistics and Applications*, 13(4), 359–365.
<https://doi.org/10.3233/MAS-180446>
- Segura, D., Khatib, E. J., & Barco, R. (2022). Dynamic Packet Duplication for Industrial URLLC. *Sensors*, 22(2). <https://doi.org/10.3390/s22020587>
- Senga, Y., Dony, A., Colin, J., Hamlat, S., & Berthaud, Y. (2013). Study of the skid resistance of blends of coarse aggregates with different polish resistances. *Construction and Building Materials*, 48, 901–907. <https://doi.org/10.1016/j.conbuildmat.2013.07.040>
- Serigos, P. A., De Fortier Smit, A., & Prozzi, J. A. (2014). Incorporating surface microtexture in the prediction of skid resistance of flexible pavements. In *Transportation Research Record* (Vol. 2457, pp. 105–113). National Research Council. <https://doi.org/10.3141/2457-11>

- Sha, A., Yun, D., Hu, L., & Tang, C. (2021). Influence of sampling interval and evaluation area on the three-dimensional pavement parameters. *Road Materials and Pavement Design*, 22(9), 1964–1985. <https://doi.org/10.1080/14680629.2020.1736607>
- Song, W. (2022). Correlation between morphology parameters and skid resistance of asphalt pavement. *Transportation Safety and Environment*, 4(1). <https://doi.org/10.1093/tse/tdac002>
- Specht, L. P., Khatchaturian, O., & Santos, R. T. Dos. (2013). Mensuração da macrotextura de pavimentos pelo processamento digital de imagens. *Acta Scientiarum - Technology*, 35(1), 31–38. <https://doi.org/10.4025/actascitechnol.v35i1.12808>
- Srirangam, S. K., Anupam, K., Kasbergen, C., & Scarpas, A. (Tom). (2017). Analysis of asphalt mix surface-tread rubber interaction by using finite element method. *Journal of Traffic and Transportation Engineering (English Edition)*, 4(4), 395–402. <https://doi.org/10.1016/j.jtte.2017.07.004>
- Sullivan, B. W. (2005). Development of a Fundamental Skid Resistance Asphalt Mix Design Procedure, *Proceedings of International Surface Friction Conference: roads and runways: improving safety through assessment and design*, Christchurch, New Zealand, <https://trid.trb.org/view/783679>
- Tadić, A., Ružić, I., Krvavica, N., & Ilić, S. (2022). Post-Nourishment Changes of an Artificial Gravel Pocket Beach Using UAV Imagery. *Journal of Marine Science and Engineering*, 10(3). <https://doi.org/10.3390/jmse10030358>
- Tang, T., Anupam, K., Kasbergen, C., Kogbara, R., Scarpas, A., & Masad, E. (2018). Finite Element Studies of Skid Resistance under Hot Weather Condition. *Transportation Research Record*, 2672(40), 382–394. <https://doi.org/10.1177/0361198118796728>
- Tang, Y., Li, L., Wang, C., Chen, M., Feng, W., Zou, X., & Huang, K. (2019). Real-time detection of surface deformation and strain in recycled aggregate concrete-filled steel tubular columns via four-ocular vision. *Robotics and Computer-Integrated Manufacturing*, 59, 36–46. <https://doi.org/10.1016/j.rcim.2019.03.001>
- Tehnički propis za asfaltne kolnike (2021), *NN 48/2021-977*, https://narodne-novine.nn.hr/clanci/sluzbeni/2021_05_48_977.html
- Tian, X., Xu, Y., Wei, F., Gungor, O., Li, Z., Wang, C., Li, S., & Shan, J. (2020). Pavement macrotexture determination using multi-view smartphone images. *Photogrammetric Engineering and Remote Sensing*, 86(10), 643–651. <https://doi.org/10.14358/PERS.86.10.643>
- Tonietto, L., Gonzaga, L., Veronez, M. R., Kazmierczak, C. de S., Arnold, D. C. M., & Costa, C. A. da. (2019). New Method for Evaluating Surface Roughness Parameters Acquired by Laser Scanning. *Scientific Reports*, 9(1). <https://doi.org/10.1038/s41598-019-51545-7>

Torbruegge, S., & Wies, B. (2015). Characterization of pavement texture by means of height difference correlation and relation to wet skid resistance. *Journal of Traffic and Transportation Engineering (English Edition)*, 2(2), 59–67.

<https://doi.org/10.1016/j.jtte.2015.02.001>

Tran, T. N., Afanador, N. L., Buydens, L. M. C., & Blanchet, L. (2014). Interpretation of variable importance in Partial Least Squares with Significance Multivariate Correlation (sMC). *Chemometrics and Intelligent Laboratory Systems*, 138, 153–160.

<https://doi.org/10.1016/j.chemolab.2014.08.005>

Transport Research Centre., International Transport Forum., & Organisation for Economic Co-operation and Development. (2008). *Towards zero : ambitious road safety targets and the safe system approach*. OECD.

Trevisan, V. (2022) Comparing Robustness of MAE, MSE and RMSE, *Towards data science*, <https://towardsdatascience.com/comparing-robustness-of-mae-mse-and-rmse-6d69da870828#:~:text=It%20is%20expected%20that%20the,is%20higher%20than%20the%20MAE.>

Ueckermann, A., Wang, D., Oeser, M., & Steinauer, B. (2015). Calculation of skid resistance from texture measurements. *Journal of Traffic and Transportation Engineering (English Edition)*, 2(1), 3–16. <https://doi.org/10.1016/j.jtte.2015.01.001>

Uyanık, G. K., & Güler, N. (2013). A Study on Multiple Linear Regression Analysis. *Procedia - Social and Behavioral Sciences*, 106, 234–240.

<https://doi.org/10.1016/j.sbspro.2013.12.027>

Vaiana, R., Capiluppi, G. F., Gallelli, V., Iuele, T., & Minani, V. (2012). Pavement Surface Performances Evolution: an Experimental Application. *Procedia - Social and Behavioral Sciences*, 53, 1149–1160. <https://doi.org/10.1016/j.sbspro.2012.09.964>

Vakis, A. I., Yastrebov, V. A., Scheibert, J., Nicola, L., Dini, D., Minfray, C., Almqvist, A., Paggi, M., Lee, S., Limbert, G., Molinari, J. F., Anciaux, G., Aghababaei, R., Echeverri Restrepo, S., Papangelo, A., Cammarata, A., Nicolini, P., Putignano, C., Carbone, G., ... Ciavarella, M. (2018). Modeling and simulation in tribology across scales: An overview. In *Tribology International* (Vol. 125, pp. 169–199). Elsevier Ltd.

<https://doi.org/10.1016/j.triboint.2018.02.005>

Wagner, P., Wriggers, P., Veltmaat, L., Clasen, H., Prange, C., & Wies, B. (2017). Numerical multiscale modelling and experimental validation of low speed rubber friction on rough road surfaces including hysteretic and adhesive effects. *Tribology International*, 111, 243–253.

<https://doi.org/10.1016/j.triboint.2017.03.015>

- Wallman, C.-G., & Åström, H. (2001). Friction measurement methods and the correlation between road friction and traffic safety: A literature review. Swedish National Road and Transport Research Institute, <http://www.diva-portal.org/smash/get/diva2:673366/FULLTEXT01.pdf>
- Wambold, J. C., Antie, C. E., Henry, J. J., & Rado, Z. (1995). International PIARC experiment to compare and harmonize texture and skid resistance measurements, *PIARC*, Paris France, <https://www.diva-portal.org/smash/get/diva2:1646664/FULLTEXT01.pdf>
- Wang, T., Hu, L., Pan, X., Xu, S., & Yun, D. (2020). Effect of the compactness on the texture and friction of asphalt concrete intended for wearing course of the road pavement. *Coatings*, *10*(2). <https://doi.org/10.3390/coatings10020192>
- Wang, W., Yan, X., Huang, H., Chu, X., & Abdel-Aty, M. (2011). Design and verification of a laser based device for pavement macrotexture measurement. *Transportation Research Part C: Emerging Technologies*, *19*(4), 682–694. <https://doi.org/10.1016/j.trc.2010.12.001>
- Wang, Y., Yang, Z., Liu, Y., & Sun, L. (2019). The characterisation of three-dimensional texture morphology of pavement for describing pavement sliding resistance. *Road Materials and Pavement Design*, *20*(5), 1076–1095. <https://doi.org/10.1080/14680629.2018.1433710>
- Woodward, D., & Jellie, A. (2003). *Predicting the early life skid resistance of asphalt surfacings*. <https://pure.ulster.ac.uk/en/publications/predicting-the-early-life-skid-resistance-of-asphalt-surfacings-3>
- Woodward, D., Millar, P., & Mcquaid, G. (2014). Use of 3D modelling techniques to better understand road surface textures, *Proceedings of International Safer Roads Conference 4th edition*, Cheltenham, United Kingdom, <https://trid.trb.org/view/1327163>
- Wriggers, P., & Reinelt, J. (2009). Multi-scale approach for frictional contact of elastomers on rough rigid surfaces. *Computer Methods in Applied Mechanics and Engineering*, *198*(21–26), 1996–2008. <https://doi.org/10.1016/j.cma.2008.12.021>
- Xie, X., Wang, C., Wang, D., Fan, Q., & Oeser, M. (2019). Evaluation of Polishing Behavior of Fine Aggregates Using an Accelerated Polishing Machine with Real Tires. *Journal of Transportation Engineering, Part B: Pavements*, *145*(2), 04019015. <https://doi.org/10.1061/jpeodx.0000116>
- Yan, Y., Ran, M., Sandberg, U., Zhou, X., & Xiao, S. (2020). Spectral techniques applied to evaluate pavement friction and surface texture. *Coatings*, *10*(4), 1–13. <https://doi.org/10.3390/coatings10040424>

- Yang, G., Li, Q. J., Zhan, Y. J., Wang, K. C. P., & Wang, C. (2018). Wavelet based macrotexture analysis for pavement friction prediction. *KSCE Journal of Civil Engineering*, 22(1), 117–124. <https://doi.org/10.1007/s12205-017-1165-x>
- Yang, G., Li, Q. J., Zhan, Y., Fei, Y., & Zhang, A. (2018). Convolutional Neural Network–Based Friction Model Using Pavement Texture Data. *Journal of Computing in Civil Engineering*, 32(6). [https://doi.org/10.1061/\(asce\)cp.1943-5487.0000797](https://doi.org/10.1061/(asce)cp.1943-5487.0000797)
- Yang, Z., Deng, X., & Li, Z. (2019). Numerical modeling of dynamic frictional rolling contact with an explicit finite element method. *Tribology International*, 129, 214–231. <https://doi.org/10.1016/j.triboint.2018.08.028>
- Yoo, W., Mayberry, R., Bae, S., Singh, K., & Lillard, J. W. (2014). A Study of Effects of MultiCollinearity in the Multivariable Analysis. In *Int J Appl Sci Technol* (Vol. 4, Issue 5).
- Yu, M., Liu, S., You, Z., Yang, Z., Li, J., Yang, L. M., & Chen, G. (2023). A prediction model of the friction coefficient of asphalt pavement considering traffic volume and road surface characteristics. *International Journal of Pavement Engineering*, 24(1). <https://doi.org/10.1080/10298436.2022.2160451>
- Yu, M., Wu, G., Kong, L., & Tang, Y. (2017). Tire-pavement friction characteristics with elastic properties of asphalt pavements. *Applied Sciences (Switzerland)*, 7(11). <https://doi.org/10.3390/app7111123>
- Yu, M., You, Z., Wu, G., Kong, L., Liu, C., & Gao, J. (2020). Measurement and modeling of skid resistance of asphalt pavement: A review. In *Construction and Building Materials* (Vol. 260). Elsevier Ltd. <https://doi.org/10.1016/j.conbuildmat.2020.119878>
- Yun, D., Hu, L., & Tang, C. (2020). Tire-Road contact area on asphalt concrete pavement and its relationship with the skid resistance. *Materials*, 13(3). <https://doi.org/10.3390/ma13030615>
- Zakon o cestama (2023), *NN 04/23*, <https://www.zakon.hr/z/244/Zakon-o-cestama>
- Zakon o sigurnosti prometa na cestama (2023), *NN 114/22*, <https://www.zakon.hr/z/78/Zakon-o-sigurnosti-prometa-na-cestama>
- Zazo, S., Rodríguez-González, P., Molina, J. L., González-Aguilera, D., Agudelo-Ruiz, C. A., & Hernández-López, D. (2018). Flood hazard assessment supported by reduced cost aerial precision photogrammetry. *Remote Sensing*, 10(10). <https://doi.org/10.3390/rs10101566>
- Zeilew, H. M., Papagiannakis, A. T., & De León Izeppi, E. D. (2013). Pavement macrotexture analysis using wavelets. *International Journal of Pavement Engineering*, 14(8), 725–735. <https://doi.org/10.1080/10298436.2012.705004>

- Zhan, Y., Li, J. Q., Liu, C., Wang, K. C. P., Pittenger, D. M., & Musharraf, Z. (2021). Effect of aggregate properties on asphalt pavement friction based on random forest analysis. *Construction and Building Materials*, 292. <https://doi.org/10.1016/j.conbuildmat.2021.123467>
- Zhan, Y., Li, J. Q., Yang, G., Wang, Kelvin. C. P., & Yu, W. (2020). Friction-ResNets: Deep Residual Network Architecture for Pavement Skid Resistance Evaluation. *Journal of Transportation Engineering, Part B: Pavements*, 146(3), 04020027. <https://doi.org/10.1061/jpeodx.0000187>
- Zou, Y., Yang, G., Huang, W., Lu, Y., Qiu, Y., & Wang, K. C. P. (2021). Study of pavement micro-and macro-texture evolution due to traffic polishing using 3d areal parameters. *Materials*, 14(19). <https://doi.org/10.3390/ma14195769>
- Zuniga-Garcia, N., & Prozzi, J. A. (2019). High-Definition Field Texture Measurements for Predicting Pavement Friction. *Transportation Research Record*, 2673(1), 246–260. <https://doi.org/10.1177/0361198118821598>

Curriculum Vitae

Ivana Ban was born on February 2nd 1990 in Travnik, Bosnia and Herzegovina. She finished the elementary school „Rikard Katalinić Jeretov“ in Opatija, Croatia and classical gymnasium „Salezijanska klasična gimnazija“ in Rijeka, Croatia. In 2008 she enrolled the university undergraduate study in civil engineering at the Faculty of Civil Engineering, University of Rijeka. In 2011 she obtained the university bachelor's degree in civil engineering and continued her academic education by enrolling the university graduate study in civil engineering at the same faculty. She obtained the university master's degree in civil engineering in 2013 by defending the master thesis titled „Analysis of traffic conditions and proposal for traffic system improvement in Turnić settlement in Rijeka“, under the supervision of prof.dr.sc. Aleksandra Deluka-Tibljaš. In 2015 she enrolled the postgraduate doctoral study in civil engineering at the Faculty of Civil Engineering, University of Rijeka. In 2022 she defended her doctoral thesis topic titled „A model for Skid Resistance Prediction Based on Non-Standard Pavement Surface Texture Parameters“, under the supervision of prof.dr.sc. Aleksandra Deluka-Tibljaš.

Ivana Ban began her professional career at the Faculty of Civil Engineering Rijeka as a temporary teaching assistant in 2013. She worked as a project administrator on a national project „Development and application of Croatian Framework for Qualifications (HKO) in the higher education of civil engineers“ from 2015 to 2016 at the same faculty. In 2017 she worked as a senior professional associate for communal affairs in Municipality Fužine, Croatia. In November 2017 she was elected to associate position of assistant at the Faculty of Civil Engineering Rijeka, Chair for Transportation, where she still works.

During her employment at the Faculty of Civil Engineering Rijeka Ivana Ban participated as a teaching associate in several courses at undergraduate and graduate university and professional studies related to the Chair for Transportation and other faculty Departments. She was an active collaborator in several professional projects managed by the Chair for Transportation and Laboratory for Transportation at the Faculty of Civil Engineering Rijeka, where she obtained a specific expertise in pavement data collection and analysis by specialized laboratory and field equipment. She collaborated on the creation of a national document „Guidelines for the design of roundabouts on Croatian state roads“ in 2014.

Ivana Ban is registered in the Croatian Register of Scientists under the number 365665. Being a doctoral student and a junior researcher, she actively participated or still collaborates on following scientific research projects:

- Sustainable pavement structures design in urban areas (2014 - 2016), managed by prof.dr.sc. Aleksandra Deluka-Tibljaš
- Traffic infrastructure as a function of sustainable urban mobility (2019 - 2022), managed by prof.dr.sc. Aleksandra Deluka-Tibljaš
- Separation of parameter influence in engineering modeling and parameter identification – SEPAEMPI (2019 -), managed by prof. dr.sc. Ivica Kožar
- Cement stabilized base courses with waste rubber for sustainable pavements – RubSuPave (2020 -), managed by assoc. prof. dr.sc. Ivana Barišić

In 2021 she spent three months at IMT School for Advanced Studies Lucca, Italy as a visiting PhD student under the supervision of prof.dr.sc. Marco Paggi. During her doctoral study she attended several summer schools and courses, domestic and international conferences and published the results of research work in papers included in conference proceedings. She participated in several conferences for doctoral students organized by University of Rijeka (My First Conference editions) and Croatian Civil Engineering Faculties Association (Zajednički Temelji editions) with oral presentations of current research work. She also participated in workshops and courses for the improvement of scientific and teaching skills organized by University of Rijeka and other institutions. She engaged in the promotion of scientific research activities of the Faculty of Civil Engineering Rijeka by participating in events such as European Researchers Night, Science Festival, Open Doors days and others. She is a member of the Board for the doctoral study at the Faculty of Civil Engineering Rijeka and administrates the social networks of the Faculty within the Group for the Promotion of faculty activities. She is a member of Croatian Society of Mechanics.

Ivana Ban published 19 papers in journals and conference proceedings, listed as follows (downloaded from Ivana Ban's CROSBI profile on July 11, 2023):

Ban, Ivana; Deluka Tibljaš, Aleksandra; Cuculić, Marijana (2022). Orthographic photogrammetry method for pavement texture characterization. // Proceedings of the 7th International Conference on Road and Rail Infrastructures CETRA 2022 / Lakušić, S. (ur.). Zagreb: Građevinski fakultet Sveučilišta u Zagrebu, 2022. str. 325-332 doi:10.5592/CO/CETRA.2022.1441

Pranjić, Ivana; Deluka-Tibljaš, Aleksandra (2022). Pavement Texture–Friction Relationship Establishment via Image Analysis Methods. // Materials, 15 (2022), 3; 846, 17 doi:10.3390/ma15030846

Kožar, Ivica; Pranjić, Ivana (2022). Nonlinear model for analysis of asphalt mixtures. // 10th International Congress of Croatian Society of Mechanics, Book of Abstracts, Pula, Hrvatska: Hrvatsko društvo za mehaniku (HDM), 2022. str. 161-162

Pranjić, Ivana; Torić Malić Neira; Kožar, Ivica (2021). Eksperimentalna analiza i numeričko modeliranje ponašanja asfaltnih mješavina. // Zbornik radova jedanaestog susreta Hrvatskog društva za mehaniku / Brčić, M. ; Skoblar, A. ; Ribarić, D. (ur.), Rijeka: Hrvatsko društvo za mehaniku (HDM), 2021. str. 227-233

Zagvozda, Martina; Zvonarić, Matija; Cuculić, Marijana; Pranjić, Ivana (2021). Waste rubber - sustainable pavements solution?. // Road and Rail Infrastructure VI, Proceedings of the Conference CETRA 2020 / Lakušić, Stjepan (ur.), Zagreb, 2021. str. 859-865 doi:10.5592/CO/CETRA.2020.1138

Brkić, Iva; Deluka Tibljaš, Aleksandra; Cuculić, Marijana; Pranjić, Ivana (2021). Comparison of standards and requirements for porous asphalt mixtures. // Road and Rail Infrastructure VI, Proceedings of the Conference CETRA 2020 / Lakušić, Stjepan (ur.), Zagreb: Građevinski fakultet Sveučilišta u Zagrebu, 2021. str. 1041-1048, doi:10.5592/CO/CETRA.2020.1135

Pranjić, Ivana; Deluka-Tibljaš, Aleksandra; Cuculić, Marijana; Šurdonja, Sanja (2020). Influence of pavement surface macrotexture on pavement skid resistance. // Transportation research procedia / Ignaccolo, M. ; Tiboni, M. (ur.), Rim, Italija, 2020. str. 747-754 doi:10.1016/j.trpro.2020.02.102

Pranjić, Ivana; Deluka-Tibljaš, Aleksandra; Berljafa, Ana; Demark, Sanel; Domijan, Ariana; Ilić, Josip; Krajnović, Anamarija; Kustić, Kristina; Petrašević, Ivan; Pogačić, Toni et al. (2020). Analiza prometnih pokazatelja na sveučilišnom kampusu – studija slučaja na Građevinskom fakultetu u Rijeci. // Zbornik radova (Građevinski fakultet Sveučilišta u Rijeci), 23 (2020), 137-152 doi:10.32762/zr.23.1.9

Cuculić, Marijana; Pranjić, Ivana; Deluka- Tibljaš, Aleksandra; Stanić, Ivan (2020). Analiza asfaltnih kolničkih konstrukcija na temelju podataka strukturalne nosivosti. // Zbornik radova (Građevinski fakultet Sveučilišta u Rijeci), 23 (2020), 41-55 doi:10.32762/zr.23.1.3

Cuculić, Marijana; Deluka Tibljaš, Aleksandra; Vasić, Fabian; Pranjić, Ivana (2019). The influence of porous asphalt mix design on raveling resistance. // 15th International Conference of Computational Methods in Sciences and Engineering (ICCMSE 2019) / Simos, Theodore E.; Kalogiratou, Zacharoula ; Monovasilis, Theodore (ur.), Rodos, Grčka: American Institute of Physics (AIP), 2019. 1063, 6 doi:10.1063/1.5138071

Pranjić, Ivana; Kožar, Ivica (2019). Burgerov reološki model za opisivanje ponašanja asfalta. // Zbornik radova devetog susreta Hrvatskog društva za mehaniku, Zagreb, 2019. str. 267-272

Pranjić, Ivana; Deluka-Tibljaš, Aleksandra; Cuculić, Marijana; Skender, Robert (2018). Pavement surface macrotexture analysis. // 5th International Conference on Road and Rail Infrastructure (CETRA 2018), Zadar, Hrvatska, 2018. str. 359-365, doi:10.5592/CO/CETRA.2018.706

Cuculić, Marijana; Deluka Tibljaš, Aleksandra; Pranjić, Ivana; Flego, Miran (2018). Analiza stanja kolničkih konstrukcija na autobusnim stajalištima u Gradu Rijeci. // Elektronički zbornik radova Građevinskog fakulteta u Mostaru, 1 (2018), 1; str. 51-59

Pranjić, Ivana; Deluka-Tibljaš, Aleksandra; Cvitanić, Dražen; Šurdonja, Sanja (2016). Analysis of sight distance at an at-grade intersection. // Road and Rail Infrastructure IV, Proceedings of the Conference CETRA 2016 / Stjepan Lakušić (ur.), Zagreb: Građevinski fakultet Sveučilišta u Zagrebu, 2016. str. 921-928

Šurdonja, Sanja; Pranjić, Ivana; Deluka-Tibljaš, Aleksandra; Renčelj, Marko (2016). Preglednost v nivojskih priključkih in križiščih: vpliv realno izmerjenih vrednosti (vhodnih podatkov) na izračun preglednih razdalj. // 13. Slovenski kongres o cestah in prometu - Proceedings / Tollazi, T. ; Lipar, P. ; Šemrov, D. (ur.), Portorož: Družba za raziskave v cestni in prometni stroki Slovenije, 2016. str. 1-7

Cuculić, Marijana; Deluka-Tibljaš, Aleksandra; Pranjić, Ivana; Skender, Robert (2016). Preliminarni rezultati interpretacije dobljenih rezultatov FWD meritev na izbranih cestnih odsekih na Hrvaškem. // 13. slovenski kongres o cestah in prometu - Proceedings / Tollazi, T. ; Lipar, P. ; Šemrov, D. (ur.), Portorož: Družba za raziskave v cestni in prometni stroki Slovenije, 2016. str. 1-6

Pranjić, Ivana; Cuculić, Marijana; Šurdonja, Sanja; Deluka-Tibljaš, Aleksandra (2015). Usporedba rezultata mjerenja trenja različitim tehnologijama. // 6. kongres o cestama 2015. - zbornik radova / Šimun, M. (ur.), Zagreb: Hrvatsko društvo za ceste - Via Vita ; Hrvatske ceste d.o.o., 2015., str. 20 - 26

Šurdonja, Sanja; Cuculić, Marijana; Pranjić, Ivana; Deluka-Tibljaš, Aleksandra; Renčelj, Marko (2015). Analiza mogućnosti unaprjeđenja sigurnosti u zonama pješačkih prijelaza izvan raskrižja-primjer iz grada Rijeke. // 6. hrvatski kongres o cestama, zbornik radova / Šimun, M. (ur.), Zagreb: Hrvatsko društvo za ceste - Via Vita ; Hrvatske ceste d.o.o., 2015. str. 1-6

Pranjić, Ivana; Deluka-Tibljaš, Aleksandra; Škunca, Srđan; Babić, Sergije; Močibob, Iva; Klarić, Martina; Golik, Tomislava (2014). Model unaprjeđenja prometnih uvjeta u stambenim naseljima - primjeri naselja u Gradu Rijeci. // Zbornik radova (Građevinski fakultet Sveučilišta u Rijeci), XVII (2014), str. 123-142